

Theoretical and Experimental Investigations of Ferrofluids Focusing on Locomotion Systems

Dissertationsschrift
zur Erlangung des akademischen Grades
Doktoringenieur (Dr.-Ing.)
2012

vorgelegt an der
Technischen Universität Ilmenau
Fakultät für Maschinenbau

von
Dipl.-Ing. Jana Popp
geboren am 20.06.1979 in Suhl, Deutschland

Gutachter:

1. Univ.-Prof. Dr.-Ing. habil. Klaus Zimmermann
Technische Universität Ilmenau, Fakultät für Maschinenbau,
Professur für Technische Mechanik
2. Univ.-Prof. Dr. rer. nat. habil. Stefan Odenbach
Technische Universität Dresden, Fakultät für Maschinenwesen
Professur für Magnetofluidynamik
3. Prof. Vera A. Naletova
M. V. Lomonosov Moskau Staatliche Universität, Russland
Fakultät für Mechanik und Mathematik

ISBN: 978-3-938843-77-2

URN:nbn:de:gbv:ilm1-2012000492

Contents

1. Introduction	1
1.1. Elementary Remarks on Ferrofluids	1
1.2. Elementary Remarks on Locomotion	5
2. State of the Art and Motivation of the Thesis	15
2.1. Structure of Projects of the Ilmenau Research Group .	15
2.2. Summary of Related Research	23
2.3. Motivation and Goals of the Study	31
3. Ferrofluid Based Locomotion due to Surface Deformation	37
3.1. The Other Way Around	37
3.2. Richter's Pump is not Ours	38
3.3. Introduction of the Problem	40
3.4. Introduction of Tools	42
3.4.1. Non-Dimensionalization	42
3.4.2. Governing Equations	42
3.4.3. Boundary Conditions	43
3.5. Approach	44
3.5.1. Approach from the Causative Agent	44
3.5.2. Determination of the Stream Function	46
3.6. Material Transport Mapped by the Flow Rate	47
3.7. Preparation of the Boundary Conditions	50
3.7.1. The Kinematic Boundary Conditions	50
3.7.2. Boundary Condition 4	51
3.8. The Existence of an Averaged Flow Rate	63
3.9. Analysis of the Analytical Results	64
3.10. The Accompanying Experiment – Setup	70
3.11. The Experimental Results	74
3.12. Discussion of the Analytical and Experimental Results	78
3.12.1. Principal Approach to the Design	78

Contents

3.12.2. Conclusion from the Current Results	81
4. Enhancement of Surface Deformation	83
4.1. Experimental Surface Manipulation	83
4.1.1. General Procedure and Strategies	83
4.1.2. Analysis and Data Extraction	86
4.1.3. Deformation and Phase Transitions	88
4.1.4. Hysteresis	95
4.2. Theoretical Description of Surface Manipulation	97
4.2.1. Introduction of the Model	97
4.2.2. Analysis of the Static Problem	100
4.2.3. Investigation of the Dynamic Problem	101
4.2.4. Critical Remarks	103
5. Applicational Study on a Bifluidic Flow Channel	105
5.1. Working Principal and Experimental Setup	105
5.2. The Measuring System	107
5.3. Analysis and Discussion of the Results	109
6. Forces for Ferrofluid Based Locomotion	115
6.1. Forces Generated by Ferrofluid for Passive Locomotion	115
6.2. Forces on Ferrofluid in Active Locomotion Systems	128
7. Instead of a Summary	139
7.1. Back to the Basic Idea	139
7.2. Active and Passive Locomotion Systems	141
7.3. Ferroelastomer Based Locomotion Systems	145
7.3.1. Worm-Like Locomotion Systems	145
7.3.2. Vibration Driven Locomotion Systems	146
7.4. Outlook	148
Appendix	151
A. Magnetic Matters Influencing Peristaltic Transport	151
A.1. Data Acquisition of the Magnetic Field	151
A.2. Data Acquisition of the Ferrofluid APG S12n	153
B. Additions to the Enhancement of Surface Deformation	155
C. Additions to the Channel Flow	156

Contents

Nomenclature	167
Bibliography	175
Acknowledgement	187

1. Introduction

1.1. Elementary Remarks on Ferrofluids

What are ferrofluids? Even though ferrofluids have not just been invented recently, but in the 1960's, they do not represent a commonly known and widely applied compound group. Therefore, some brief words about their nature.

Ferrofluids have no natural source, but have been developed in the mid-1960s by Steven Papell, [Pap65]. Working for NASA, he was occupied with fueling problems of the early space flight. The early samples of ferrofluid contained kerosene, oleic acid and magnetite particles, which had been grounded for several weeks to achieve the required minimal size. Around the same time, ferrofluids were also developed in the former Soviet Union, probably with a similar background. Scientific schools in Moscow, [Gog75, Nal76], and Kharkov, [Tar69, Tar73, Tar80], focused on magnetizable media and solved numerous theoretical problems. In the late 1960's and 1970's, in both hemispheres excellent scientists were working on ferrofluid matters and published substantial contributions on the basic theory already. Other early pioneers were for example Neuringer and Rosensweig, [Neu64], Zaitsev and Shliomis, [Zai68] and Bashtovoi and Berkovsky, [Bas73] - Marcus Zahn's bibliography, [Zah80], bears witness. By the way, free surface deformation in ferrofluids can be found along these early studies, too, [Ber73]. In the early 1980's, in Germany the research of magnetic fluids was established mainly by Stierstadt, [Wes85, Amb92, Liu09]. Odenbach, student of Stierstadt around that time, now the next generation, strongly pushes the German scientific landscape on ferrofluids further, [Ode01, Ode02a, Ode09].

1. Introduction

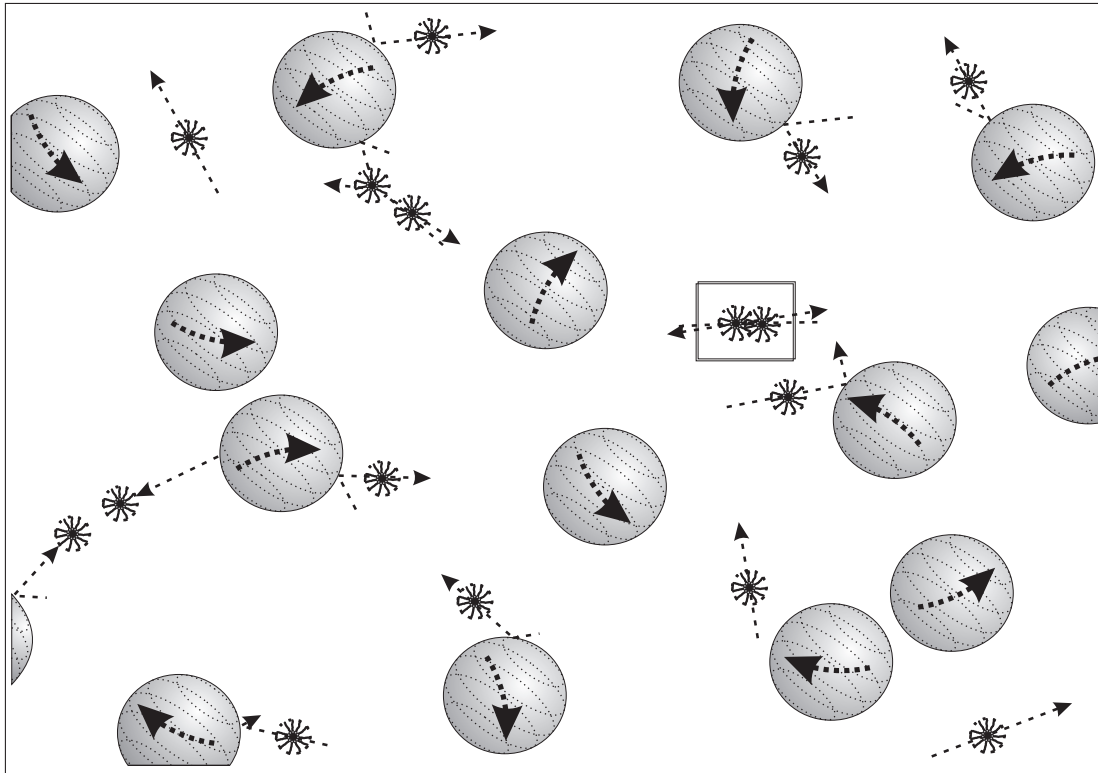


Figure 1.1.: *Molecule interaction: scheme of the BROWNIAN motion of magnetic particles and massive fluid molecules; homogeneous composition due to energy transfer.*

Modern ferrofluids still consist of colloidal sized particles, surfactant, and carrier liquid. The particles are of a ferromagnetic material, mostly of magnetite. Other iron or iron zinc alloys and cobalt are in use, too, but less commonly. Since a stable mixture is based on a balanced relation of thermal motion and counteracting weight forces, small masses and scales are required. Suitable particles are 2 to approximately 20 nm in size, below 1 – 2 nm they cannot maintain their magnetization, above a particle diameter of 20 nm the fluid enters the related group of magnetorheological fluids (MRFs), whose viscosity properties differ from those of ferrofluids. The MRF transition already starts at around 15 nm. The particle size is suitably conditioned either by grinding or by bacteria precipitation. Quantitatively, the former beats the biological retrieval by far.

Attracting forces, VAN DER WAALS and magnetic forces, act between the nanoparticles similar to intermolecular forces. Resulting agglom-

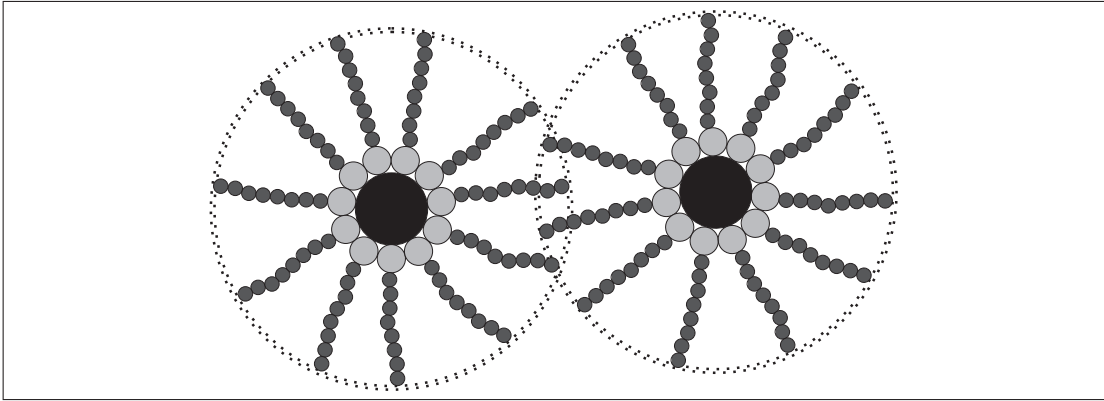


Figure 1.2.: *Sketch of a magnetic particle with nanometer sized metal core surrounded by polar surfactant molecules, the monomolecule layer prohibits the approach and agglomeration of metal particles due to VAN DER WAALS forces.*

erates tend to separate from the liquid phase especially under gravity and magnetic field influence. Its prevention is desired. The attracting forces depend on the distance between particles, VAN DER WAALS forces diminish faster than magnetic forces, and magnetic forces depend also on the particle size. To keep it brief, for sufficiently small particles it is possible to exceed the attraction range of the mentioned forces by providing a barrier of surfactant molecules. They are long chains with functional groups. Tail and head are tailored to fit particles and liquid base. The polar ends attach firmly to the magnetic particles creating a monomolecular layer. The tails are suitable for the fluid molecules (according to [Ber93, p 1-5]). Normally, water, isoparaffin (cerosin) or ester serve as carrier liquids. Their selection depends mostly on the field of application, e.g. water-based ferrofluids are chosen in biomedical practice. By collision due to BROWNIAN motion, the massive fluid molecules keep the smaller and lighter magnetite particles in abeyance. The energy transfer ensures a long-term stable suspension.

Although the integrated metal is ferromagnetic, the fluid itself shows (super)paramagnetic properties. Within a paramagnetic substance, the magnetic torques of the single atoms are orientated in all directions with equal probability, thus no magnetic moment results at the exterior of the body. When exposed to a magnetic field, the atoms acting as magnetic dipoles (particle size ensures single domains) aim to align

1. Introduction

along the field direction, whereupon the density of the magnetic force lines densifies slightly. As a visible effect, the paramagnetic substance is drawn inside an inhomogeneous magnetic field. The effective force is, however, small, [Sch81, p 429-430], [Ros85, p 5-8]. In other words, in an external magnetic field ferrofluids change their shape and position. To emphasize this, the characteristics of a conventional fluid shall be compared with those of a magnetizable fluid. The definition of a conventional fluid (according to White [Whi08, p 6]) is: “A solid can resist a shear stress by static deflection; a fluid cannot. Any shear stress applied to a fluid, no matter how small, will result in motion of that fluid. ...” Schnack [Sch09, p 2-3] compares it directly with magnetic fluids, see 1.3, and also illustrates the compensation deformation due to shear stress within conventional fluids. He indicates the resistance against external pressure. In the absence of external magnetic fields magnetizable fluids behave like any conventional fluid. But within a magnetic field, when charged by shear stress, they generate resisting forces against deformation.

Under certain conditions, magnetizable fluids develop a magneto-viscous effect. They react to an external magnetic field by the change of viscosity. Odenbach investigated the phenomenon in detail, [Ode02b]. Some magnetizable fluids incorporate strong magneto-dependent viscosities, in the utmost extent of the effect the fluid can turn solid-like. This group is called magnetorheological fluids. In the case of a weakly developed or non existing effect the fluid remains liquid. While still liquid, ferrofluids flow to the point of the highest magnetic field gradient and deform correspondingly to their aim. Rosensweig presents in his book of ferrofluid fundamentals, [Ros85], some impressive examples of ferrofluid 'flowing upwards' based on of the energy equilibrium. This magneto-influenced deformation is our starting point for research on ferrofluid based locomotion.

Despite ferrofluids being amazing and addressing to the play instinct in people, they are rarely used in engineering applications nor in commercial products. This lack of 'useful' application is mainly due to the costs, quality of longterm stability and chemical compatibility, difficult handling, and low usable forces [Pop06]. Observing the science communities, one can see the tendency of focusing on a 'better' ferrofluid fit, tailored for their tasks. Although they have been around for more

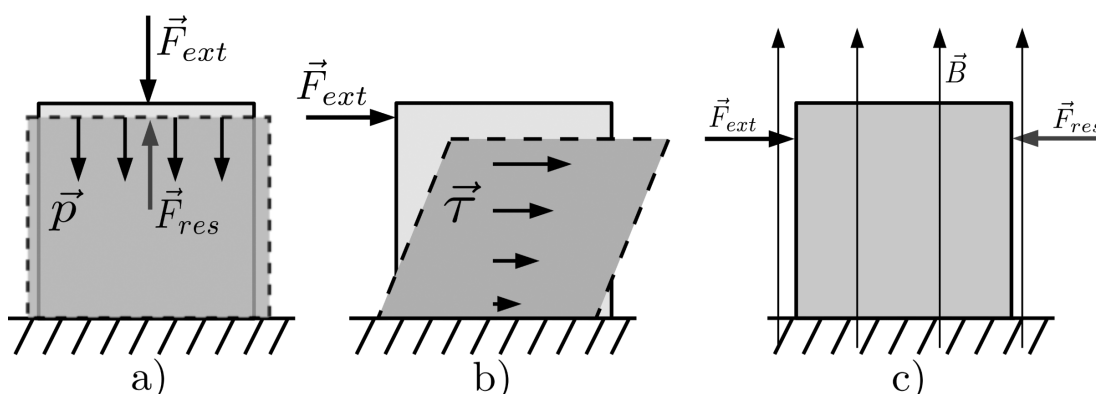


Figure 1.3.: a) Conventional (incompressible) fluids resist normal stress (pressure, caused by external force) by internal resisting forces. b) The conventional fluid does not stand against shear stress, but tends to minimize shear by deformation. c) Unlike a conventional fluid a magnetizable fluid builds up resisting forces against shear stress and maintains the original shape. [referring to [Sch09]]

than 50 years, basic research still dominates applied research. But after all, a recognizable amount of engineering solutions started to appear in the 1990's of the last century, [Pop06, Sch05a], most of them live inconspicuously rarely noticed by the public.

1.2. Elementary Remarks on Locomotion

When asked, most people have an intuitive idea of what locomotion is and what not. But if requesting a firm definition, it is difficult for most of us to correctly define the word. As far as the author knows, the perfect definition is not found, yet. Although (or due to?) the ability of intuitive distinction, finding an accurate, precise and exhaustive definition is a rather sophisticated feat. Steigenberger compiled [Ste11] several definitions. On basis of his work, the term *locomotion* shall be discussed.

Bögelsack and Schilling state in their contribution for IFTOMM, [od11], locomotion is an “autonomous, internally driven change of location ... during which the base of support and the center of mass of

1. Introduction

the body are displaced”. Huang, [Hua02], defines locomotion in the same manner as “a change of the location of a natural or technical system characterized by the steady change of the position of the center of mass including its contact layer to its environmental surroundings”. Abaza, [Aba06], demands the non-zero displacement of every point of a body for the distinction between motion and locomotion. But in [Ste11], Steigenberger successfully argues the necessity to widen the vista to criteria like shape and orientation in the (three-dimensional) space.

Like Ostrowski and Burdick, [Ost95, Ost98], who propose the idea of involved periodic processes, Steigenberger notes the hugest fraction of all locomotive processes is undulatory. He illustrates the subject of a body (either compliant or a multi body system of n rigid bodies), which is assigned to a reference configuration including its position $X(t_0)$ in the 3d-space and shape $q(t_0)$ at an initial time t_0 , fulfills a periodic motion within the period time T . Within the period, every specification of shape is assigned to a single specification of position due to kinematic constraints to the environment. At the time $t = t_0 + T$, one can observe the original shape is regained $q(t_0) = q(t_0 + T)$, but the position has changed $X(t_0) \neq X(t_0 + T)$. Consequently, position is not bijective regarding the shape, but in reverse, shape is bijective to the position, because the position X is a monotone function, whereas shape is a cyclic function and both are functions of time.

Several scientists, Bögelsack and Schilling, [od11], Steigenberger and Behn, [Ste11, Ste12], and Ostrowski, [Ost98], among them, set the condition of autonomous motion as stringent requirement for motion as locomotion. This demand implies the complete absence of external forces, which execute work. The locomotion must be solely propelled by internal driving forces. However, this does not exclude the external stiction forces, as they count as non-driving.

The *Ilmenau School* builds its term of 'locomotion' mainly upon the definitions of Bögelsack and Steigenberger, [od11, Ste11]. As the present thesis will focus strongly on field induced driving forces, we find a controversy about the criteria of completely internally generated driving forces. The idea of autonomy is interpreted differently. We understand energy autonomy as a detachment of supplying channels like cables or

1.2. Elementary Remarks on Locomotion

tubes. The energy source may be external, but the transmission to the locomotive object is unbound; it is field transferred. To discern between both modes (on board and field transferred energy supply), we orientate – orientate, not mimic in each detail – on the view of Forth and Schewitzer, [For76].

Investigating from the point of bionics and biomedical sciences, their differently structured classification system of locomotion distinguishes between active and passive locomotion (of biological systems). The former class discerns between locomotion at boundary layers (amoeboid motion, creeping, and three classes of extremity motion) and locomotion in media able of flow (air and gases – flying, liquids – swimming). The second category, passive locomotion, includes small biological systems with low specific weight, but comparatively, sometimes featured with additional extensions, huge surface areas to enable passages over up to a hundred kilometers through the carrier medium.

This thesis does not investigate biological systems. On the other hand, it analyses biologically inspired locomotion. So, why not take a page out of Forth and Schewitzer’s book, using the term of passive and active locomotion? Admittedly, a rearrangement according to the technical subject has to be done. Therefore we state:

Definition 1. *A system, which achieves motion driven by internally generated forces, which results in locomotion, is called an **active locomotion system**. The accordant activity is active locomotion.*

(The term ‘system’ is kept fuzzy on purpose.) In contrast to the internally supplied locomotion we define:

Definition 2. *A system producing motion, which is internally powered and is utilized for locomotion of a second object, incapable of independent locomotion, is called a **passive locomotion system**. The activity is called passive locomotion.*

The huge field of locomotion is craving for structure. From the point of view of biological inspiration for technical locomotion systems a helpful classification is given by [Wit03], see the figure 1.4 (translated, original in German).

¹Figure 1.4 by courtesy of H. Witte and C. Schilling.

1. Introduction

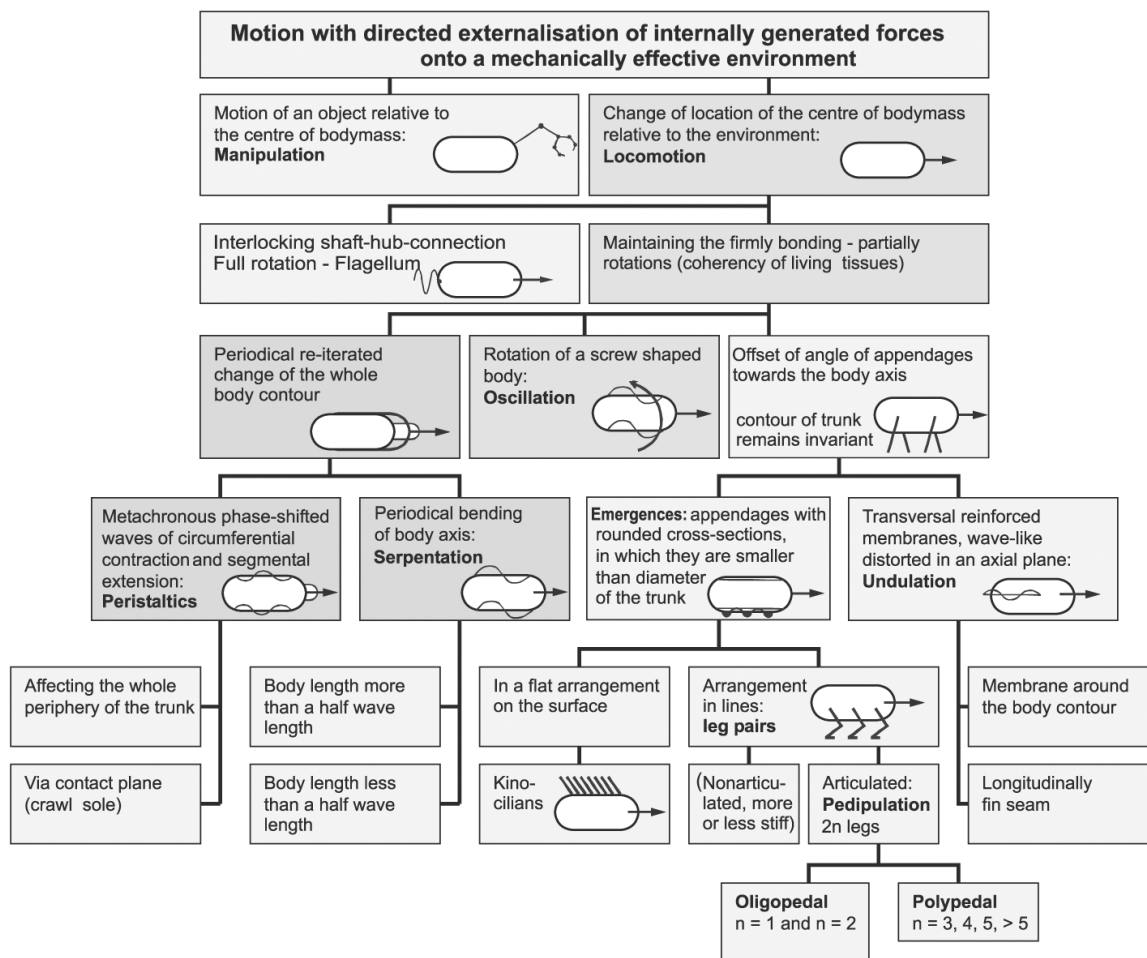


Figure 1.4.: *Structure and variety of biological means of locomotion, according to [Wit03].¹*

On the immense variety of locomotion principles, in this thesis we concentrate on non-pedal locomotion, while we neglect every system making use of wheels, rotors, arms, legs, wings, fins, or any extremities – however altered – for locomotion purposes. Like most forms of locomotion, also the limbless locomotion involves mostly periodic motion processes. In the case of the latter, the periodicity shows in sinuous (undulatory) deformations of a contact layer to achieve a thrust against the foundation, which rests relatively to the considered system. Nature offers versatile examples.

Some designs use additives to reduce friction. The snail as gastropod performs surface waves with its muscular 'foot' and uses a protective slime layer to ease sliding on the firm ground. Other constructions,

1.2. Elementary Remarks on Locomotion

like the earthworm (Lumbricidae), who generates a transversal traveling wave of radial thickening and thinning, supports the motion by growing bristles to increase selectively friction. We call this locomotion by asymmetric friction.

Also rather interesting in the view of biologically inspired, surface deformation employing locomotion systems are ameboids. They accomplish locomotion using pseudopodia, which, one might argue, are a kind of extremities, thus being banned from the aimed category. On the other hand, Amebae, Mycetozoa, also leukocytes and tumor cells possess the ability to utterly change their shape. Although biologists do not agree entirely on how and why they move, ameboids control the viscosity of the endoplasm, which flows from the central areas to the outskirts, establishes pseudopods, and repositions the whole protozoon, by biochemical processes.

So ameboids relocate their interior with the result of transferring the center of mass, which is 'just easy' with variably shapeable boundaries. Although the effect seems simple, the underlying mechanism involves the combined action of the hydrostatic pressure within, tension stress on the boundary layer and traction forces on the adhesive contact area to the surroundings and inside the cell along molecules filaments, see [BH05]. Part of the chain of consequences in the act of initializing locomotion is for one a viscosity reduction of the endoplasm, progressing a flow to the leading edge, which gets wrapped by instant cortex polymerization. Some protozoans enhance the locomotion effect by improved power transmission. Preferentially, they move actively on surfaces and have chemically working receptor molecules at their exterior shell for controlling adhesion and friction to the contact area, [Möh05, Web02]. Even creatures which can act with biochemical methods only on the molecule site – as they are only one single cell – employ complex techniques for manipulation of solid body friction and fluid friction in order to achieve locomotion.

By the way, when watching fast-forward videos of slime mold growth, [euf11], e.g. at the popular Internet video sharing platform, YouTube, one can often watch a kind of pulsative proceeding. It can be observed, that the (periodical) growth cycle of this fungus affects its motion and locomotion pattern.

Other periodic, sinuous locomotion is covered by peristalsis. Reese,

1. Introduction

[Ree87], reports that not until the late 1950's peristalsis shifted into the scientific focus driven by urology. First investigations were of experimental nature by Kiil in 1957, [Kii58], and Boyarski in 1964, [Boy64], performed in vivo. In the middle of the 1960's, the calculation of peristaltic flows started with theoretical models. In this regard, Burns and Parkes, [Bur67], presented theoretical basics about the peristaltic motion in 1967. Also around that time, flow mechanical investigations were accomplished with experimental setups. The industry took interest in this alternative conveying principle. Despite half a century of research, peristaltic motion is still a topic of current research. Fluid transport by undulatory surface or boundary waves is still studied experimentally and theoretically.

Why is non-pedal locomotion, with peristalsis as a part of it, an interesting occupation for an engineer, anyway? Because as a very different locomotion principle it holds diverse properties. This offers new operation fields, where other locomotion principles using wheels or extremities fail or, at least, lead to difficulties and intense labor.

From the engineer point of view, an important question is: What are the costs for locomotion? In [Wol90], Woledge and Curtin presented an interesting comparison of various forms of animal locomotion, including undulatory locomotion, with regard to the energy consumption, see figure 1.5. Similar results are given in [Gab50], here for a wider perspective.

With peristaltic systems, the parts or the whole exterior skin work as the locomotive functional entity, while with limb or wheel systems the locomotive extremities are always additionally attached to the actual object. This gives peristaltic systems a comparatively higher functional density and the advantage of a better adaption to the unevenness of the ground. This term can be contemplated more closely. It can be classified into roughness in scales smaller and higher than the locomotive unit. In both landscapes, the peristaltic system is the fittest. The peristalsis design offers maneuverability between boulders or narrow bendings (high-scaled roughness) and ensures a tighter fit to small-scaled roughness providing higher stability and better grip. Of course, several concepts exist enabling limb or wheel driven systems access to the lunar landscape or to spiral staircases. But additional constructions

1.2. Elementary Remarks on Locomotion

The metabolic cost of locomotion of different animals.

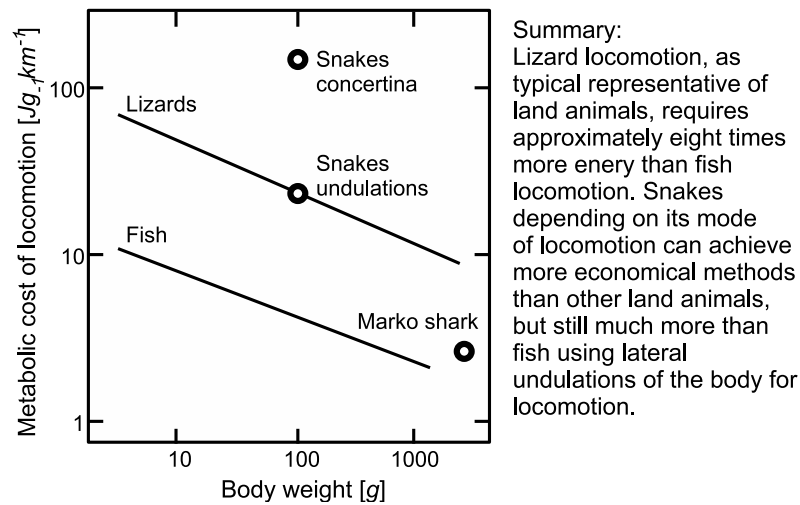


Figure 1.5.: *Diagram and summary according to [Wol90]: snake undulation as a potentially energy effective form of terrestrial locomotion.*

or an extension of control effort is always needed. In this category, the basic limb or wheel system is disadvantaged. To put it differently, a peristaltic locomotion system requires comparatively lower control effort.

Due to the beneficial relative space requirement (relation between required space of the moving parts compared to object size), peristalsis can take place in terrains minimally bigger than the object itself. The limit is reached, when, at whole body contact, the earthworm cannot pass enough normal forces to the surroundings for higher static – at the holding segments – than kinetic friction – at the sliding segments. The earthworm or its technical pendant produces an inner force pressing the boundary layer upon the surrounding. Depending on the inclination angle, this fortifies the effect of the weight and results in enhanced static friction, whereas at the contact area of a wheel or a foot, only a normal gravitational force component is transferred. Most limb robots have fixed ankles and do not, unlike humans, straighten the foot and by this induced torque produce an additional normal force to the ground. For this reason, peristaltic systems are able to climb stronger inclined

1. Introduction

slopes than the comparative concepts. This includes the improved ability to transcend strong resistances. Peristalsis driven systems fail, too, when the lateral (downhill directing) component of the weight exceeds the static friction. The exception is an area enabling 'chimney climbing' by successive clamping and trailing (low ceilings or tubes). Here, at least some limb constructions are maneuverable, too.

Most designs for peristaltic systems offer further potentials for low-effort side effect improvement. Coming from a background of the technical implementation of biological paradigms, the selection of compliant materials is sensible. This idea can be followed up to strong shape variability. Benefits of these designs include enhanced adaptation to high- and small-scale roughnesses of the surroundings and improved friction properties. For some applications, a gentle treatment of the contact area is convenient. So abrasion is avoided with pliable contacting. Compliant materials further reduce the amount of single parts, which simplifies miniaturization and reduces failures. Modular assembly can easily be accomplished and brings along the notorious benefits: cost-effective production, simplified construction, and technical reliability due to redundancy.

If peristaltic systems are superior to conventional locomotion systems in all the mentioned disciplines, why do they not replace conventionally driven vehicles, automobiles, and robots? Firstly, peristaltic systems produce lower absolute locomotion velocities. This is linked to the lower performance density of peristaltic systems, meaning the velocities in relation to the object size. Secondly, the relative load capacity is less than for conventionally driven – especially wheel – vehicles. This drawback can be eased by lighter constructions, e.g. most compliant materials for peristaltic systems possess low densities. But since the theorem of the constancy of all problems is also valid here, other problems occur, like weakened durability and resilience. Thirdly, it is no coincidence that the first reproductions resemble the human image whether in fictional literature or later as actual technical constructions. Humans incessantly scan their environment for familiar and/ or human-like shapes and motion patterns. People do feel more comfortable indeed when recognizing these patterns. In contrast, many humans react with defense or revulsion, when confronted with alien, e.g. spider- or invertebrate-like, movement. Therefore, no service robots will ever exist in shape

1.2. *Elementary Remarks on Locomotion*

or in motion tactics mimicking worms or spiders, even if with highest-possible performance. So, peristaltic locomotion is a valuable, robust and capable concept within the range of certain application fields. Automobile drive for freeways does not belong to them, but peristaltic locomotion is already successfully used for in vivo examinations (by endoscopes). It can be developed for minimally invasive surgery tools, or even cell manipulation within the living organism. Peristalsis is also already applied for inspection purposes in tube systems. A development is possible, like advanced preservation and repair tasks for areas difficult or impossible, inconvenient or dangerous for humans to access. Examples might be operation in deep sea or underground caves, in the canalization, for rescue missions within buildings destroyed by earthquakes or, as recently proved, scout missions in nuclear hazarded areas. A more ordinary application is the media transport without potentially impurifying valves and turbines, as the food and cosmetics industry most often applies.

As nature proves, the design variety is immense despite the constriction of the peristaltic function. One does not have to browse scientific publications. A quick glance at the Internet gives a stunning survey of all kinds of amazing (robot) beasts. A prominent example among these is an artificial sand fish, which 'swims' through solid sand, [Mal11]. Though not strictly related to peristalsis, the imitation of amoebic ability of contour variance is featured by Mozeika's group, [Moz09]. The stunning example of a biologically inspired robot alters its exterior or membrane firmness with the jamming skin effect to perform locomotion.

The operational range of technical devices generally depends on the kind of power supply used. The case of passive locomotion is simple. The range of the locomotive object is as wide as the expansion of the motion generating substrate. On the other hand, active locomotion systems can be equipped with an internal or external power supply. For online supply, though low-weighted, it does not matter whether an electrical, pneumatic or hydraulic line connects functional unit and power generator, the limitation is the link dimension. Plus, the operation resources are not everywhere available, e.g. pressurized hydraulic air. Systems with energy storages are restricted by the charge capacity. The additional weight increases the costs. Tactics for recharging op-

1. Introduction

opportunities in the operating room ease the problem. The infrastructure must be ensured but becomes more economic for a group of devices. Energy autarkic concepts offer a wide-range opportunity, at the price of high developmental efforts, higher weight, and expensive technology of the individual unit. Those are probably only profitable for a low amount of individuals. Currently existing solutions for power autarky are mainly specialized and are suitable only to a limited extent.

The short (and by far not exhaustive) discussion names some criteria. Apart from the boundary conditions given by the special task, the crucial points for robot or locomotion system design are range, weight, efficiency rate of the principle(s), and single player or swarm application. In each way, a compromise needs to be found.

2. State of the Art and Motivation of the Thesis

2.1. Structure of Projects of the Ilmenau Research Group

Although the core of the present thesis covers non-podal, ferrofluid based locomotion, the examination of the state of the art touches neighboring areas, too. Subjects like apodal locomotion working on other materials are included. Special focus is put on smart mechanisms using surface effects like peristalsis or other technical adaptations from biological or biologically inspired systems.

The domain of ferrofluids regards the physical view (prominent here: viscosity matters), theoretical (both analytically and numerically) descriptions of ferrofluid behavior in external magnetic fields, as well as various applications. In contrast with other scientific fields, experimental publications here do not always provide thoroughly prepared theoretical backgrounds, but occasionally, the presented experimental results seem rather 'hand crafted' instead of following from a methodical approach. If simple experiments still count as technical novelty, we should note that ferrofluid research is still close at the very beginning. Studying ferrofluids also exposes related topics. We comment on ferroelastomers and ferrogels as well as on magnetic nanoparticles and observe ferrofluid based manipulation systems, where the ferrofluid motion is relevant for the function, but not featuring real locomotion. Interesting side shows of physical effects and noticeable ferrofluid applications without any motion characteristics close the inquiry. Nevertheless, this paper focuses on the combination of ferrofluids and locomotion, reflecting the current state of the art.

2. State of the Art and Motivation of the Thesis

How can this variety be structured? Figure 2.1 puts the multifaceted fields into relation with each other. On the left side, there is *locomotion*, bearing pure theoretical mechanic issues, technical implementations and biological archetypes (which are mentioned as inspirational source, but not cited as state of the art, due to their original and ancient existence). *Ferrofluids* dominate the right side covering theoretically or applicationally orientated publications, effects, and inventions.

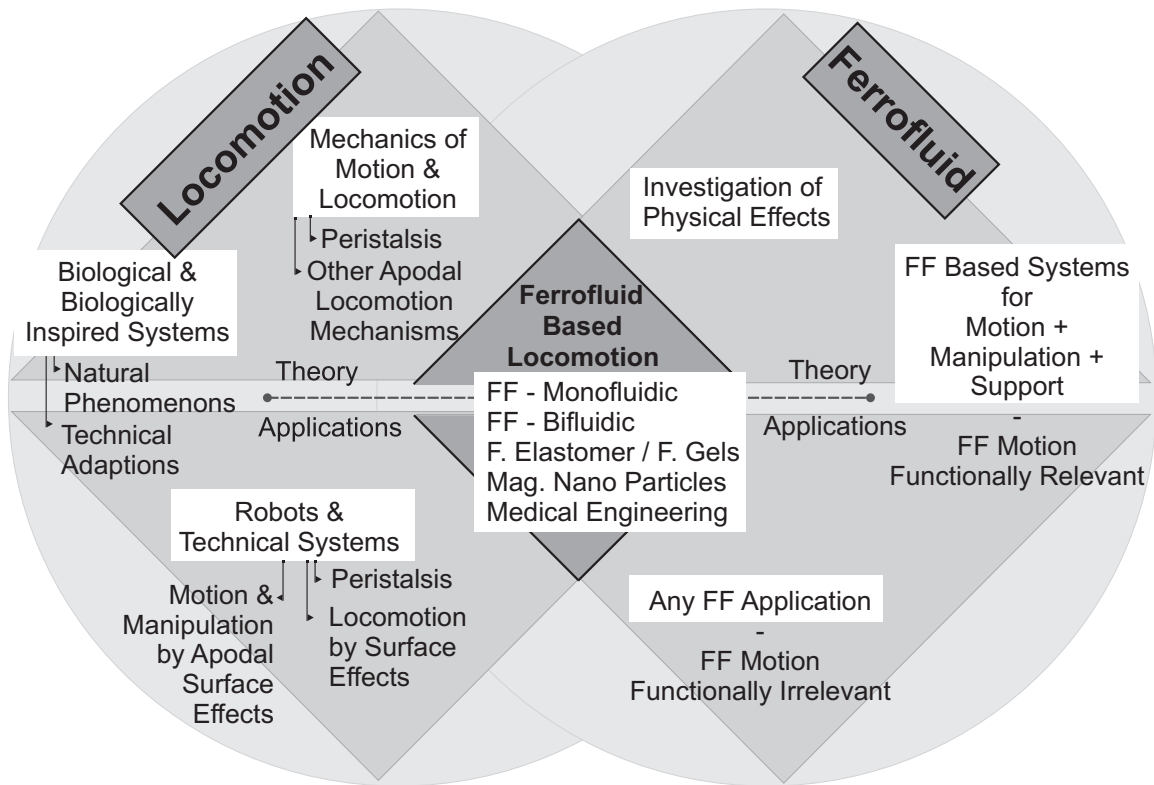


Figure 2.1.: An idea of structuring the State of the Art of ferrofluids and locomotion and their conjuncture; the following cube of configurations regards the classification of ferrofluid based locomotion regarding only ferrofluids (mono- and bifluidic).

The most important area is in the middle, where *locomotion* and *ferrofluids* meet, *ferrofluid based locomotion systems*. This is the largest quantity. The center occupation is further structured as seen in the following figures 2.2 to 2.5. The distinction between theoretical and applicational studies is not strict, but provides a tendency. Figure 2.2

2.1. Structure of Projects of the Ilmenau Research Group

structures *ferrofluid locomotion* systems cubically, since several configurations are possible. The left and right planes discern *active* (ferrofluid portion itself executes locomotion) and *passive locomotion* (ferrofluid enables other solids/liquids to perform locomotion), respectively.

The bottom and top level categorize the position of the magnets within the system, as it affects magnetic efficiency and moving mass. They refer to applications in which the electro- or permanent magnets are either covered by the ferrofluid (internal) or located outside of the ferrofluid (external).

The front plane gathers devices with a free surface of the ferrofluid, the rear plane covers surface devices. The housing is thought to be a flexible or pliable film made from a solid material, e.g. silicone, thin polythene, rather than from a liquid. An interlayer between the front/free surface and rear/covered surface planes incorporates bifluidic devices, where the ferrofluid is 'covered' by a secondary (immiscible) fluid. The bifluidic plane exists only on the top level, only for external magnets. In figures 2.3, 2.4 and 2.5 the separate planes are illustrated in detail.

The rear plane of figure 2.2 is given by figure 2.3. Devices with the ferrofluid covered are discussed here. The presented categories are *active* (left) and *passive* (right) locomotion systems with *externally* (top) or *internally* (bottom) located magnets.

In the section of *active* locomotion, systems are imaginable with integrated sources of the magnetic field (left, bottom). According to our estimation, those may be feasible, although moving mass and available net forces rival against each other and provide a challenge. The other option with external electromagnets is already proven to work, see [Zim07b, Zim08b].

The class *passive* locomotion includes a feasibility study, [Spi06], for external electromagnets and a variation with integrated magnets. A prototype as an example for the latter is not known to the author. However, a suitably sized and thus mobile 'cushion', filled with ferrofluid, may serve as the locomotion base of other objects.

Figure 2.4 presents the intermediate level of figure 2.2. Here, the term 'bifluidic' means the use of two liquids, considered are only setups with external magnets.

[Gre06, Zim09] give an idea of a hexane suspended ferrofluid swarm moving within the horizontal plane. This presents an *active locomo-*

2. State of the Art and Motivation of the Thesis

tion system with mobile ferrofluid portions. [Zim09] might be regarded as the opposite class, *passive locomotion*, where the ferrofluid portion produces a bidirectional duct flow. The shifting of swimming objects can be adjusted, even though the accessible positions are delimited.

Locomotion systems operating with the free ferrofluid surface are collected in figure 2.5 – this image is similar to the front plane of figure 2.2. The square divides into *active* (left) and *passive* (right) locomotion systems with external (top) and internal (bottom) magnetic sources.

The intersection of *active* locomotion with external magnets may contain actually working devices. Potential friction losses can be minimized by low-friction surfaces and materials such as PTFE which was successfully applied in [Ngu06].

According to our estimation, the integrated model (*active* locomotion, *internal* magnet) is not feasible (at least within the range of resources available and known to us). Even though the magnetic stress within the fluid antagonizes the common property of liquids to ease shear stress, this effect is insufficient to maintain a closed entity including the magnet and to accelerate the total mass. The presumed power density of the available magnets and the saturation magnetization of ferrofluids (which is proportional to the magnetic stress) is (currently) badly conditioned.

On the right side of figure 2.5, both arrangements (*external* and *internal* magnets) of *passive locomotion* systems may be feasible. [Pop06, Zim08a] present different prototypes. While in [Pop06] a shallow pool is positioned on top of an EM array, which, when appropriately switched, produce a traveling surface wave for object transport. [Zim09] proclaims a doubly underpinned vehicle gliding on periodically changing surface waves. Originally, the waves are generated by a series of opposite-polarized permanent magnets and additionally influenced by the electromagnet's globally homogeneous field. The EM changes alternatingly the polarization which inflicts support or reduction, respectively, on the local action of the PM.

Lastly, the *passive locomotion* system with internal magnets may not work when self-propulsion is expected. But it may do well, when arranged as a ferrofluid layer housing magnets. Similar to the covered model of figure 2.3, one may imagine a ferrofluid underground generating surface waves for solid body or fluid transport.

2.1. Structure of Projects of the Ilmenau Research Group

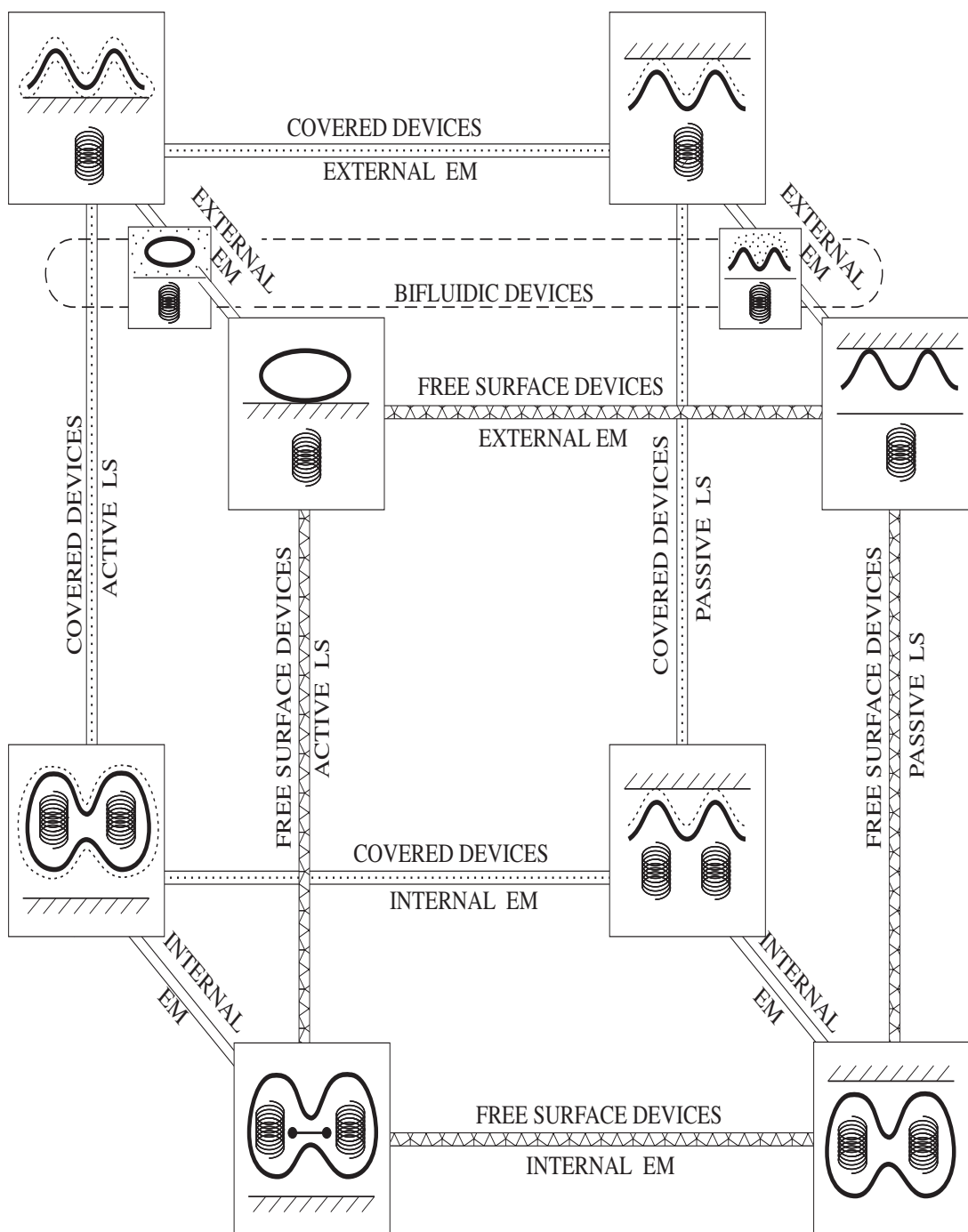


Figure 2.2.: The cube of configurations puts active and passive locomotion systems in relation to covered, free ferrofluid surface and bifluidic versions as well as internal or external magnet solutions.

2. State of the Art and Motivation of the Thesis

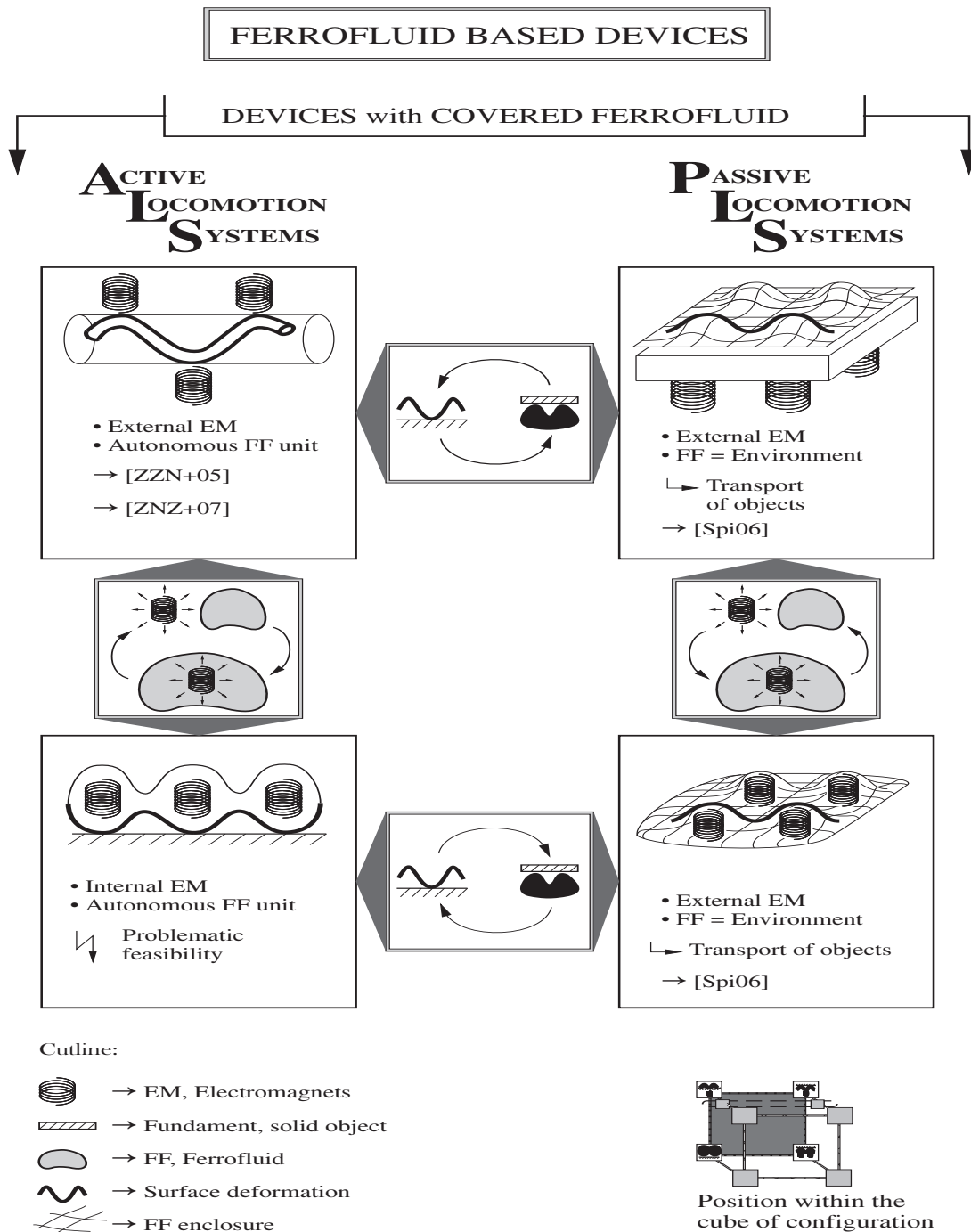
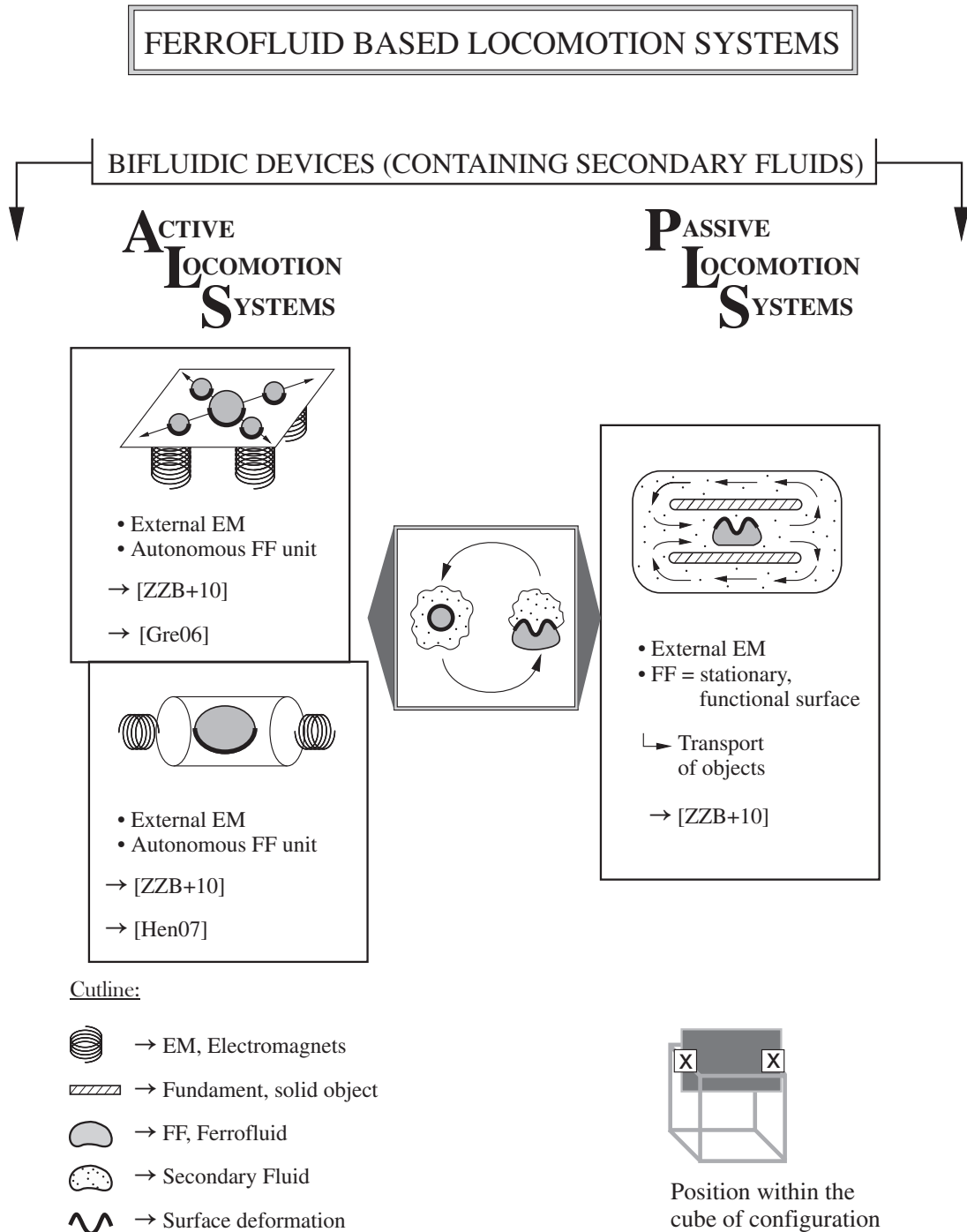


Figure 2.3.: Plane of covered devices as detail of the cube of configurations.

2.1. Structure of Projects of the Ilmenau Research Group



Cutline:

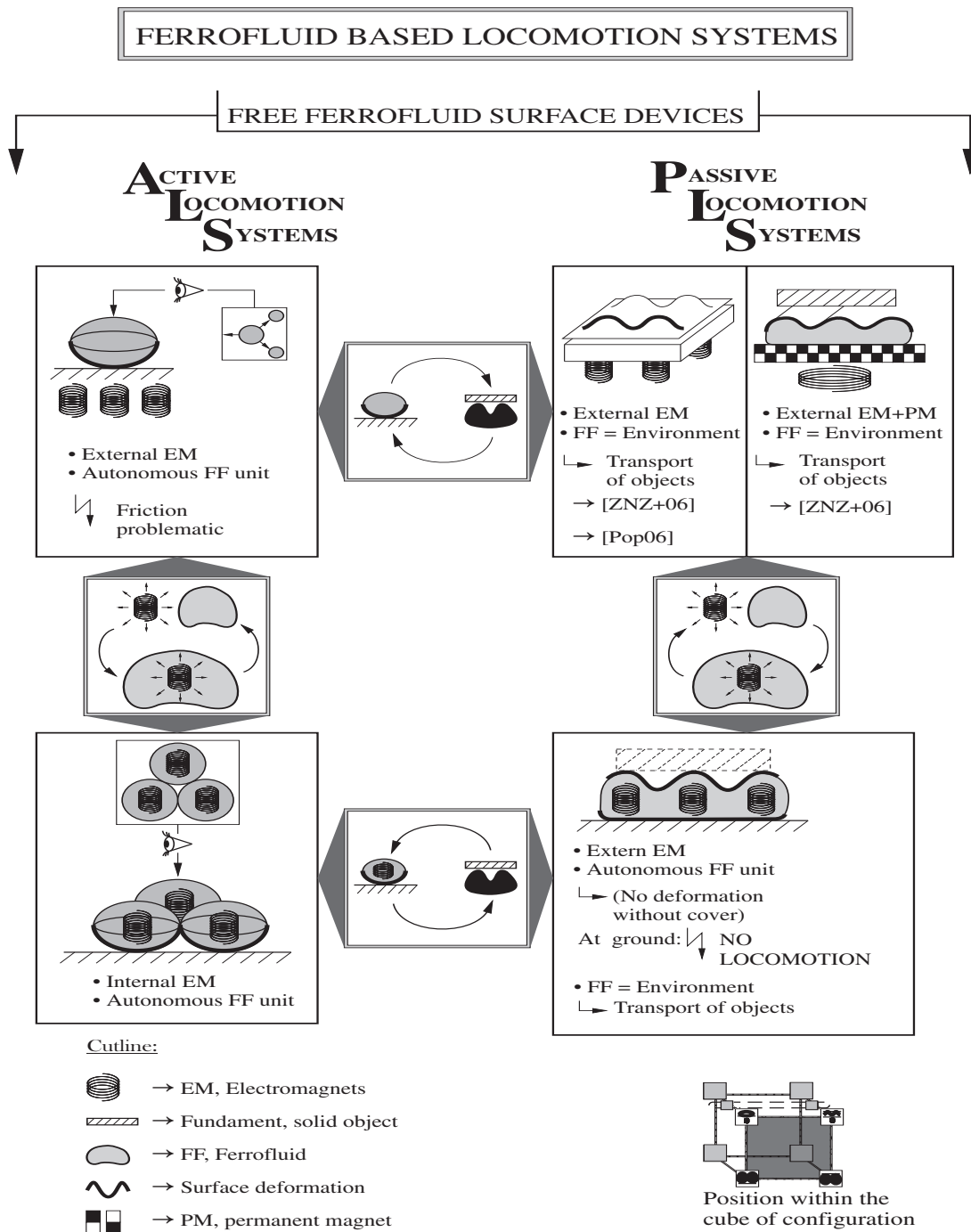
-  → EM, Electromagnets
-  → Fundament, solid object
-  → FF, Ferrofluid
-  → Secondary Fluid
-  → Surface deformation



Position within the cube of configuration

Figure 2.4.: Intermediate level of bifluidic devices, which use secondary fluids as a semi-cover, bridges the gap between a free ferrofluid surface and a firm film.

2. State of the Art and Motivation of the Thesis



2.2. Summary of Related Research

In this section the author gives an overview about papers close to the subject of the thesis. This includes ferrofluid based motion and locomotion in a wider context. Mainly studies from other researchers are mentioned and are partly put in relation to the work of the author or her work group. Occasional references to own publications round up the overview of the currently existing state.

This list is divided into three main categories: boundary deformation of single ferrofluid portions for motion or locomotion purposes, deformation of a ferrofluid surface with variously conditioned magnetic fields and bifluidic devices as a basis for transport of third objects.

Category One - Magnetomechanical Behavior (Especially Deformation Phenomenons) of Single Ferrofluid or Magneto-sensitive Elastomer Units for Motion or Locomotion Purposes

[Ceb05], *Flexible Magnetic Swimmer*, 2005, is a theoretical diploma thesis. Cebers offers an analytic model of flexible magnetic filament and investigates self-propulsion ability in an alternating magnetic field. He emphasizes the asymmetry, like magnetic heterogeneity or anisotropy of friction, being essential for self-propulsion.

In [Gau05], *Hydrodynamics of nanomachines in biology*, 2005, background and functional principles of a flexible superparamagnetic filament are discussed intensely. It is an interesting paper as well, since in chapter 4, derived from the filament motion, a worm-like deformation structure is considered. This relates to the problem of the vermicular locomotion in [Zim08b], see figure 2.6.

The articles [Zim07b, Zim08b], *Calculation of a magnetizable worm deformation in a magnetic field*, 2007, and *A deformable magnetizable worm in a magnetic field – A prototype of a mobile crawling robot*, 2008, investigate by analytics, numerical simulation and experimental measurement series the deformation of a (superparamagnetic) ferroelastomer rod (worm) in a traveling magnetic field in order to achieve locomotion. Different ratios of rod length to thickness to tube diameter are tested for their influence on the locomotion and velocity.

2. State of the Art and Motivation of the Thesis

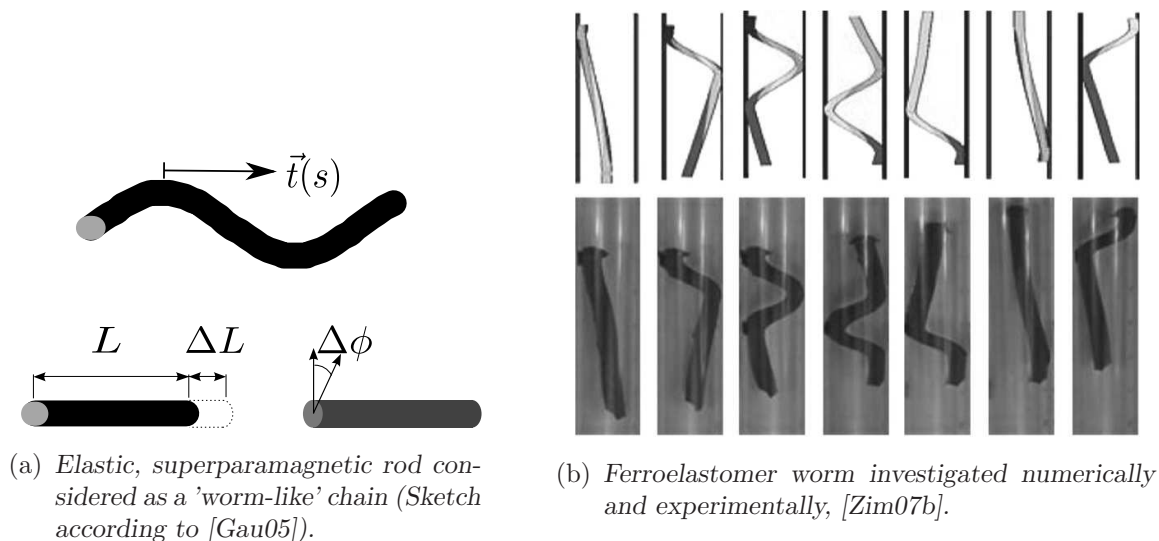


Figure 2.6.: *Different studies about flexible, magnetically sensitive rods performing periodical deformation to achieve locomotion.*

In [Ngu06], *Manipulation of ferrofluid droplets using planar coils*, 2006, a smart bidirectional locomotion system is presented incorporating a single ferrofluid portion set under a magnetic pressure gradient by a PM on each side. On a double-sided printed circuit board (PCB) the field of the top-level pair of planar coils creates a virtual path (by lateral guidance). The second pair of coils (at bottom level) decides on the motion direction. For friction reduction, they incorporated a ferrofluid-PTFE coupling.

[Fra03], *Ferrofluid Flow Phenomena*, 2003, is a well-written master thesis focused on ferrofluid as a smart material. An effort has been put into providing a great number of experimental tube flow data.

In [Zr105], *Direct Observation of Discrete and Reversible Shape Transition in Magnetic Field Sensitive Polymer Gels*, 2005, Zrínyi reports about the production technology of magnetically sensitive polymer gels in a magnetic field. Theory and experiments are concerned about the magnetically induced deformation behavior of magnetized polymer rods made of stacked units. [Gre10b], *Position control of magnetic beads by means of electromagnetic fields with respect to apodal locomotion systems*, 2010, presents a FPGA position control for future locomotion systems employing ferrofluid portions. The control algorithms are derived analytically, acting forces as input parameter are obtained by simulation and measurement.

2.2. Summary of Related Research

[Dob02], *Peristaltic Transport as the Travelling Deformation Waves*, 2002, investigates the peristalsis phenomenon with regard to the mass transport using the theory on traveling wave deformation. Especially slow motion is considered, which enables non-dynamic approaches.

[Kav11], *Peristaltic flow of a micropolar fluid in a vertical channel with longwave length approximation*, 2011, is an article about the flow of a micropolar fluid by means of peristalsis. They make use of the long wave approximation to eliminate inertia members and furthermore work with low REYNOLDS numbers, like in this thesis, too.

[Mek05], *Peristaltic Transport of a Newtonian Fluid Through a Uniform and Non-uniform Annulus*, 2005, reports about the investigation of the endoscope problem - a viscous incompressible fluid peristaltically driven between two tubes, the exterior wall is undulating, the interior has a fixed diameter. Mekheimer gives a model to analyze the flow rate depending on different functional parameters.

[Mis03], *Peristaltic transport of a Newtonian fluid in an asymmetric channel*, 2003, considers a two-dimensional peristaltic problem in a conventional viscous and incompressible fluid with low REYNOLDS numbers. The long wave approximation is applied. In contrast with many other publications, the undulation of two walls performs different amplitudes and phases. The subsequent analysis regards parameter influences on velocity and flow rate.

In [Pra09], *Effect of Peripheral Layer on Peristaltic Transport of a Micropolar Fluid*, 2009, the peristaltic problem of two fluids in two tubes inside one another is described. The core fluid is a micropolar, the exterior fluid a NEWTONian fluid. Both tube walls perform undulation deformation with identical phases. The transport capacity is modeled by using the long wave approximation and assuming low REYNOLDS numbers. The flow rate is put into relation with different functional parameters in the analysis of the problem.

A publication not concerning ferrofluids, but handling very detailed limbless locomotion: [Gon08], *Modular Robotics and Locomotion: Application to Limbless Robots*, 2008, is a thesis with a very detailed overview over the state of the art concerning robots, especially limbless robots. Furthermore, González Gómez investigates kinematically and analyzes various gaits for non-pedal locomotion with respect to the suitability for different terrains and configurations of the minimal amount

2. State of the Art and Motivation of the Thesis

of modules. From these, he develops a modular non-pedal snake-robot prototype.

Category Two - Periodic Deformation of a Boundary Layer and Subsequent Transportation Effects Considering Magnetizable Fluids and Other Media

[Bro99], *Surface waves in ferrofluids under vertical magnetic field*, 1999, is concerned with the free surface deformation of a magnetic fluid as a theoretical problem. Here are investigated wave dispersion and propagation in weakly modulated magnetic fields, causing ROSENSWEIG instabilities. Shadowgraphy experiments verify the theory commencing at the dispersion equation of waves at the free surface. They are not related to any locomotion matters.

[Zim05], *Locomotion based on a two-layers flow of magnetizable nanosuspensions*, 2005, is an earlier study of the authors working party. A flow of two incompressible, viscous and magnetizable fluids, separated by an impermeable film is already considered. An external alternating magnetic field produces the undulation of the separation boundary, which states the peristaltic drive.

[Zim08b], *Surface of a magnetic fluid containing magnetizable bodies in an applied uniform magnetic field*, 2008, is a theoretical analysis of the deformed contour function of the free surface of a magnetizable fluid. The manipulation is produced by a constant magnetic field, which is concentrated by high permeable bodies inserted into the fluid. Cases of an iron core cylinder (plane problem) and an iron core sphere (axis-symmetric problem) are discussed.

[AA11], *Peristaltic transport of micropolar fluid in a tube under influence of rotation*, 2011, is a paper very close to section 3 of the authors thesis. It investigates a peristaltic material transport, whereas the boundary wall is undulating, see figure 2.7(a). Similarly, the perturbation method is used. Differences within the setting are an axis-symmetrical contemplation, their perturbation coefficient is the small ratio of amplitudes and instead of a superparamagnetic ferrofluid, their subject is a micropolar fluid. The article includes a numerical solution using the RUNGE-KUTTA method and discusses the influence of the initiating magnetic field and a rotation of the tube.

2.2. Summary of Related Research

[Rub93], *Transport phenomena in ferrofluids*, 1993, is an early investigation and includes some of the main ideas about transport phenomena in suspensions of ferromagnetic particles. In particular, an explicit calculation of the viscosities for spherical particles, based on the solution of the corresponding SMOLUCHOWSKI equation, is carried out.

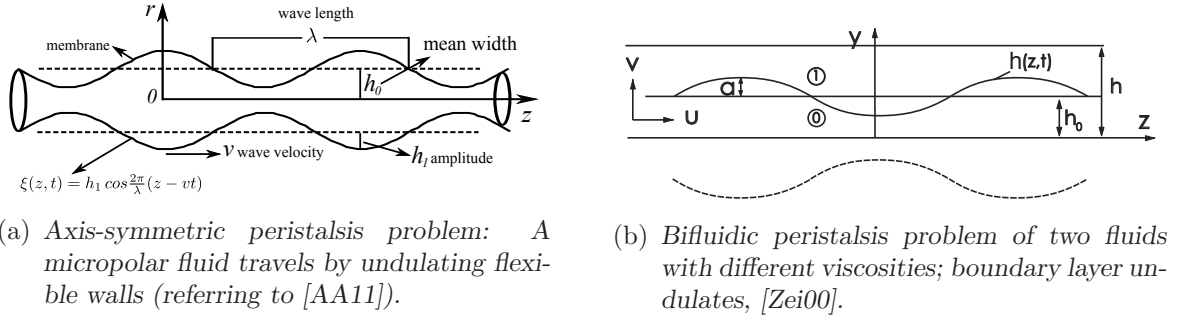


Figure 2.7.: Peristaltic problems are a massive part of current non-podal locomotion research.

[Kra05], *Fluid pumped by magnetic stress*, 2005, publishes a ferrofluid pump driven by circularly traveling magnetic fields. The motion principle requires a free surface of the magnetizable fluid. Analysis of the correlation between velocity and other functional parameters, like the frequency, are supported by experimentally obtained data.

In [Dor11], *Wave turbulence on the surface of a ferrofluid in a horizontal magnetic field*, 2011, one can find the investigation of wave generation, dispersion and propagation on the free surface of ferrofluid. Theory and experiment regard the case of horizontal wave excitation by under critical alternating magnetic fields and mechanical shakers.

[Mao05b, Mao05a], *An Integrated, High Flow Rate MEMS Ferrofluid Pump and Ferrohydrodynamic pumping in spatially traveling sinusoidally time-varying magnetic fields*, 2005, reports about an integrated MEMS pump transporting ferrofluid. Instructions on the production are given as well as simulation data on the flow performance and a prototype. Similarly to the case discussed in this thesis, they generate the flow by spatiotemporal traveling magnetic fields.

[Fri10], *Magnetic traveling-stripe forcing: Enhanced transport in the advent of the Rosensweig instability*, 2010, is an article close to this thesis. Free surface waves perform a material transport of ferrofluid.

2. State of the Art and Motivation of the Thesis

The deformation is induced by an alternating traveling magnetic field. The article gives details on the magnetic field and transport capacity by numerical simulations and experiments. The characteristic velocities are slightly higher than those in the thesis, which result, apart from the peristaltic effect, from another one, the ferrohydrodynamic pumping.

Category Three - Motion and Locomotion due to Interaction of a Liquid and a Magnetosensitive Medium (Ferrofluid, Ferroelastomer or Magnetic Nanobeads)

The team of Bruno Andò, Alberto Ascia, Salvatore Baglio (and others) published several articles, each presenting a more or less modified bifluidic assembly incorporating a fixed ferrofluid portion and electromagnetic control or sensor for a number of different applications.

[And07, And10a, And10b], *A Ferrofluidic Inclinator in the Resonant Configuration*, 2010, and *A Ferrofluidic Inertial Sensor Exploiting the Rosensweig Effect*, 2010, relate to an inclinometer or inertia sensor, respectively. The displacement of a magnetically fixed ferrofluid portion is measured using a pair of lateral sensor electromagnets. In short, the desired effect is the backtracking of an externally initiated ferrofluid motion.

The ferrofluid based pump, [And06, And09]: *Ferrofluidic Pumps: A Valuable Implementation Without Moving Parts*, 2009, produces a water flow within a pipe by a three-stage actuator consisting of single ferrofluid droplets locally fixed and deformed by external electromagnets. The flow arises by a certain shifting order of the actuators. The ferrofluidic pump may be interpreted as a variation of the passive locomotion concept discussed in this thesis: The ferrofluid is stationary while the surrounding medium is propelled, either to end in itself or to carry along other (solid) objects.

[Ber02], *Numerical modeling of ferrofluid flow instabilities in a capillary tube at the vicinity of a magnet*, 2002, models a plug flow of ferrofluid portions surrounded by different media (reagents), flow instabilities are regarded. The model features a ferrofluid plug in a pipe with microelectromagnets located outside. The importance for microfluidic systems is emphasized.

2.2. Summary of Related Research

[Zim10], *Ferrofluid-based Flow Manipulation and Locomotion Systems*, 2009, publishes prototypes as well as experimental measurements on bifluidic devices using ferrofluid actuators for indirect (passive) fluid or solid body transport.

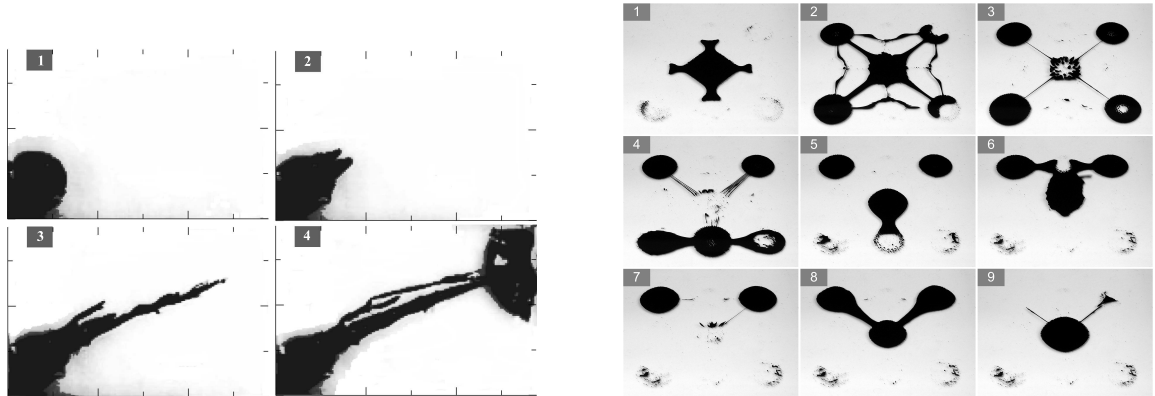
[Mor97], *Theoretical and Experimental Investigations of Ferrofluids for Guiding Aid Detecting Liquids in the Subsurface*, 1997, is a paper on ferrofluid basics featuring a high didactic quality. Simple but inspiring experiments about motion of ferrofluids using electro- and permanent magnets are produced. Publications succeeding from this group investigate the means of positioning water miscible ferrofluid portion in porous media, like water imbibed sand, see figure 2.8(a). Although they have a geological background, with the idea of magnetically fixed chemical barriers or magnetically driven relocation of microbes or chemicals using ferrofluids, the goals of Moridis' and the author's team are similar. The comparison is appropriate because earlier publications of the author's work group [Zim10] attempted the creation of a manipulation system of fluid supported ferrofluid actuators, see figure 2.8(b).

[Par00,Seo05], *New Structure of the Magnetic Fluid Linear Pump*, 2000, and *A Research on the Pumping Forces in the Magnetic Fluid Linear Pump*, 2005, publish an application concept (and its succession) of a pump utilizing the undulating deformation of a flexible ferrofluid filled chamber to initiate the transport of a second fluid. The control works using a series of electromagnets. The second article includes principal calculations of the required pressure and derives requirements for the control.

[Afk08], *Field-induced motion of ferrofluid droplets through immiscible viscous media*, 2008, discusses the case of the motion of a single ferrofluid portion onto a horizontal plate within an immiscible secondary fluid by means of a magnetic field. The subject is treated by calculations using the MAXWELL equations and numerical simulations concerning the contour deformation. Different conditions are investigated. This article is interesting due to the acquisition of the physical data, which can be used to derive the control of a ferrofluid positioning system.

[Har04], *Ferrofluid-based microchip pump and valve*, 2004, features a ferrofluid actuated pump and valve suitable for microfluidic applications. Although the motion mechanism is simple by moving permanent

2. State of the Art and Motivation of the Thesis



(a) [Old00]: Successful experiments on controlled ferrofluid positioning in water – despite water miscibility (EMG 805, Ferrotec) and limited solvation due to restricted BROWNIAN motion.

(b) [Zim10]: Immiscible media; ferrofluid droplets as potentially co-working swarm for object manipulation.

Figure 2.8.: Experiments regarding base positioning and a concept of a ferrofluid actuated manipulation system, both achieve relocation of ferrofluid portions in secondary fluids.

magnets close by, the main effort focuses on valves and pumps working against the resistance of several kilopascal of pressure.

[Hat01], *A ferrofluidic magnetic micropump*, 2001, documents a rotary bifluidic ferrofluid pump. The idea is smart, as the driving motion is a simple one; one wheeling ferrofluid plunger and a fixed one make the carrier fluid pass through an annular tube.

[Lov05], *Ferrofluid Field Induced Flow for Microfluidic Applications*, 2005, introduces a ferrofluid pump using the magnetocaloric effect. The theoretical background of the effect and its influence on the flow are given, temperature-magnetization relation investigated for different ferrofluids and flow velocity measurements conclude the article.

In [Zim10], *Ferrofluid-based Flow Manipulation and Locomotion Systems*, 2010, the authors present two principles of ferrofluid actuated locomotion systems. In both cases, by indirect motion the ferrofluid induces a motion or locomotion to a second fluid or object, respectively. The functional relevance of the driving frequency of the ferrofluid is analyzed based on experimental data.

2.3. Motivation and Goals of the Study

By [Sch05b, Sch06], *Miniaturized electromagnetic ferrofluid actuator*, 2006, a miniaturized hydraulic pump is proposed. The MEMS structure includes a ferrofluid actuator producing a pressure gradient by lateral displacement of a membrane. FE simulations are given for the working pressure and the membrane displacement.

[Yel05], *Arranging matter by magnetic nanoparticle assemblers*, 2005, presents a means of the manipulation of micro and nanoparticle transport on a substrate by magnetic nanobeads. The method is guided by a program of magnetic information stored on the substrate, which can be altered on the fly. The prospect of trajectory control is given.

2.3. Motivation and Goals of the Study

According to NEWTONS second law, an external force is needed, if the position of the center of mass of a body is desired to change. So, when first looking at new ideas for locomotion systems basing on ferrofluids, the following question should be answered: How big are the forces, which are generated by a ferrofluid in a moderate magnetic field? An experimental setup, which was realized solve this matter, is given in figure 2.9. The measuring procedure was realized with the parameters from table 2.1.

The applied measurement system includes the head of the sensor attached to a parallel spring with high stiffness. At contact between ferrofluid and head, a force charges at the probe body. The force measurement is operated by acquisition of the axial displacement of the head employing a contact-free laser distance measurement system, see figure 2.10. As the desired quantity is captured indirectly, we derive the force due to knowledge of the spring stiffness and the measured axial displacement of the sensor head. At the procedure, a positioning system repositions the unit, sensor head and parallel spring, incrementally in negative z -direction (see coordinate direction in figure 2.10) and immerses the head in the fluid. The fluid pressure affects the axial displacement of the sensor head (in positive z -direction) due to the compliance of the parallel spring. The subsequently calculated force is analyzed in dependency of the depth of immersion.

2. State of the Art and Motivation of the Thesis

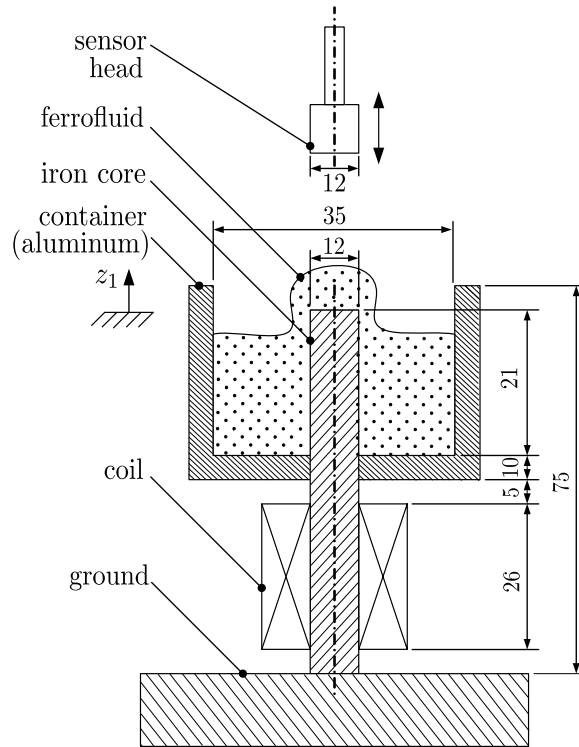


Figure 2.9.: *Experimental setup for determination of forces generated by ferrofluid [Gre06].*

Table 2.1.: *Parameters of the investigated ferrofluid.*

Ferrofluid:	Description	APG S10n
	Carrier fluid	Synthetic ester
	Saturation magnetization	44 mT \pm 10%
	Dynamic viscosity	300 mPa s \pm 10%
	Density	1330 kg m ⁻³
Electromagnet:	Inner diameter	14 mm
	Outer diameter	29 mm
	Wire material	Copper
	Wire diameter	0.4 mm
	Number of windings	1200
	Electrical current	1 A
	Value of magnetic flux above center of iron core	42 mT (measured)

2.3. Motivation and Goals of the Study

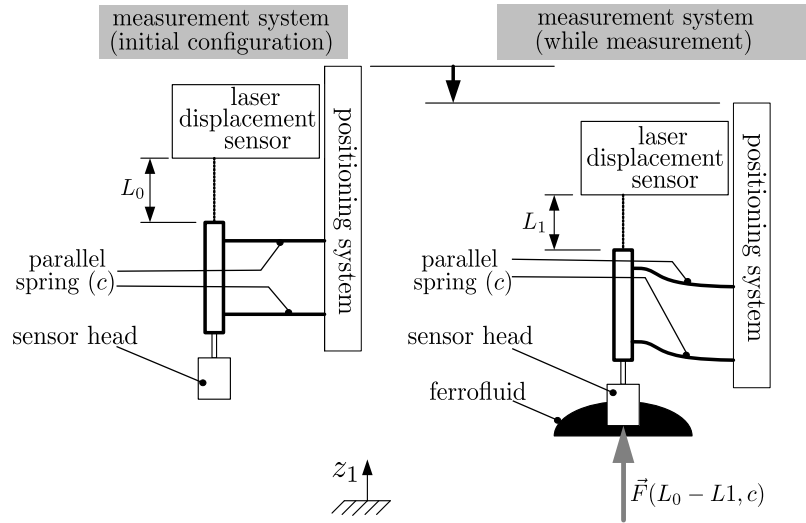


Figure 2.10.: Indirect measurement system.

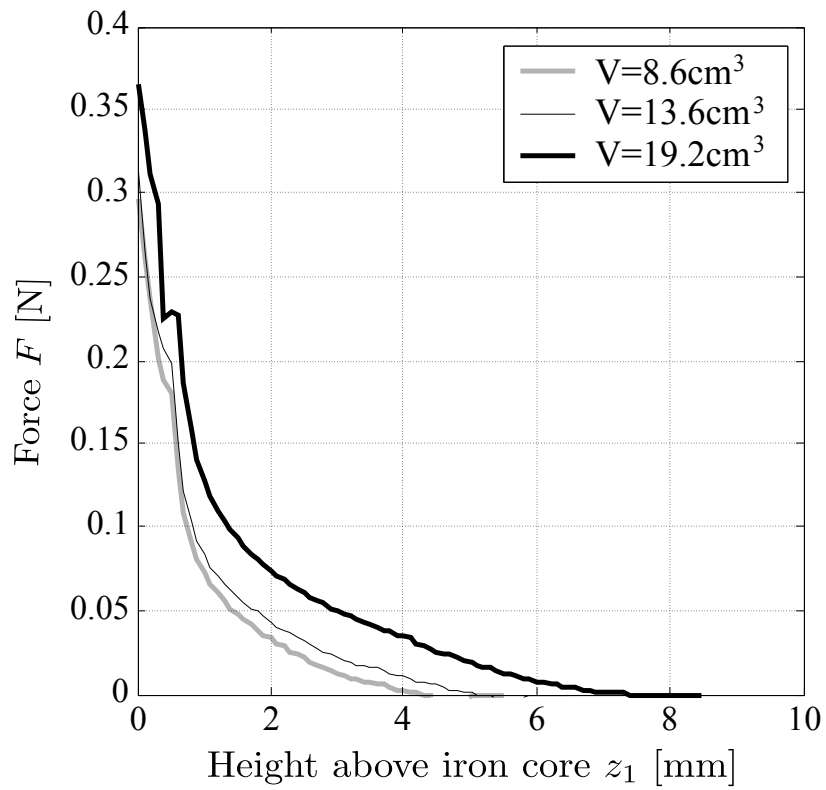


Figure 2.11.: Ferrofluid generated force $F(z_1)$ in close proximity of the magnetic field source [Gre06].

2. State of the Art and Motivation of the Thesis

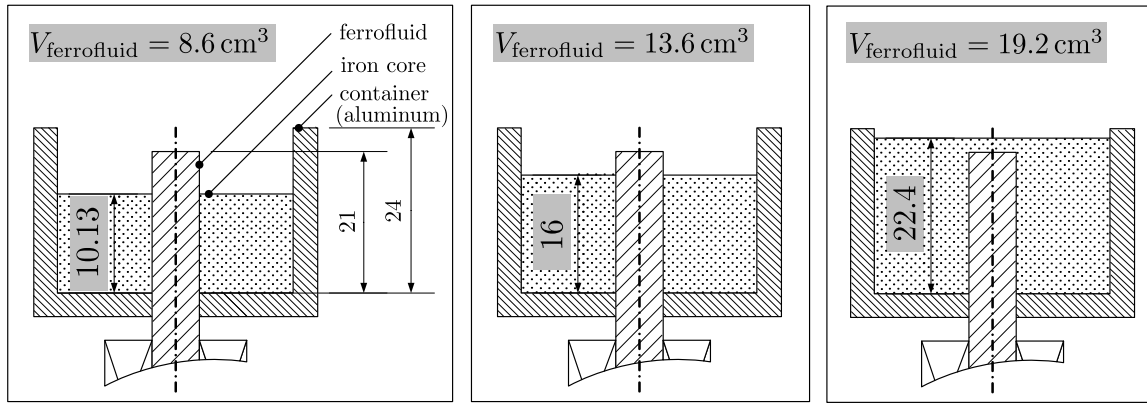


Figure 2.12.: Force measurement for different fillings.

Figure 2.11 gives an impression of the obtained forces. The referred volumes in figure 2.11 correspond to three modes of filling level. These are $h_{f1} = 10.13 \text{ mm}$ with $V_{f1} = 8.6 \text{ cm}^{-3}$ (partly filled), $h_{f2} = 16 \text{ mm}$ with $V_{f2} = 13.6 \text{ cm}^{-3}$ (partly filled) and $h_{f3} = 22.4 \text{ mm}$ with $V_{f3} = 19.2 \text{ cm}^{-3}$ (iron core covered by 100%), see figure 2.12.

On this basis, we conclude, that forces induced by application of a magnetic field are relatively small with regard to motion purposes of ferrofluid entities (at least beginning at certain quantities) and especially of secondary objects or fluids, the locomotion of which is intended to be affected by ferrofluid operation.

These facts lead to the following tasks and goals of this work.

1. Due to the excellently controllable deformation processes of the ferrofluid surface, their suitability for peristaltic locomotion shall be investigated.
2. Further, resulting from measurements mentioned above, we have to consider possible means to enhance the serviceable forces or to amplify the surface deformation, respectively, with regard to the prior.
3. Bifluidic systems with ferrofluid actuated channel flow will be studied referring to the ferrofluid application for passive locomotion, as already described in section 1.1.

Apart from the direct application of ferrofluids within the context of locomotion, we used the theoretical and practical results of the inves-

2.3. Motivation and Goals of the Study

tigations on magnetic field control (serial and parallel aligned solenoid systems) for model-based developing the designs and technologies of apodal locomotion systems with ferrofluid filled membrane structures or ferroelastomers.

3. Ferrofluid Based Locomotion due to Surface Deformation

3.1. The Other Way Around

The idea of influencing a flow of a magnetizable fluid by an alternating magnetic field is not entirely new. Already in 2004, Naletova and her group analyzed the inverse problem [Zim04] of a problem with an assembly and material properties similar to the one described later in this chapter. Apart from smaller modifications, the main difference between Naletova's study and this thesis is the transposition of the given and the required quantities, see 3.1.

Naletova's article starts with the known contour function of the perturbed surface, looking for the description of the causative magnetic field. We investigate the direct problem. At the beginning, the causative magnetic field is given and flow parameters like the contour and the stream function are procured. [Zim04] works with the same foundation of properties like the one discussed here, which is a plane flow of an incompressible, magnetizable fluid with constant magnetic permeability, viscosity and density, without gravitational consideration. Both calculations use the STOKES approximation and the two-dimensional continuity equation. The use of the boundary conditions is similar, too, as well as the non-inductive approximation.

In addition to the foregoing approximations, the earlier paper considers a small layer thickness, which leads to a more convenient treatment of the fluid height dependent functions. Both studies use the power series method with regard to a small parameter, which is defined by the offset of a chosen unperturbed quantity in relation to its perturbation amplitude. On basis of the originally given functions, Naletova's small parameter consists of the constant fluid height and the amplitude of

3. Ferrofluid Based Locomotion due to Surface Deformation

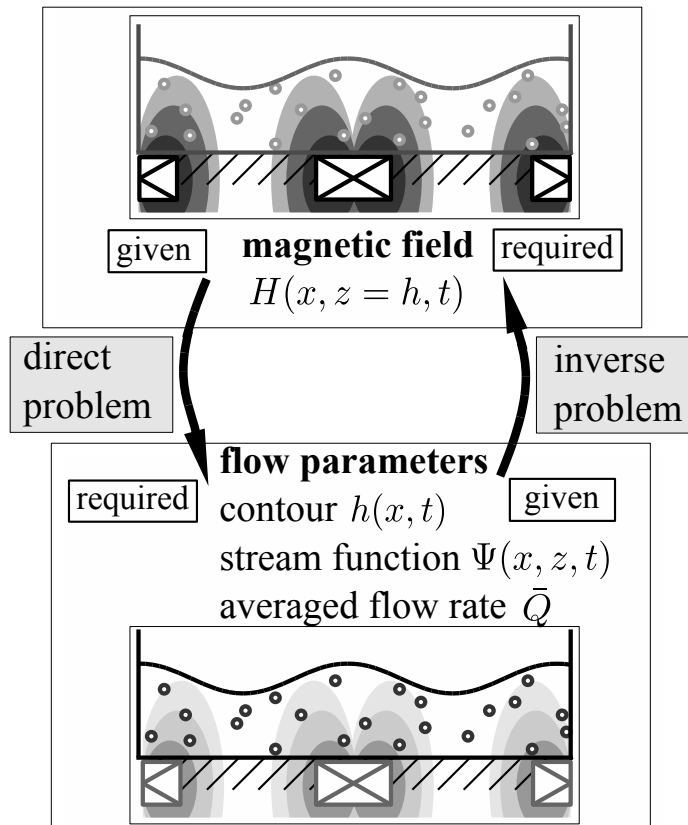


Figure 3.1.: *Reverse contemplation of similarities of the comparative and own analytics.*

the surface curvature, the one of this chapter involves the magnetic offset and its perturbation.

Lastly, an intriguing fact closes the comparison. Naletova shows how the flow proceeds in the opposite direction to the applied magnetic field, quite like an earth worm, whose contraction wave moves reverse to the propagation of the animal. Our calculation, though, reveals a material transport in the same direction as the causative magnetic field goes.

3.2. Richter's Pump is not Ours

The group of experimental physicists around Rehberg and Richter in Bayreuth, Germany is occupied with behavior and creation of structures originally with other media, now intensively with ferrofluids. While exposing the ferrofluid to a traveling, stripe-shaped magnetic

3.2. Richter's Pump is not Ours

field, they found not only alterations in the ROSENSWEIG patterns, but also developed a device pumping ferrofluid, [Bee08]. Some refinement cycles later, it changed its design and abilities, [Fri10]. Friedrich and Richter's device employs a container positioned between a helmholtz coil pair, see figure 3.2. Directly beneath the ferrofluid container (above the lower coil), a flat belt with thin wire rods attached runs under the fluid. The iron rods aligned perpendicular to the proceeding direction superimpose a sinusoidal modulation onto the field. Field measurements inside the air-filled container confirmed this. This leads to passing stripe shaped wave formations at the ferrofluid surface. The magnetic field strength was held at a level just below ROSENSWEIG peak growth. This setup ensures a maximal field strength due to a very close distance to magnet and concentrator at the very bottom of the ferrofluid layer.

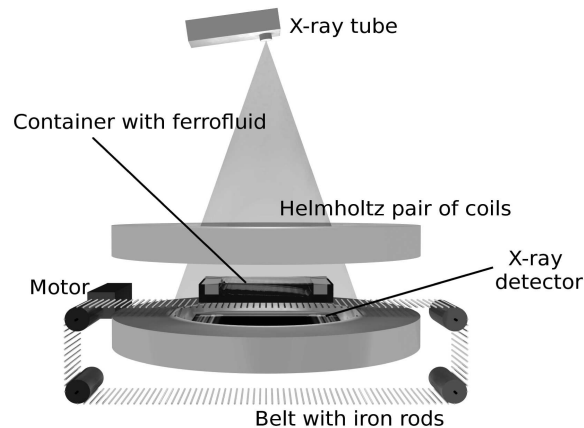


Figure 3.2.: *Experimental setup of the comparative case, see [Fri10].*¹

Friedrich and his colleagues used driving velocities of the belt $v_{\text{belt}} = 0 - 11.2$ cm/s and a fluid level of $h_0 = 2.5$ mm (resulting from the statement of 30 ml volume distributed in a container of $120 \times 100 \times 25$ mm³). They applied the ferrofluid (EMG 909, Ferrotec²), which possesses a low kinematic viscosity. Consequently, this causes high REYNOLDS numbers. According to the authors of [Fri10], the reasons for the established flow are 'ferrohydrodynamic' pumping and peristaltic effects

¹Figure 3.2 by courtesy of T. Friedrich.

²Ferrotec GmbH, 72669 Unterensingen, Germany, <http://www.ferrotec-europe.de>

3. Ferrofluid Based Locomotion due to Surface Deformation

from the waved surface. Nevertheless, one can expect a velocity profile with non-zero velocities ranging along the best part of the fluid height. Here, the peristaltic waves at the surface and the ferrohydrodynamic effect at the ground (close to the highest field gradient) accompany each other.

The problem above differs in the velocity and magnetic field distribution from the one presented in this section. While inertia loads never truly cease in a mass-carrying system, we attempted to reduce it to a minimum to achieve a sole peristaltic transport, by a lower drive velocity and a higher viscosity resulting in a REYNOLDS number one to two orders of magnitude smaller. The velocity profile features a peak at the surface diminishing rapidly towards the ground. Real fluids hold a non-constant permeability μ , which results in a gradually changing magnetic field within the fluid and conditions magnetic volume forces. As we adopt the assumption of a magnetic surface load in the calculation due to a small susceptibility, for an accompanying experiment, we attempt to keep any transporting effect by a real magnetic body force as small as possible. Thus, our setup applies the alternating field from above, exposing the free fluid surface to strongest magnetic gradient. The mentioned article [Fri10] is occupied with the thorough analysis of the magnetic field by means of measurement and calculation and its effects on driving pressure gradient or the shape of the aggregated fluid, respectively. Whereas the main focus of the following phenomenon is put on the description of motion and locomotion, the causative magnetic field is considered to be given.

3.3. Introduction of the Problem

This study considers is a two-dimensional problem incorporating a sufficiently wide layer of a magnetizable, incompressible fluid, resting on a horizontal, rigid plane, see figure 3.3. Neither surrounding air nor bottom are magnetizable. A periodically alternating magnetic field H^*2

3.3. Introduction of the Problem

is applied to that fluid, which causes a periodic curvature of the free surface of the ferrofluid. The field description is satisfied by

$$H^{*2} = H_0^2 + A^2(z^*) \sin(\zeta), \quad (3.1)$$

$$\text{where } \zeta = k^* x^* - \omega^* t^*. \quad (3.2)$$

Here, H_0^2 is the constant part, and A^2 the amplitude of the periodic perturbation of H^{*2} . k^* is the wavenumber, ω^* the angular frequency and t^* the time. The fluid properties density ρ , kinematic viscosity ν , and magnetic permeability μ are taken into account, also the atmospheric pressure p_a and the acceleration g due to gravity. Finally, the drawing of the setup in figure 3.3 introduces certain geometric parameters, which are the free fluid surface $z^* = h^*(x^*, t^*)$, the unperturbed fluid height h_0 . The Cartesian coordinate system names x^* and z^* as the relevant spatial dimensions.

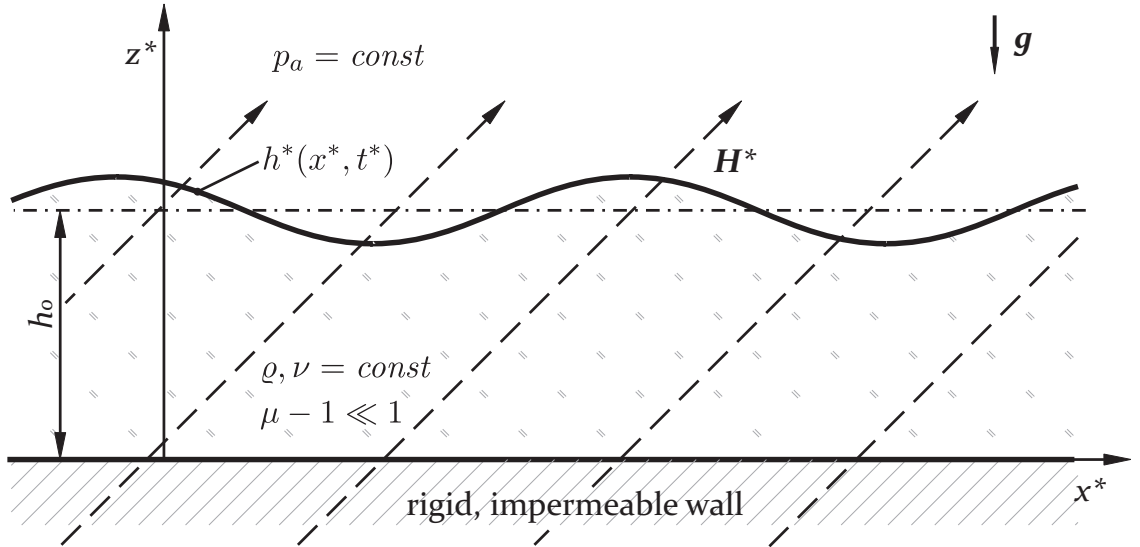


Figure 3.3.: Drawing of the considered system.

As the fluid surface is influenced by the magnetic field, an establishing flow is expected with the velocity $\mathbf{v}^* = u^* \mathbf{e}_x + w^* \mathbf{e}_z$. This occurs while no external pressure gradient works on the magnetic fluid. It is unknown, whether an effective fluid transport does take place at all. Consequently, the task is to prove the existence of a non-zero averaged flow rate. The description is done in the GAUSSIAN cgs system.

3.4. Introduction of Tools

3.4.1. Non-Dimensionalization

According to custom, all parameters are transferred into a dimensionless form by consorting the following relations. (The asterisk factors contain dimensions.):

$$(x^*, z^*) = (x, z)h_0, \quad (3.3a) \quad (u^*, w^*) = (u, w)U_c, \quad (3.3f)$$

$$h^* = hh_0, \quad (3.3b) \quad U_c = h_0\omega^*, \quad (3.3g)$$

$$k^* = k/h_0, \quad (3.3c) \quad t^* = tT_c, \quad (3.3h)$$

$$(p^*, \tau_{ij}^*) = (p, \tau_{ij})P_c, \quad (3.3d) \quad T_c = 1/\omega^*, \quad (3.3i)$$

$$P_c = \nu \rho U_c / h_0 \quad H^* = HH_0, \quad (3.3j)$$

$$= \omega^* \nu \rho, \quad (3.3e) \quad \mathbf{F}^* = \mathbf{F} \rho g. \quad (3.3k)$$

The abbreviations relate to T_c the characteristic period time, U_c the characteristic velocity, P_c the characteristic pressure, whereas p is the fluid pressure and τ_{ij} is the viscosity stress tensor. \mathbf{F}^* is the volume density of the gravity force action upon the fluid, its non-dimensional vector has the value $\mathbf{F} = -\mathbf{e}_z$.

3.4.2. Governing Equations

The equation of motion is the NAVIER STOKES equation

$$Re \, Sr \frac{\partial}{\partial t} \mathbf{v} + Re(\mathbf{v} \nabla) \mathbf{v} = -Re \, Eu \nabla p + \Delta \mathbf{v} + \frac{Re}{Fr} \mathbf{F}. \quad (3.4)$$

The characteristic parameters STROUHAL, REYNOLDS, EULER and FROUDE numbers, [Whi08, p 307ff], are

$$Sr = \frac{h_0}{U_c T_c} = \frac{h_0 \omega^*}{U_c} \quad (3.5a) \quad Eu = \frac{P_c}{\rho U_c^2} = \frac{\nu}{h_0^2 \omega^*} \quad (3.5c)$$

$$Re = \frac{h_0 U_c}{\nu} = \frac{h_0^2 \omega^*}{\nu} \quad (3.5b) \quad Fr = \frac{U_c^2}{gh_0} = \frac{h_0 \omega^*}{g} \quad (3.5d)$$

STROUHAL, REYNOLDS, EULER and FROUDE refer to (3.3a) to (3.3k). A creeping flow is expected for the given setup, in that case REYNOLDS shall be small. Consequently, it can be specified:

$$Re \ll 1 \quad (3.6a)$$

$$Sr = 1 \quad (3.6b)$$

$$Re Eu = 1 \quad (3.6c)$$

By balancing the influences of the individual members, we decide on the use of the STOKES approximation

$$\nabla p = \Delta \mathbf{v} + \delta \mathbf{F}, \quad (3.7a)$$

$$\text{where } \delta = \frac{Re}{Fr} = \frac{gh_0^2}{\nu U_c^2}, \quad (3.7b)$$

and the continuity equation for incompressible fluids

$$0 = \frac{\partial u}{\partial x} + \frac{\partial w}{\partial z}. \quad (3.8)$$

The stream function Ψ is introduced by (3.9),

$$u = -\frac{\partial}{\partial z}\Psi(x, z, t), \quad (3.9a) \quad w = \frac{\partial}{\partial x}\Psi(x, z, t). \quad (3.9b)$$

When (3.9) is inserted into (3.7a) and the pressure p is eliminated, the biharmonic homogeneous differential equation (3.10) can be obtained

$$0 = \Delta \Delta \Psi(x, z, t). \quad (3.10)$$

3.4.3. Boundary Conditions

From the setting of the task, figure 3.3, the kinematic boundary conditions on the free surface $z^* = h^*(x^*, t^*)$ are derived. In first presentation they appear in dimensional form.

Equations (3.11) are valid at the base and note the velocity of the frictional fluid equals the one of the tangent, motionless wall,

3. Ferrofluid Based Locomotion due to Surface Deformation

$$u^*(x^*, z^* = 0, t^*) = 0 \quad (3.11a) \quad w^*(x^*, z^* = 0, t^*) = 0 \quad (3.11b)$$

$$\begin{aligned} \frac{d}{dt}h^*(x^*, t^*) &= \frac{\partial}{\partial t^*}h^*(x^*, t^*) + \frac{\partial}{\partial x^*}h(x^*, t^*)\frac{dx^*}{dt^*} \\ &= w^*(x^*, z^* = h^*, t^*) \end{aligned}$$

$$0 = h_{t^*}^* + h_{x^*}^*u^*(x^*, z^* = h^*, t^*) - w^*(x^*, z^* = h^*, t^*). \quad (3.12)$$

Lastly, at the boundary of fluid and atmosphere, at $z^* = h^*(x^*, t^*)$, stress builds a steady function, which means the sum of all considered stresses is zero. The hydrostatic pressure p^* of the liquid, the surface tension and the magnetic pressure are considered, both forms resumed from [Whi08, p 32] and [Nal05], completed by the viscous friction represented by the stress tensor:

$$\left[-p^* + \frac{\gamma}{R} + \frac{B_n^{*2}}{8\pi} \left(\frac{1}{\mu} - 1 \right) - \frac{H_\tau^{*2}}{8\pi} (\mu - 1) \right] \mathbf{n} + \tau_{ij}^* n_j \mathbf{e}_i = \mathbf{0}. \quad (3.13)$$

Here, (3.13) includes dimensions, R is the radius of the surface curvature at the respective point and γ the coefficient of the surface tension. The magnetic pressure is reflected by B_n^* , the flux density in normal direction and H_τ^* , the tangential field strength component. Thus, the indices n and τ refer to the normal or tangential direction, respectively. \mathbf{n} , the normal vector, is pointing out of the fluid. \mathbf{e}_i is the unit vector along the i -th coordinate axis, ($\mathbf{e}_1 = \mathbf{e}_x$, $\mathbf{e}_2 = \mathbf{e}_y$, $\mathbf{e}_3 = \mathbf{e}_z$).

3.5. Approach

3.5.1. Approach from the Causative Agent

Finding an approach for trading the problem, its source, the periodically alternating magnetic field, has to be investigated regarding its intention and consequence. Originally from (3.1), the magnetic field

exists of a homogeneous, constant fraction added by a periodic part, here in the dimensionless description

$$H^2 = 1 + \frac{A^2(zh_0)}{H_0^2} \sin(\zeta). \quad (3.14)$$

If the description of the magnetic field is further specified by assuming a considerably smaller perturbation relative to the constant part, at the position of the unperturbed surface, $z^* = h_0$,

$$\varepsilon = \frac{A^2(h_0)}{H_0^2} \ll 1, \quad (3.15)$$

one can recognize a power series with regard to small ε . What consequences can be drawn from this information? Above all, an idea of its influence. A thought experiment regarding the directly visible effect of the magnetic field on the fluid contour will clarify the matter. In case of an absent field, the fluid surface will lie plane at a low level. When exposed to a constant homogeneous field, which states the zeroth order of the potential series, the surface is still horizontal, but risen to the level h_0 . As the fluid cannot multiply or expand its volume, one can imagine a supply from the infinite width of the pool. A field of first order, as given in the original task, will induce a periodical curvature, see figure 3.3. This wave pattern aligns around the level of the former h_0 . Fields of second or higher orders would superordinate a further curvature pattern onto the already curved contour.

By watching the individual phenomenon, a concept can be obtained on how the magnetic field interferes with every other aspect of the system. Due to this reason the structure of the field description will be adapted to every parameter and process of the system.

The stream function $\Psi(x, z, t)$ will be registered in the form of a power series

$$\Psi(x, z, t) = \Psi(z, \zeta) = \Psi_0 + \sum_{n=1}^{\infty} \varepsilon^n \Psi_n(z, \zeta), \quad \text{with } n \in \mathbb{N}. \quad (3.16)$$

3. Ferrofluid Based Locomotion due to Surface Deformation

For $\varepsilon = 0$, which corresponds to the static magnetic field, the pressure gradient in x -direction is zero, hence $\Psi_0(x, z, t) = 0$. Consequently, the same structure will be superimposed on the function $h(x, t)$, too. By doing so, it appears dimensionalized

$$h^*(x^*, t^*) = h_0 + \sum_{n=1}^{\infty} \varepsilon^n h_n^*(x^*, t^*), \quad \text{with } n \in \mathbb{N} \quad (3.17)$$

and in dimensionless form as

$$h(x, t) = 1 + \sum_{n=1}^{\infty} \varepsilon^n h_n(x, t). \quad (3.18)$$

The orders of higher members of the stream function, $\Psi_n(x, z, t)$, $n \geq 1$, require an approach, too. Therefore, the form of the wave equation is inherited from (3.14) to express the periodic character, which can also be assumed as appropriate structure for every other parameter involved

$$\Psi_n(x, z, t) = \Psi_n(z, \zeta) = \sum_{m=1}^{\infty} \Psi_{nm}(z, \zeta) \quad (3.19)$$

$$\Psi_{nm}(z, \zeta) = \eta_{nm}(z) \cos(m\zeta) + \xi_{nm}(z) \sin(m\zeta). \quad (3.20)$$

For shorter writing, abbreviations for inserted values of z like $\Psi_{nm}(1)$ or $\Psi_{nm}(h)$ are used instead of $\Psi_{nm}(x, z = 1, t)$ or $\Psi_{nm}(x, z = h(x, t), t)$, respectively, the same terms apply for the pressure p and the derivations of Ψ and p .

3.5.2. Determination of the Stream Function

Equation (3.20) emphasizes that the horizontal and temporal dependencies are enveloped in the trigonometric functions and merely the amplitudes $\eta(z)$ and $\xi(z)$ depend vertically on z . So, when partially derived four times like indicated by (3.10), the periodicity will not have changed at all. This suggests a treatment such as an ordinary differential equation depending on z rather than the partial differential equation of (3.10).

3.6. Material Transport Mapped by the Flow Rate

By inserting the function (3.20) in power mode (3.16) into the differential equation (3.10), an expression is found, which, separated by equation coefficients, leads to two ordinary differential equations.

$$0 = m^4 k^4 \eta_{nm}(z) - 2m^2 k^2 \eta_{nm'zz}(z) + \eta_{nm'zzzz}(z) \quad (3.21a)$$

$$0 = m^4 k^4 \xi_{nm}(z) - 2m^2 k^2 \xi_{nm'zz}(z) + \xi_{nm'zzzz}(z). \quad (3.21b)$$

The e^λ ansatz leads to the eigenvalues $\lambda_1 = \lambda_2 = +mk$ and $\lambda_3 = \lambda_4 = -mk$, with $m \geq 1$. Thus, the general solution states

$$\begin{aligned} \eta_{nm}(z) = & a_{nm}^{(1)} \cosh(mkz) + a_{nm}^{(2)} z \cosh(mkz) + \\ & + a_{nm}^{(3)} \sinh(mkz) + a_{nm}^{(4)} z \sinh(mkz) \end{aligned} \quad (3.22a)$$

$$\begin{aligned} \xi_{nm}(z) = & b_{nm}^{(1)} \cosh(mkz) + b_{nm}^{(2)} z \cosh(mkz) + \\ & + b_{nm}^{(3)} \sinh(mkz) + b_{nm}^{(4)} z \sinh(mkz). \end{aligned} \quad (3.22b)$$

3.6. Material Transport Mapped by the Flow Rate

We intend to give evidence of an efficacious material transport by the peristaltic motion of the surface deformation (caused by the alternating magnetic field). A suitable instrument of doing so is the volume rate Q , which, if integrated over the period time T , will account for the conveyed fluid beyond the commuting within a period. Consequently, it is expected

$$\bar{Q} = \frac{1}{T} \int_0^T Q(x, t) dt \neq 0. \quad (3.23)$$

For classical, three-dimensional flow mechanics, Q is obtained by recording the fluid velocity passing the perpendicular cross section, see [Whi08, p 141]. However, for the given problem we attend to the two-dimensional (3.24)

3. Ferrofluid Based Locomotion due to Surface Deformation

$$Q = \int_0^{h(x,t)} u(z, \zeta) dz \quad (3.24)$$

and replace u by Ψ employing the relation linking these parameters (3.9).

$$Q = - \int_0^{h(\zeta)} \frac{\partial \Psi(z, \zeta)}{\partial z} dz = -\Psi(h, \zeta) + \Psi(0, \zeta). \quad (3.25)$$

Like stated in the last section (3.5.1), the stream function Ψ , the upper limit $h(x, t)$, and the flow rate Q are power series. When h in power mode is inserted in Ψ , a TAYLOR series expansion is required, which is operated according to the definition [Mey99, p 239]

$$T_f(z, a) = \sum_{i=0}^{\infty} \frac{f^{(i)}(a)}{i!} (z - a)^i. \quad (3.26)$$

Here, a is the point of expansion of the function T_f , applied to the function $\Psi_n(h)$ with $a = 1$ and $i = \{0; 2\}$. We gain for $\Psi(1, \zeta)$

$$\begin{aligned} T_f &= \Psi_n(1) + \Psi_{n'z}(1)(\varepsilon h_1 + \varepsilon^2 h_2) + \\ &+ \frac{1}{2} \Psi_{n'zz}(1)(\varepsilon h_1 + \varepsilon^2 h_2)^2 + \dots \\ &= \Psi_n(1) + \varepsilon h_1 \Psi_{n'z}(1) + \frac{1}{2} h_1^2 \Psi_{n'zz} + o(\varepsilon^2). \end{aligned} \quad (3.27)$$

Subsequently, from (3.25) and (3.27) follows for Q

$$Q = Q_0 + \varepsilon Q_1 + \varepsilon^2 Q_2 + o(\varepsilon^2), \quad (3.28)$$

incorporating

$$Q_0 = \Psi_0(0, \zeta) - \Psi_0(1, \zeta) = 0 \quad (3.29a)$$

$$Q_1 = \Psi_1(0, \zeta) - \Psi_1(1, \zeta) \quad (3.29b)$$

$$Q_2 = \Psi_2(0, \zeta) - \Psi_2(1, \zeta) - h_1 \Psi_{1,z}(1, \zeta). \quad (3.29c)$$

The equations (3.28) and (3.29) may now be integrated, as (3.23) indicates. This involves averaging the volume rate over the time t . Yet, the volume flow oscillates not only with time, but its periodicity includes

3.6. Material Transport Mapped by the Flow Rate

also the horizontal expansion x . Whilst both, x and t , can be varied arbitrarily, they geometrically condition each other implicitly fixed by ζ . The function $\zeta(x, t)$, from (3.2), filled with dimensionless variables produces a redefinition of dt

$$\zeta = kx - t \quad \Rightarrow \quad dt = -d\zeta. \quad (3.30)$$

This information enters (3.23)

$$\bar{Q} = -\frac{1}{2\pi} \int_{kx}^{kx-2\pi} Q(\zeta) d\zeta, \quad \text{where } T = 2\pi, \quad (3.31)$$

$$\begin{aligned} \bar{Q} = \frac{1}{2\pi} \int_{kx-2\pi}^{kx} & [\varepsilon(\Psi_1(1) - \Psi_1(0)) + \varepsilon^2(h_1\Psi_{1'z}(1) + \\ & + \Psi_2(1) - \Psi_2(0))] d\zeta. \end{aligned} \quad (3.32)$$

Without going into detail already, a brief estimation of the integration at issue shows, every member consisting of a single Ψ will be eliminated when integrating sine and cosine over a range of double π . On the other hand, being aware that h_1 and $\Psi_{1'z}$ contain similar periodic structures, one can expect the doubly occupied term integrated will not render to nil.

Already here, it becomes clear, the final result and first non-zero member will be built up by a multiplication of εh_1 and $\varepsilon \Psi_{1'z}$. Although the result will be of the second order (ε^2), its constituents are of the first order (ε^1). Therefore, when aiming for descriptions of the required parameters, a limitation up to the first order will be adequate for the desired evidence-giving.

Due to the given reasoning we constrain \bar{Q} to

$$\bar{Q} = -\frac{1}{2\pi} \int_{kx-2\pi}^{kx} \varepsilon^2 \Psi_{1'z}(1) h_1 d\zeta + \mathcal{O}(\varepsilon^3) \quad (3.33)$$

and proceed for the boundary conditions in order to find solutions for h_1 and $\Psi_{1'z}$.

3.7. Preparation of the Boundary Conditions

To get rid (3.22) of the coefficients $a_{nm}^{(1)}$ to $a_{nm}^{(4)}$ and $b_{nm}^{(1)}$ to $b_{nm}^{(4)}$, respectively, and gain the special solution, the boundary conditions (3.11a) to (3.13) have to be applied. Already at the present state, the complexity of the special solution can be estimated. A limitation is sensible, as the most general form is not required.

3.7.1. The Kinematic Boundary Conditions

The third boundary condition, valid at $z = h(x, t)$, does not contribute directly to the termination of the coefficients $a_{nm}^{(1-4)}$ and $b_{nm}^{(1-4)}$. In fact, it provides a connection between the contour function $h(x, t)$ and the velocity components u and w , or the stream function Ψ , respectively, which will be used for the preparation of the last boundary condition.

The equation (3.12) can be altered into

$$0 = h_{1't} - h_{1'x} \Psi_{1'z}|_{z=h(x,t)} - \Psi_{1'x}|_{z=h(x,t)}. \quad (3.34)$$

In (3.34), the power series character of $h(x, t)$ and $\Psi(x, z, t)$ is implied. As the condition is only valid at a special position, z will be localized by the power series function $h(x, t) = 1 + \varepsilon h_1 + \varepsilon^2 h_2 + o(\varepsilon^2)$, (3.18). Thus, the stream function has to undergo a development of TAYLOR power series. Consequent shortening, which excludes any member higher than order 2, does provide

$$0 = \varepsilon h_{1't} + \varepsilon^2 h_{2't} - \varepsilon^2 h_{1'x} \Psi_{1'z}(1) - \varepsilon \Psi_{1'x}(1) - \varepsilon^2 h_1 \Psi_{1'xz}(1) + \varepsilon^2 \Psi_{2'x} + o(\varepsilon^2). \quad (3.35)$$

Comparison of coefficients regarding to ε^n yields to

$$\varepsilon : \quad 0 = h_{1't} - \Psi_{1'x}(1) \quad (3.36a)$$

$$\varepsilon^2 : \quad 0 = h_{2't} - \Psi_{1'z}(1) h_{1'x} - \Psi_{1'xz}(1) h_1 - \Psi_{2'x}(1). \quad (3.36b)$$

Due to the close relation between stream function Ψ in (3.20) and surface function $h(x, t)$ a similar structure is assumed for the latter

3.7. Preparation of the Boundary Conditions

$$h_1(x, t) = h_1(\zeta) = \tilde{h}_1 \cos(\zeta) + \tilde{\tilde{h}}_1 \sin(\zeta), \quad (3.37)$$

where $\tilde{h}_1, \tilde{\tilde{h}}_1 = \text{const.}$

We proceed with (3.36a) and insert the required derivations following from (3.20) and (3.37). Hence,

$$h_1(x, t) = -k\Psi_1(x, 1, t). \quad (3.38)$$

is gained. More information can be extracted from boundary condition (3.12). For this, we regard the contour function $h(x, t)$. x and t are arguments of h and are kinematically fixed in the way ζ describes in (3.2). Thus, it is also possible to write $h = h(\zeta)$. Derivations regarding the mentioned arguments require a total differentiation

$$\frac{\partial}{\partial t} h_1(x, t) = \frac{\partial h_1}{\partial \zeta} \frac{\partial \zeta}{\partial t} = -\frac{\partial h_1}{\partial \zeta} \quad (3.39a)$$

$$\frac{\partial}{\partial x} h_1(x, t) = \frac{\partial h_1}{\partial \zeta} \frac{\partial \zeta}{\partial x} = k \frac{\partial h_1}{\partial \zeta} \quad (3.39b)$$

and deliver the desired relation between the temporal and the spacial derivation of the free surface

$$h_{1't} = -kh_{1'x}. \quad (3.40)$$

3.7.2. Boundary Condition 4

Condition 3 educed a relation between contour function h_1 and Ψ_1 , see section 3.7.1. Thus, the fourth condition has to be employed to solve the four remaining unknown coefficients.

The preparation of (3.13) requires comprehensive operations to find relations between parameters and to replace them in search for an expression holding nothing but the stream function $\Psi(z = 1)$ with the coefficients a_3 to b_4 .

3. Ferrofluid Based Locomotion due to Surface Deformation

How can this goal be accomplished? First, all parameters are transformed either into the surface or stream function. Both, the STOKES approximation (3.7a) and the potential equation (3.10) are needed here. By the application of the relations (3.38) and (3.40), extracted from condition (3.12), the final conversion to Ψ can be done. Furthermore, the insertion of $z = h$, the contour function being in power mode, will require several TAYLOR series expansions.

Lastly, due to splitting of the vector equations into scalars and to disassembling these, by comparison of coefficients four equations are generated to solve the four amplitude parameters a_3 to b_4 .

Prior to the preparation of (3.13), some considerations are taken into account. Equation (3.13) is transferred into non-dimensionalized form, too. During this, we assume the magnetic permeability satisfies the term $\mu - 1 \ll 1$, which states the condition for the non-inductive approximation. This approach recognizes the magnetic load as magnetic pressure p_{mag} working at the surface

$$p_{mag} = \frac{B_n^2}{8\pi} \left(\frac{1}{\mu} - 1 \right) - \frac{H_\tau^2}{8\pi} (\mu - 1), \quad (3.41a)$$

applying $B_n^2 = \mu^2 H_n^2$, where $\mu = \mu_0 \mu_r$, produces

$$p_{mag} = -\frac{(\mu - 1)}{8\pi} (\mu H_n^2 + H_\tau^2). \quad (3.41b)$$

Since the value of a vector is $H^2 = H_n^2 + H_\tau^2$, it follows

$$p_{mag} = -\frac{(\mu - 1)}{8\pi} ((\mu - 1) H_n^2 + H^2). \quad (3.41c)$$

As we consider $\mu - 1 \ll 1$, the quadratic $(\mu - 1)^2$ can be neglected due to diminutiveness compared to the basic one. The magnetic surface pressure is

$$p_{mag} = -\frac{(\mu - 1)}{8\pi} H^2 \quad (3.41d)$$

3.7. Preparation of the Boundary Conditions

The equations (3.3) are employed for non-dimensionalization as well as for the conversion in conjunction with (3.14) and the substitution (3.42)

$$\varkappa = \frac{(\mu - 1) H_0^2}{8\pi P_c}, \quad (3.42)$$

hence (3.13) returns

$$\left[-p + \frac{\gamma}{h_0 P_c R} - \varkappa(1 + X(h) \sin(\zeta)) \right] \mathbf{n} + \tau_{ij} n_j \mathbf{e}_i = \mathbf{0} \quad (3.43)$$

here is

$$X(z) = \frac{A^2(h_0 z)}{H_0^2}, \quad X(1) = \varepsilon \ll 1. \quad (3.44)$$

We assume that derivations of the function $X(z)$ are the order $\varepsilon \ll 1$ at $z = 1$. So are $X'_{z}(1) = \varepsilon c_{1X}$, $X''_{zz}(1) = \varepsilon c_{2X}$, where $c_{1X}, c_{2X} = \text{const.}$ The WEBER number, as indicator for the influence of surface tension, is introduced

$$We = \frac{\gamma}{h_0 P_c} = \frac{\gamma}{h_0 \omega^* \rho \nu}, \quad (3.45)$$

A short remark concerning the WEBER number. The We presented here differs slightly from the usually defined version, like given in [Whi08, p 308], $We = \gamma/(h_0 \rho U_c^2)$. The difference occurs due to the specification on the fluid characteristics – a small Re and large Eu , see (3.6b) and (3.6c), and the magnetic driving force as the source of this problem. In consequence, the given We focuses on the magnetic pressure, rather than on the dynamic pressure, which the original We underlines. The appearance of the magnetic surface pressure will be wrapped into the parameter

$$\varkappa = \frac{(\mu - 1) H_0^2}{8\pi \omega^* \rho \nu}. \quad (3.46)$$

In this form, the emphasis of the relation between magnetic surface pressure and characteristic pressure caused by the viscosity of an ex-

3. Ferrofluid Based Locomotion due to Surface Deformation

cited fluid is more stringent. The radius of the surface curvature R is kinematical expressed

$$R = -\frac{(1 + h_{r_x}^2)^{3/2}}{h_{r_{xx}}}. \quad (3.47)$$

This yields to

$$\left[-p - We \frac{h_{r_{xx}}}{(1 + h_{r_x}^2)^{3/2}} - \varkappa(1 + X(h) \sin(\zeta)) \right] \mathbf{n} + \tau_{ij} n^j \mathbf{e}_i = \mathbf{0}. \quad (3.48)$$

Seeking an equation system, the vectorial equation (3.48) is split into two scalars by multiplication with the normal \mathbf{n} and tangential vector \mathbf{s} , respectively:

$$\begin{aligned} \mathbf{e}_n : \quad 0 = & -p - We \frac{h_{r_{xx}}}{(1 + h_{r_x}^2)^{3/2}} - \varkappa(1 + X(h) \sin(\zeta)) + \\ & + \tau_{xx} n_x^2 + 2\tau_{xz} n_x n_z + \tau_{zz} n_z^2 \end{aligned} \quad (3.49a)$$

and

$$\mathbf{e}_\tau : \quad 0 = (\tau_{xx} - \tau_{zz}) n_x n_z + \tau_{xz} (n_z^2 - n_x^2). \quad (3.49b)$$

At the earlier transformation of τ_{ij}^* to the dimensionless τ_{ij} , the kinematic viscosity included in the material equation for incompressible fluids disappears when operating the relations (3.3)

$$\tau_{ij} = \left(\frac{\partial v_i}{\partial x_j} + \frac{\partial v_j}{\partial x_i} \right). \quad (3.50)$$

The substitution of n_i and n_j leads to rethinking of the formulation $z = h(x, t)$, which produces the implicit expression

$$\varphi(z, x, t) = z - h(x, t) = 0. \quad (3.51)$$

Due to parallelism between \mathbf{n} and $\nabla\varphi$, the kinematic description of the normal vector is established by

3.7. Preparation of the Boundary Conditions

$$\mathbf{n} = \left[-h'_{1x}(h_{1x}^2 + 1)^{-1/2}, (h_{1x}^2 + 1)^{-1/2} \right]. \quad (3.52)$$

When the surface function $h(x, t) = 1 + \varepsilon h_1 + \varepsilon^2 h_2 + o(\varepsilon^2)$, (3.18), in power mode is introduced into the terms which originate from n_x , n_z and the curvature radius R , TAYLOR series expansions are required to obey the instruction (3.26)

$$T_f(\varepsilon) = f(\varepsilon)|_{\varepsilon=0} + \frac{\varepsilon}{1!} f'_{\varepsilon}(\varepsilon)|_{\varepsilon=0} + \frac{\varepsilon^2}{2!} f''_{\varepsilon\varepsilon}(\varepsilon)|_{\varepsilon=0} + o(\varepsilon^2). \quad (3.53)$$

The first term to be transfigured is $n_x n_z$. For the expansion, the function

$$f_{\varepsilon} = \frac{1}{(1 + h_{1x}^2)} \quad (3.54a)$$

is considered, which produces

$$T_{f1}(\varepsilon) = 1 - \varepsilon^2 h_{1'x}^2 + o(\varepsilon^2). \quad (3.54b)$$

Put into the original phrase, the new term is

$$\begin{aligned} -\frac{h'_{1x}}{(h_{1x}^2 + 1)} &= -(\varepsilon h_{1'x} + \varepsilon^2 h_{2'x})(1 - \varepsilon^2 h_{1'x}^2) + o(\varepsilon^2) \\ &= -\varepsilon h_{1'x} - \varepsilon^2 h_{2'x}^2 + o(\varepsilon^2) \end{aligned} \quad (3.54c)$$

The next transformation operates $n_z^2 - n_x^2$, equally (3.54a) is applied to (3.53) and multiplied with the numerator yields to

$$\begin{aligned} \frac{1 - h_{1x}^2}{1 + h_{1x}^2} &= (1 - 2\varepsilon^2 h_{1'x}^2)^2 + o(\varepsilon^2) \\ &= 1 - 2\varepsilon^2 h_{1'x}^2 + o(\varepsilon^2). \end{aligned} \quad (3.55)$$

For the conversion of the curvature radius R , the function

$$f_{\varepsilon} = \frac{1}{\sqrt{1 + h_{1x}^2}} \quad (3.56a)$$

is considered for series expansion, which produces

3. Ferrofluid Based Locomotion due to Surface Deformation

$$T_{f2}(\varepsilon) = 1 - \varepsilon^2 \frac{h_{1'x}^2}{2} + o(\varepsilon^2). \quad (3.56b)$$

This turns the curvature radius to

$$\begin{aligned} \frac{h'_{xx}}{(1 + h_{1'x}^2)^{3/2}} &= (\varepsilon h_{1'xx} + \varepsilon^2 h_{2'xx}) \left(1 - \frac{3}{2} \varepsilon^2 h_{1'x}^2\right) + o(\varepsilon^2) \\ &= \varepsilon h_{1'xx} + \varepsilon^2 h_{2'xx} + o(\varepsilon^2). \end{aligned} \quad (3.56c)$$

The function $X(h)$ is

$$X(h) = X(1) + \varepsilon h_1 X'_{1z}(1) + \dots \quad (3.57)$$

Equations (3.50) and the symmetry of the stress tensor ($\tau_{xx} = -\tau_{zz}$ and $\tau_{xz} = \tau_{zx}$)

$$\tau_{xx} = -2\Psi'_{xz}, \quad \tau_{xz} = \Psi'_{xx} - \Psi'_{zz} = \tau_{zx}, \quad \tau_{zz} = 2\Psi'_{zx}.$$

combined with the newly found forms (3.54c), (3.55), and (3.56c) are used to compress (3.49)

$$\begin{aligned} \mathbf{e}_n : \quad 0 &= -p - We(\varepsilon h_{1'xx} + \varepsilon^2 h_{2'xx}) - \varkappa - \\ &\quad - \varkappa(\varepsilon + \varepsilon^2 c_{1X} h_1) \sin(\zeta) + 2\Psi'_{xz}(1 - 2\varepsilon^2 h_{1'x}^2) - \\ &\quad - 2(\Psi'_{xx} - \Psi'_{zz})(\varepsilon h_{1'x} + \varepsilon^2 h_{2'x}^2) + o(\varepsilon^2), \end{aligned} \quad (3.58a)$$

$$\begin{aligned} \mathbf{e}_\tau : \quad 0 &= 4\Psi'_{xz}(\varepsilon h_{1'x} + \varepsilon^2 h_{2'x}^2) + \\ &\quad + (\Psi'_{xx} - \Psi'_{zz})(1 - 2\varepsilon^2 h_{1'x}^2) + o(\varepsilon^2). \end{aligned} \quad (3.58b)$$

We proceed in turning the parameters into power series, next is the pressure $p(x, z, t)$ in \mathbf{e}_n . At the application of the power series of $h(x, t)$ in the position z , another TAYLOR series expansion is necessary. The following substitutions by the STOKES approximation, see (3.7a), and the relations from boundary condition 3, see (3.38) and (3.40), are explained in due course.

The pressure p can be written in power mode as any other fluid parameter

3.7. Preparation of the Boundary Conditions

$$p(x, z, t) = p(z, \zeta) = p_0(z, \zeta) + \varepsilon p_1(z, \zeta) + \varepsilon^2 p_2(z, \zeta) + o(\varepsilon^2), \quad (3.59)$$

while $h(x, t) = 1 + \varepsilon h_1 + \varepsilon^2 h_2 + o(\varepsilon^2)$ is inserted in z . Thus, according to the instruction of [Mey99, p 232], see (3.53), the TAYLOR series is developed

$$\begin{aligned} p_n(h, \zeta) &= p_n(1) + p_{n'z}(1)|_{z=1} (\varepsilon h_1 + \varepsilon^2 h_2) + \\ &+ \frac{1}{2} p_{n'zz}(1)|_{z=1} (\varepsilon h_1 + \varepsilon^2 h_2)^2 + o(\varepsilon^2). \end{aligned} \quad (3.60)$$

The resulting derivations of p with respect to z are replaced by the relation taken from the z -component $p'_z = w'_{xx} + w'_{zz} - \delta$ of the STOKES approximation (3.7a)

$$\begin{aligned} p_n(h, \zeta) &= p_n(1) + (\Psi_{n'xxx}(z)|_{z=1} + \Psi_{n'xzz}(z)|_{z=1} - \delta) \times \\ &\times (\varepsilon h_1 + \varepsilon^2 h_2 + \dots) + o(\varepsilon^2). \end{aligned} \quad (3.61)$$

The equation (3.61) holds $\Psi'_{xxx}(z)|_{z=1}$ and $\Psi'_{xzz}(z)|_{z=1}$, when z is replaced by the power series of the contour h , a further power series expansion is necessary.

$$\begin{aligned} \Psi_{n'xxx}(z)|_{z=1} &= \Psi_{n'xxx}(1) + \frac{\partial}{\partial z} \Big|_{z=1} \Psi_{n'xxx}(1) (\varepsilon h_1 + \varepsilon^2 h_2) + \\ &+ \frac{1}{2} \frac{\partial^2}{\partial z^2} \Big|_{z=1} \Psi_{n'xxx}(1) (\varepsilon h_1 + \varepsilon^2 h_2)^2 + o(\varepsilon^2) \end{aligned} \quad (3.62)$$

Analog, the insertion is accomplished for $\Psi_{n'xzz}$. The separate states of (3.59), (3.60), (3.61), and (3.62) yields to a $p(z = 1, \zeta)$

$$\begin{aligned} p(1) &= p_0(1) + \varepsilon (p_1(1) - \delta h_1) + \varepsilon^2 p_2(1) + \\ &+ \varepsilon^2 (h_1 \Psi_{1'xxx}(1) + h_1 \Psi_{1'xzz}(1) - \delta h_1 - \delta h_2) + o(\varepsilon^2). \end{aligned} \quad (3.63)$$

The derivations of $\Psi(h, \zeta)$ – they result from the shear stress tensor τ_{ij} and are turned into power series $\Psi'(1, \zeta)$ – are, like (3.63), added to (3.58). Thus, (3.58a) becomes in normal direction

3. Ferrofluid Based Locomotion due to Surface Deformation

$$\begin{aligned}
\mathbf{e}_n : \quad 0 = & -p_0(1) - \varepsilon p_1(1) + \varepsilon h_1 \delta - \varepsilon^2 p_2(1) + \varepsilon^2 (h_1 + h_2) \delta - \\
& - We(\varepsilon h_{1'xx} + \varepsilon^2 h_{2'xx}) - \varkappa - \\
& - \varkappa(\varepsilon + \varepsilon^2 c_{1X} h_1) \sin(\zeta) + 2\varepsilon \Psi_{1'xz}(1) + \\
& + 2\varepsilon^2 \Psi_{2'xz}(1) - \varepsilon^2 h_1 \Psi_{1'xzz}(1) - \varepsilon^2 h_1 \Psi_{1'xxx}(1) - \\
& - 2\varepsilon^2 h_{1'x} (\Psi_{1'xx}(1) - \Psi_{1'zz}(1)) + o(\varepsilon^2)
\end{aligned} \tag{3.64a}$$

and (3.58b) in tangential direction

$$\begin{aligned}
\mathbf{e}_\tau : \quad 0 = & \varepsilon (\Psi_{1'xx}(1) - \Psi_{1'zz}(1)) + 4\varepsilon^2 h_{1'x} \Psi_{1'xz}(1) + \\
& + \varepsilon^2 h_1 (\Psi_{1'xxz}(1) - \Psi_{1'zzz}(1)) + \\
& + \varepsilon^2 (\Psi_{2'xx}(1) - \Psi_{2'zz}(1)) + o(\varepsilon^2).
\end{aligned} \tag{3.64b}$$

The remaining members $p_n(1)$ shall be replaced by the x -component $p'_x = w_{xx} + w_{zz}$ of (3.7a). Therefore, (3.64b) has to be prepared. Only at this state of development, a derivation with respect to x is able to deliver an equation with true assertion. This appears because the condition (3.64) is only valid at the contour $z = h$, which turned out to $z = 1$ due to the power series character of h . $z = 1$ states a horizontal line of the unperturbed surface. Owing to the dependency on z , all included parameters of (3.64) are fixed on this straight horizontal. At derivation with regard to x , the function is infinitesimally shifted in x , since the position stays *on* the free surface by this lateral shifting, the derived equation remains valid. Nevertheless, the periodical perturbation of the contour and every other parameter are still given by the superposed members of higher orders $n > 0$. \mathbf{e}_n is once derived with regard to x and turns to

$$\begin{aligned}
\mathbf{e}_n : \quad 0 = & -p_{0'x}(1) - \varepsilon p_{1'x}(1) + \varepsilon h_{1'x} \delta - \varepsilon^2 p_{2'x}(1) + \\
& + \varepsilon^2 (h_{1'x} + h_{2'x}) \delta - We(\varepsilon h_{1'xxx} + \varepsilon^2 h_{2'xxx}) - \\
& - \varkappa(\varepsilon k \cos(\zeta) + \varepsilon^2 c_{1X} (h_{1'x} \sin(\zeta) + h_1 k \cos(\zeta))) + \\
& + 2\varepsilon \Psi_{1'xxz}(1) + 2\varepsilon^2 \Psi_{2'xxz}(1) - 3\varepsilon^2 h_{1'x} \Psi_{1'xxx}(1) - \\
& - \varepsilon^2 h_1 \Psi_{1'xxxx}(1) + \varepsilon^2 h_{1'x} \Psi_{1'xzz}(1) - \varepsilon^2 h_1 \Psi_{1'xxzz} - \\
& - 2\varepsilon^2 h_{1'xx} (\Psi_{1'xx}(1) - \Psi_{1'zz}(1)) + o(\varepsilon^2).
\end{aligned} \tag{3.65}$$

3.7. Preparation of the Boundary Conditions

The derivations of p contained in (3.65) are replaced by (3.7a), the implicit forms of Ψ build power series themselves, and while z is set $z = 1$, a TAYLOR series expansion is necessary, see (3.66)

$$\begin{aligned} p_{0'x}(1) + \varepsilon p_{1'x}(1) + \varepsilon^2 p_{2'x}(1) + o(\varepsilon^2) = \\ = -\varepsilon(\Psi_{1'xxz}(1) + \Psi_{1'zzz}(1)) - \varepsilon^2 h_1(\Psi_{1'xxzz}(1) + \Psi_{1'zzzz}(1)) - \\ - \varepsilon^2(\Psi_{2'xxz}(1) + \Psi_{2'zzz}(1)) + o(\varepsilon^2). \end{aligned} \quad (3.66)$$

The equation (3.66) is inserted into (3.65)

$$\begin{aligned} \mathbf{e}_n : \quad 0 = \varepsilon h_{1'x} \delta + \varepsilon^2 (h_{1'x} + h_{2'x}) \delta - We(\varepsilon h_{1'xxx} + \varepsilon^2 h_{2'xxx}) - \\ - \varkappa(\varepsilon k \cos(\zeta) + \varepsilon^2 c_{1X}(h_{1'x} \sin(\zeta) + h_1 k \cos(\zeta))) + \\ + 3\varepsilon \Psi_{1'xxz}(1) + 3\varepsilon^2 \Psi_{2'xxz}(1) - 3\varepsilon^2 h_{1'x} \Psi_{1'xxx}(1) - \\ - \varepsilon^2 h_1 \Psi_{1'xxxx}(1) + \varepsilon^2 h_{1'x} \Psi_{1'xzz}(1) - \\ - 2\varepsilon^2 h_{1'xx}(\Psi_{1'xx}(1) - \Psi_{1'zz}(1)) + \varepsilon \Psi_{1'zzz}(1) + \\ + \varepsilon^2 h_1 \Psi_{1'zzzz}(1) + \varepsilon^2 \Psi_{2'zzz}(1) + o(\varepsilon^2). \end{aligned} \quad (3.67)$$

A comparison of the coefficients with respect to the orders of ε produces from (3.64b) and (3.67) the group of (3.68)

$$\mathbf{e}_n, \varepsilon^1 : 0 = h_{1'x} \delta - We h_{1'xxx} - \varkappa k \cos(\zeta) + 3\Psi_{1'xxz}(1) + \Psi_{1'zzz}(1) \quad (3.68a)$$

$$\mathbf{e}_t, \varepsilon^1 : 0 = \Psi_{1'xx}(1) - \Psi_{1'zz}(1) \quad (3.68b)$$

$$\begin{aligned} \mathbf{e}_n, \varepsilon^2 : 0 = (h_{1'x} + h_{2'x}) \delta - We h_{2'xxx} - \varkappa c_{1X}(h_{1'x} \sin(\zeta) + \\ + h_1 k \cos(\zeta)) + 3\Psi_{2'xxz}(1) - 3h_{1'x} \Psi_{1'xxx}(1) - \\ - h_1 \Psi_{1'xxxx}(1) + h_{1'x} \Psi_{1'xzz}(1) - 2h_{1'xx}(\Psi_{1'xx}(1) - \\ - \Psi_{1'zz}(1)) + h_1 \Psi_{1'zzzz}(1) + \Psi_{2'zzz}(1) \end{aligned} \quad (3.68c)$$

$$\begin{aligned} \mathbf{e}_t, \varepsilon^2 : 0 = 4h_{1'x} \Psi_{1'xz}(1) + h_1(\Psi_{1'xxz}(1) - \Psi_{1'zzz}(1)) + \\ + (\Psi_{2'xx}(1) - \Psi_{2'zz}(1)) \end{aligned} \quad (3.68d)$$

According to the explanation of section 3.6 and (3.33), the desired functions for the evidence of material transport have to be of first order.

3. Ferrofluid Based Locomotion due to Surface Deformation

Consequently, the focus is set on the first pair of (3.68) with regard to ε^1 . Lastly, for elimination of the contour function h_1 , the condition (3.38) is employed. Now four equations are available; (3.69c and b) following from the previous procedure, (3.69a and d) non-dimensionalized from (3.11). These are used to solve the amplitude coefficients.

$$0 = -\Psi_{1'z}(0), \quad (3.69a)$$

$$0 = \Psi_{1'x}(0). \quad (3.69b)$$

$$0 = -k\Psi_{1'x}(1)\delta + Wek\Psi_{1'xxx}(1) + 3\Psi_{1'xxz}(1) + \Psi_{1'zzz}(1) - \varkappa k \cos(\zeta) \quad (3.69c)$$

$$0 = \Psi_{1'xx}(1) - \Psi_{1'zz}(1) \quad (3.69d)$$

The equations (3.69) mainly incorporate forms of Ψ , which contain trigonometric structures with amplitude function, see (3.20), and they incorporate a single cosine function originating from the magnetic field. Here, the order of $\cos(m\zeta)$ is $m = 1$. As other orders are absent, the order $m = 1$ is adopted for the trigonometric structures of $\Psi(\zeta)$.

While (3.69a) and (3.69b) will reduce the number of eight unknown $a_{11}^{(1-4)}$ and $b_{11}^{(1-4)}$ to four, (3.69c) and (3.69d) will produce another two equations by comparison of coefficients, whose system of equations will bring the solution of the remaining amplitude coefficients and lastly the function $\Psi_1(z)$.

Equations (3.69a) and (3.69b) provide

$$0 = \left(a_{11}^{(2)} + ka_{11}^{(3)}\right) \cos(\zeta) + \left(b_{11}^{(2)} + kb_{11}^{(3)}\right) \sin(\zeta) \quad (3.70)$$

$$0 = -a_{11}^{(1)}k \cos(\zeta) + b_{11}^{(1)}k \sin(\zeta). \quad (3.71)$$

From this we procure

$$a_{11}^{(2)} = -ka_{11}^{(3)} \quad (3.72a) \quad a_{11}^{(1)} = 0 \quad (3.72c)$$

$$b_{11}^{(2)} = -kb_{11}^{(3)} \quad (3.72b) \quad b_{11}^{(1)} = 0. \quad (3.72d)$$

3.7. Preparation of the Boundary Conditions

The remaining coefficients shall be written more shortly $a_{11}^{(3)} = a_3$, $a_{11}^{(4)} = a_4$, $b_{11}^{(3)} = b_3$ and $b_{11}^{(4)} = b_4$. This abridges $\eta(z)$ and $\xi(z)$ (3.22) to

$$\eta_{11}(z) = a_3(\sinh(kz) - kz \cosh(kz)) + a_4z \sinh(kz) \quad (3.73a)$$

$$\xi_{11}(z) = b_3(\sinh(kz) - kz \cosh(kz)) + b_4z \sinh(kz) \quad (3.73b)$$

The next steps include the derivations of Ψ , in forms of (3.19) and (3.22), into (3.69c and b). A comparison of coefficients with respect to the trigonometric functions delivers four equations, which are sufficient to write an homogeneous, algebraic system of equations to solve the remaining four unknown coefficients of the amplitude function $\eta_1(z)$ and $\xi_1(z)$ within the stream function.

$$\mathbf{e}_{\tau, \sin(\zeta)} : 0 = -k^2 \xi_1(1) - \xi_{1'zz}(1) \quad (3.74a)$$

$$\mathbf{e}_{\tau, \cos(\zeta)} : 0 = -k^2 \eta_1(1) - \eta_{1'zz}(1) \quad (3.74b)$$

$$\begin{aligned} \mathbf{e}_{n, \sin(\zeta)} : 0 = & -3k^2 \xi_{1'z}(1) + \xi_{1'zzz}(1) + k^2 \delta \eta_1(1) - \\ & - k^4 We \eta_1(1) \end{aligned} \quad (3.74c)$$

$$\begin{aligned} \mathbf{e}_{n, \cos(\zeta)} : 0 = & -3k^2 \eta_{1'z}(1) + \eta_{1'zzz}(1) - k^2 \delta \xi_1(1) + \\ & + k^4 We \xi_1(1) - \varkappa k \end{aligned} \quad (3.74d)$$

By insertion of $\eta_1(z)$ and $\xi_1(z)$, or their derivations, respectively, the system gets voluminous. For a clearer view, several coefficients are substituted as stated

3. Ferrofluid Based Locomotion due to Surface Deformation

$$T_1 := 2k^3 \cosh(k), \quad (3.75a)$$

$$T_2 := -2k(k \sinh(k) + \cosh(k)), \quad (3.75b)$$

$$T_3 := \frac{k^2}{\omega}(\delta + Wek^2)(k \sinh(k) - k \cosh(k)), \quad (3.75c)$$

$$T_4 := \frac{k^2}{\omega}(\delta + Wek^2) \sinh(k), \quad (3.75d)$$

$$T_5 := 2k^3(k \sinh(k) - \cosh(k)), \quad (3.75e)$$

$$T_6 := -2k^3 \cosh(k), \quad (3.75f)$$

$$K := \varkappa k \quad (3.75g)$$

and the system of (3.74) is turned into a vector matrix mode

$$\begin{bmatrix} 0 & 0 & T_1 & T_2 \\ T_1 & T_2 & 0 & 0 \\ T_3 & T_4 & T_5 & T_6 \\ T_5 & T_6 & -T_3 & -T_4 \end{bmatrix} \begin{pmatrix} a_3 \\ a_4 \\ b_3 \\ b_4 \end{pmatrix} = \begin{pmatrix} 0 \\ 0 \\ 0 \\ K \end{pmatrix}. \quad (3.76)$$

The coefficients have to be solved. We call \mathbf{M} the coefficient matrix, $\det(\mathbf{M})$ and \mathbf{M}_i its determinant and its according subordinate matrix, respectively. $D = \det(\mathbf{M})$ and $D_i = \det(\mathbf{M}_i)$.

$$D = -4 \frac{k^6}{\omega^2} [(\delta + Wek^2)^2 (\sinh(k) \cosh(k) - k)^2 + 4k^2 \omega^2 (\cosh^2(k) + k^2)^2] \quad (3.77a)$$

$$D_1 = 8\varkappa k^6 (k \sinh(k) + \cosh(k)) (\cosh^2(k) + k^2) \quad (3.77b)$$

$$D_2 = 8\varkappa k^8 \cosh(k) (\cosh^2(k) + k^2) \quad (3.77c)$$

$$D_3 = 4 \frac{\varkappa k^5}{\omega} (\delta + Wek^2) (k \sinh(k) + \cosh(k)) \times (\sinh(k) \cosh(k) - k) \quad (3.77d)$$

$$D_4 = 4\varkappa \frac{k^7}{\omega} (\delta + Wek^2) \cosh(k) (\sinh(k) \cosh(k) - k) \quad (3.77e)$$

3.8. The Existence of an Averaged Flow Rate

Thus, the coefficients are

$$\begin{aligned} a_3 &= \frac{D_1}{D}, \\ &= -2 \frac{\varkappa \omega^2}{\Lambda} (k \sinh(k) + \cosh(k)) (\cosh^2(k) + k^2), \end{aligned} \quad (3.78a)$$

$$\begin{aligned} a_4 &= \frac{D_2}{D}, \\ &= -2 \frac{\varkappa k^2 \omega^2}{\Lambda} \cosh(k) (\cosh^2(k) + k^2), \end{aligned} \quad (3.78b)$$

$$\begin{aligned} b_3 &= \frac{D_3}{D}, \\ &= -\frac{\varkappa \omega}{k \Lambda} (\delta + We k^2) \times \\ &\quad \times (k \sinh(k) + \cosh(k)) (\sinh(k) \cosh(k) - k), \end{aligned} \quad (3.78c)$$

$$\begin{aligned} b_4 &= \frac{D_4}{D}, \\ &= -\frac{\varkappa k \omega}{\Lambda} (\delta + We k^2) \cosh(k) (\sinh(k) \cosh(k) - k), \end{aligned} \quad (3.78d)$$

$$\begin{aligned} \Lambda &= (\delta + We k^2)^2 (\sinh(k) \cosh(k) - k)^2 + \\ &\quad + 4k^2 \omega^2 (\cosh^2(k) + k^2)^2. \end{aligned} \quad (3.78e)$$

3.8. The Existence of an Averaged Flow Rate

Section 3.6 already prepared the expression (3.33) of the averaged volume flow \bar{Q} . Now after the establishment of the amplitude coefficients a_3 , a_4 , b_3 and b_4 (3.78) and with this the establishment of the stream function $\Psi_1(x, z, t)$, this information will be applied to each other in order to form a closed expression for \bar{Q} .

On (3.33), the contour function h_1 is replaced by the relation (3.38).

$$\bar{Q} = \frac{1}{2\pi} \int_{kx-2\pi}^{kx} \varepsilon^2 k \Psi_{1,z}(1) \Psi_1(1) d\zeta + \mathcal{O}(\varepsilon^3) \quad (3.79a)$$

3. Ferrofluid Based Locomotion due to Surface Deformation

$$\begin{aligned} \bar{Q} = \frac{1}{2\pi} \int_{kx-2\pi}^{kx} \varepsilon^2 k & (\eta_{1'z}(1)\eta_1(1) \cos^2(\zeta) + (\eta_{1'z}(1)\xi_1(1)+ \\ & + \xi_{1'z}(1)\eta_1(1)) \sin(\zeta) \cos(\zeta)+ \\ & + \xi_{1'z}(1)\xi_1(1) \sin^2(\zeta)) d\zeta + \mathcal{O}(\varepsilon^3) \end{aligned} \quad (3.79b)$$

From (3.33) merely the former quadratic expressions remains and a symmetric form is generated

$$\bar{Q} = \frac{1}{2} \varepsilon^2 k (\eta_1(1)\eta_{1'z}(1) + \xi_1(1)\xi_{1'z}(1)) + \mathcal{O}(\varepsilon^3) \quad (3.79c)$$

Before inserting the found coefficients a_3 , a_4 , b_3 , and b_4 of the amplitude functions η_1 and ξ_1 (3.79), the relation

$$\frac{a_3}{a_4} = \frac{k \sinh(k) + \cosh(k)}{k^2 \cosh(k)} = \frac{b_3}{b_4} \quad (3.80)$$

is used besides addition theorems to contain the expression of \bar{Q} .

$$\bar{Q} = \frac{\varepsilon^2 (a_4^2 + b_4^2)}{2\omega} \frac{(\sinh(k) \cosh(k) - k)}{\cosh^2(k)} + \mathcal{O}(\varepsilon^3) \quad (3.81)$$

From (3.78b and d), we gain

$$\bar{Q} = \frac{\varepsilon^2 \omega k^2 \varkappa^2 (\sinh(2k) - 2k)}{\Lambda} + \mathcal{O}(\varepsilon^3). \quad (3.82)$$

3.9. Analysis of the Analytical Results

A similar structure of the result is already known by [Bur67], when the external pressure gradient is set to zero. Burns and Parkes then presented the solution of a plane, symmetric peristaltic flow and developed the stream function up the fourth order.

In our case, the averaged volume flow (3.82) depends on the parameters of the quadratic ratio of perturbation to the constant part of the magnetic field ε , wavenumber k , angular frequency ω , surface tension, covered by We , \varkappa_0 and δ , representing the influences of permeability

3.9. Analysis of the Analytical Results

and gravity. As none of these parameters turn zero and the expression $(\sinh(2k) - 2k)$ for $k > 0$ is positive, the material transport is non-zero and positive, $\bar{Q} \geq 0$. This means, the transport takes a similar direction like the propelling curvature, like the propelling magnetic field perturbation. For the estimation of the quantity of the achieved material transport, \bar{Q} , (3.82) is redimensionalized

$$\bar{Q}^* = \frac{A^4 \varkappa_0^2 k^{*2} h_0^2 \omega^* (\sinh(2k) - 2k)}{\Lambda^*} \quad (3.83)$$

with

$$\Lambda^* = (\varrho g + \gamma k^{*2})^2 (\sinh(2k) - 2k)^2 + 4k^{*2} \varrho^2 \nu^2 \omega^{*2} (1 + \cosh(2k) - 2k^2)^2,$$

$$k = k^* h_0 \text{ and } \varkappa_0 = (\mu - 1)/(8\pi).$$

Because \varkappa_0 , ϱ , ν (and γ) are material parameters and thus cannot be changed reasonably, for the analysis of the solution we concentrate on the angular frequency ω , wavenumber k , unperturbed fluid height h_0 .

The structure concerning ω^* can be brought into the form

$$\bar{Q}^* = \frac{K_0}{K_1/\omega^* + K_2\omega^*} \quad (3.84)$$

where B_i are

$$K_0 = A^4 \varkappa_0^2 k^{*2} h_0^2 (\sinh(2k^* h_0) - 2k^* h_0), \quad (3.85)$$

$$K_1 = (\varrho g + \gamma k^{*2})^2 (\sinh(2k^* h_0) - 2k^* h_0)^2, \quad (3.86)$$

$$K_2 = 4k^{*2} \varrho^2 \nu^2 (1 + \cosh(2k^* h_0) - 2k^{*2} h_0^2). \quad (3.87)$$

Working with the inequality

$$\frac{K_1}{\omega^*} + K_2\omega^* \geq 2\sqrt{K_1 K_2} \quad (3.88)$$

we seek the minimum $\omega^* = \omega_{max}^*$

3. Ferrofluid Based Locomotion due to Surface Deformation

$$\omega_{max}^* = \frac{(\rho g + \gamma k^{*2})(\sinh(2k^*h_0) - 2k^*h_0)}{2k^*\rho\nu(1 + \cosh(2k^*h_0) - 2k^{*2}h_0^2)}, \quad (3.89)$$

which conditions the maximum average volume flow $\bar{Q}^* = \bar{Q}_{max}^*$

$$\bar{Q}_{max}^* = \frac{A^4 \varkappa_0^2 k^* h_0^2}{2k^*\rho\nu(1 + \cosh(2k^*h_0) - 2k^{*2}h_0^2)}. \quad (3.90)$$

If we refer to the original assumption of long waves with $k = k^*h_0 \ll 1$, (3.90) and (3.89), the expressions for \bar{Q}^* and ω^* , can be shortened

$$\bar{Q}_{max}^* = \frac{A^4 \varkappa_0^2 k^* h_0}{8g\rho^2\nu} + \mathcal{O}(k)^3, \quad (3.91)$$

$$\omega_{max}^* = \frac{2gh_0k^{*2}}{3\nu} + \mathcal{O}(k)^3. \quad (3.92)$$

For numerical calculations, the values provided by the accompanying experimental setup are adopted, see section 3.10. In the experimental evaluation, the angular frequency $\omega^* = 2.2 \text{ s}^{-1}$, wavenumber $k^* = 1 \text{ cm}^{-1}$ and unperturbed fluid height $h_0 = 0.4 \text{ cm}$ are used as summarized in table 3.1. From the originally stated demand of small $Re \ll 1$, we procure the condition for the angular frequency

$$\omega^* \ll \nu/h_0^2 = 11.8 \text{ s}^{-1}. \quad (3.93)$$

The second assumption concerning the quadratic relation of perturbed to unperturbed magnetic field

$$\varepsilon = \frac{A^2(h_0)}{H_0^2} = 0.044 \ll 1 \quad (3.94)$$

with $A = 7.83 \text{ Oe}$, $H_0 = 37.46 \text{ Oe}$ is fulfilled in numerical values, too.

3.9. Analysis of the Analytical Results

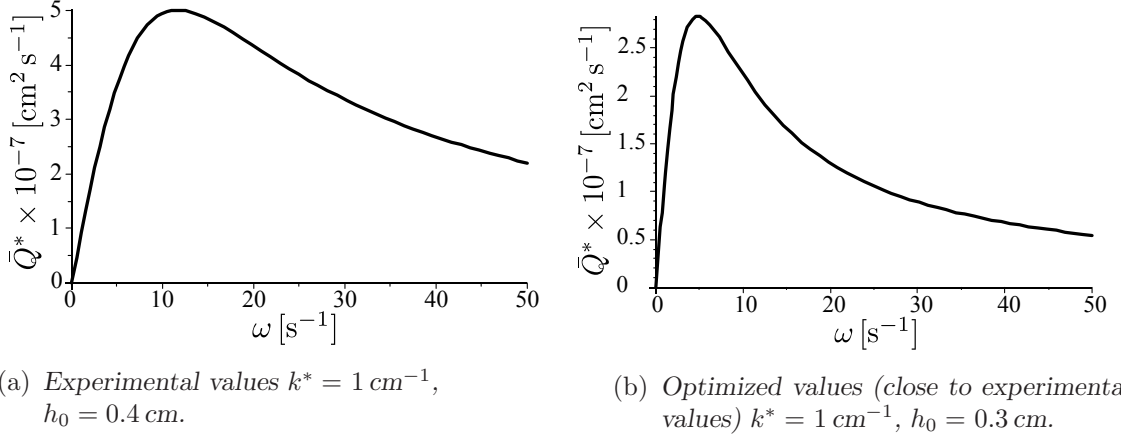


Figure 3.4.: Average flow rate \bar{Q}^* vs. angular frequency ω^* with $g = 981 \text{ cm s}^{-2}$, $A = 7.84 \text{ Oe}$, $\chi_f = 0.118$, $\nu = 1.89 \text{ cm}^2 \text{ s}^{-1}$, $\rho = 1.32 \text{ g cm}^{-3}$, $\gamma = 30 \text{ g s}^{-2}$.

The average flow rate \bar{Q}^* can be optimized by three parameters ω^* , k^* , h_0^* . Figure 3.4(a) shows the relation of $\bar{Q}^* = \bar{Q}^*(\omega^*)$ conditioned by the values of the experimental setup ($k = 1 \text{ cm}^{-1}$, $h_0 = 0.4 \text{ cm}$). Here,

$$\omega_{max}^* = 11.6 \text{ s}^{-1}, \quad \bar{Q}_{max}^* = 5.0 \times 10^{-7} \text{ cm}^2 \text{ s}^{-1}$$

The frequency actually used in experiment yields in theory

$$\omega^* = 2.2 \text{ s}^{-1}, \quad \bar{Q}^* = 1.85 \times 10^{-7} \text{ cm}^2 \text{ s}^{-1}. \quad (3.95)$$

Therefore, $\omega_{max}^* = 11.6 \text{ s}^{-1}$ is not $\ll 11.8 \text{ s}^{-1}$, but $\omega^* = 2.2 \text{ s}^{-1} \ll 11.8 \text{ s}^{-1}$. Although the working point is not close to the maximum value, the actually used values are within the required range. The diagram of figure 3.4(b) is plotted with the optimum values inserted ($k = 1 \text{ cm}^{-1}$, $h_0 = 0.3 \text{ cm}$). Here, the restrictions are included given by the previous assumptions, e.g. a small wavenumber ($k \leq 1$) for the long wave approximation. $\omega_{opt,max}^*$ is also better conditioned: $\omega_{opt,max}^* \ll \nu/h_0^2 = 21 \text{ s}^{-1}$.

$$\omega_{opt,max}^* = 4.85 \text{ s}^{-1}, \quad \bar{Q}_{opt,max}^* = 2.83 \times 10^{-7} \text{ cm}^2 \text{ s}^{-1}$$

3. Ferrofluid Based Locomotion due to Surface Deformation

Due to the constraints of the real implementation, the experimental values differ from the optimum. All the same, speaking in real relations, the difference of $0.1 \text{ cm} = 1 \text{ mm}$ is not only very small, but it is also the tolerance of adjusting the fluid height. Due to surface deformation at the measurement equipment, we cannot set the fluid height with higher precision than 1 mm . However, the difference between the achievable \bar{Q}^* and $\bar{Q}_{opt,max}^*$ is small ($\bar{Q}_{opt,max}^* \approx 1.5\bar{Q}^*$).

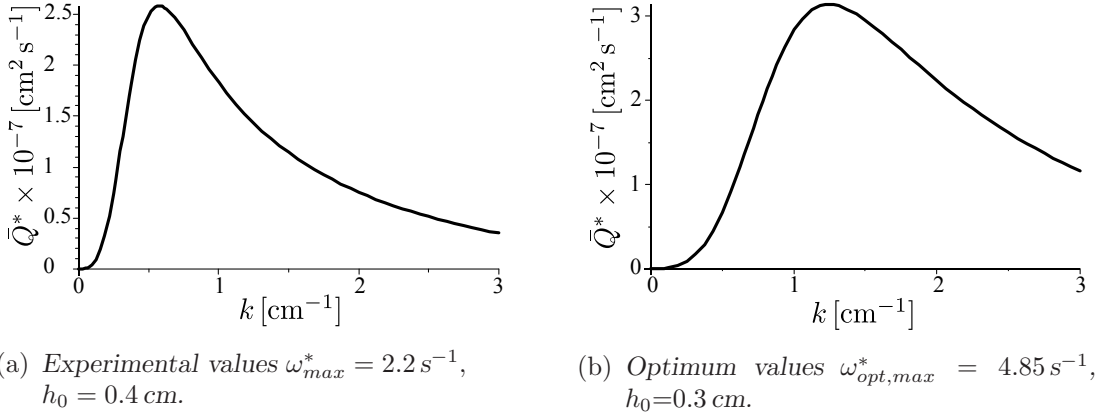


Figure 3.5.: Average flow rate \bar{Q}^* vs. wavenumber k^* with $g = 981 \text{ cm s}^{-2}$, $A = 7.84 \text{ Oe}$, $\chi_f = 0.118$, $\nu = 1.89 \text{ cm}^2 \text{ s}^{-1}$, $\rho = 1.32 \text{ g cm}^{-3}$, $\gamma = 30 \text{ g s}^{-2}$.

The function of $\bar{Q}^*(k^*)$ is plotted in figure 3.5(a), using the experimentally conditioned values ($\omega_{max}^* = 2.2 \text{ s}^{-1}$, $h_0 = 0.4 \text{ cm}$). Here,

$$k_{max}^* = 0.58 \text{ cm}^{-1}, \quad \bar{Q}_{max}^* = 2.58 \times 10^{-7} \text{ cm}^2 \text{ s}^{-1}.$$

The actual wavenumber of the design obtains

$$k^* = 1 \text{ cm}^{-1}, \quad \bar{Q}_{max}^* = 1.84 \times 10^{-7} \text{ cm}^2 \text{ s}^{-1}.$$

Figure 3.5(b) illustrates $\bar{Q}^*(k^*)$ with the optimal numerical values ($\omega_{opt,max}^* = 4.85 \text{ s}^{-1}$, $h_0 = 0.3 \text{ cm}$).

$$k_{opt,max}^* = 1.25 \text{ cm}^{-1}, \quad \bar{Q}_{opt,max}^* = 3.14 \times 10^{-7} \text{ cm}^2 \text{ s}^{-1}$$

3.9. Analysis of the Analytical Results

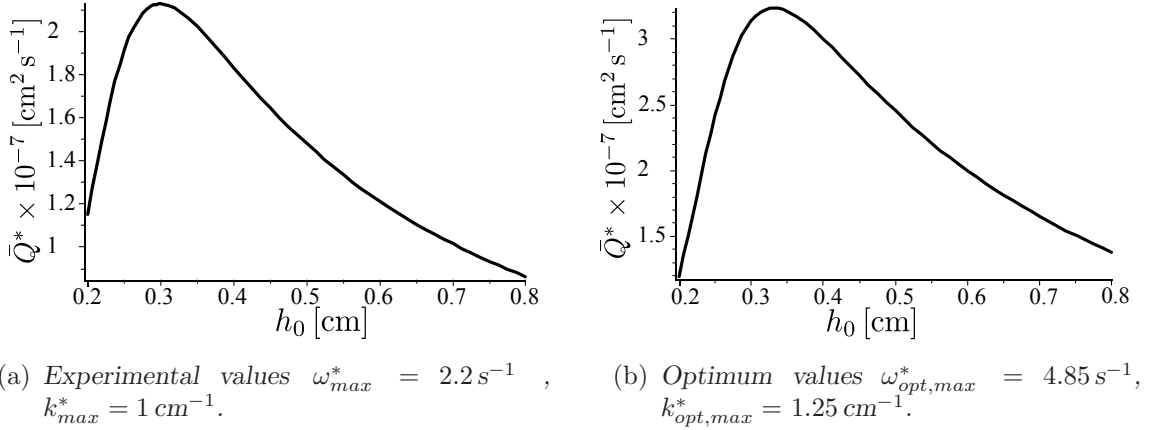


Figure 3.6.: Average flow rate \bar{Q}^* vs. unperturbed fluid height h_0 with $g = 981 cm s^{-2}$, $A = 7.84 Oe$, $\chi_f = 0.118$, $\nu = 1.89 cm^2 s^{-1}$, $\rho = 1.32 g cm^{-3}$, $\gamma = 30 g s^{-2}$.

On the basis of figures 3.6, the dependency of \bar{Q}^* on h_0 is investigated. The graph of figure 3.6(a) incorporates values, whose optimization originates from the experimental design.

$$h_{0,max}^* = 0.3 cm, \quad \bar{Q}_{max}^* = 2.13 \times 10^{-7} cm^2 s^{-1}$$

Basing on this plot, the fluid height used in experiment yields in theory

$$h_0^* = 0.4 cm, \quad \bar{Q}^* = 1.84 \times 10^{-7} cm^2 s^{-1}.$$

Figure 3.6(b) has been developed on optimum numerical values, here

$$h_{0,opt,max}^* = 0.33 cm, \quad \bar{Q}_{opt,max}^* = 3.24 \times 10^{-7} cm^2 s^{-1}.$$

In spite of the most effective influence of the unperturbed fluid height h_0 (among other things visible by the strongest gradient of \bar{Q}^* in figures 3.4 to 3.6, despite varying scales), the data derived by the experimental design parameters are close to the optimum values and differ only by factors smaller 10.

3. Ferrofluid Based Locomotion due to Surface Deformation

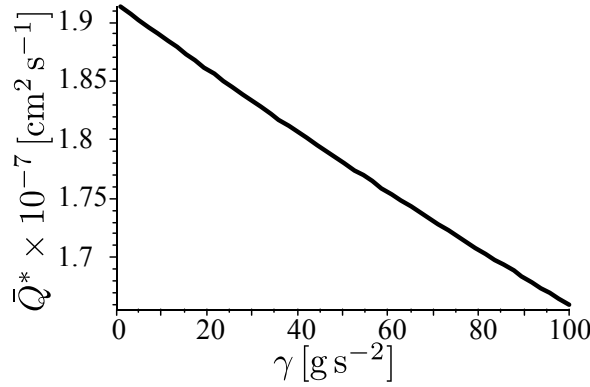


Figure 3.7.: Average flow rate \bar{Q}^* vs. coefficient of surface tension γ with $g = 981 \text{ cm s}^{-2}$, $A = 7.84 \text{ Oe}$, $\chi_f = 0.118$, $\nu = 1.89 \text{ cm}^2 \text{ s}^{-1}$, $\rho = 1.32 \text{ g cm}^{-3}$, $\omega_{max}^* = 2.2 \text{ s}^{-1}$, $h_{0,max} = 0.4 \text{ cm}$, $k_{max}^* = 1 \text{ cm}^{-1}$.

The influence of the surface tension is hyperbolic according to (3.83), this becomes discernible only in comparatively huge scales. In the physically relevant range of the surface tension coefficient, the plot resembles a linear declining line and chances of γ effect only negligibly small variation of \bar{Q}^* , see figure 3.7.

The plot confirms the expectancy regarding the dependency on the surface tension parameter γ . With an increasingly rigid cover membrane, which the free surface is, the transport is gradually restrained.

3.10. The Accompanying Experiment – Setup

An experiment was performed for quantitative verification and as a feasibility study. It focuses on the principle proof of material transport by magnetically induced peristalsis. This implies the deformation of the free surface of a magnetizable fluid by suitable magnetic fields and the locomotion of the fluid by transversal motion of the undulating boundary layer.

The design of the setup comprises the two core pieces; the source of the magnetic field and the design of the magnetizable fluid container.

3.10. The Accompanying Experiment – Setup

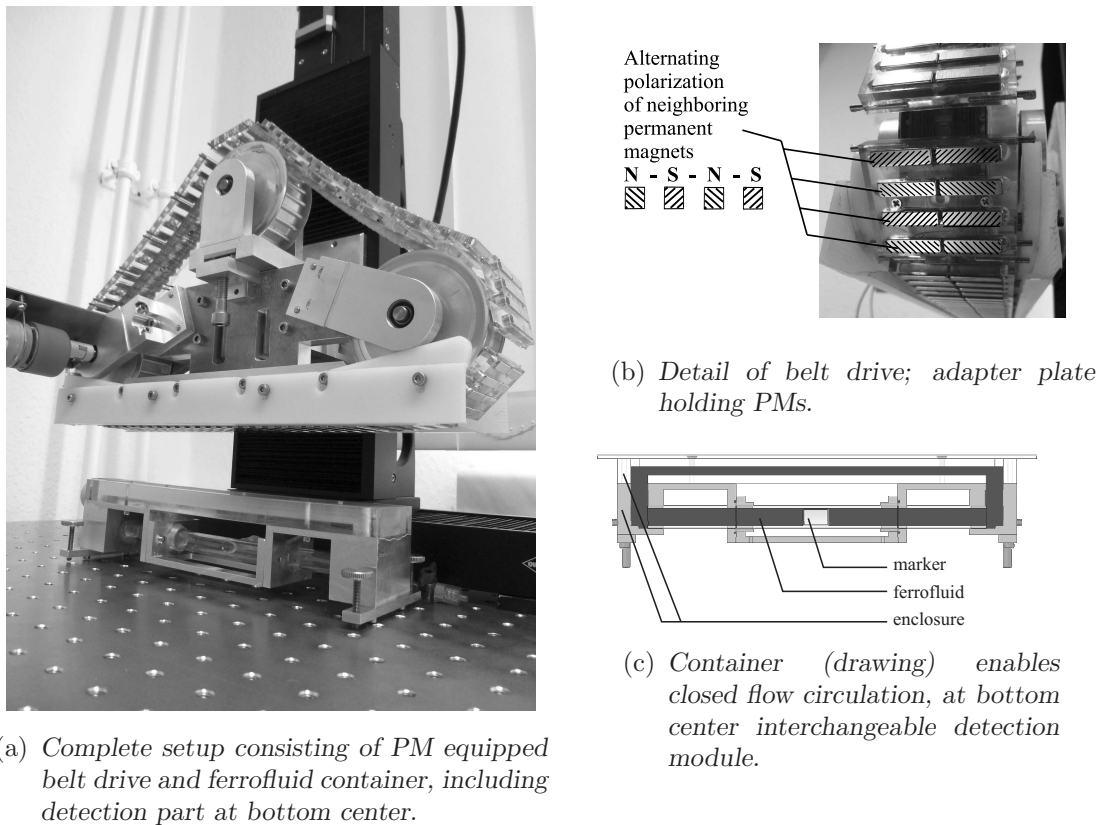
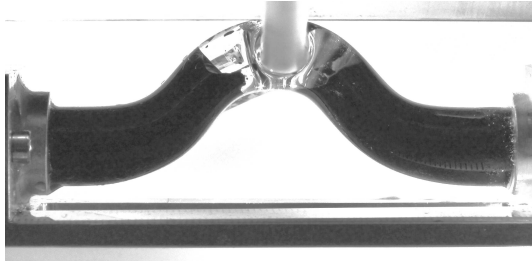


Figure 3.8.: *Experimental setup.*

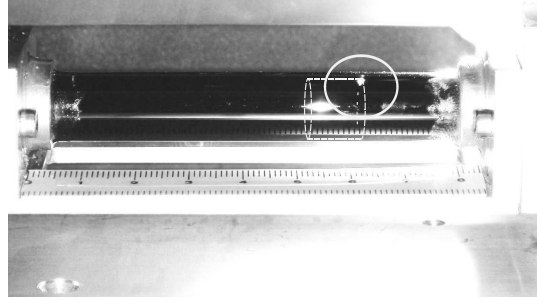
Figure 3.8(c) features the fluid container. The main chamber for peristaltic excitation is on top. The free surface spreads over an area of $22 \times 4 \text{ cm}^2$. Two lateral ascending or descending pipes at each side and the bottom connection complete a circular channel.

Since the predicted transport effect is small, a robust quantification method is required to reduce errors. Furthermore, the measurement must match with the completely opaque fluid. We measure the displacement of the fluid cross section within the center piece of the bottom pipe. Two strategies of displacement detection were used. For this, the detection piece of the lower pipe is interchangeable with differently equipped glass tubes. The first version utilized a glass cylinder (air-filled for lightweight) inserted within and swimming at the upper rim of the fluid filled glass tube. The horizontal displacement of the translucent light mark is monitored, see figure 3.9(b). The second version incorporates an upward bend glass tube holding the marker

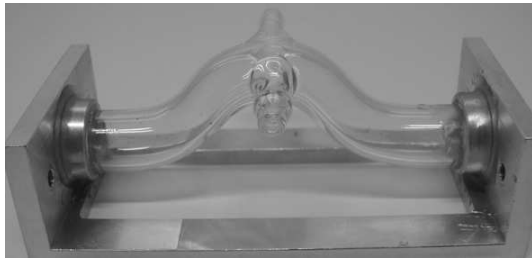
3. Ferrofluid Based Locomotion due to Surface Deformation



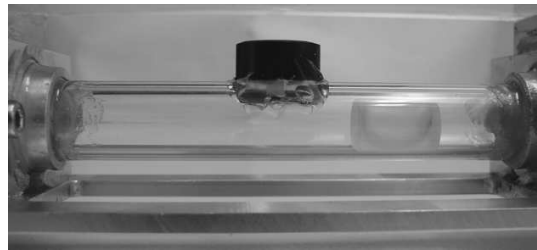
(a) Detection module: fluid-filled glass tube, secondary marker fluid in u-bent.



(b) Detection module: fluid-filled, shifting cylinder invisible due to opaqueness, translucent shimmer marks position of cylinder (according to drawing).



(c) Detection module: prior to charge, glass tube with u-bent and inlet for secondary marker fluid or deaeration output, respectively.



(d) Detection module: prior to charge, inside: shifting glass cylinder (above: bubble level for horizontal adjustment).

Figure 3.9.: Interchangeable detection modules.

fluid glycol (immiscible, transparent, slightly higher density [difference $\Delta\rho = 0.02 \text{ g cm}^{-3}$ at 21°C]). The displacement of the fluid-fluid boundary layers is monitored, see figure 3.9(a).

The magnetic field is generated by permanent magnets (PMs) aligned with opposite polarization neighboring each other. Attached to a circular, motor driven belt drive, the PMs ensure a temporally and spatially consistent alternating magnetic field for an arbitrary duration. Figures 3.8(a) and 3.8(b) show the whole assembly and the PM equipped belt drive.

The chosen parameters of design, material and magnetic field characteristics are given in table 3.1. The discussion on how these values have been defined may be found in section 3.12.

3.10. The Accompanying Experiment – Setup

Table 3.1.: *Parameters of the experiment (in cgs).*

Design Dimensions			
Main pool area	$b \times l$	4×22	cm^2
Diameter - detection pipe	d_m	1	cm
Ferrofluid volume	V	50.6	cm^3
Distance PM - PM	d_{PM}	1	cm
Velocity - belt drive	v_{belt}	2.2	cm s^{-1}
Magnetic field strength			
Constant part	H_0	37.46	Oe
		2981.96	A m^{-1}
Perturbation amplitude	A	7.84	Oe
Fluid height	h_0	0.4	cm
Fluid amplitude	h_1		cm
Wavelength (fluid surface)	λ	1	cm
Wavenumber (fluid surface)	k	1	cm
Characteristic velocity	U_c	0.89	cm s^{-1}
Characteristic period time	T_c	0.45	s
Angular velocity	ω	2.2	s^{-1}
Characteristic pressure	P_c	5.49	$\text{g cm}^{-1} \text{s}^{-2}$
Gravitational acceleration	g	981	cm s^{-2}
Gravitational parameter	$\delta = Re/Fr$		
Fluid parameters (APG S12n)			
Density	ϱ	1.32	g cm^{-3}
Dynamic viscosity	η	2.5	$\text{g cm}^{-1} \text{s}^{-1}$
Kinematic viscosity	ν	1.89	$\text{g cm}^{-1} \text{s}^{-1}$
Coefficient - surface tension	γ	30	g s^{-2}
Initial susceptibility			
Fluid	$\chi_{f,(cgs)}$	0.118	
Air	$\chi_{a,(cgs)}$	3.2×10^{-8}	
Relative mag. permeability	$\mu_r = \chi + 1$		
Absolute permeability	$\mu_{0,(cgs)}$	1	
	$\mu_{0,(SI)}$	$4\pi 10^{-7}$	$\text{V s A}^{-1} \text{m}^{-1}$
Magnetic parameter	\varkappa	2.23	

3.11. The Experimental Results

We received one measurement series suitable for analysis, apart from other samples with unclear outcome. Thereby, a shift of the fluid cross section of $s_d = 1.13$ mm was witnessed. The moving direction of the marker was in accordance to the direction of the peristaltic drive (and subsequently, similar to the moving direction of the PMs). For the measurement we tracked the translucent light point, see figure 3.9(b), within a duration of $t = 22$ h taking photographs. The long recording time was chosen to improve the measurability by accumulation of a slow motion process.

When translating the detected displacement into a volume flow, $\bar{Q} = 1.125 \times 10^{-6} \text{ cm}^3 \text{ s}^{-1}$ is established. This matches a (three-dimensional) volume transport of $V = 8.9 \times 10^{-2} \text{ cm}^{-3}$ per 22 h.

In (3.95), an averaged flow rate of $\bar{Q}^* = 1.85 \times 10^{-7} \text{ cm}^2 \text{ s}^{-1}$ has been predicted on a theoretical basis (fed by numerical design parameters). Transformed into three-dimensional figures (the width of the pool is $y = 4$ cm) we compare

$$\bar{Q}_{\text{analytics}}^* = 0.74 \times 10^{-6} \text{ cm}^3 \text{ s}^{-1}, \quad \bar{Q}_{\text{experiment}}^* = 1.12 \times 10^{-6} \text{ cm}^3 \text{ s}^{-1}.$$

Thus, $\bar{Q}_{\text{analytics}}^*$ and $\bar{Q}_{\text{experiment}}^*$ differ from each other by

$$\bar{Q}_{\text{analytics}}^* = c_Q \times \bar{Q}_{\text{experiment}}^* \quad \text{with} \quad c_Q = 0.66.$$

This states a difference, which is too large for a quantitative examination from the engineering point of view. However, for feasibility purposes, seeking quantitative confirmation, it serves as an acceptable outcome.

Support for the experimental approach is provided by the second strategy on watching a material transport. Here, the detection area incorporated a bend glass tube filled with an immiscible transparent secondary fluid, see figure 3.9(a). The procedure delivered images documenting a general tendency of fluid motion, see figure 3.10. The quality of data is not sufficient for quantitative figures. Further series of measurement resulted in less suitable results. Some runs generated material transport in the opposite direction compared to the surface

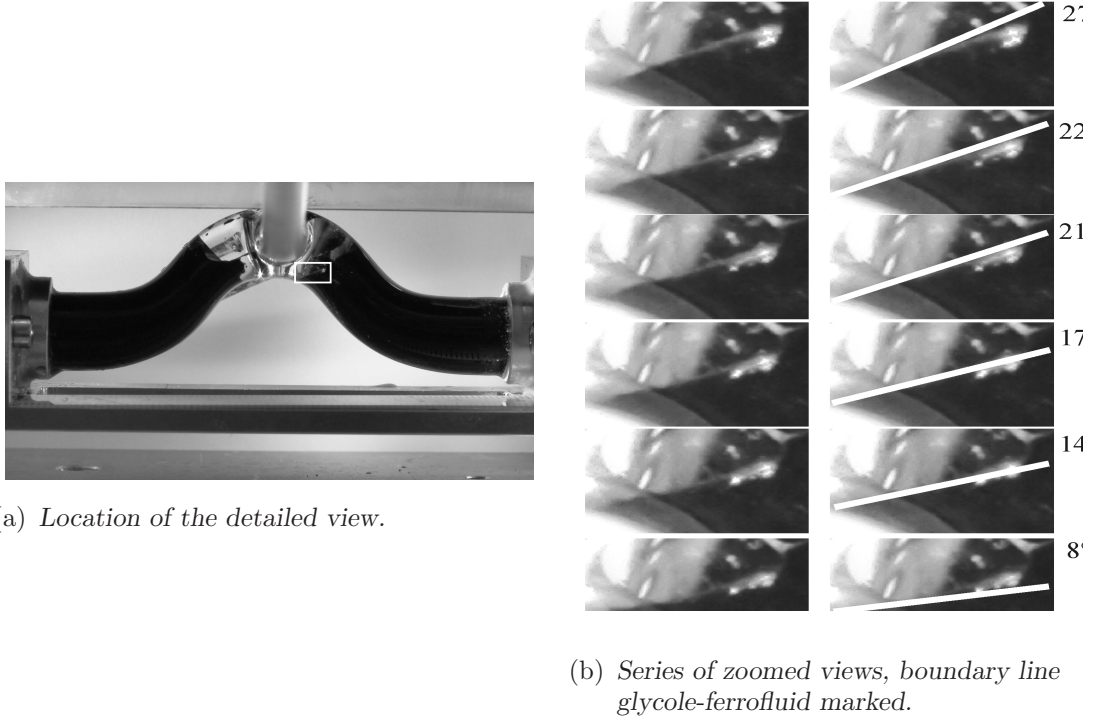


Figure 3.10.: *Tendency of ferrofluid motion visualized by shifted boundary layer over a duration of 5 hours.*

deformation and PMs motion. The reasons for this kind of behavior is still unknown. A reversal of direction working close to resonance is a phenomenon notorious from the solid body mechanics. Since our considerations did not include the (potentially vibrating) mechanic system of the drive, this is a valid possibility, too.

The exposed magnetic field is a potential source of errors, too. We examined the magnetic flux density using a hall-effect probe. The investigating of 56 out of 88 PMs aligned in a straight row like in the experimental arrangement, yielded to data of the horizontal and vertical component of the magnetic flux density B_x and B_z , respectively. The magnetic field strength H , whose perturbation amplitude A contributes to $\bar{Q}_{\text{analytics}}$, is derived from that. Diagram A.1 shows B_x and B_z and the consequent total quantity $B_0 = \sqrt{B_x^2 + B_z^2}$. Minimums and maximums of B_x and B_z are added to emphasize the origin of the variation of measured values. Figure A.2 produces data of the magnetic field strength H (mean value) and its standard deviation $S(H)$ over the measurement series of 56 PMs. The constant offset is $H_0 = 37.46$ Oe.

3. Ferrofluid Based Locomotion due to Surface Deformation

In particular, we are interested in values of the amplitude A of the perturbation and its standard deviation $S(A)$. Proceeding from the mean of H , we develop the average amplitude (taken from the peak positions) $\bar{A} = 7.84 \text{ Oe}$ and its standard deviation $S(A) = 1.25 \text{ Oe}$. The averaged flow rate \bar{Q} incorporates A^4 . Thus, the fluctuation of the perturbation amplitude has a large effect on the volume flow. The analytically obtained values of \bar{Q} (on basis of the actual values of the experiment) vary by -49.5% and $+79.5\%$.

The fluctuation of the magnetic field quantities can be found also in the surface deformation. Figure 3.11 gives details of the optical examination of the surface waves. The detection of the fluid deformation acts merely as an indication, the mathematical description of the averaged flow rate \bar{Q} does not depend on the wave amplitude \hat{h} . Nevertheless, the evidence of an undulating surface is a further confirmation of the peristalsis. We obtain a wave amplitude of $\hat{h} = 0.2 \text{ mm}$. The record was taken for a horizontal way $x = 4 \text{ cm}$ and a gross time of $t = 60 \text{ s}$.

An impression of the visual conditions is shown in figure 3.11(a). The detected contour is marked. Using MATLAB³, an algorithm extracted from the single frames of a recorded video file the surface contour by edge detection. From that we received the undulating surface line in dependency on x and t . The diagram of figure 3.11(b) depicts the plot of the detected contour of the video image. The distortions of the plot line result from the mediocre image quality. Figure 3.11(c) presents a three dimensional plot including the dependency on x and time t . Both figures 3.11(b) and 3.11(c) show, that the extremal values of the fluid deformation are not constant. This is due to the differing magnetic flux values of the individual PMs, which will be considered in the following. The usage of magnets of only a single batch did not prevent the variation. In a raw approach one can take the given undulation as a sine signal, but it does not fulfill a higher precision. The even diagonal stripes in figure 3.11(c) indicate a steady conversion of position and time progress, meaning a bucking-free driving velocity.

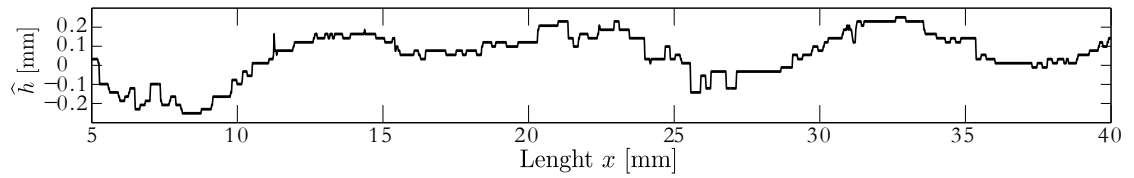
Other reasons for the discrepancies will be discussed more detailed in section 3.12.2 (after an introduction of the reasons for the design of the employed experimental setup in the first place, in section 3.12).

³by The MathWorks, Inc.

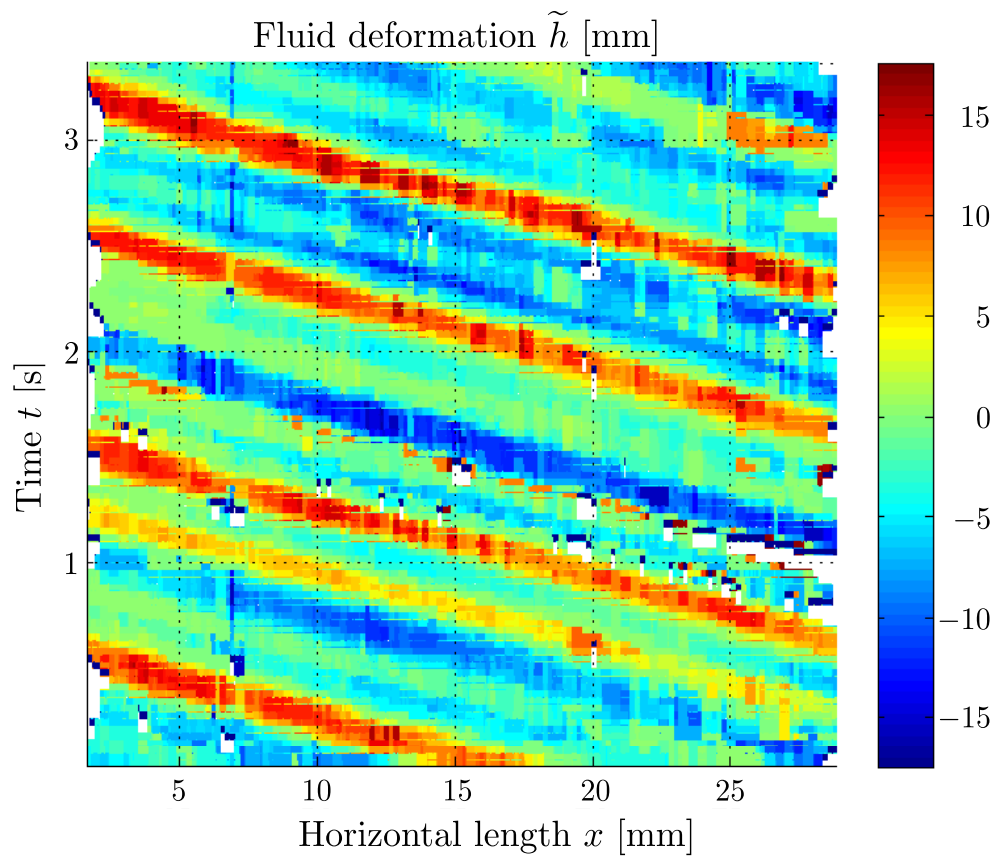
3.11. The Experimental Results



(a) Single image of recorded video.



(b) Surface undulation \hat{h} vs. length x .



(c) Fluid deformation \hat{h} vs. length x and time t .

Figure 3.11.: Different productions of the perturbed fluid surface.

3.12. Discussion of the Analytical and Experimental Results

3.12.1. Principal Approach to the Design

For the practical realization of the experiment, we had to consider the ferrofluid, design of fluid container and magnetic equipment, measurement method and system, as well as feasibility and measurability, see the drawing 3.12.

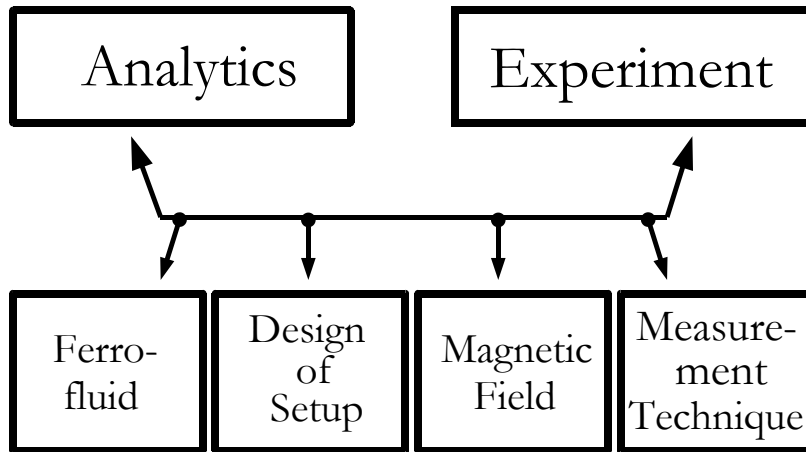


Figure 3.12.: *Issues building the bridge between theory and real implementation.*

Ferrofluid

The commercial ferrofluid APG S12n by Ferrotec GmbH was used. Obviously, the purchase of a convenience product includes the acceptance of fixed properties (within each charge) and material data with high tolerances. The ferrofluid APG S12n by Ferrotec GmbH served as the magnetizable fluid. The selection criteria were inspired by practical aspects such as persistent properties and usability, low flammability for safety reasons, which led to ester-based ferrofluids and potentially high deployable forces, meaning a high saturation magnetization. Data from the manufacturer underlie an uncertainty up to 10%.

Design of the Setup

The design space greatly influences the REYNOLDS, EULER, STROUHAL and FROUDE numbers and vice versa. Because of the rivalry of some aspects, a compromise was made between compatibility and requirements from the analytics, especially regarding the scale of the setup.

For drafting the latter, various issues were considered. Initial points for the concept were, firstly, the assumption $Re \ll 1$, (3.6b), and, secondly, $Sr = 1$, derived from (3.6a), it renders the convenient relation $U_c = h_0/T_c$.

A minimum fluid level h_0 is required to avoid boundary effects in vertical direction. Also, the ratio ε is influencing the setting for h_0 . Originally presenting the ratio of the (squared) amplitudes of perturbed to unperturbed magnetic field strength, it mirrors the ratio between perturbed and unperturbed fluid height, h_1 and h_0 , respectively. If we consider $h_1 \ll h_0$, due to (3.15), it does not make sense to assess h_0 much smaller than at a centimeter scale. With the interest of the small REYNOLDS, a compromise is found with $h_0 = 0.4$ cm and $h_1 \approx 2 \times 10^{-2}$ cm.

In the consequence, the characteristic velocity U_c was chosen small. This manipulation can be achieved by a diminutive fluid height h_0 or a large characteristic period time T_c . Since h_0 is assigned for conceptive reasons, the selection of $T_c = \lambda/v_{\text{belt}}$ is found as agreement between required space of the magnets and low velocity.

The reduction of boundary effects is based on a sufficiently wide free surface extension. Velocity derogation at the motionless, and the dragging up of fluid at the vertical wall reigns within millimeter range. Thus, by setting an adequate dimension of the pool, for data see table 3.1, twenty wave repetitions are ensured at minimum.

The detection area is separated from the functional area to avoid disturbance. With the two-storey design, a good accessibility is gained, while keeping a compact design. The potential difference is supposed to be balanced between the delivering and diverting side. The tight arrangement principally reduces potential errors resulting by imprecision at horizontal adjustment and vibration (from drive belt, motor and environment), thus enhancing the precision of measurement.

3. Ferrofluid Based Locomotion due to Surface Deformation

Magnetic Field Source

The aim was to create a magnetic field consisting of a weak perturbation superposed onto a comparatively higher constant part at the free surface of the fluid. As the magnetic field decreases with the squared reciprocal distance, which makes the design of the demanded field more difficult; and as the chosen ferrofluid incorporates a slight magneto-viscous effect at low field strengths, the interpretation led to a setting with the magnets positioned above the free surface. Subsequently, the field gradient is higher at the free surface than in other layers.

Generally, two options exist to produce a magnetic field: utilizing electromagnets or permanent magnets (or a combination of both). Electromagnets enable configurable settings in comparison to permanent magnets, but require a higher control effort for special field settings. With the consideration of small λ (for low REYNOLDS numbers), a closed construction space favored permanent magnets, due to their high power density. In addition, they ensure operation under constant magnetic conditions and are not limited in operation time.

Another implementation is the smart version the Bayreuth experimental physicists used for a number of investigations, e.g. published in [Fri10]. It employs a large helmholtz coil pair, water-cooled, and generated the field perturbation with iron rods attached transversally to a driving belt. The perturbing belt runs below the fluid container. The recording equipment includes an x-ray-detector. Copying the design concept did not seem wise for our intentions, as the perturbation influence is strong within the fluid layer and weakest at the surface. An equally important point, PM do not heat while operating, thus, they work under constant magnetic field conditions, do not change temperature close to the sensitive fluid and are unrestricted in operation time.

Measurement Strategy

A less obvious item of consideration is the required time of measurement to capture the supposedly diminutive transport effect. The longer the recording takes, the more difficult it is to ensure constant laboratory conditions. Nevertheless, the experiment is being watched above several hours. The flow rate is recorded directly. Although, a less sensitive measuring equipment is required, due to effect accumulation, the rate of methodical errors can be decreased significantly. We decided

3.12. Discussion of the Analytical and Experimental Results

on converting the flow effect into a robustly readable displacement of a solid plug or of the cross section of a marker fluid, see figure 3.9.

3.12.2. Conclusion from the Current Results

The experimental arrangement and the measurements of influencing parameters as well as the volume flow \bar{Q} led to a discrepancy between theoretically calculated and experimentally verified average volume flows $\bar{Q}_{\text{analytics}}$ and $\bar{Q}_{\text{experiment}}$ by the factor $c_Q = 0.66$. Though the difference is considerably low, the reasons for it should be discussed. Furthermore, some test series yielded to a reverse directed material transport, which according to the analytical model should not happen. These cases also must be analyzed with regard to potential errors.

It has to be discerned between defective influences on the calculated and on the experimentally obtained \bar{Q} . The prediction of the flow rate is based on the analytical description, see (3.83), and is numerically fed by material and design parameters. Uncertainties of manufacturer's data about the materials contribute their part, see details in section 3.12. This concerns mainly the ferrofluid and the PMs. The amplitude of the perturbed magnetic field strength A has a strong influence on the flow rate, since A is introduced by the power of four: $\bar{Q} = f(A^4)$. As the perturbation amplitude is $A = 7.84 \text{ Oe}$ with a standard deviation $S(A) = 1.25 \text{ Oe}$ due to the individual PMs, see figure A.2, this generates a variance of the theoretical predicted $\bar{Q} = 1.85 \times 10^{-7} \begin{matrix} +1.47 \times 10^{-7} \\ -9.35 \times 10^{-8} \end{matrix} \text{ cm}^2 \text{ s}^{-1}$. Nevertheless, the experimentally achieved \bar{Q} does not register the variation of A over several hours. But, the consequence of the inexact sine signal stays unknown. Most problematic are, however, the long detection time. Although it enables an enhanced measurability, constant conditions cannot be guaranteed over those long durations. Temperature conditioned changes of the viscosity do occur most certainly. General imperfection in the precision of the measurement equipment and the influence of the measurement strategy (e.g. friction of glass on glass of tube and glass marker or the counteracting buoyant force of the lighter fluid) will add to the difference of \bar{Q} . A renewed experimental approach should implement the consequences from the defective results.

4. Enhancement of Surface Deformation

4.1. Experimental Surface Manipulation

4.1.1. General Procedure and Strategies

Previously, ferrofluid based locomotion resulted in most cases in small surface deformation, low applicable forces, weak, slow or inefficient locomotion; in short, in higher frustration levels. Since abandoning the ferrofluid material would miss the goal, a new strategy is scheduled. Extending the logic chain to the stage of surface deformation, the concept envisions an increase of force by enhancing of the surface deformation. So, by exceeding the conventional scale of ferrofluid deformation, we aim to enlarge forces and multiply locomotion capability.

Here, we examine the case of a magnetizable fluid harboring a magnetically high permeable object, both are exposed to a uniform magnetic field. In [Zim08b], this case has been theoretically discussed already (analytically derived and numerical supported) using cylindrical and spherical highly magnetizable artifacts. The axis-symmetrical and spherical concentrators focus the magnetic field in close proximity to the ferrofluid. The resultant fluid deformation is intensified and bifurcation effects at the concentrator surface are predicted. Depending of the inclination angle of the magnetic field, different contour shapes bifurcation transitions are adopted by the fluid. Also, like in [Nal12], the theoretical predictions are experimentally verified and compared.

The experimental setup is designed as described in the following. The magnetizable fluid is the cerosin-based ferrofluid EMG 905, com-

4. Enhancement of Surface Deformation

mercially available from Ferrotec¹. The low viscosity of the cerosine based ferrofluid was one reason for the choice.

The magnetizable fluid is filled in a transparent container made of polymethylmethacrylat (PMMA) with a squared display window and a narrow interior gap. The squared side lengths are $L_c = 0.1$ m, the gap is $s_g = 3 \times 10^{-3}$ m wide. The free fluid surface adjoins to air, which is termed as non-magnetic fluid (NMF). As figures 4.1(a) and 4.1(b) illustrate, the heart of the construction is a cylindrical rod of magnetizable steel with a radius of $R_c = 10^{-2}$ m. The iron core penetrates the vessel, so that its peripheral surface touches the bottom and the fluid levels horizontally at 2×10^{-3} m above its upper periphery in an absent magnetic field. As the cylinder is used to warp the magnetic field, boundary effects are avoided by an overlong design (length $s_c = 0.3$ m). Thus, the iron core protrudes sufficiently to both sides of the container.

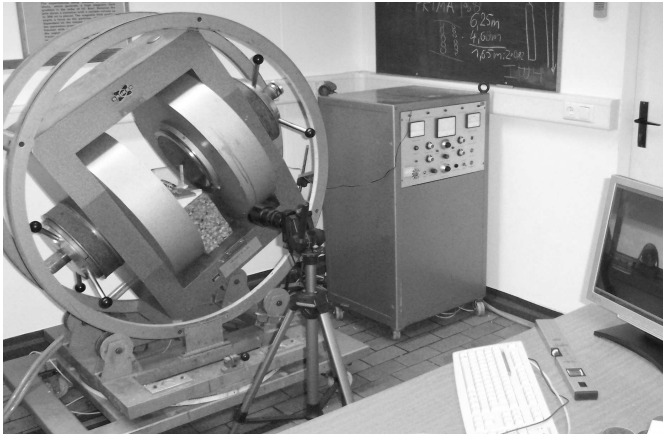
Spatial relations are given by a Cartesian coordinate system. Its origin is set into the center of the iron core, as shown in figure 4.1(c). The inclination angle of the magnetic field is recorded by the angle spreading from the x-axis in mathematical positive direction.

The experimental setup is completed by a pivot electromagnet, see figure 4.1(a), which ensures a sufficiently homogeneous field (without inserted iron core) $\mathbf{H}_\infty = (H_\infty \cos \alpha, 0, H_\infty \sin \alpha)$. The analysis comprehends the variation of field inclination angles of $\alpha = 0^\circ, 30^\circ, 45^\circ, 60^\circ$ and 90° . Image recordings are taken for these angles as movie and photographs. The surface deformation of the ferrofluid is subject of interest as well as special contour configurations and their abrupt transitions into each other.

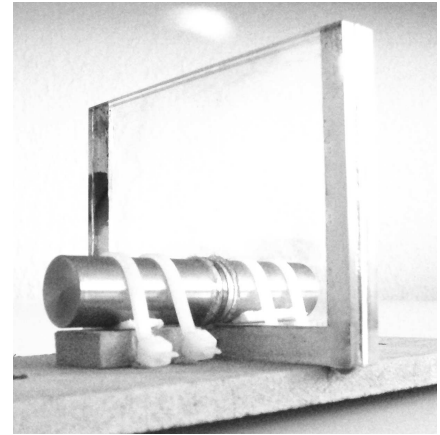
The electromagnet is current driven. Thus, the determination of the magnetic field strength H is accomplished by measurement using an Oersted meter. The simultaneous data acquisition of magnetic field strength and the recording of ferrofluid deformation is problematic due to delays in measurement techniques. – The available Oerstedt meter is not integrated within the electromagnet's outfit. An external device is used, which have to be positioned within the field range for record taking and than removed for not disturbing the photographic image. To handle this, the procedure is executed by increasing the magnetic

¹Ferrotec GmbH, 72669 Unterensingen, Germany, <http://www.ferrotec-europe.de>

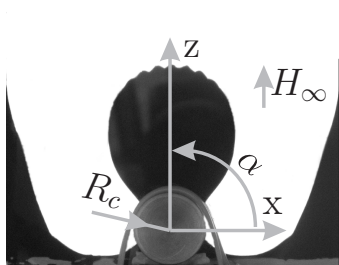
4.1. Experimental Surface Manipulation



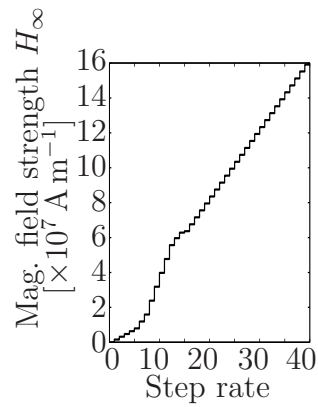
(a) General view of pivot electromagnet, electrical power supply, control unit and camera.



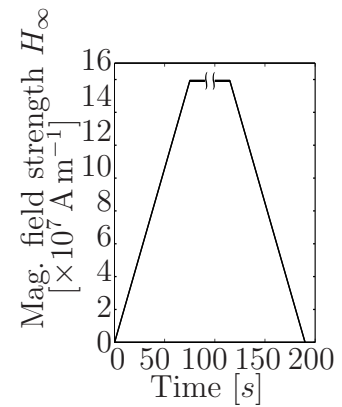
(b) PMMA housing and highly permeable steel cylinder.



(c) Introduction of Cartesian coordinates and inclination angle [Nal12].



(d) Progression of the magnetic field, successive strategy.



(e) Progression of the magnetic field, continuous strategy.

Figure 4.1.: Introduction to the setup and field application strategies.

4. Enhancement of Surface Deformation

field successively, see the strategy in figure 4.1(d) taking record of the magnetic field strength and freeze frames of the contour deformation (of the ferrofluid). In the second cycle, the electric current (and magnetic field) is steadily increased and decreased, see figure 4.1(e), while the process of the ferrofluid deformation is logged in motion pictures. Both both, photograph and video acquisition, a CCD camera is used.

The values of the magnetic field strength are added retrospectively to the continuous data series. For this, the first definite contour configuration, i.e. is the first phase transition, is identified in both, the successively increased data series (with established field values) and the continuously increased data series (with unidentified field values). The corresponding magnetic field value is assigned to the continuous series and the field progression is approximated linearly up to the known maximum point (2000 Oe [$\approx 160 \text{ kA m}^{-1}$]) and reverse.

4.1.2. Analysis and Data Extraction

The extraction of relevant data is accomplished by using the numerical tool MATLAB (The MathWorks, Inc.). Its process is depicted in figure 4.2. The movie clip is cut into single frames, while each frame is binary converted. Each pixel holds either the property 'white' or 'black'. The edge between fluid (= black) and background (= white) is extricated. For control reasons, two positions are monitored: the absolute fluid height of each frame and the fluid height vertically above the cylinder center, the relative height. Since the progression lines of both markers are fairly parallel, in further analysis only the relative fluid height is used. For estimation, the error induced by data conditioning the fluid volume, the amount of black area, was monitored, too. The controlling entity of the fluid volume is fluctuating, while the fluid deformation proceeds by approximately 23% of the total of pixel per frames.

The controlling entity of the fluid volume alters while the fluid deformation process by approximately 23% of the whole amount of pixel per frame. As a side effect, sudden chances in this graph indicate the watched phase transitions. The smearing of ferrofluid at the pane, though disturbing, is not corrected in order to keep the data as original as possible.

4.1. Experimental Surface Manipulation



Frame = 1203
Height X = 46.2222 mm
Height O = 38.8889 mm
Fluid vol. = 38.4827 %

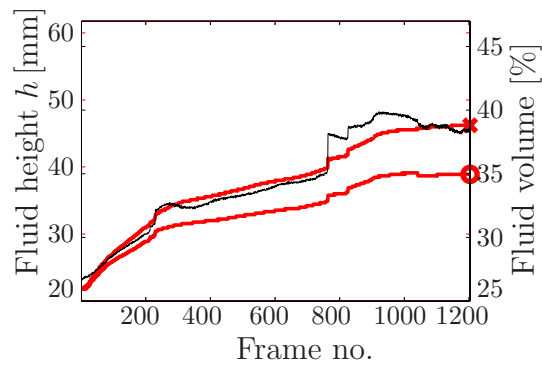


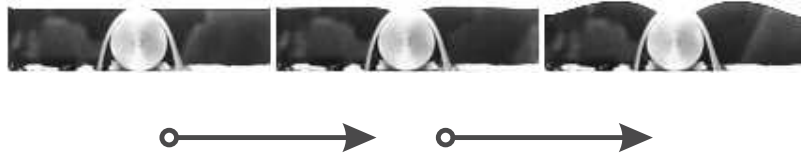
Figure 4.2.: Data extraction at the example of the process of a rising field at 60° , top: photography of the CCD camera, middle: monochrome binary picture including edge detection, marker for maximum height (x) and height above core (O), bottom: 2d-plot fluid heights versus frame numbers.

4. Enhancement of Surface Deformation

4.1.3. Deformation and Phase Transitions

Field Inclination of 0° (Horizontal Magnetic Field)

Though of minor interest, the behavior of the ferrofluid surface exposed to a horizontal magnetic field is documented for completeness reasons. The disposition for deformation is weak and a single phase transition from one to two separate fluid volumes takes place. Figure 4.3 displays the process. The unitary splitting at $H_\infty = 6.3 \times 10^3$ A/m is followed by a surface curvature in both fluid portions. Here, the surface deformation enlarges continuously until the field maximizes.



(a) 0°

Figure 4.3.: *Temporal progress of fluid deformation at $\alpha = 0^\circ$ (photo series) [Na112].*

Field Inclination of 30° , 45° and 60° (Obliques Magnetic Field)

The ferrofluid contour reacts similarly under magnetic fields of various inclination angles (30° , 45° , 60°). But phase transitions are triggered by different magnetic field strengths. In the magnetic field rising from zero, the deformation process starts with the disconnection of the previously closed ferrofluid volume into two separate volumes. Parting object is the cylindrical iron core. Proceeding, the surfaces of both fluid portions curve convexly. This creates an asymmetric configuration, as one portion warps into the free area, which lies alongside the magnetic field above the high permeable concentrator. This is the right hand side for our experiment. The left sided portion avoids the tangential field direction below the concentrator. For field inclinations of 30° and 45° , a cavity appears at the bottom of the right side of the cylinder, as the fluid passage is constricted and air enters compensating the under pressure. The pinching is caused by magnetic and gravitational forces acting in

4.1. *Experimental Surface Manipulation*

opposite directions and surface tension aiming for a low-energy, closed fluid entity. These effects lead to a complete cutoff, which presents the phase transition from a two-volume to a three-volume configuration. The further increasing magnetic field induces the spasmodically transfer of small amounts of ferrofluid from the bottom to the elevated volume. This is continued, until the complete ground level ferrofluid is captured by the concentrated field and levitates on the cylinder. At the completed passage, the total amount of individual volumes is two. The splitting into or consumption of individual fluid portions are definite events and, therefore, are called markers for subsequent phases.

Critical field strength values are reported in the bar chart of figure 4.9(a), while figure 4.4(a) to 4.4(c) as well as figure 4.5 give impressions of the surface variations. The data are given additionally in tabular form in the appendix, see tables 4.1 and 4.2 or appendix B.1.

4. Enhancement of Surface Deformation

Table 4.1.: *Phase transitions at successive and continuous field increase at $\alpha = 45^\circ$.*

Transition	Field inclination angle 45°			
	successive increase	continuous	absolute	percentaged abberation
	H [kA m $^{-1}$]		H [kA m $^{-1}$]	H %
I	6.3	7.08	0.78	0.49
II	59.7	50.88	8.82	5.51
III	71.64	55.49	16.15	10.09
IV	147.26	159.2	11.94	7.46

(160 kA m $^{-1}$ \equiv 100%)

Table 4.2.: *Phase transitions at successive and continuous field increase at $\alpha = 60^\circ$.*

Transition	Field inclination angle 60°			
	successive increase	continuous	absolute	percentaged abberation
	H [kA m $^{-1}$]		H [kA m $^{-1}$]	H %
I	7.9	7.9	0	0
II	---	---	---	---
III	35.82	59.57	23.75	14.84
IV	135.32	149.33	14.01	8.76

(160 kA m $^{-1}$ \equiv 100%)

4.1. Experimental Surface Manipulation

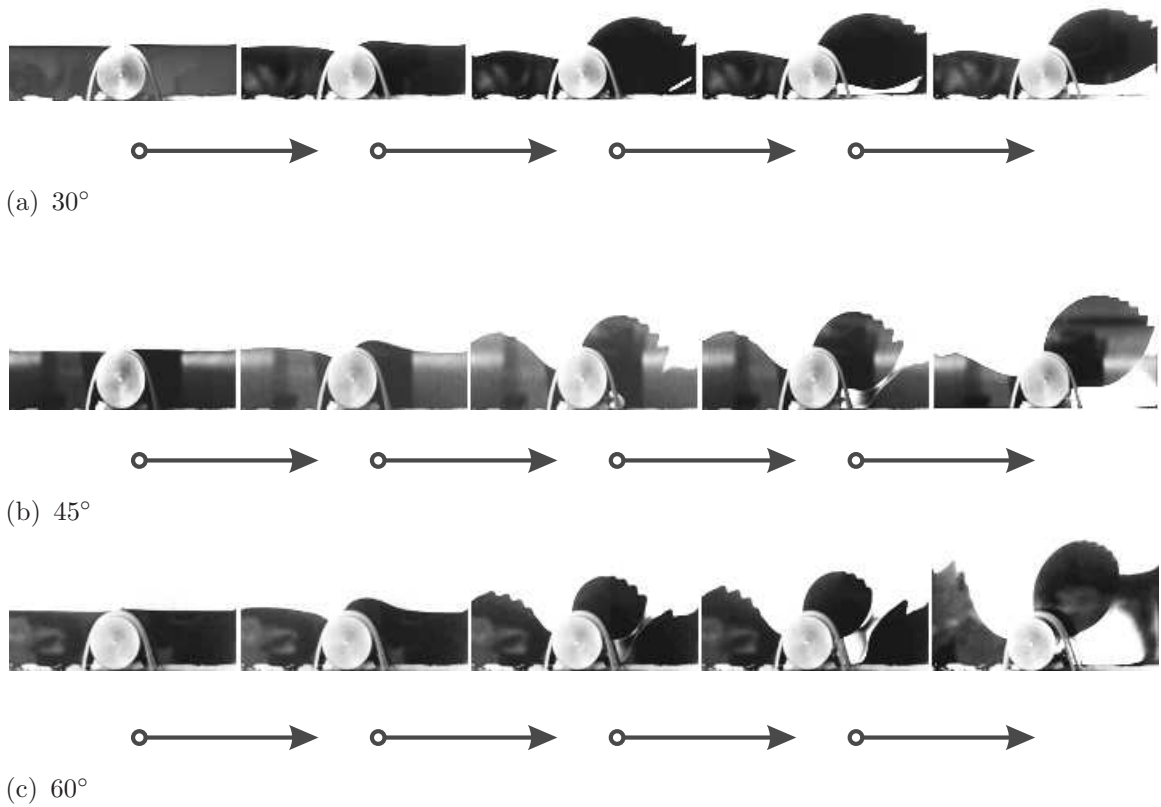


Figure 4.4.: *Progression of the surface deformation in the inclined magnetic field (photo series) [Nal12].*

4. Enhancement of Surface Deformation

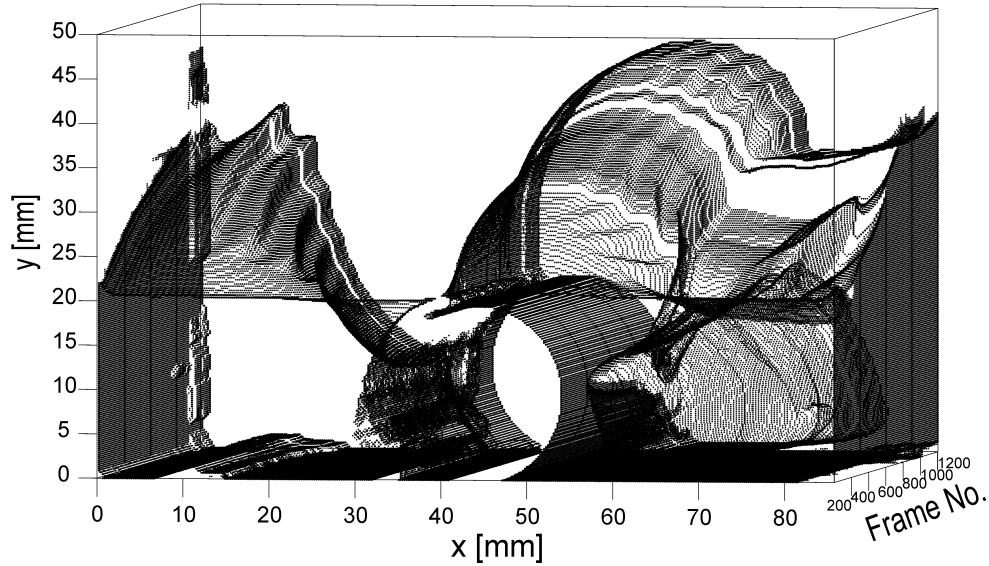


Figure 4.5.: Temporal progress of fluid deformation at $\alpha = 60^\circ$ (extraction from image processing).

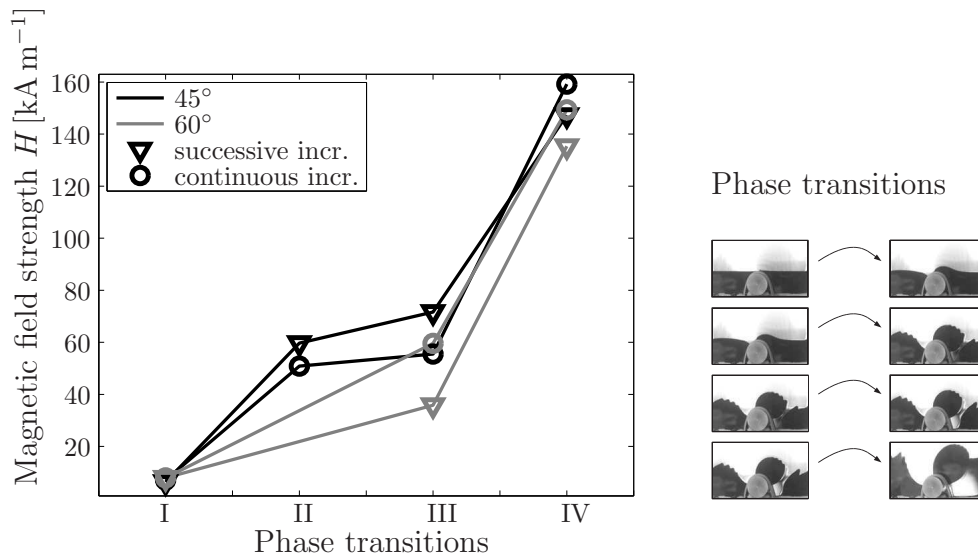


Figure 4.6.: Comparison of fluid behavior in the successive and continuous field progression.

Field Inclination of 90° (Vertical Magnetic Field)

With rising magnetic field strength – at vertical application – the fluid surface warps up around the direct proximity of the highly permeable cylinder. At the trigger point of 1.4×10^4 A/mm the coherent fluid volume disconnects into three separates; two laterals, one of which riding on top of the field concentrator. While the field strength rises, the lateral volumes stretch up and form three peaks on each side. Taking turns, the inner most to both sides jump at arrival of critical field values as a sudden transition to the center fluid volume. See figure 4.7 for illustration and table 4.3 for the trigger values.

The descending field reverses the process, but different shapes are witnessed. At the beginning field decrease, the center portion sinks and crouches, but is held as a separate portion steadily on top of the concentrator. Only at a considerable lower field strength, compared to the fluid raise in the increasing field, the suspended fluid opens the closed formation. The passage appears first at the left side, which creates an asymmetric setting of two separate volumes. After a delay, the elevated portion bridges to the right sided ground volume. This reinstates the symmetry and generates a re-conjunction to one coherent volume.

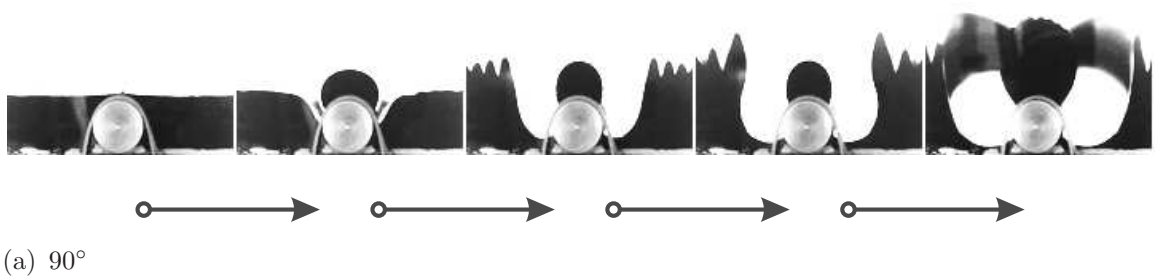


Figure 4.7.: Temporal progress of fluid deformation at $\alpha = 90^\circ$ (photo series) [Nal12].

4. Enhancement of Surface Deformation

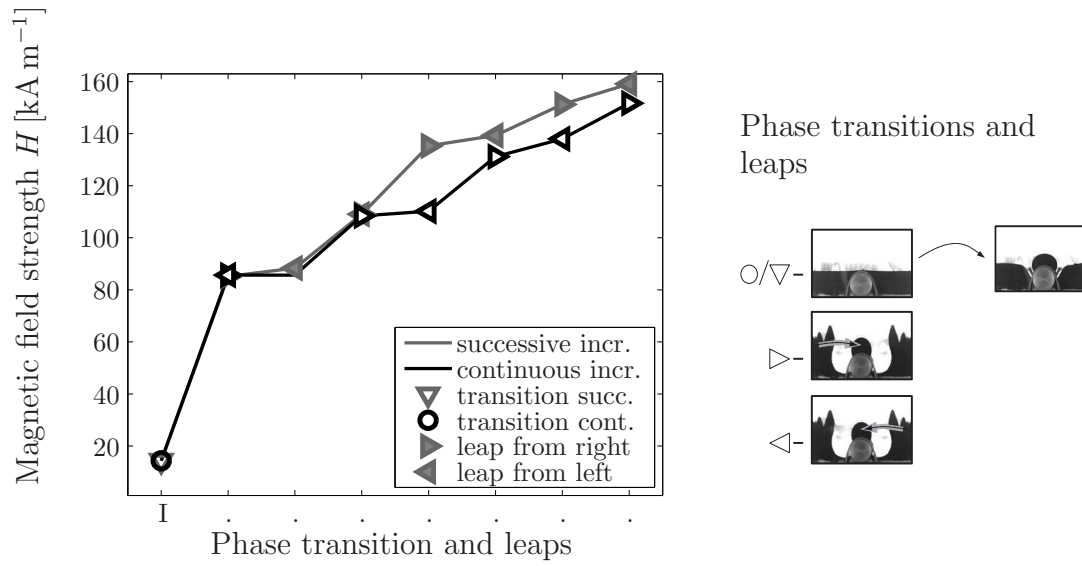


Figure 4.8.: Comparison of the deformation progress for successive and continuous field progress at $\alpha = 90^\circ$.

Table 4.3.: Phase transitions at successive and continuous field increase at $\alpha = 90^\circ$.

Transition	Field inclination angle 90°			
	successive	continuous	absolute	percentaged
	increase		abberation	
	H [kA m $^{-1}$]		H [kA m $^{-1}$]	H %
I	14.33	14.33	0	0
.r	85.17	85.63	0.46	1.085
.l	88.36	85.63	2.73	1.71
.r	109.05	108.4	0.65	0.41
.l	109.05	110.2	1.15	0.72
.r	135.32	131.17	4.15	2.59
.l	139.3	138.0	1.3	0.81
.r	151.24	151.67	0.43	0.27
.l	159.15	---	---	---

(160 kA m $^{-1}$ \equiv 100%)

4.1. Experimental Surface Manipulation

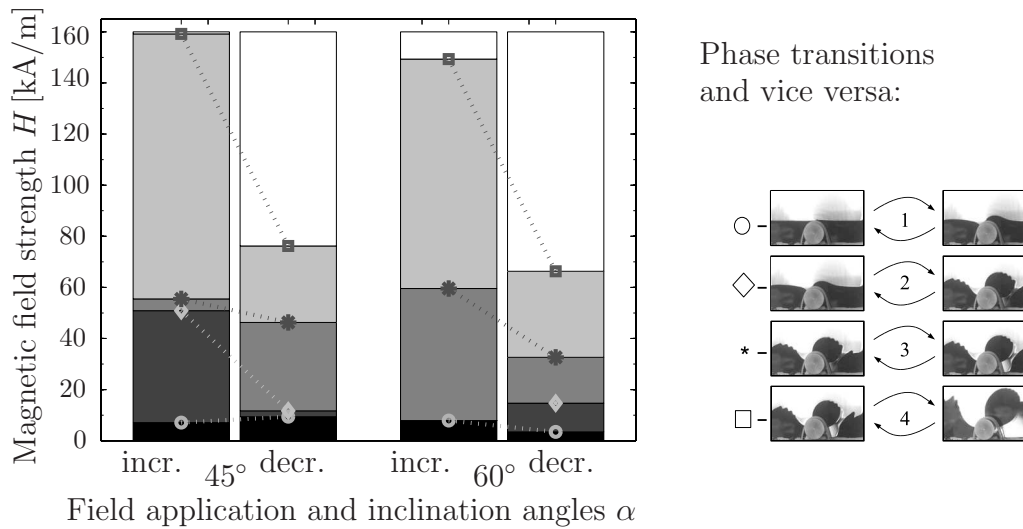


Figure 4.9.: *Hysteresis of the phase transitions for the continuously, obliquely applied magnetic field at $\alpha = 45^\circ$ and 60° .*

4.1.4. Hysteresis

The behavior of the magnetizable fluid in a rising and the descending magnetic field do not equal each other. A hysteresis effect can be recognized. Phase transitions in the declining field comprise a delay. The complete separation of individual volumes and the consumption of them (by the neighbor) occur at comparatively lower magnetic field strengths than in the increasing field.

Hysteresis for the Obliqued Field (Inclination of $\alpha = 45$ and 60°)

Figures 4.9(a) points out the ranges of the magnetic field strengths lying between phase transitions, which are highly variable. The dotted lines link associated transitions of the increasing and decreasing fields. Figure 4.10 presents the relative fluid height against the magnetic field strength, which gives a better impression of the stored energy.

Hysteresis for the Vertical Field (Inclination of $\alpha = 90^\circ$)

The fluid motion in the vertical field produces only one transition between the one to the three-divided volume configuration. Nonetheless, the plot of figure 4.11 illustrates the fluid leaps by the sudden discontinuities – for the increasing magnetic field. The declining field generates none of the kind, the fluid declination is a steady process. The cen-

4. Enhancement of Surface Deformation

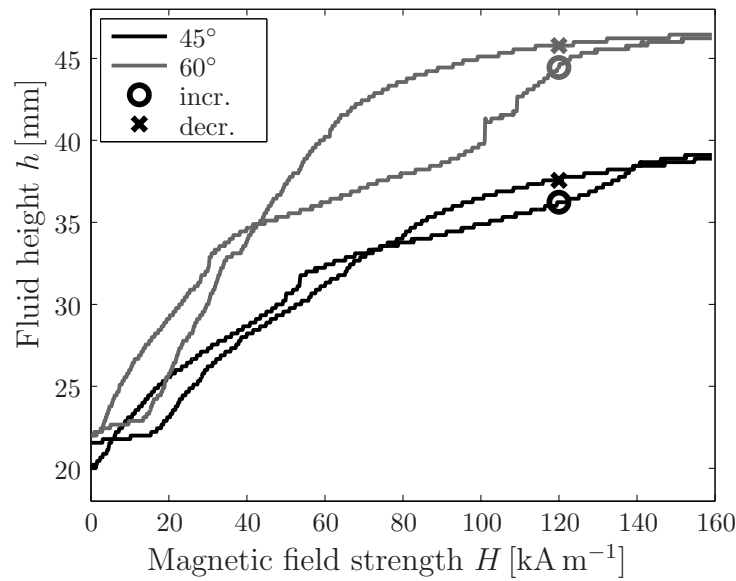


Figure 4.10.: Ascending and descending fluid level at accordant field progress incorporates hysteresis at $\alpha = 45^\circ$ and 60° .

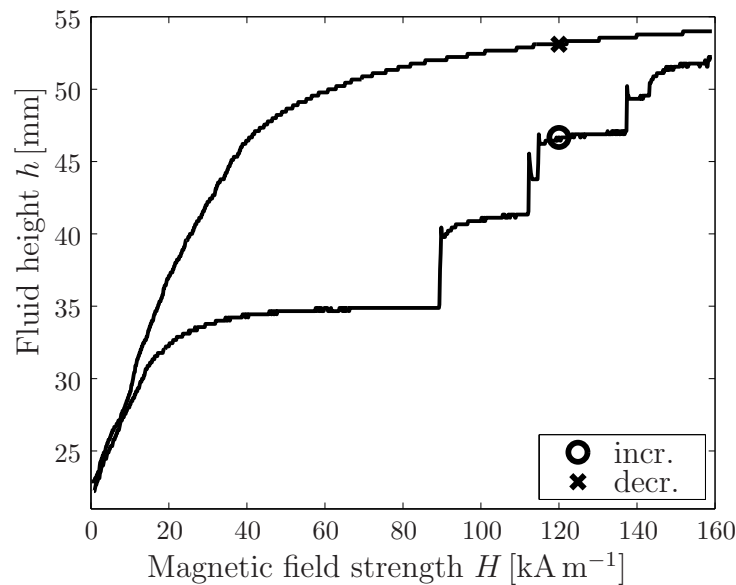


Figure 4.11.: Ascending and descending fluid level at accordant field progress incorporates hysteresis at $\alpha = 90^\circ$.

ter volume, where the control mark of the plot is positioned, is kept elevated for a wide range of the field. Comparing the hysteresis areas of the three field inclination angles, the 90° configuration registers the highest effect. The potential and magnetic energy stored within (at field declination) or fed to the moving system, can be identified as reasons for the hysteresis itself. The difference between the varying angles can be explained by the supporting function of the iron cylinder carrying more parts of the fluid mass with higher angles.

4.2. Theoretical Description of Surface Manipulation due to Field Concentration

4.2.1. Introduction of the Model

Since the previous section discussed experimental surface deformation of a magnetizable fluid pierced by a field concentrating iron cylinder, the matter shall now also to be analyzed in theory. The discussion is closely related to [Zim08b], where the cases of surface manipulation by a field concentrating cylinder and sphere are investigated. In this section, we focus on the cylindrical concentrator, which refers to the experiments. We also aim for a quantitative verification of the hysteresis and the thresholds of phase transitions.

We begin by presenting the terms of the contemplated model. Here, the indices b , f and s name the high permeable body, the magnetizable fluid and the non-magnetizable environment, respectively. The magnetization of the fluid depends on the magnetic field

$$M^{(f)} = M_{mf}L(\xi.),$$

$$\text{where } L = \text{cth}(\xi.) - \frac{1}{\xi.} \quad \text{and} \quad \xi. = \frac{\mu_0 m H}{kT}. \quad (4.1a)$$

M_{mf} represents the saturation magnetization of the fluid, k is the BOLTZMANN constant and T is the temperature. Further parameters include, the absolute permeability $\mu_0 = 4\pi \times 10^{-7} \text{ m kg s}^{-2} \text{ A}^{-2}$ and the magnetic moment of the ferromagnetic particles the fluid is made of

4. Enhancement of Surface Deformation

$m = \mu_0 M_{mf}/n$, where n is the concentration of these particles.

Applying the LANGEVIN function for magnetization description of the fluid is a usual approach, see [Ros85, p 56ff], illustrating the real magnetization curve with high accuracy. The magnetization of the concentrating high permeable iron core is proportional to the magnetic field

$$M_b = \chi_b H \quad \text{where} \quad \chi_b = \mu_b - 1, \quad (4.1b)$$

while, as we assume, the permeability of the core is constant ($\mu_b = \text{const}$) and much higher than the one of the surroundings $\mu_b \gg 1$. Hence, the non-magnetic environment has, with a permeability of $\mu_s \approx 1$, a negligibly small magnetization $M_s = 0$.

The non-inductive approximation ($H \gg M_f$) is applied to the magnetic field, which is expanded to a TAYLOR series ($\mathbf{H} = \mathbf{H}(0,0) + (\nabla_i H_j)x^i \mathbf{e}^j + \dots$), according to [Zim08b, p 46]).

As the magnetic field is uniform, one can conclude from the adapted description

$$\mathbf{H} = \nabla \varphi, \quad \varphi = \mathbf{H}_\infty \mathbf{r} + A \mathbf{H}_\infty \mathbf{r}/r^2, \quad (4.2a)$$

where $A = -L_c^2$, a geometrical subsumption and $r = \sqrt{x^2 + z^2}$, the position from the coordinate origin, the final form

$$H(x, z) = \sqrt{H_x^2 + H_z^2}, \quad (4.2b)$$

$$H_x = H_\infty \cos \alpha + \frac{A H_\infty \cos \alpha}{x^2 + z^2} - \frac{2 A H_\infty x (x \cos \alpha + z \sin \alpha)}{(x^2 + z^2)^2}, \quad (4.2c)$$

$$H_z = H_\infty \sin \alpha + \frac{A H_\infty \sin \alpha}{x^2 + z^2} - \frac{2 A H_\infty z (x \cos \alpha + z \sin \alpha)}{(x^2 + z^2)^2}. \quad (4.2d)$$

The ferrohydrodynamic NAVIER STOKES equation and the continuity equation describe the plane fluid motion, where $\mathbf{v} = v_i \mathbf{e}_i$ is the fluid velocity $\mathbf{v} = u \mathbf{e}_x + w \mathbf{e}_z$

$$\varrho^{(i)} \frac{\partial \mathbf{v}}{\partial t} = -\nabla p^{(i)} + \mu_0 M^{(i)}(H) \nabla H + \eta^{(i)} \Delta \mathbf{v}^{(i)} + \varrho^{(i)} \mathbf{g}, \quad (4.3a)$$

$$\nabla \mathbf{v}^{(i)} = 0, \quad \text{with} \quad i = f, s. \quad (4.3b)$$

4.2. Theoretical Description of Surface Manipulation

The parameters $\mathbf{v}^{(i)}$ and $p^{(i)}$ stand for the velocity and pressure, while $\rho^{(i)}$ and $\eta^{(i)}$ represent the material properties density and kinematic viscosity of fluid and environment. The normal tension of the fluid is balanced by the surface tension at the free surface and states a steady function there. Kinematic and dynamic boundary conditions for $z = h(x, t)$ are given in the non-inductive approximation

$$[-p\mathbf{n} + \tau_{ij}^\nu n^j \mathbf{e}^i]_f^s = \mp \frac{2\gamma}{R} \mathbf{n}, \quad \text{where} \quad (4.4a)$$

$$1/R = \frac{1}{2} h_{,xx} (1 + h_{,x}^2)^{-3/2} \quad \text{and} \quad \tau_{ij}^\nu = \eta (\nabla_i v_j + \nabla_j v_i),$$

$$w = \frac{d}{dt} h(x, t), \quad (4.4b)$$

$$[\mathbf{v}]_f^s = \mathbf{0}. \quad (4.4c)$$

In the equations, are γ coefficient of the surface tension and $1/R$ the radius of the mean surface curvature. The sign '-' is selected, since the non-magnetic, environmental fluid lies above the magnetic fluid ('+' is valid for the reverse case). The magnetic fluid is motionless at the solid walls

$$u = 0, \quad w = 0. \quad (4.4d)$$

For a numerical calculation of the static and dynamic problem, the following parameter values are used: $T = 300 \text{ K}$, $k = 1.38 \times 10^{-16} \text{ N m K}^{-1}$, $g = 9.8 \text{ m s}^{-2}$, $\rho^s = 1.172 \text{ kg m}^{-3}$, $\eta^s = 14.67 \text{ m}^2 \text{ s}^{-1}$, $V_0 = 18.75 \times 10^{-4} \text{ m}^2$, V_0 is the volume of the magnetic fluid. The numerical quantity values of the material parameters are taken from table 4.4.

4. Enhancement of Surface Deformation

Table 4.4.: *Parameters of the ferrofluid EMG 905 (Ferrotec).*

Saturation magnetization	M_{mf}	31.8×10^3	A m^{-1}
Concentration of the ferromagnetic particles	n	5.4×10^{22}	m^{-3}
Surface tension coefficient	γ	$\approx 0.047 \text{ N/m}$	
Density	$\rho^{(f)}$	1240	kg m^3
Coefficient of viscosity	$\eta^{(f)}$	7.258×10^{-6}	$\text{m}^2 \text{s}^{-1}$
Contact angle between MF and wall	θ_0	43°	
Contact angle between MF and concentrator	θ_s	90°	

4.2.2. Analysis of the Static Problem

For the analysis of the static state, the boundary conditions (4.4) at $z = h(x)$ are operated with the governing motion equations (4.3). These are $w = 0$, $C = \text{const}$ and $\Delta\varrho = \varrho^{(s)} - \varrho^{(f)}$.

$$C + \Delta\varrho gh + P(h, x) = \pm \frac{\gamma h_{xx}}{(1 + h_x^2)^{-3/2}}, \quad (4.5)$$

$$\text{where } P = \mu_0 \int_0^{H(x,t)} M_f(H) dH.$$

With the application of further boundary conditions as well as the volume conservation condition of the fluid, the numerical solution of (4.5) and C are obtained. For every fixed value of the magnetic field, the deformed magnetic fluid surface can take a variation of several contour configurations. These can be numerically calculated and proved by the specific material values chosen for the task. Unlike the experimental outcome, the theoretical results do not only allow a transition from the single, coherent volume splitting into three separate volumes – this happens in theory within a field range of $12.1 \times 10^3 < H_\infty < 16.7 \times 10^3 \text{ A m}^{-1}$ at a field rise. The experimental data lie within, with $H_\infty = 14.3 \times 10^3 \text{ A m}^{-1}$, see figure 4.12.

4.2. Theoretical Description of Surface Manipulation

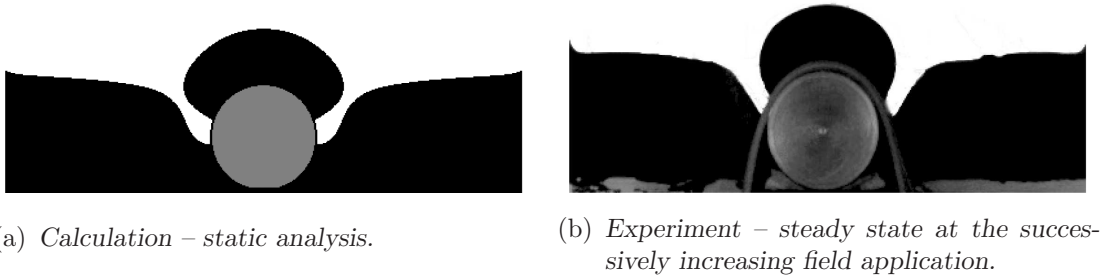


Figure 4.12.: *Surface deformation for the vertical magnetic field at $H_\infty = 14.3 \times 10^3 \text{ A m}^{-1}$ [Nal12].*

According to the calculations, an asymmetric splitting into two separate portions is also possible at a field increase. The numerical solution for this phenomenon states a field value of $H_\infty = 11.9 \text{ A m}^{-1}$. This was only watched in experiment for the decreasing field, see figure 4.13, at $H_\infty = 15.3 \times 10^3 \text{ A m}^{-1}$.

4.2.3. Investigation of the Dynamic Problem

The equations (4.2b) till (4.4) have been numerically calculated also for a dynamically alternating magnetic field. Initially, the magnetic field is absent. The magnetizable fluid lies flat and covers the concentrating iron core by 2 mm. At the beginning of the procedure, the magnetic field H_∞ rises with an constant rate of δ . ($H_\infty = \delta \cdot t$, $\delta = 2.1 \times 10^3 \text{ A m}^{-1} \text{ s}$) to a maximum of $1.6 \times 10^5 \text{ A m}^{-1}$. At the peak value, the field is held steadily and then decreases to zero at the similar rate $-\delta$.

The comparison between the dynamic calculations and the experimental data reveals similar behavior. The increasing as well as the decreasing field evokes identical phases and transitions between them. The calculational prediction of the appearance of gas cavities is confirmed by the experiment, see figures 4.13 and 4.14. Events like ruptures or junctures of fluid portions are triggered by a slightly lower magnetic field strength in the experiment, than in the calculations. The late response may have been induced by the non-inductive approximation, which had been used in the theoretical work.

4. Enhancement of Surface Deformation

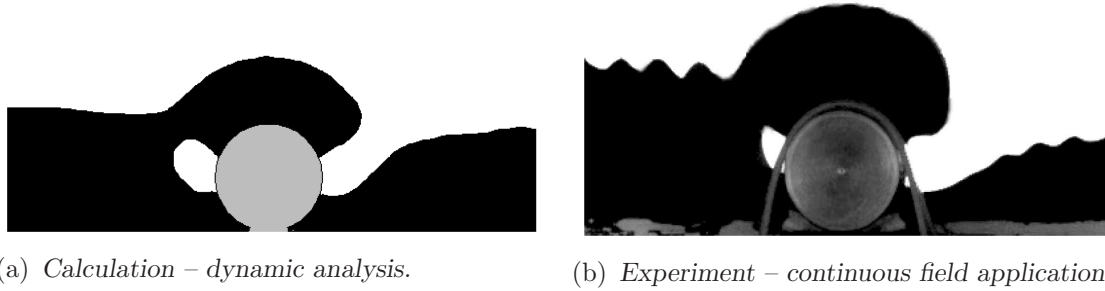


Figure 4.13.: *Surface contour for the decreasing vertical magnetic field at $H_\infty = 17.5 \times 10^3 \text{ A m}^{-1}$ [Na112].*

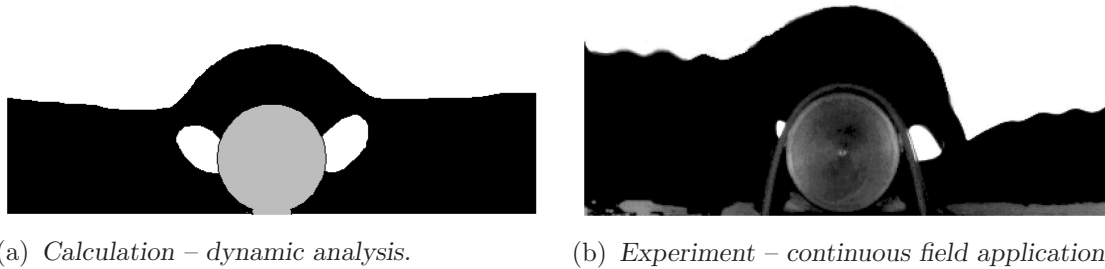


Figure 4.14.: *Surface contour with gas cavities, in the magnetic field decrease, vertical application at $H_\infty = 15.3 \times 10^3 \text{ A m}^{-1}$ [Na112].*

The hysteresis effect described in section 4.1.4 is compared between the continuously changing field in experiment and the dynamic simulation, respectively. The compared values are the surface height $z = h$ in the very middle at $x = 0$, figure 4.15 depicts both graphs.

Apart from the high similarity of the two hysteresis shapes, the one of the calculation shows a smaller range of the surface height. Although both cases start at the same initial level, the real fluid lifts less in the first place, but in the process gains more height than the calculational surface. In the decreasing phase, both graphs run parallel, but for the experimental fluid, the hysteresis loop closes later. The calculational fluid takes slightly more of the described abrupt jumps by 'fluid pumping' than the experimental fluid. The latter shows a more consistent behavior here. The use of the non-inductive approximation is seen as a reason for the differences at the hysteresis observations, too.

4.2. Theoretical Description of Surface Manipulation

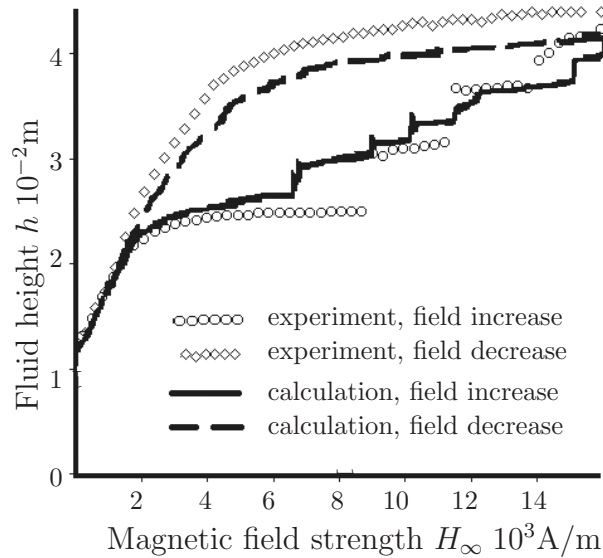


Figure 4.15.: *Hysteresis effect monitored by fluid level at $x = 0$ [Nal12].*

4.2.4. Critical Remarks

The reasons for the occurring inaccuracies are discussed in the following. Firstly, potential imprecision at the assignment of values of the magnetic field strength and the corresponding phase transitions may have introduced errors in the first place. The first splitting situation works as a reference point for the comparison between the successively and continuously increased data series. Uncertainty can arise from a faulty recognition of the transition situation and from the assignment of faulty field values. According to our interpretation, the identification can be accomplished with high accuracy due to the definite distinction of states. The determination of exact field values carries the potential of additional errors. A reduced sensibility of the Oersted meter below 80 Oe ($\approx 6.4 \text{ kA m}^{-1}$) subjects low magnetic field strength values to a wider tolerance. Further, the field control was accomplished manually, the increase rate represents a mean value. Within the act of field alteration, the ascent rate can differ. Consequently, the actual field value can differ from the linearly approximated field value, which is assigned to a transition phenomenon. The way of data acquisition carries is prone to errors, too. The successively increased data line has been recorded in steps: increase of the magnetic field, due to the delay in the fluid motion, waiting until the fluid rests, and taking a photograph.

4. Enhancement of Surface Deformation

The continuously increased data line is captured by a steady increase of the magnetic field while continuous monitoring. This strategy results in two counterbalancing effects. On the one hand, the field strength is further increased compared to the successive line, until the transition takes place. This is counteracted by a slow increase. On the other hand, due to the higher field strength, the impulsion for the transition is more urgent, which accelerates the transition phenomenon. Other effects, which can cause errors, may be: The rising ohmic resistance restricts the magnetic field, due to increasing temperature over the running time. For remedy, a cooling system for the electromagnet was used for basic temperature moderation. The uncertainty of magnetic field determination and time delay of fluid motion contribute to the deviation most.

5. Application Study on a Bifluidic Flow Channel

5.1. Working Principal and Experimental Setup

Ferrofluid is highly adhesive, which is due to the additives to ensure its homogeneous, long-term stable texture. The effect is apparent when staining any surface a ferrofluid gets in contact with – with rare exceptions. This inclination makes ferrofluid ill-adapted to work in material-, form- and force-connected functions, where direct contact is required, unless a third medium is involved. Instead of using separating films for the selection of which a detailed knowledge of the chemical consistence of the commercial ferrofluid would be necessary, we decided to use a second, immiscible fluid. In this case, the ferrofluid and the secondary fluid built a functional entity. The ferrofluid is the actuator. The secondary fluid is the manipulated object.

Bifluidic solutions are already employed by several other research projects using ferrofluid for manipulation tasks. [Seo05] presented a peristaltic pump for transport purposes of the second fluid. [Sch05b] published a feasibility study using a ferrofluid portion as a plunger in a micro structure to drag or press other fluids in and out of a cavity.

As most locomotion systems involve periodic processes coupled with some kind of asymmetry, the following system for flow manipulation or fluid transport is exactly of this scheme. While the design of the container is completely symmetric, the position of the actuator, which is the ferrofluid portion, creates the required asymmetry, see figure 5.1. The actuator fluid is stationary fixed by two permanent magnets underneath the container. These rare earth magnets lie side-by-side and

5. Applicational Study on a Bifluidic Flow Channel

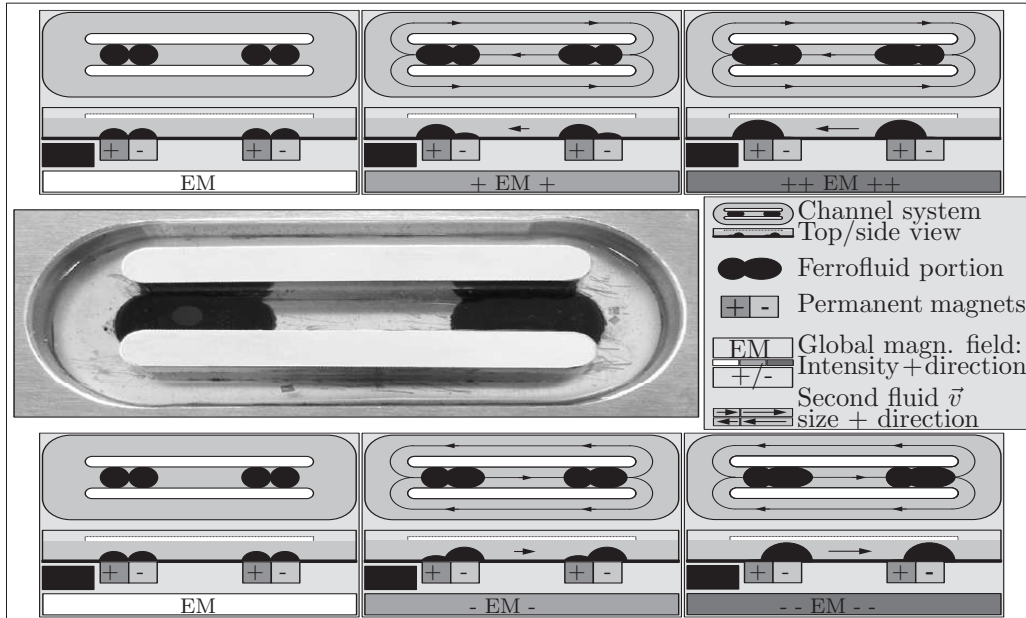


Figure 5.1.: Working principle of the channel flow [Zim10].

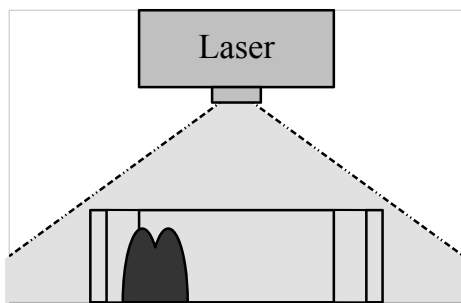
produce a high, local and inhomogeneous magnetic field. The polarizations of the magnets are opposite to each other, consequently the magnetic field lines close between both magnets. By this, a ferrofluid 'bridge' is obtained (the ferrofluid is following the field lines) rather than two separate fluid centers caused by a zone free of field lines. A global, homogeneous magnetic field generated by a helmholtz coil pair interferes with the local field. The global magnetic field is sufficiently homogeneous and produces mainly vertical components (within the range of the experimental container).

The field manipulation by the helmholtz coil pair depends on its polarity. Either way, always one side of the permanent magnet field is enhanced and the other subdued. The ferrofluid portion is deformed accordingly. Thus, at changing the polarity of the electromagnets, the magnetic fluid is tilting alternately to each side, see figure 5.1. The container is filled with water, which works as the secondary, immisci-

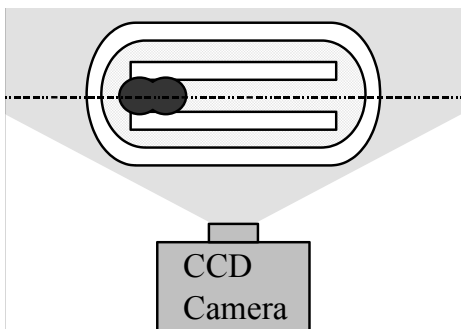
ble fluid. At certain excitation frequencies of the polarization alteration of the helmholtz coils, the actuating ferrofluid portion forces a directed channel flow of the secondary fluid.

5.2. The Measuring System

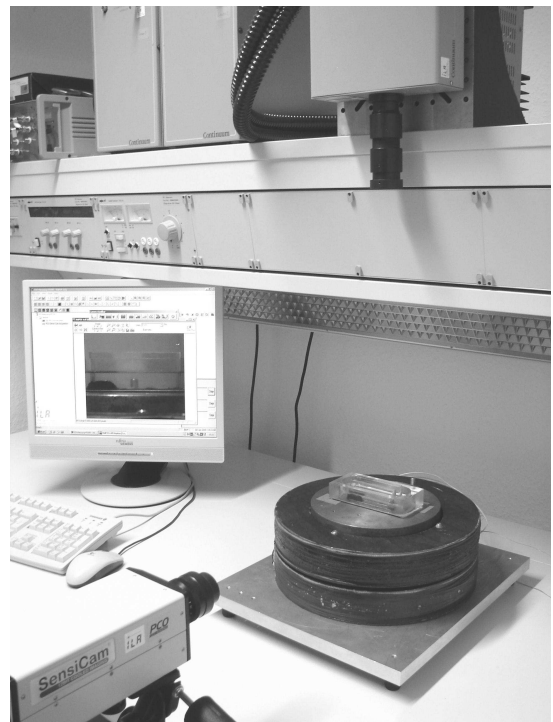
We were interested in two kinds of information. Firstly, the influence of the frequency on the flow behavior and, secondly, the velocity disposition. Although the flow dependency on the frequency could be analyzed with insufficient precision at the water surface, the second task requires a tool, which provides data along the lateral cross section. The choice fell on the measurement technique particle image velocimetry (PIV), as it can provide the required data.



(a) Side view.



(b) Top view.



(c) Actual setup (Photo).

Figure 5.2.: Measurement system with particle image velocimetry.

5. *Applicational Study on a Bifluidic Flow Channel*

For the purpose of distinct nomenclature, a coordinate system is introduced. The x -axis lies in horizontal direction along the central channel length. This direction is also called lateral. The y -axis points in vertical direction orthogonal to the central channel direction. This is also called normal direction.

The particle image velocimetry (PIV) system was integrated in the setup like shown in figure 5.2. To briefly describe the measuring principle, the measuring system consists of a double laser, a charge-coupled device (CCD) camera and a signal synchronizer. The fluid filled container is made of transparent PMMA, wherein the secondary fluid is supplemented by tracer particles. A laser sheet, a beam spread into a two-dimensional plane by prisms, is directed to the tangential channel cross section in question. The tracer particles reflect a highly illuminated speck detected by the camera. The camera system is adjusted orthogonally to the illuminated sheet. Each picture contains two half frames. The synchronization of the double laser bursts and the referring frame captures are managed by the synchronizer. A cross correlations algorithm identifying individual tracer particles in a frame pair reveals the spatial deviation. Knowing the time delay between two laser bursts, a two-dimensional velocity field, a velocity vector plot, can be calculated.

The influence of the frequency of the polarization alteration of the global magnetic field as the most important functional parameter was investigated. The observed driving frequencies lay in an interval of 2 to 20 kHz in steps of 2 kHz. The capturing frequency f_{PIV} of the measurement system was dependent on the driving frequency of the ferrofluid actuation f_{FF} . One actuation period T_{FF} was split into 20 isochronous measurement periods T_{PIV} : $f_{PIV} = 20 \times f_{FF}$.

The analysis of the subsequent vector plots involved three kinds of information. Firstly, characteristic flow patterns can be detected – similar deformation structures are known in the mechanics of rigid bodies as modes. These appearance of these structures depend on the excitation frequency and they move along the central channel. Thus, the patterns depend on the position within the channel (a spatial dependency) and on the time within the excitation period (a temporal dependency). The temporal and spatial argument are linked.

An averaging algorithm provides the mean value of lateral velocity

5.3. Analysis and Discussion of the Results

components. Each spatial data set is averaged over velocities along the channel height (in y) and assigned to a fixed x along the channel. The output is a vector of the lateral velocity depending on the channel length x . Due to the desire to reduce the noise influence, the randomly distributed velocity vectors at the lower half of the channel height ($y = 0..0.5h$) were excluded from the spatial mean value.

The next step for the velocity analysis assigned the spatial velocity distribution to the corresponding time slot within the excitation period – each period was divided into 20 isochronous parts. The output is a matrix containing the lateral velocity data depending on channel length x and the period T of the polarization alteration. This way of data presentation provides a spatial-temporal view on the velocity behavior. It may make it easier to recognize, whether 'high velocity' spots are passed through the period or through the channel, respectively, while the 'high velocity' spots represent the material transport.

5.3. Analysis and Discussion of the Results

The contour diagrams illustrate the velocity distribution (in varying shades of gray) over the period T and the length x . Light gray marks velocities in positive x -direction, dark gray indicates a flow in negative x -direction. As expected within the observed frequency interval of polarization alteration, some frequencies proved to induce a highly effective channel flow of the secondary fluid. The highly active frequencies, $f = 2$ Hz, 10 Hz, 16 Hz, are discussed in further detail. The data sets of the frequencies $f = \{4; 8; 12; 14; 18; 20\}$ Hz display velocities closely around zero. As this behavior is of minor interest, they are not discussed in detail. The full diagrams of these excitation frequencies are listed in the Appendix C.

Figures 5.3 to 5.5 show high velocity amplitudes to both directions. While figure 5.3 contains (at an excitation of $f = 2$ Hz) a similar distribution of lateral velocities in positive and negative channel direction with values up to $v = -50$ mm/s and $v = +70$ mm/s, respectively, the average material transport through the channel is minimal, see figure 5.6.

5. Applicational Study on a Bifluidic Flow Channel

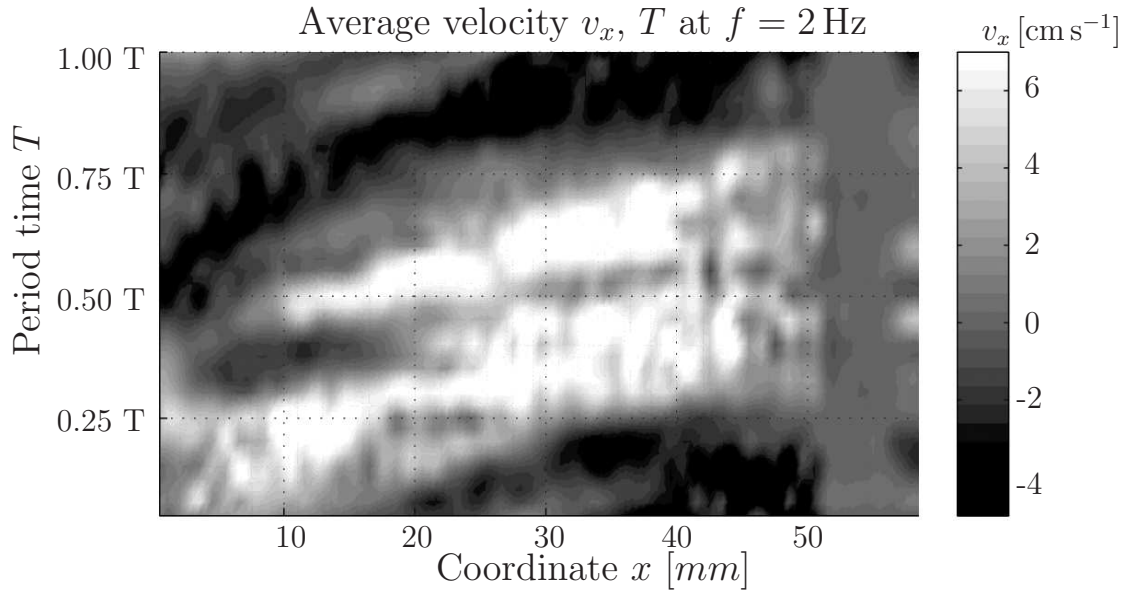


Figure 5.3.: Average velocity* distribution at excitation period of $T = 0.5$ s ($f = 2$ Hz) along the channel length x ; * data include lateral velocity components (x -direction) and altitudinal averaging over upper half of fluid height.

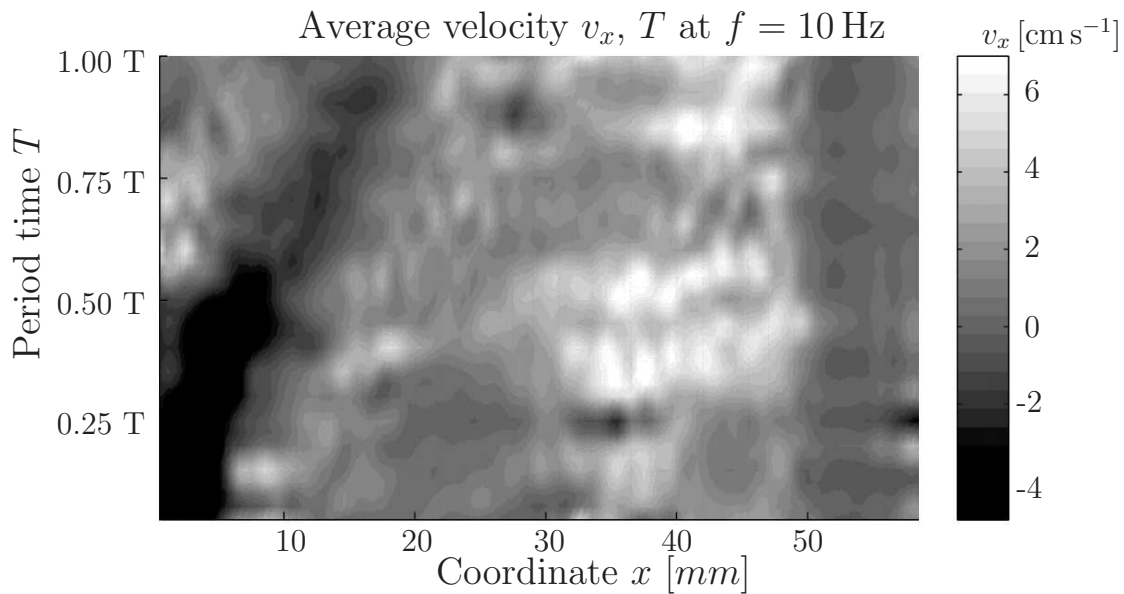


Figure 5.4.: Average velocity* distribution at excitation period of $T = 0.1$ s ($f = 10$ Hz) along the channel length x ; * data include lateral velocity components (x -direction) and altitudinal averaging over upper half of fluid height.

5.3. Analysis and Discussion of the Results

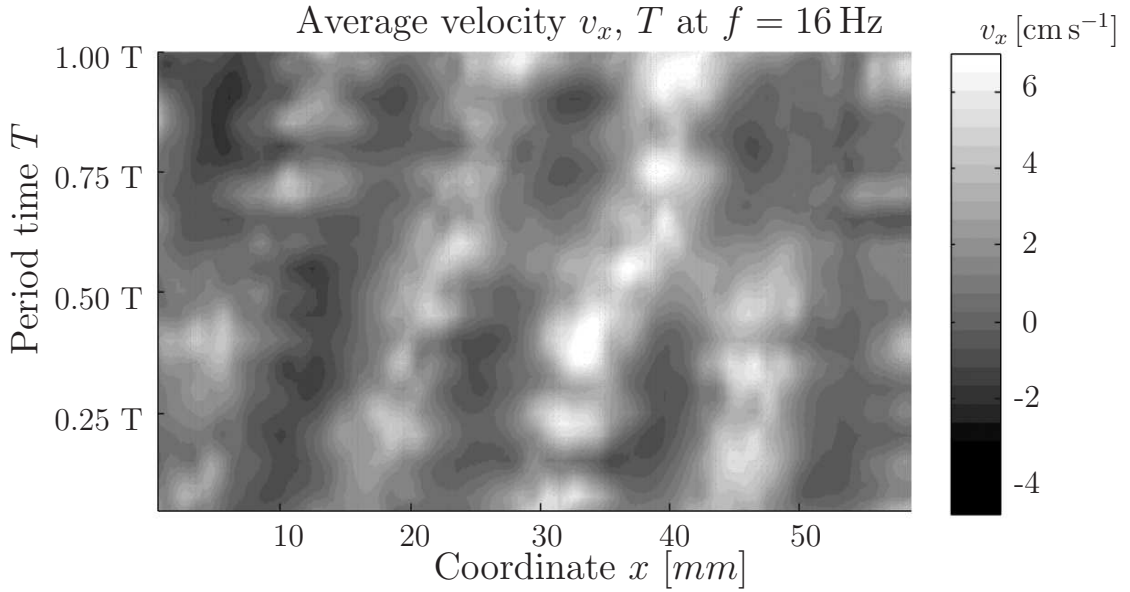


Figure 5.5.: Average velocity* distribution at excitation period of $T = 0.0625$ s ($f = 16$ Hz) along the channel length x ; * data include lateral velocity components (x -direction) and altitudinal averaging over upper half of fluid height [Zim10].

An excitation frequency of $f = 10$ Hz generates stripe structures of comparatively high velocities up to 60 mm/s at the right side of the channel. These persistingly high velocity formations lead from the middle of the channel to the right exit within the duration of one period. Without counteracting reverse flows, a high averaged velocity $v_{av} = 10$ mm/s is achieved. The accordant contour diagram of a $f = 16$ Hz excitation reveals an evenly high velocity distribution from the middle of the channel to the right end. Its values lie mainly between 25 and 60 mm/s with occasional peaks up to $v = 70$ mm/s. This behavior provokes highest average velocities of $v_{av} = 21.5$ mm/s and with that a comparatively high material transport.

The area with zero velocity at the very left channel side is where the actuating ferrofluid portion is positioned (from the channel mouth 20 to 30 mm). There, the ferrofluid actuator is positioned, whose opaque appearance interferes with the visibility of the tracer particles. The resulting faulty vectors are removed by filters.

5. Applicational Study on a Bifluidic Flow Channel

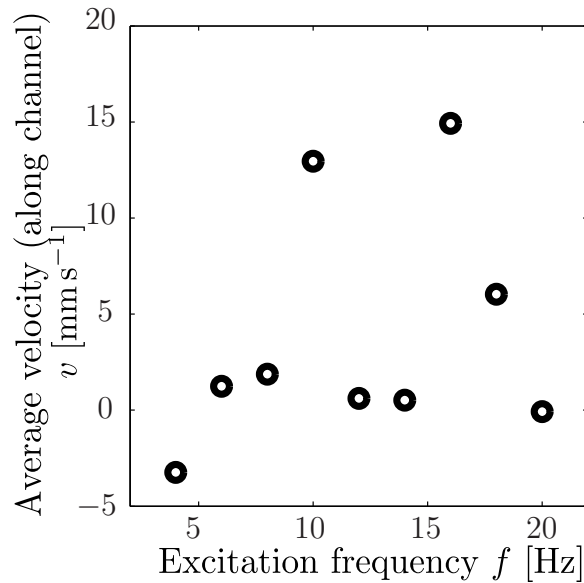


Figure 5.6.: Average velocity v vs. excitation frequency f [Zim10].

The response may be classified into either a clear directional flow of the secondary fluid or the latter moves chaotic. The classification is very distinct. The directive reaction features two criteria. These are the formation of a directed flow through the channel length and the generation of a clear oscillation, accompanied by a characteristically shaped surface wave propagation. The surface waves extend their motion into deeper layers of the secondary fluid.

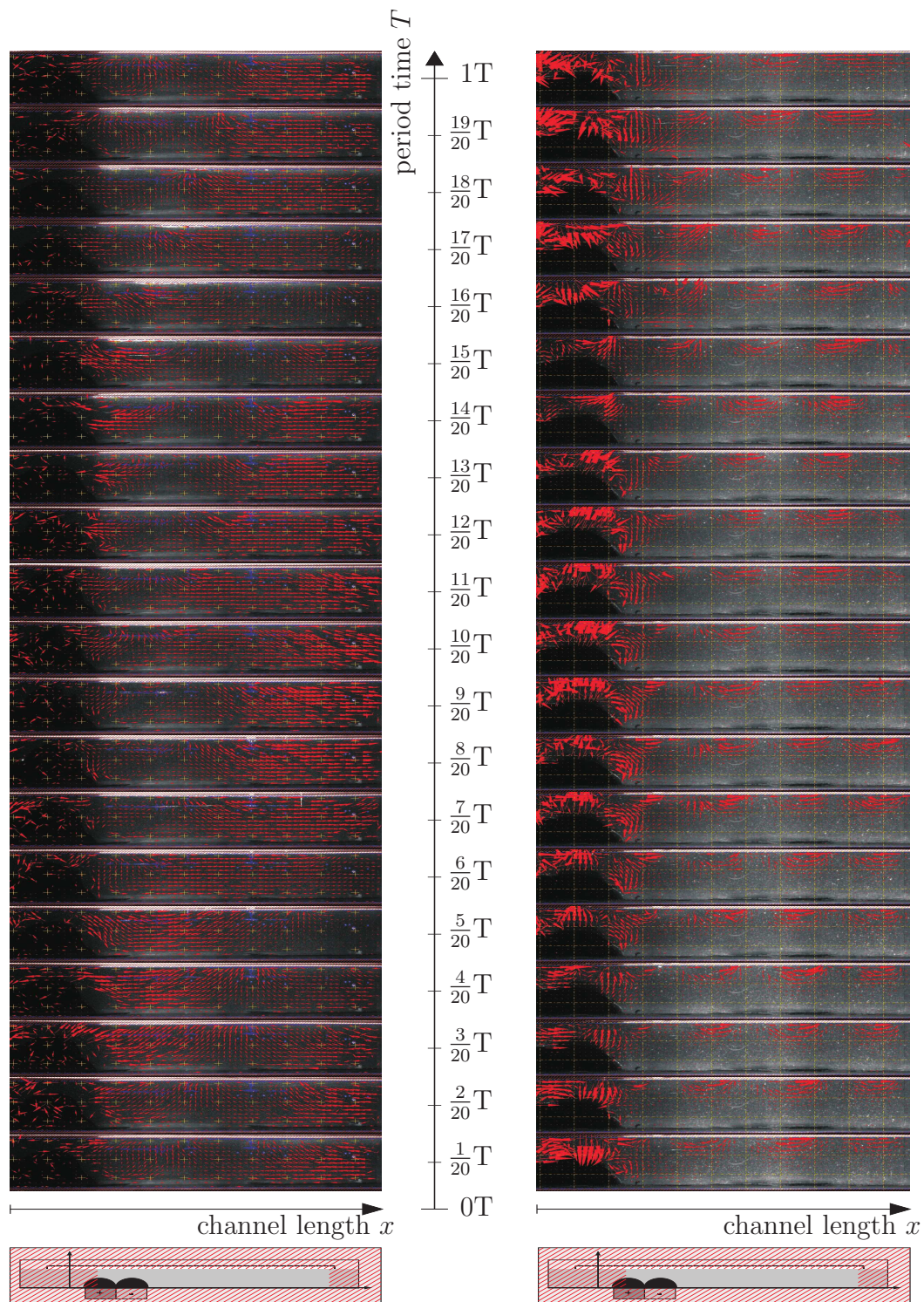
The excitation with 2 Hz creates an oscillation as well as surface waves running along the channel length. The PIV plot shows that these modes engage the complete fluid height and resemble garland-shaped waves, as figure 5.7(a) shows. The excitations given by 10 Hz and 16 Hz produce oscillation and wave formations, too. For comparison see figure 5.7(b). The expansion depth diminishes with higher frequencies. But only these frequencies produce the desired duct channel flow. A similar observation have been made by using swimming surface markers.

The frequencies, at which clear oscillations or a duct flow are generated, are naturally dependent on the periphery. This includes the container, the channel walls, both glued onto the ground plate, the ground plate, the permanent and electromagnets and its core. Mi-

5.3. Analysis and Discussion of the Results

nor modification of these parts prior to or during their assembly will shift the effective frequencies slightly. The maintenance of the asymmetry is most important for the function. Thus, the presented results are only valid for the presented container design (including dimensions and materials). However, this experiment, which belongs to the fluid mechanics, exhibits phenomenons known from the mechanics of rigid body systems. There, an accordant system would be classified as a damped, forced vibration system with excitation at the mass. The frequencies causing resonant effects in an oscillating rigid body system are eigenfrequencies. They cause similar effects, as witnessed within the flow experiment, like the fundamental oscillation (similar to the reciprocal motion through the length of the pool) and superposing harmonic oscillations, which are known to cause changes of the direction within rigid body systems.

5. Applicational Study on a Bifluidic Flow Channel



(a) $f = 2$ Hz.

(b) $f = 16$ Hz.

Figure 5.7.: *Traveling flow modes of different excitation frequencies, unshaded area in sketches typifies area of vector plots.*

6. Forces for Ferrofluid Based Locomotion

6.1. Forces Generated by Ferrofluid for Passive Locomotion

Newtons well known statement, a body remains either in calm or in steady translation, as long as external forces do not force it to change its state, is essential for ferrofluid based locomotion, too. For this reason, the available active and constraining forces, which lead to motion and locomotion in ferrofluid operation, shall be examined within this section. Section 6.1 concerns the forces required for systems, where the local motion of the ferrofluid portion enables another object (or fluid) to perform locomotion. Section 6.2 presents the required forces for ferrofluid portions to change their position (to achieve locomotion).

A locomotion scenario of a ferrofluid layer representing a magnetizable environment or surface is considered. It completely fills a shallow pool, see figure 6.1(b). Due to space constriction the subjacent electromagnets (EMs) are aligned in two layers, see figure 6.1(c). By the application of a local and inhomogeneous external magnetic field, limited areas of ferrofluid gather around and deform its surface. By a temporally controlled sequence, this mechanism is used for the motion of a secondary object. We call the object transport due to manipulation of the contact area of the suspending plane a 'passive locomotion system'.

As we are focusing on the means of locomotion rather than on the phenomenons taking place within the ferrofluids, we consider the more simple approach; exposed to an external magnetic field, a surface force appears at the permeable interface between fluid and air.

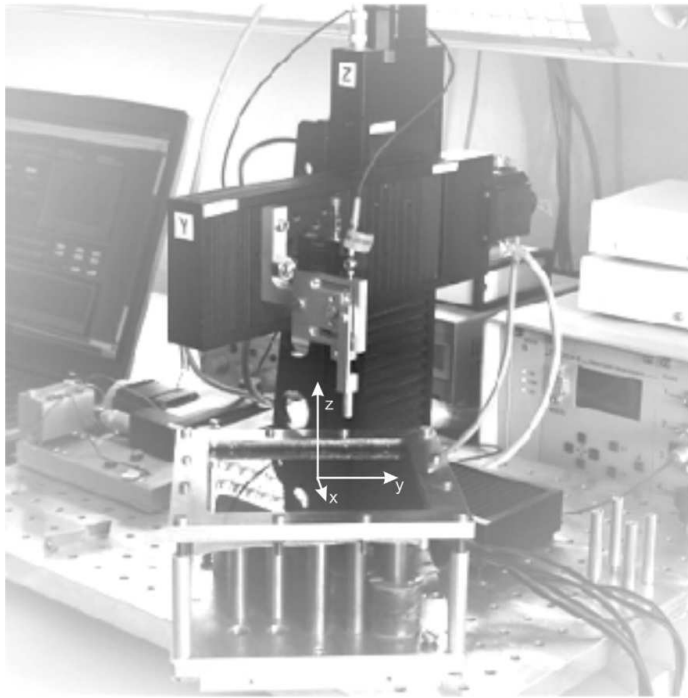
6. Forces for Ferrofluid Based Locomotion

Instead of recording a force, the measurement is translated in a pressure data acquisition. When in contact to each other, the interface of the ferrofluid and an object is an area, indeed. As surface load of an ferrofluid is a normal force, it is consequent to interpret pressure. [Pop06] identifies driving and buoyant forces for object carrying and friction reduction tasks by extensive series of measurement. Of interest is the spatial pressure distribution, horizontally (x - y -plane) and vertically (z -axis) sited, caused by a temporally steady (static) magnetic field.

In a first approach the magnetic field of a single electromagnet and of the transition between two neighboring electromagnets is investigated. The data acquisition is performed for the steady field, only the vertical pressure component is recorded, see figure 6.1(e). The effects of temporally and locally changing (dynamic) magnetic fields, successively activating two or more consecutive electromagnets, are analyzed in a second series. Here, spatial and temporal pressure distribution and its transition between magnet positions are monitored. For this dynamic classification we obtained data of the horizontal and vertical pressure components, see figures 6.1(d) and 6.1(e). The measurements were accomplished with the pressure dependent on the electric current I due to its easier measurability.

Figures 6.1(e) and 6.1(d) show parallel springs. The actually recorded quantity was the displacement of the spring, which was translated into a pressure (elastic force per area of the probe). A detailed explanation of this measuring technique is given in section 2.3. The spatial resolution of the resultant pressure (or serviceable forces) depends on the size of the chosen contact piece. The obtained data are influenced by the displacement of the spring, as the originally intended measurement position and the actual do not coincide with each other. Those errors have been minimized by highly spring rigidity. A detailed discussion of the occurring errors is given in [Pop06].

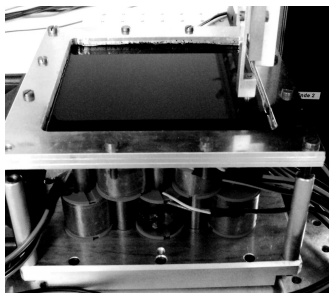
6.1. Forces Generated by Ferrofluid for Passive Locomotion



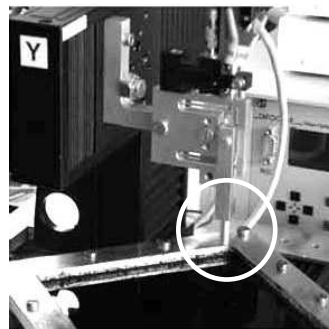
(a) Complete setup with positioning system for the probes and the global coordinate system.



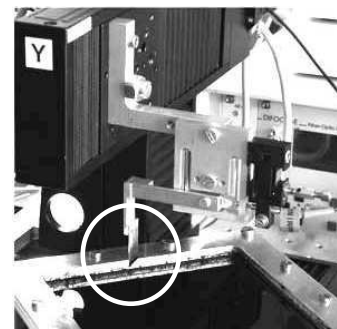
(b) Top and bottom layer of EMs.



(c) Ferrofluid pool with adjacent EMs.



(d) Parallel spring with adapter for vertical pressures.



(e) Parallel spring with adapter for horizontal pressures.

Figure 6.1.: Experimental setup, pressure measurement with a parallel bending spring [Pop06].

6. Forces for Ferrofluid Based Locomotion

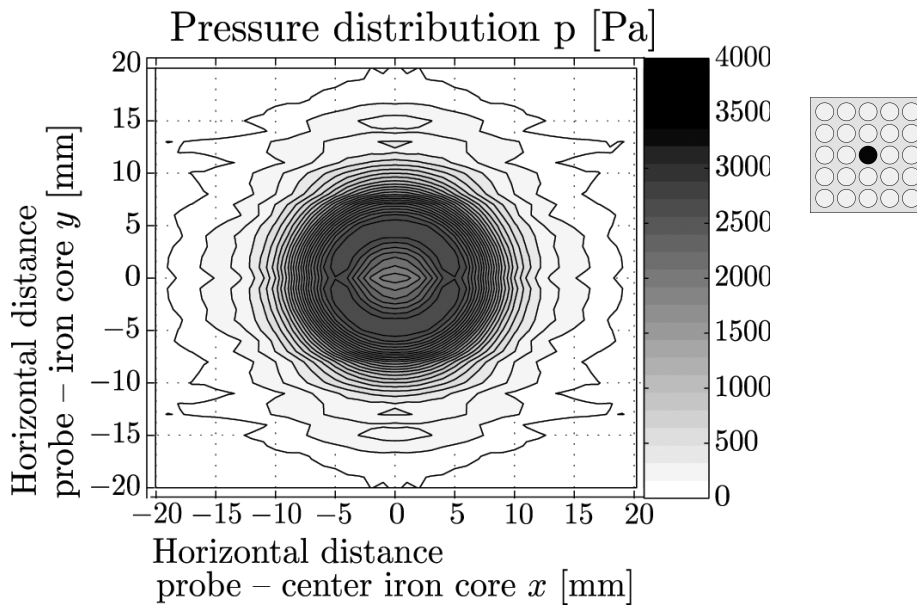


Figure 6.2.: Pressure distribution generated by a single solenoid configuration (probe diameter 5 mm, vertical distance probe - solenoid $z = 1$ mm) [Pop06].

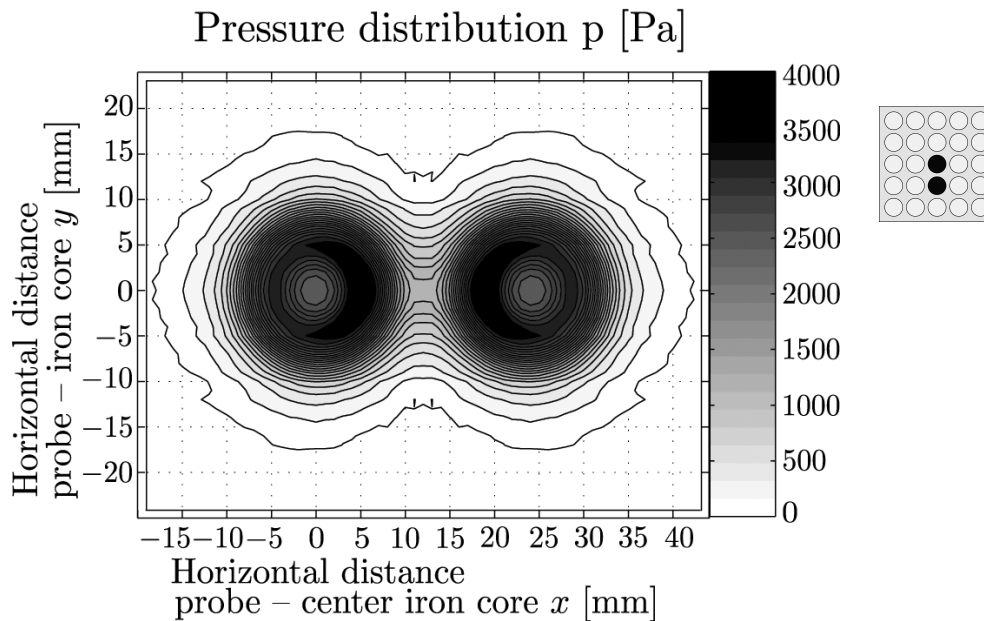


Figure 6.3.: Pressure distribution generated by a solenoid pair with opposite polarization (probe diameter 5 mm, vertical distance probe - solenoid $z = 1$ mm) [Pop06].

6.1. Forces Generated by Ferrofluid for Passive Locomotion

The initial (vertical) pressure distribution is shown in figures 6.2 and 6.3. The diagram provides a vertical pressure of $p = 2500$ Pa directly above the iron core. As an example, the magnetic force suffices to carry lightweight objects of approximately 5 g (on an area of 19.6 mm^2). But it is possible to elevate slightly heavier and bigger objects, too. The mass, then, can be better distributed. The alteration of the distribution and maximum values of the pressure due to condition modification is discussed in the following.

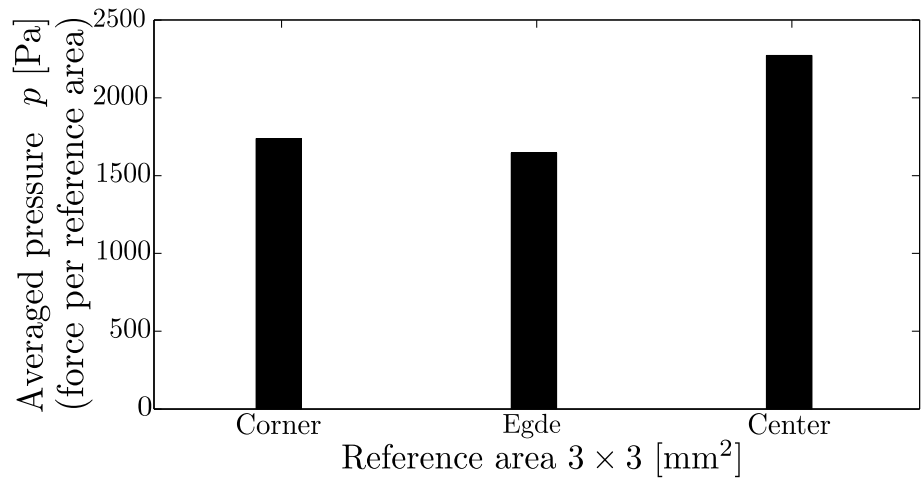


Figure 6.4.: Comparison of vertically directed pressure at center, boundary and corner position, pressure averaged over a reference area of $3 \times 3 \text{ mm}^2$.

With the change of position in mind, we investigated whether the place within the pool interferes with the pressure amount. Compared are the positions in the center, at the rim and in the corner, see figure 6.4. Recorded is a vertically directed average pressure. The probe moved over a vertically reference area, spanned between axial and radial direction of the iron core, the starting point was in the center of the upper core surface. The boundary positions reach a pressure of approximately three quarters of the center, while the difference between the boundary points is marginally. The reason for this behavior should be by the hindered accumulation of ferrofluid at the edge instead of the all-side accessibility in the middle.

6. Forces for Ferrofluid Based Locomotion

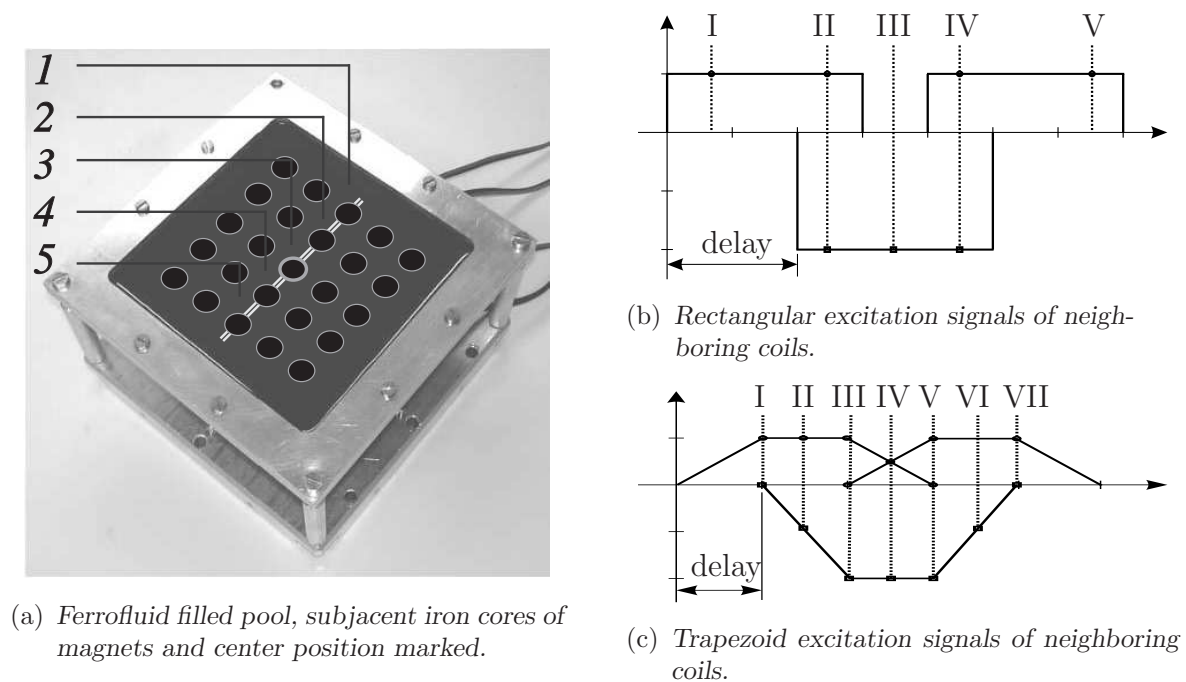


Figure 6.5.: Measurement of ferrofluid generated pressure along marked line of neighboring EMs.

In a next step, the capability of carrying objects across the pool surface was investigated. First measurement series regarded the static and vertical pressures, which are available along a straight path between three neighboring electromagnets, see figure 6.5(a), positions 2–3–4. A trapezoid and a rectangular signal set have been applied to the indicated magnets, see figures 6.5(b) and 6.5(c). The resulting vertical pressure values however do not differ spatially, see figures 6.7(a) and 6.7(b). The transitions are smoother by a trapezoid signal.

When excited by a spatio-temporally changing magnetic field, the absolute (vertical) pressure values of trapezoid or rectangular signals reach a maximum of 1600 Pa, see figures 6.8(b) and 6.9(b). The differently shaped high levels of the vertical pressure, compare figures 6.8(c) and 6.9(c), may benefit different driving strategies for object motion.

A delay variation between the excitation signals of two consecutive solenoids have less influence on local pressure accumulation than temporally jolted or dilated impulses, which, again, are a basic property

6.1. Forces Generated by Ferrofluid for Passive Locomotion

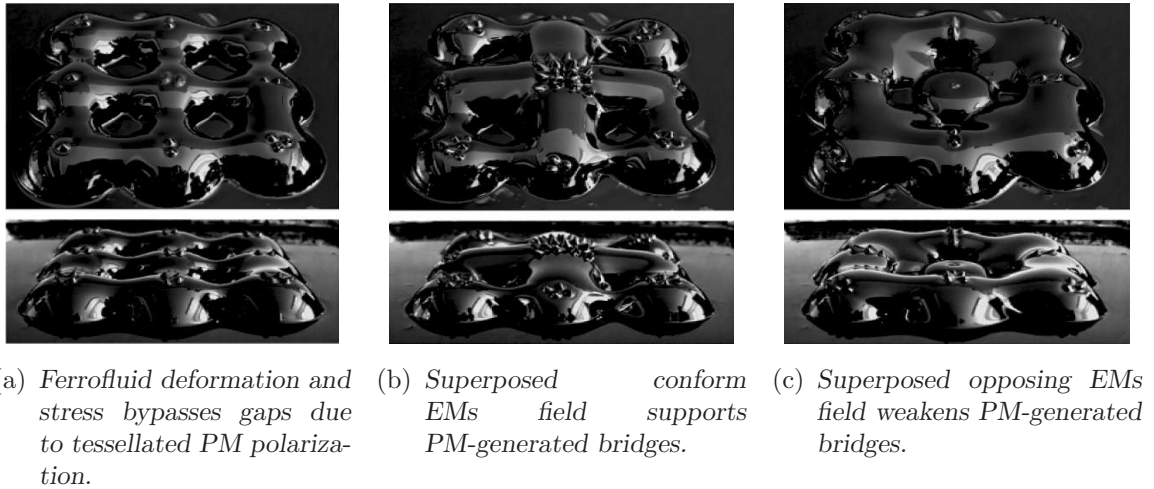


Figure 6.6.: Visualization of field-induced stress of ferrofluid by corresponding deformation, PMs induce primary stress [Pop06].

on motion planning. Presumably, the locomotion of an object across the length of the pool cannot be achieved in a single stroke, due to the pressure drop to nil between the solenoid positions. But locomotion by several strokes is realistic.

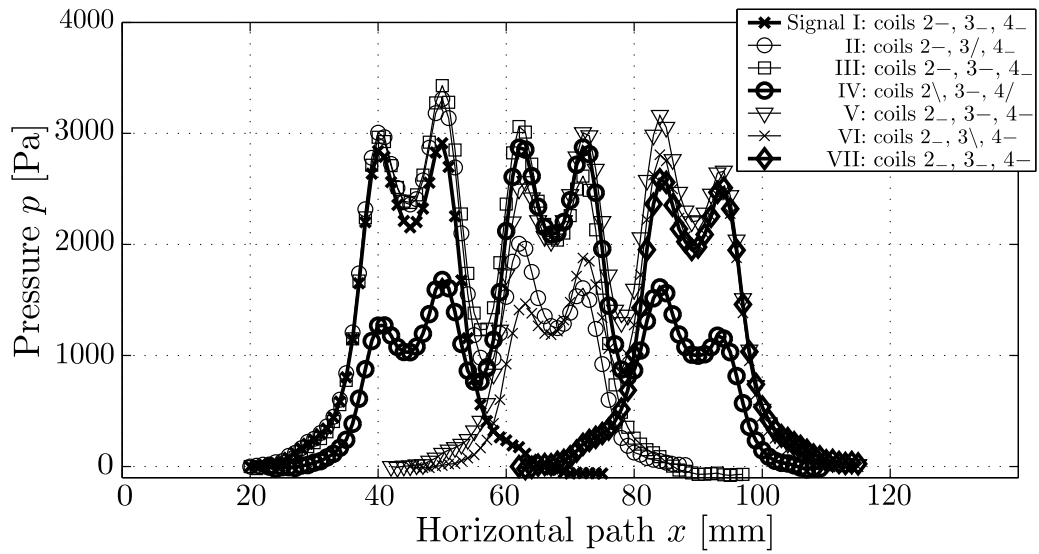
Potential arrangements to bridge the solenoid–solenoid distance include the introduction of assisting magnetic fields generated by permanent magnets. The steady magnetic field can support the limited values of the driving magnetic fields by superposition and extend their reach. The alignment of these prestresses has to ensure opposing polarization of neighboring permanent magnets. In this case, magnetic field lines close between and bridge two solenoid positions. The reverse case would result in a field-free space without any supporting function. Figure 6.6 illustrate a prestressed ferrofluid with and without additional influence of superposing EMs.

Horizontal driving pressures can only be examined in the dynamic process. Here, the rectangular excitation leads to higher pressure peaks (horizontal, 210 Pa) than the (slighter) trapezoid signal (180 Pa) due to a higher acceleration gradient, see figures 6.10 and 6.11. The difference comes up to 14.3%. The horizontal pressures reach a maximum of 11.25 to 13.1% of the maximal available vertical pressure (1600 Pa, dynamic excitation). Thus, the actual driving is accomplished by horizontally directed pressure or forces, while the vertically directed pressures have

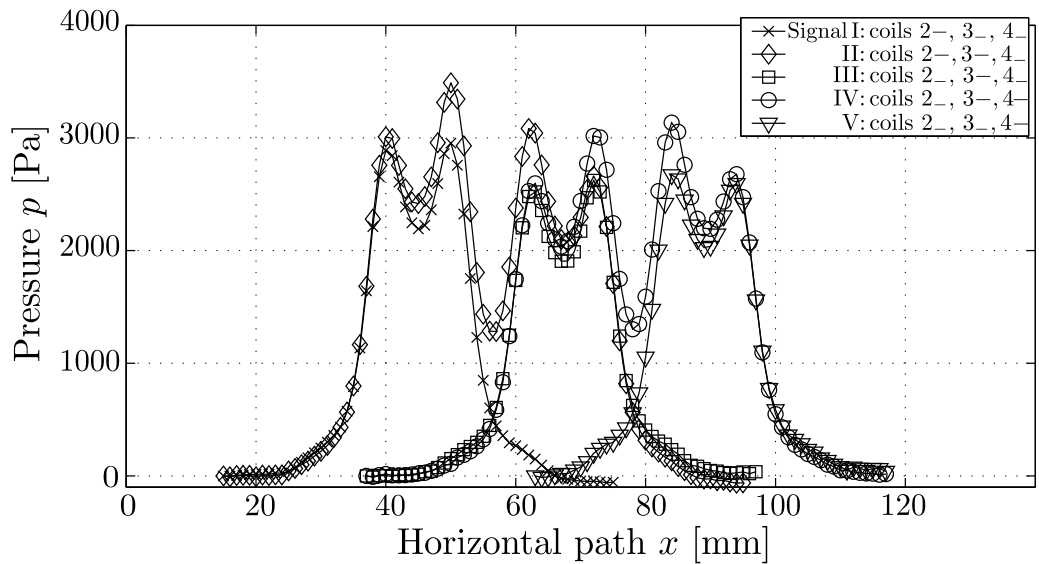
6. *Forces for Ferrofluid Based Locomotion*

to lift the object. Locomotion with those pressures or forces, respectively, is possible. But it is realistic only for very light bodies. With increasing mass more strokes (of the EMs line) will be necessary up to a critical combination of mass and size of the contact area, where the available forces of the passive locomotion system will fail.

6.1. Forces Generated by Ferrofluid for Passive Locomotion



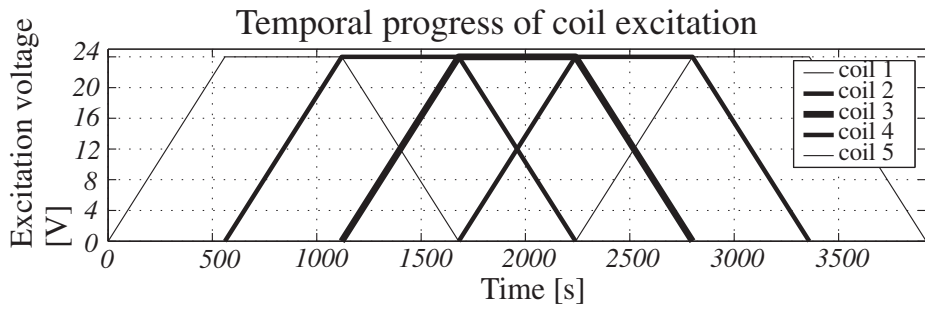
(a) Trapezoid excitation signal.



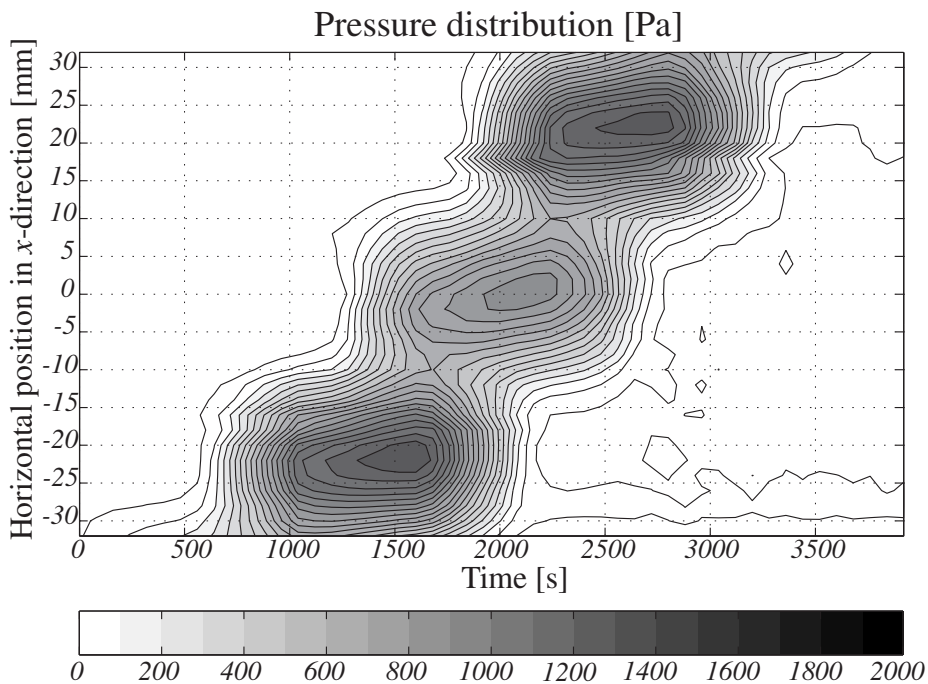
(b) Rectangular excitation signal.

Figure 6.7.: Vertical pressure along horizontal length x , (probe diameter 5 mm, vertical distance probe – solenoid $z = 1$ mm), steady state [Pop06].

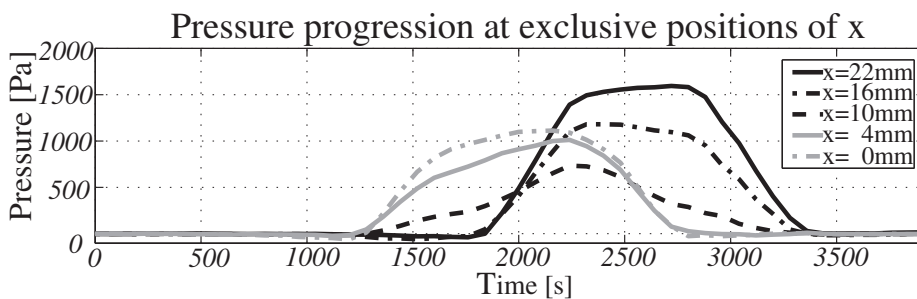
6. Forces for Ferrofluid Based Locomotion



(a) Excitation voltage.



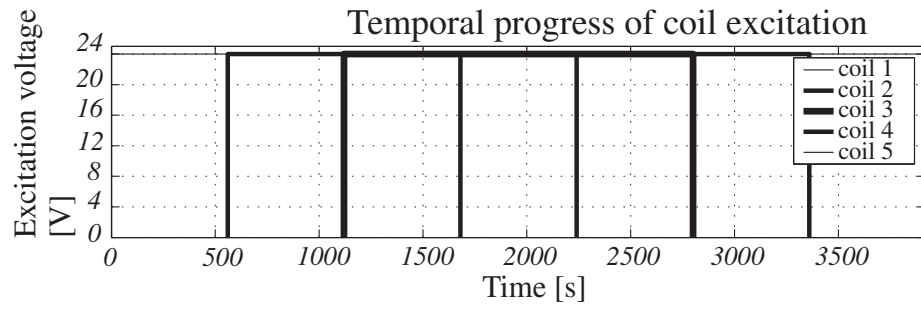
(b) Pressure distribution.



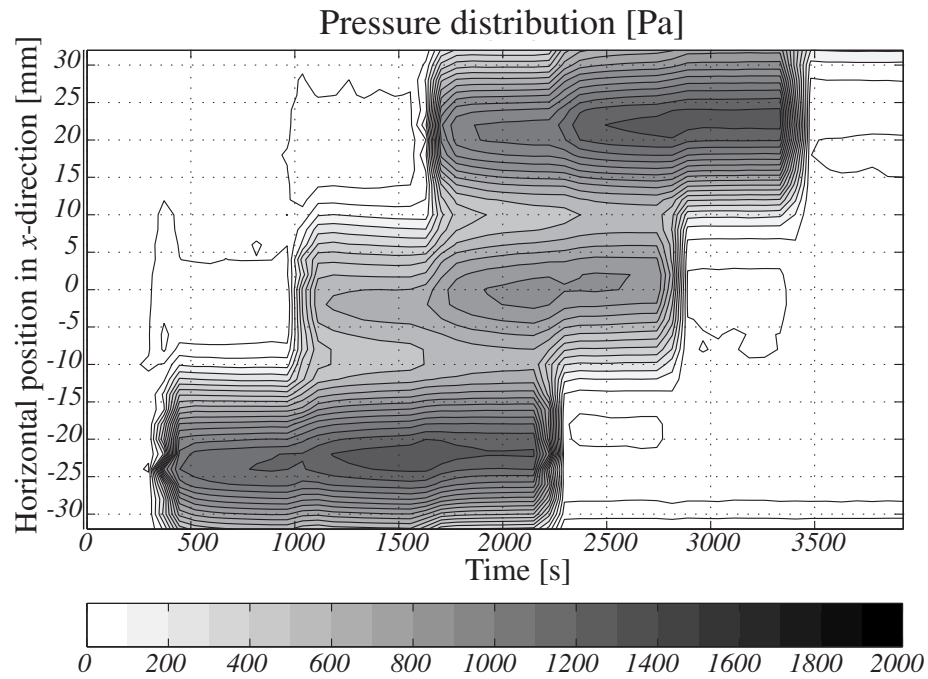
(c) Pressure progression.

Figure 6.8.: Set of diagrams: vertical pressure in center row trapezoid voltage signal, delay $v = 10$ units ground distance $z = 1$ mm probe diameter $d = 12$ mm [Pop06].

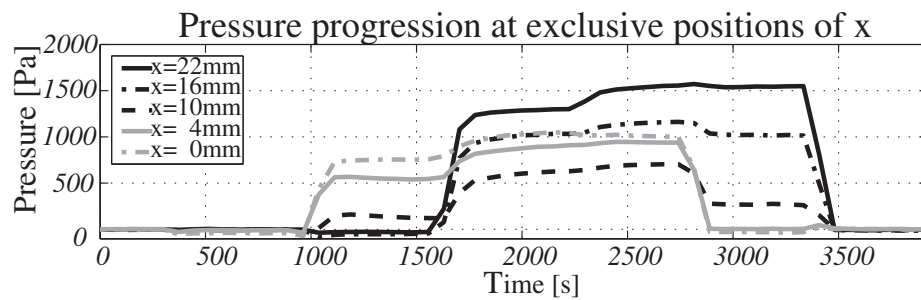
6.1. Forces Generated by Ferrofluid for Passive Locomotion



(a) Excitation voltage.



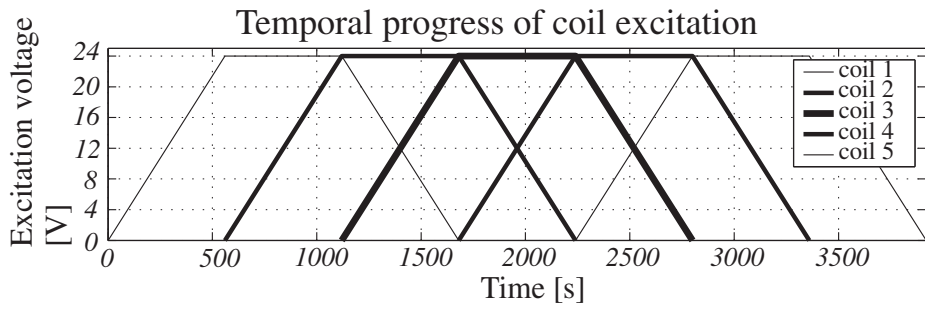
(b) Pressure distribution.



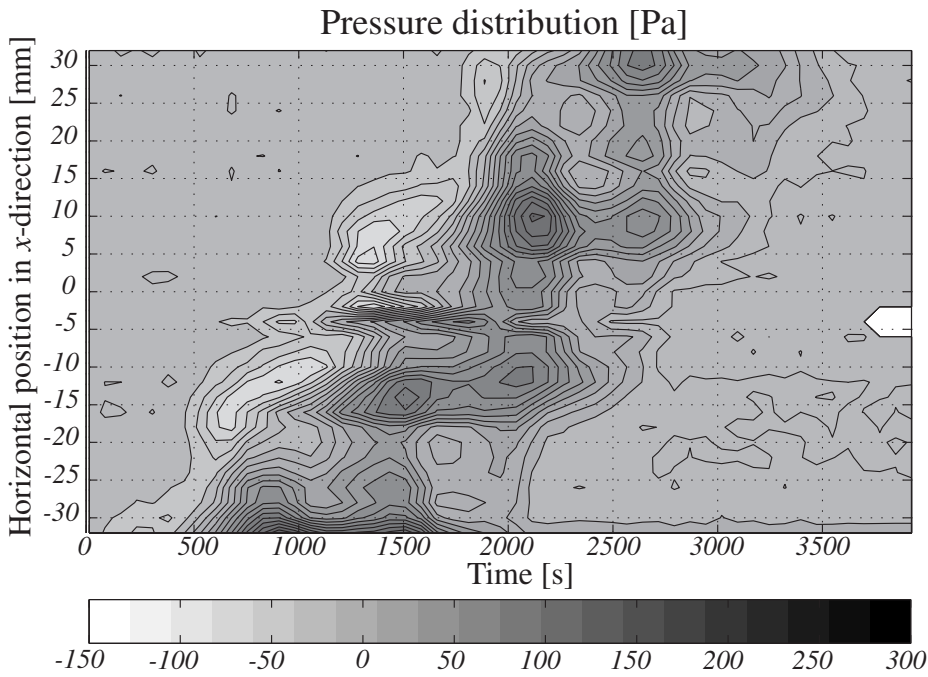
(c) Pressure progression.

Figure 6.9.: Set of diagrams: vertical pressure in center row
rectangular voltage signal, delay $v = 10$ units
ground distance $z = 1$ mm
probe diameter $d = 12$ mm [Pop06].

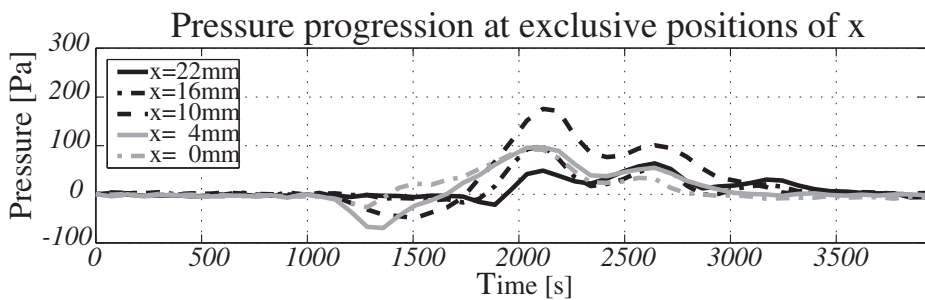
6. Forces for Ferrofluid Based Locomotion



(a) Excitation voltage.



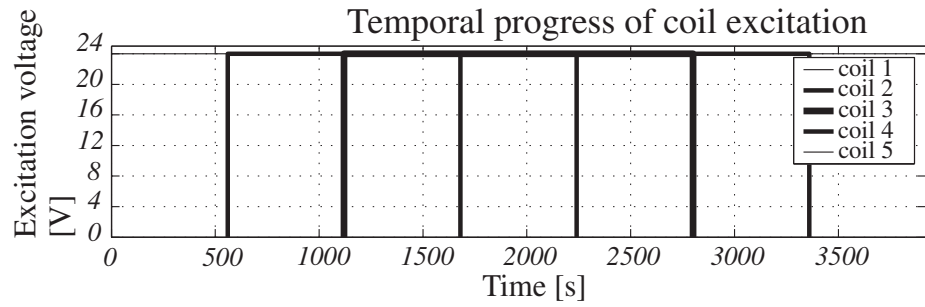
(b) Pressure distribution.



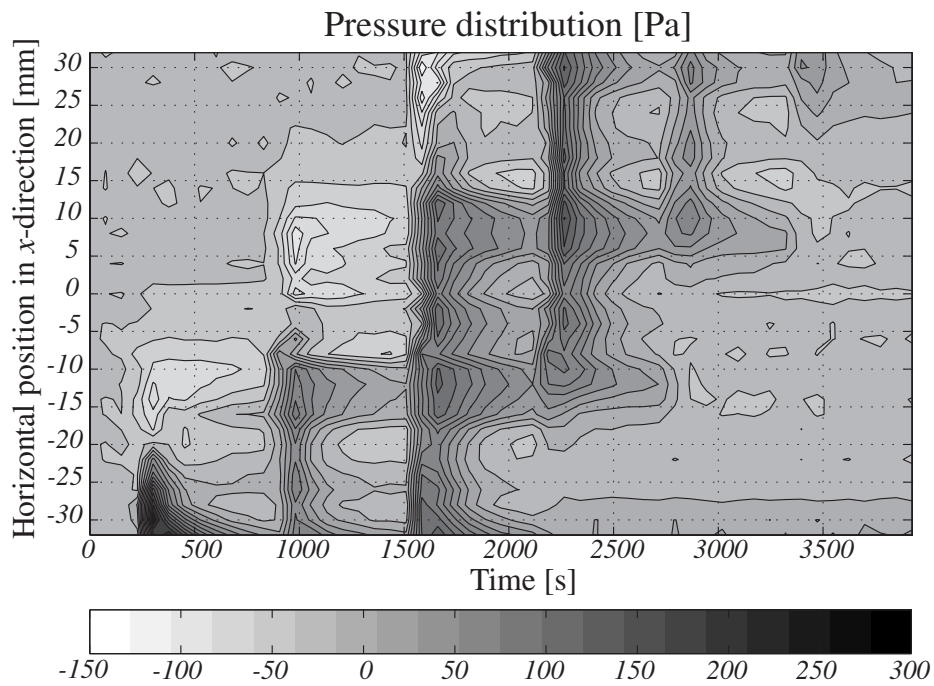
(c) Pressure progression.

Figure 6.10.: Set of diagrams: horizontal pressure in center row
trapezoid voltage signal, delay $v = 10$ units
ground distance $z = 1$ mm
probe reference area $A = 12 \times 8 \text{ mm}^2$ [Pop06].

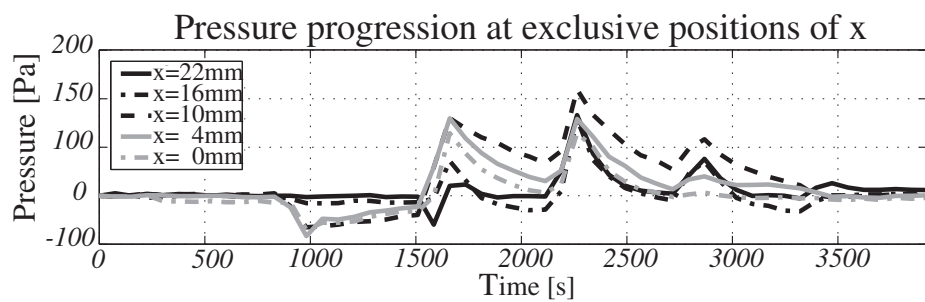
6.1. Forces Generated by Ferrofluid for Passive Locomotion



(a) Excitation voltage.



(b) Pressure distribution.



(c) Pressure progression.

Figure 6.11.: Set of diagrams: horizontal pressure in center row
 rectangular voltage signal, delay $v = 10$ units
 ground distance $z = 1$ mm
 probe reference area $A = 12 \times 8$ mm² [Pop06].

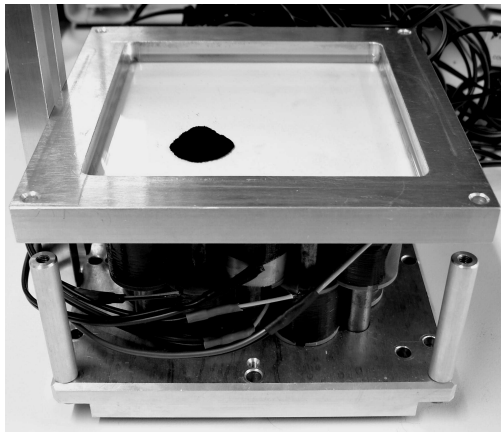
6.2. Forces on Ferrofluid in Active Locomotion Systems

Continuative to an actively controlled suspension (made of ferrofluid), which can pass bodies from point to point, (*passive locomotion system*), we consider a single droplet or a swarm of delimited ferrofluid entities traveling their routes. In contrast to a *passive locomotion system*, this may be called an *active locomotion system*.

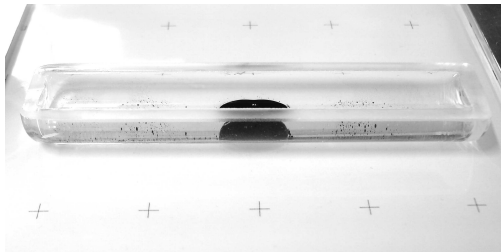
Each motion or locomotion requires a driving force. Thus, we consider the matter of these driving forces and the preceding magnetic fields in this section and put them in relation to their application. The idea of *active locomotion systems* may be developed further into manipulation systems, where one ferrofluid entity or a swarm of droplets is used for the positioning of impassive solid objects (by pushing). For applications like this or other imaginable solutions, two concepts may be followed: discrete and continuous repositioning of the ferrofluid droplet(s). The discrete moving ferrofluid unit passes from point to point, while the target point is the position of a subjacent magnet. The advanced type aims at a continuous positioning from and to arbitrary points or routes. Both versions require a control system. In our case, the control system comprehends an actuator, which is the power control element, the process including electromagnets, ferrofluid and physical operation area, the feedback is provided by optical elements (a camera or a photoelectric barrier, respectively). While the desired quantity is the position of the ferrofluid unit and the electrical current works as correcting variable, the magnetic flux and the magnetic force are the intermediate and required links.

An accompanying experimental setup assists the analytical and numerical calculation of magnetic field and derived driving forces. In the first approach, the analysis concentrates on the discrete bidirectional motion within a channel or a straight line, see figure 6.12. The subjacent electromagnets are aligned next to each other in separate layers due to the limited space. Practical aspects made us to suspended the ferrofluid droplet within its container in a secondary carrier fluid, which reduces friction and adhesion between ground and droplet. This simple

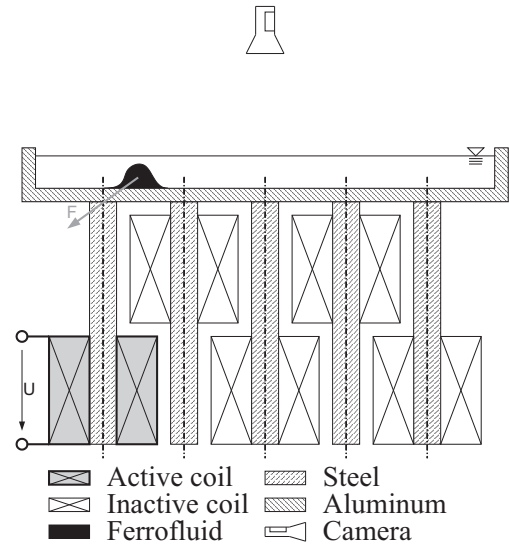
6.2. Forces on Ferrofluid in Active Locomotion Systems



(a) Pool for planar positioning.



(b) Channel for bidirectional positioning.



(c) Arrangement of a control system.

Figure 6.12.: Setup of locomotion system with controlled positioning of ferrofluid entity, experimental view and functional drawing [Gre07].

design assists the primary understanding of the acting tangential and normal forces. Analytics and finite element (FE) simulations of the magnetic field and the subsequent forces are prepared and compared. Concept, calculation, measurements and analysis have first been described in [Gre06, Gre07] and [Gre08].

The considered model comprises the approximation of the ferrofluid unit as point mass. This goes along with the assumptions that all forces charge at the center of mass, distortions are neglected, the fluid volume is small, thermic influence is neglected, too. We do not consider induction by the ferrofluid within the solenoids. Since velocities are generally small, we ignore interfering flows (within the moving ferrofluid or superseded secondary fluid, glycol). Therefore, friction is included into the model in form of a damping constant proportional to velocity.

6. Forces for Ferrofluid Based Locomotion

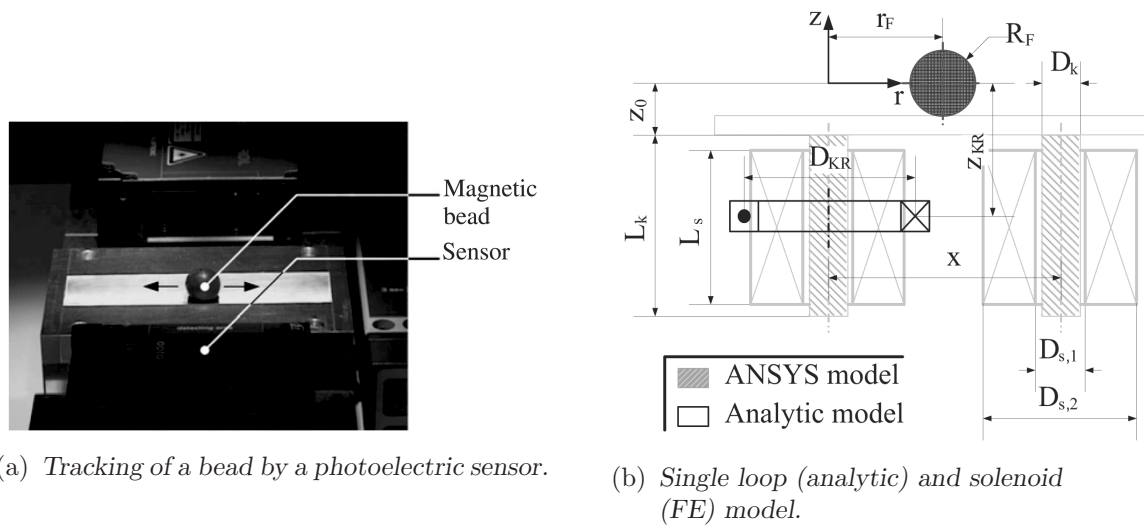
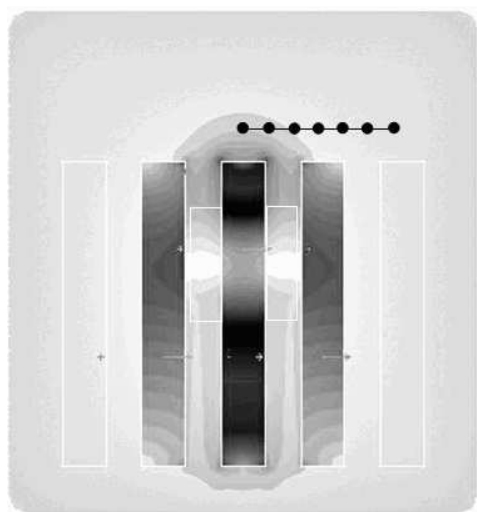


Figure 6.13.: *Alternative setup referring to a model of position control of a steel bead, functional scheme includes analytic and numeric model drawing [Gre10b].*

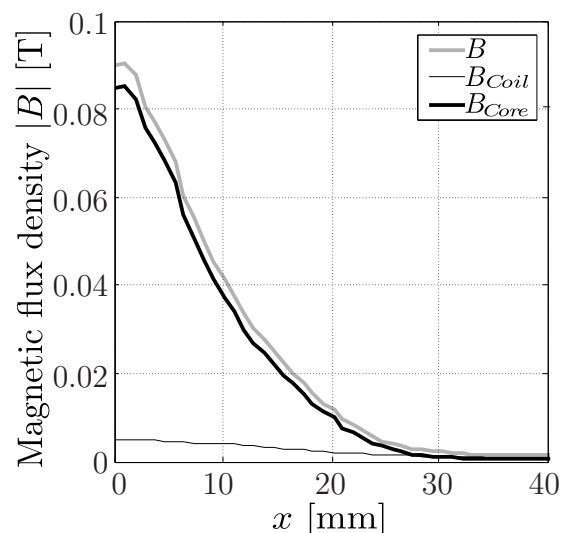
These abstractions lead to a more simple model and experimental arrangement, where the ferrofluid unit is replaced by a steel bead. The new model is used for the general analysis of the interaction of electrical and magnetic circuit due to simplicity; its experimental implementation is more suitable for tests of continuous positioning. The representation of the moving point mass is sufficient, although friction conditions are different and permeability is higher. The supplement helps to verify the suitability of the mentioned assumptions. Figure 6.13 shows the accordant development of the bidirectional track with steel bead and position sensor and the drawings on which the model of the analytics and FE simulation are based.

Due to the unknown friction, the determination of the steady force on a permeable body within the magnetic field is difficult by measurement. Therefore, the identification is achieved by analytical approximation (stationary case), the results of which must be verified by numerical methods. The parameters found by model based optimization are used to fit numerical and analytical graphs.

6.2. Forces on Ferrofluid in Active Locomotion Systems



(a) Magnetic field distribution, finite element simulation.



(b) Total (absolute value) magnetic field along drawn path including components of core and solenoid.

Figure 6.14.: FE calculated magnetic field of a solenoid ($I = 1\text{ A}$) [Gre07].

A realistic and precise modeling suggests the consideration of the iron core equipped solenoid. This procedure is very complex, because the magnetic field of solenoids is highly inhomogeneous. The simulation via FE method in figure 6.14(a) indicates this.

The field consists of components contributed by the solenoid and by the iron core. The iron core amplified field is not only considerably higher than the fraction from the solenoids, which can be seen in figure 6.14(b), but the amplification factor is non-linear. However, the effect of the iron core in the far field is considered to be a constant amplification. The reasons for this decision is given by empiricism – the ferrofluid droplet operates within the distant field, indeed. Naturally, the assumption goes along with reduced field distortion. The parameter optimization enhances the precision of the field and force calculations (by analytics and FE method). Their matching is verified by comparison. Thus, the approximation of the electromagnet as a single current loop yields reliable results, that are sufficiently precise purpose given. On the contrary, advanced information about the near region of the electromagnet are neither possible to acquire, nor are

6. Forces for Ferrofluid Based Locomotion

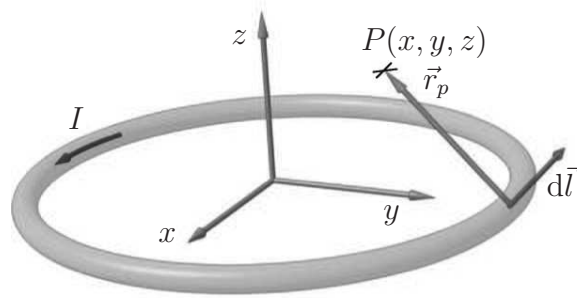
they required. [Gre06] contains a detailed documentation of the modeling of an air-filled solenoid. Analytical and numerical descriptions of a single current loop and of a long cylindrical coil and the subsequent comparison of both conclude in realistic results.

Analytics

The magnetic field of a current loop is described by the BIOT-SAVART law. The geometry is depicted in figure 6.15. The vector of the electric current I is tangentially directed within the loop. Equation (6.1) presents the magnetic field in point $P(r, \phi, z)$

$$d\mathbf{H} = \frac{I}{4\pi} \frac{d\mathbf{l} \times \mathbf{r}_p}{r_r^3}. \quad (6.1)$$

The assumptions of a linear, temporally constant current and a closed geometry have to be kept.



I	Electric current of the loop ($w \cdot I_{sp}$)
x, y, z	Cartesian coordinates
$d\vec{l}$	Direction of current flow
\vec{r}_p	Position vector of point $P(x, y, z)$

Figure 6.15.: Electric current loop of the BIOT SAVART law [Gre06].

The line integral of (6.1) produces

$$H_r = \frac{I}{4\pi} \int_0^{2\pi} 2\pi \frac{R_{KR} z \cos(t)}{(z^2 + R^2 + r^2 - 2r R_{KR} \cos(t))^{3/2}} dt \quad (6.2a)$$

$$H_z = \frac{I}{4\pi} \int_0^{2\pi} \frac{R_{KR}^2 - R_{KR} r \cos(t)}{(z^2 + R_{KR}^2 + r^2 - 2R_{KR} r \cos(t))^{3/2}} dt. \quad (6.2b)$$

6.2. Forces on Ferrofluid in Active Locomotion Systems

To elude solving the elliptical integrals resulting from (6.2), but to yield closed solutions, TAYLOR series are developed. Thus, we gain the magnetic field strength of one current loop

$$H_r \approx \frac{3}{2}I \frac{R_{\text{KR}}^2 z r}{z^2 + (R_{\text{KR}} - r)^2} \frac{1}{(z^2 + (R_{\text{KR}} + r)^2)^{3/2}} \quad (6.3a)$$

$$H_z \approx \frac{1}{2}I \frac{R_{\text{KR}}^2 (z^2 + R_{\text{KR}}^2 + R_{\text{KR}}r - 2r^2)}{z^2 + (R_{\text{KR}} - r)^2} \frac{1}{(z^2 + (R_{\text{KR}} + r)^2)^{3/2}}. \quad (6.3b)$$

The field of a circular ring conductor may be assumed to represent the distant field of a more complex cylindrical solenoid. Information about the near field cannot be reproduced by this description in a sufficient quality. We take (6.3) and the relation to the magnetic flux to obtain the force acting on the ferrofluid portion. With the magnetic dipole being constant, the force is defined as

$$\mathbf{F}(r, \phi, z) = \nabla (\mathbf{m} \cdot \mathbf{B}) \approx \frac{1}{\mu_0} (\mathbf{m} \nabla) \mathbf{B} \quad \text{with} \quad \nabla \mathbf{m} = 0. \quad (6.4)$$

For a superparamagnetic material, the permeability can be expressed as a function of the magnetic field density, see [Gij04]. Assuming a mean relative permeability, the force on the ferrofluid can be calculated depending on the volume V and the magnetic field density B

$$\mathbf{F}(r, \phi, z) = \frac{\chi V}{\mu_0} (\mathbf{B} \nabla) \mathbf{B} \quad (6.5)$$

$$\mathbf{F}(r, \phi, z) = \frac{\chi V}{\mu_0} \left(B_r \frac{\partial}{\partial r} + B_\phi \frac{\partial}{r \partial \phi} + B_z \frac{\partial}{\partial z} \right) (B_r + B_\phi + B_z)^T. \quad (6.6)$$

From this, the force components in radial and axial direction can be found

$$F_r = f_0 r R_{\text{KR}}^4 \frac{S u_r}{\left((z - R_{\text{KR}})^2 + r^2 \right)^2 \left((z + R_{\text{KR}})^2 + r^2 \right)^4} \quad (6.7a)$$

6. Forces for Ferrofluid Based Locomotion

$$F_z = f_0 z R_{KR}^4 \frac{Su_z}{\left((z - R_{KR})^2 + r^2\right)^2 \left((z + R_{KR})^2 + r^2\right)^4} \quad (6.7b)$$

$$\text{with } f_0 = -\frac{3}{4} I^2 \alpha V \mu_0 \chi, \quad (6.7c)$$

$$Su_r = z^4 + 2r^4 - R_{KR}^4 + 3R_{KR}r^3 - 3R_{KR}r - 2R_{KR}^2r^2 + 3r^2z^2 + 7rz^2R_{KR},$$

$$Su_z = z^4 + 2r^4 + R_{KR}^4 + 4rR_{KR}^3 + 5r^2R_{KR}^2 + 3r^2z^2 + 2z^2R_{KR}^2 + 4rz^2R_{KR}.$$

For qualitative values of the magnetic force, the geometry of the current loop and the amplification by the iron core need to be inserted. The quantities radius of the current loop R_{KR} , distance from the current loop $z = z_{KR}$ and the amplification factor α are the effecting parameters for numerical calculation. By fitting the analytical results with numerical calculations accomplished by the FE method, these parameters are optimized. The optimization is not a rigid process, amplitudes of the forces may be altered. Thus, the optimization function depends on

$$F_r(r, z) = \tilde{\beta}_r f_0 \tilde{F}_r(r, z_{KR}, R_{KR}) \quad (6.8a)$$

$$F_z(r, z) = \tilde{\beta}_z f_0 \tilde{F}_z(r, z_{KR}, R_{KR}). \quad (6.8b)$$

FE-Model

For verification of the analytically obtained results and optimization of the free parameters, a FE model based calculation is used aiming for a realistic reproduction of the force function $F(r)$. The model is implemented within the simulation environment *ANSYS* by ANSYS, Inc. It is based on the geometric data given by design, see figure 6.16(a). The electromagnetic parameters are given by table 6.1, except for the number of windings. The latter is found by (6.9)

$$w = \sqrt{R_{coil} \frac{\kappa_{Cu} (D_{coil2} - D_{coil1}) L}{\pi (D_{coil2} + D_{coil1})}}. \quad (6.9)$$

The optimization of the parameters R_{KR} and z_{KR} requires a function of the force. This is obtained by calculation of the force progression for a fixed radial position. Here, the force refers to the center of mass of the

6.2. Forces on Ferrofluid in Active Locomotion Systems

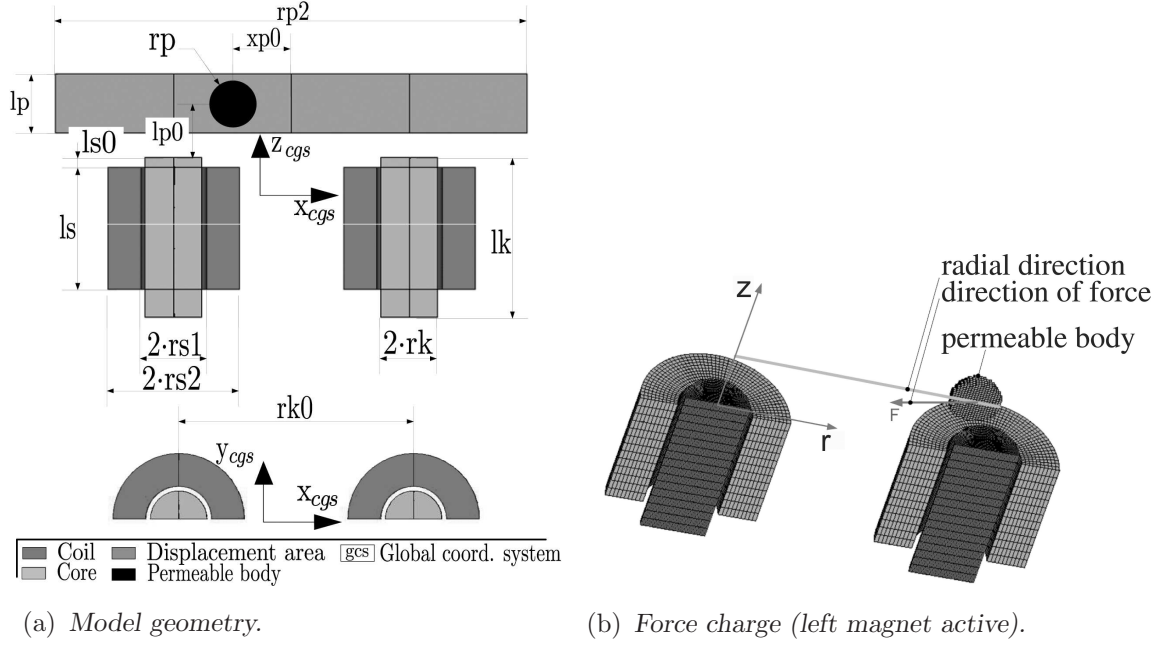


Figure 6.16.: Model and numerical force calculation with ANSYS [Gre06].

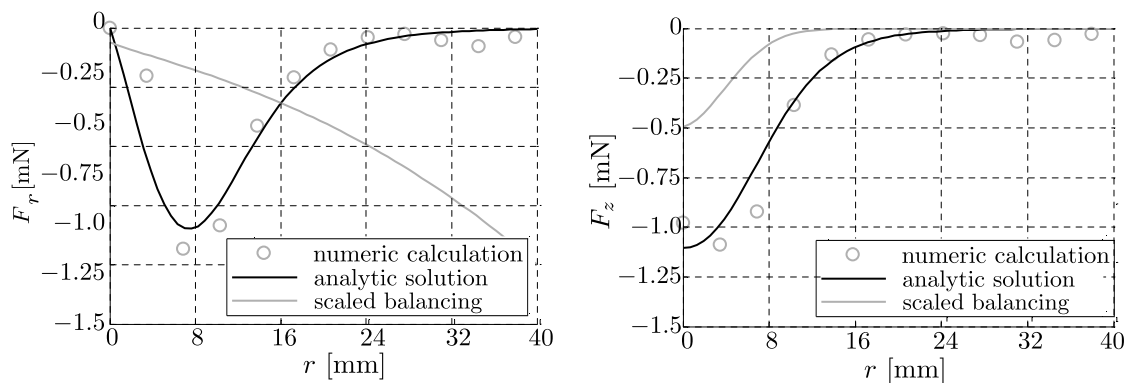
Table 6.1.: Parameters for the calculation of the forces on the ferrofluid portion.

Notation	Parameter	Value
Electric current	I [A]	1
Number of windings	w []	1230
Vertical distance iron core - ferrofluid	z_0 [mm]	8
Force density	f_0 [Nm ³]	2.6×10^{-5}
Relative permeability of ferrofluid	$\mu_{r,FF}$	$\mu(H)$
Relative permeability of iron core	$\mu_{r,EK}$	1000
Radius of current loop	R [mm]	6.5
Vertical distance current loop - ferrofluid	z_{KR} [mm]	14.2
Radial correction factor	β_r	0.007
Vertical correction factor	β_y	0.006

ferrofluid unit. The geometric extension is neglected. The radius is varied for the resultant steady function, which yields an one-dimensional function F_r and is the basis for parameter optimization.

6. Forces for Ferrofluid Based Locomotion

Figure 6.17 features radial and vertical force functions $F_r(r)$ and $F_z(r)$ depending on the radial distance. The diagrams compare results drawn from FE, analytic calculations and a scaled quantifier. The latter underlines the error weighting in the different areas. While neither of the diagrams for radial $F_r(r)$ and vertical force $F_z(r)$ does present an absolute analogy, the agreement rate is generally high. The quality of the results increases with higher distance from the iron core or, on the contrary, decreases close to the iron core. Therefore, one can summarize quantitative predictions based on these calculations are sufficiently precise for the far field. For the near field, only qualitative information can be reproduced. The extent, to which these results mirror reality, can be established only by measurements. In this thesis, they are not subject of investigation.



(a) Radial force F_r vs. radius r of ferrofluid drop. (b) Axial force F_z vs. radius r of ferrofluid drop.

Figure 6.17.: *Optimized fitting of the analytical solution to the numerical by error square sum method, consideration of the error rate [Gre08].*

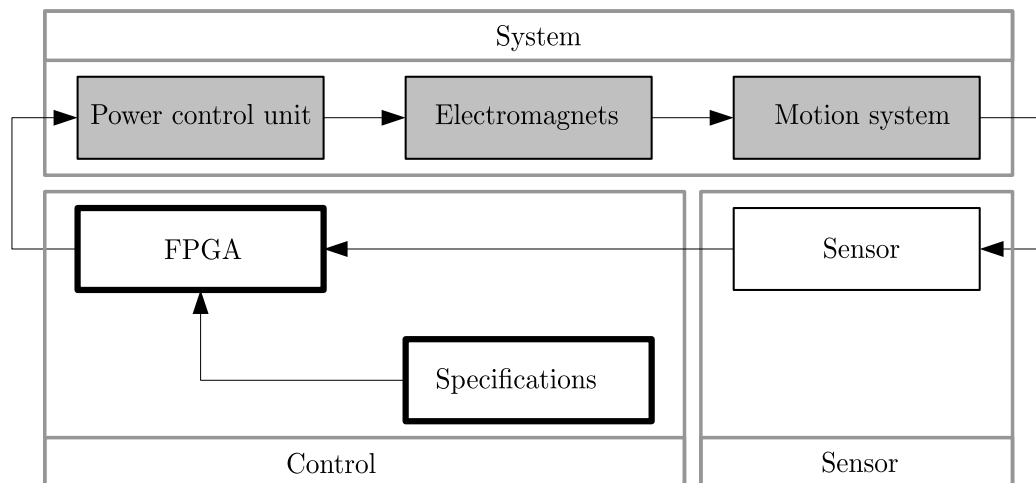
The presented results of the magnetic field and force calculation may be used to build a close-loop control for analog positioning of magnetically influenced small entities. They will work as actuating variables. In [Gre06, Gre08], a study for controlled positioning of small ferrofluid entities has been published already, see the concept in figure 6.18(a). Here, the potential of discrete positioning was experimentally analyzed for a different path planning, see figures 6.18(b) and 6.18(c), incorporating ferrofluid portions in glycol, and the continuous positioning

6.2. Forces on Ferrofluid in Active Locomotion Systems

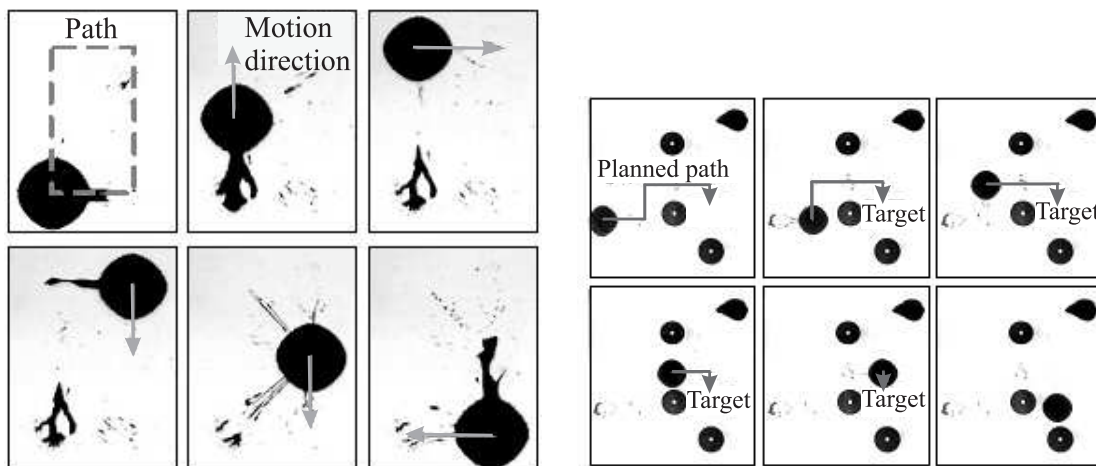
between magnetic field sources. For the latter, bidirectionally moving steel beads have been used, see figure 6.13.

Though calculations for the advanced (analogous) position control are prepared for a high permeable steel bead, the results can be transferred to serve controlled ferrofluid locomotion. This may be further developed for manipulation and support systems, where a swarm of ferrofluid entities cooperate in order to navigate and shift impassive solid (otherwise immobile) bodies on a horizontal plane. Following the definition defined in this paper, this is called *active locomotion*.

6. Forces for Ferrofluid Based Locomotion



(a) Scheme of closed-loop control [Gre08].



(b) Continuous path planning (CP).

(c) Point-to-point (PTP) path planning.

Figure 6.18.: Control system for ferrofluid positioning with different strategies [Gre07].

7. Instead of a Summary

7.1. Back to the Basic Idea

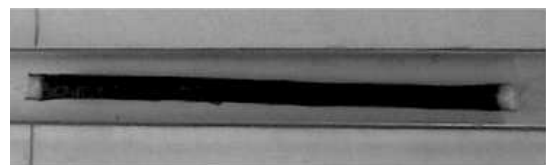
Instead of a detailed summary, the author returns to the main idea of the thesis – the combination of ferrofluid and locomotion. So, in the following, conclusions can be found of the author’s research implemented in several hardware designs of non-pedal locomotion systems, created by the research group led by ZIMMERMANN/BÖHM.

In 2006, at the beginning of project NALETOVA, TURKOV a.o., [Zim06b], based on the idea mentioned; an experiment was realized with a flexible cylindrical capsule filled with a magnetic fluid (in short: ‘worm’) inside a cylindrical channel, figure 7.1(a).

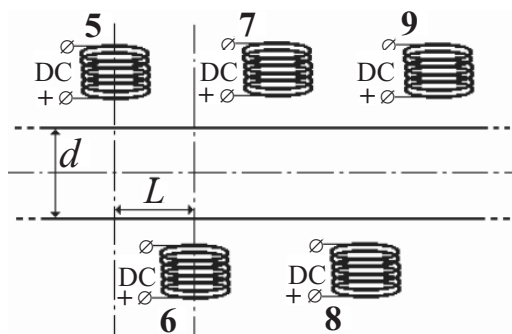
The magnetic field is created by electromagnets. The symmetry axes of the solenoids lie within the horizontal plane, L is the distance between the individual axes of the coils, see figure 7.1(b). The coils are placed laterally along the channel with a diameter d . Three solenoids establish the driving magnetic field simultaneously (for example, coils numbers 6–8 in figure 7.1). Thus, the axis of the center coil matches with the symmetry axis of the magnetic field. While three electromagnets have to be active, the periodic switching schedule provides the power-on in proceeding and the synchronous power-off in rear direction. n is the number of coil switches per second (the frequency), thus $T = 1/n$ is the period of the solenoid commutation. The electrical signals supplying the electromagnets are unidirectional. This electromagnetic source yields a traveling magnetic field \mathbf{H} , which is a complex function of x, y, z (x is the coordinate along the channel, z is parallel to axis of the electromagnets) and time t .

A periodic magnetic field, conditioned as described, enables the worm to move along the channel. The direction of the body motion is the op-

7. Instead of a Summary



(a) Worm design: ferffluid filled flexible tube [Zim06a].



(b) Arrangement: coils lateral along the tunnel [Zim06a].

Figure 7.1.: Active locomotion system – ferffluid based artificial worm.

posite of the traveling magnetic field. The prototype incorporates the following scale: The diameters of channel and capsule are $d = 10$ mm and $d_c = 4$ mm, while the capsule is $l_c = 75$ mm long. Frequencies n from 5 s^{-1} to 1000 s^{-1} are experimentally analyzed. An impression of the phases of worm deformations is provided in figure 7.2.

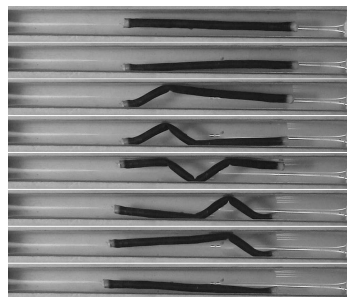


Figure 7.2.: Ferffluid worm in a traveling magnetic field [Zim06a].

This first, successful experiment had given the authors and her team hope, that the realization of an autonomous worm-like locomotion system for technical applications may be feasible. During long-term experiments testing the compatibility of different (flexible) housing materials to encapsulate the ferffluid, a persistent technological problem occurred and is still unsolved. On one side, the membrane for the envelope is preferably as thin as possible, to achieve a very flexible worm structure and a high force extraction. The already diminutive forces, which arise in the ferffluid when exposed to the magnetic field, must

7.2. Active and Passive Locomotion Systems

not be reduced any further. On the other side, due to ingredients ensuring ferrofluid long-term stability, the available 'high-performance' ferrofluids are strongly chemical reactive and require a thickish cover layer to counteract diffusion of the ferrofluid's carrier fluid through the capsule, e.g. organic solvent or water. The membrane should also protect against environmental influences to improve the long-term stability. These two problems and actually rivaling demands should be solved in the upcoming years.

In addition to basic analysis in connection with the direct usage of commercially available FERROFLUIDS for locomotion processes (active and passive locomotion systems, see section 7.2), the mentioned technological problems lead to different analysis. Continuing adherence to the principles of a wireless transfer of control signals and energy to the locomotion system by a magnetic field FERROELASTOMERS were developed for application in mobile systems (ferroelastomer based locomotion systems, see section 7.3).

7.2. Active and Passive Locomotion Systems

Within the frame of ferrofluid based locomotion systems, *active* means that the system contains one or more ferrofluid portions (beads or drops, e.g. [Ste08, Ste09, Böh08]), which are moving, i.e. locomoting, due to the interaction with a controlled magnetic field. In *passive* systems, the ferrofluid represents the transfer medium for the locomotion. Thus, the terminology *active* and *passive* is not connected to the existence or the position of a drive system, as Steigenberger argues in [Ste11], the classification depends on the role of the ferrofluid.

An *active locomotion* is realized by a single ferrofluid portion (in the range of 1.5 ml) moving uniaxially and bidirectionally in a low-viscous carrier fluid, see figure 7.3. The locomotion is forced by a temporary, localized electromagnetic gradient field. A high velocity can be achieved using an open-loop control, but considering the controllability and the given size of the vessel, it should be limited to 10–15 mm s⁻¹. The moving prototype strongly corresponds to bionic archetypes.

7. Instead of a Summary

Generally, the presented experimental setup also enables the analog positioning of magnetic beads. A closed-loop control basing on an abstracted model concerning the dynamics of a moving body and the corresponding electromagnets was derived and fitted to the simulation results for the magnetic field executed by the numerical finite element method, [Gre10a, Zim10, Gre10b].

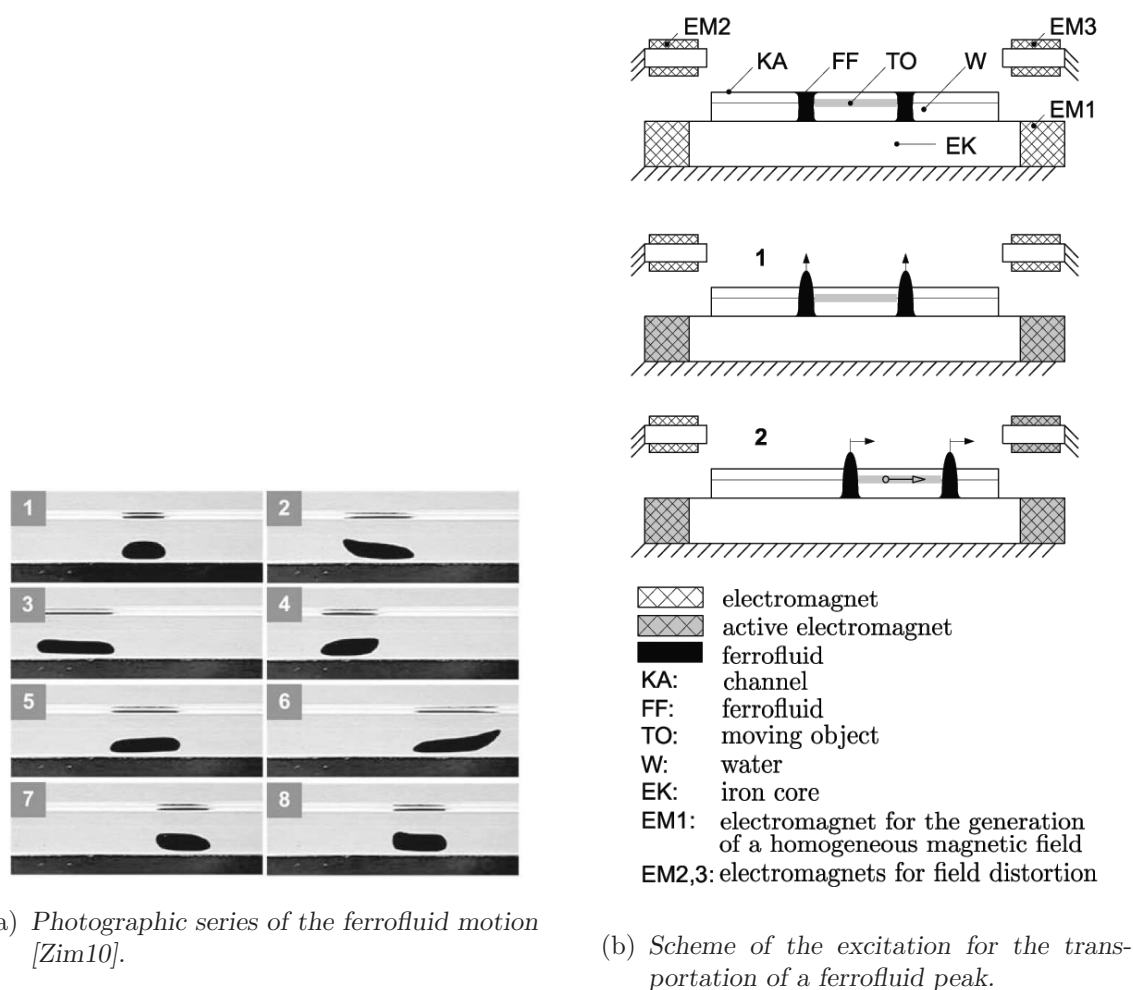


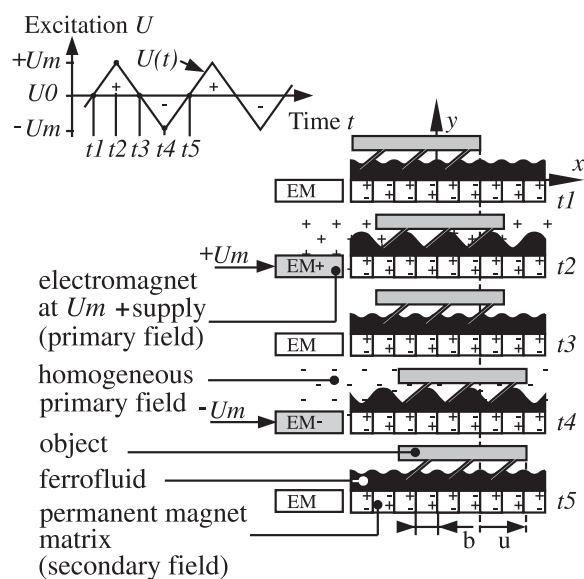
Figure 7.3.: Uniaxial locomotion of a ferrofluid portion.

A *passive locomotion* system generates a traveling wave on the ferrofluid surface in order to move a non-magnetic object. Figure 7.4, [Zim08a], shows an example. In order to maintain a low controlling effort, the ferrofluid is fixed in position by a permanent, inhomogeneous and locally fixed magnetic field (secondary field). This field incorpo-

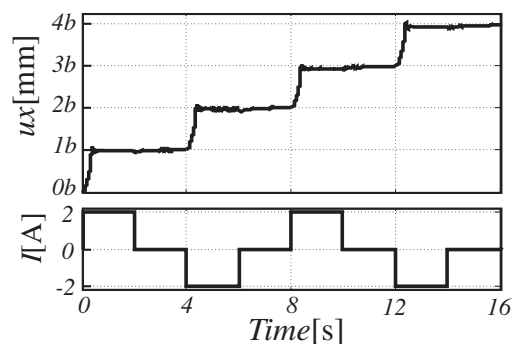
7.2. *Active and Passive Locomotion Systems*

rates two neighboring, oppositely polarized areas. The alignment lies in horizontal direction of the object and is realized by permanent magnets. Additionally, the ferrofluid pressure experiences a change, due to superposition by a global, homogeneous and temporally alternating magnetic field (primary field), which is generated by a single electromagnet. Both fields, the primary and secondary, are vertically aligned. By aligning the secondary field, the ferrofluid pressure changes in the alternating polarity of the global primary field spatially (horizontally) as well as temporally periodical and simultaneously in the areas next but one. The changing pressure in combination with the geometric asymmetry of the non-magnetic object generates the uniaxial locomotion of the object.

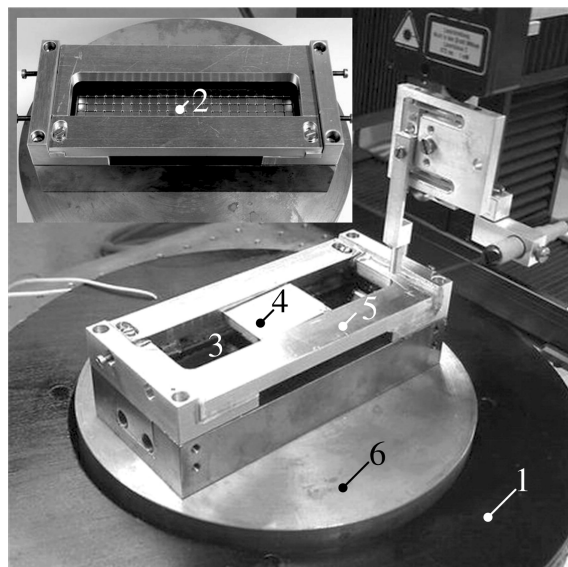
7. Instead of a Summary



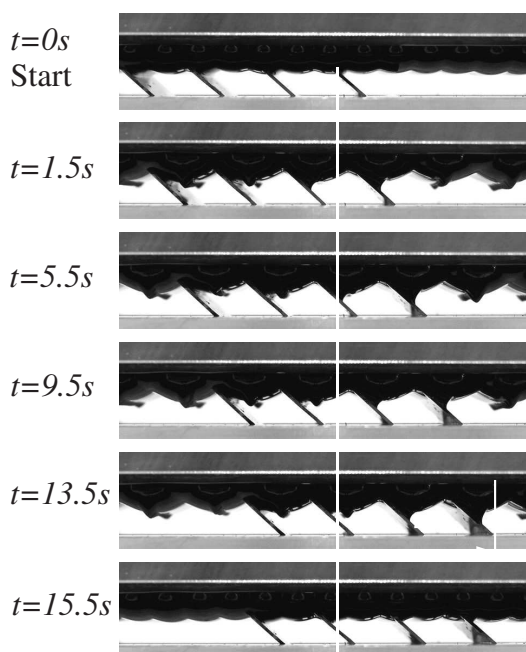
(a) Working principle.



(b) Horizontal displacement u_x of the slider after two complete excitation periods.



(c) Photo of the setup: 1: Helmholtz coil, 2: Permanent magnet, +/-: opposing polarizations, 3: Ferrofluid, 4: Non-magnetic object with bristle-shaped contact area, 5: Lateral guidance, 6: iron core.



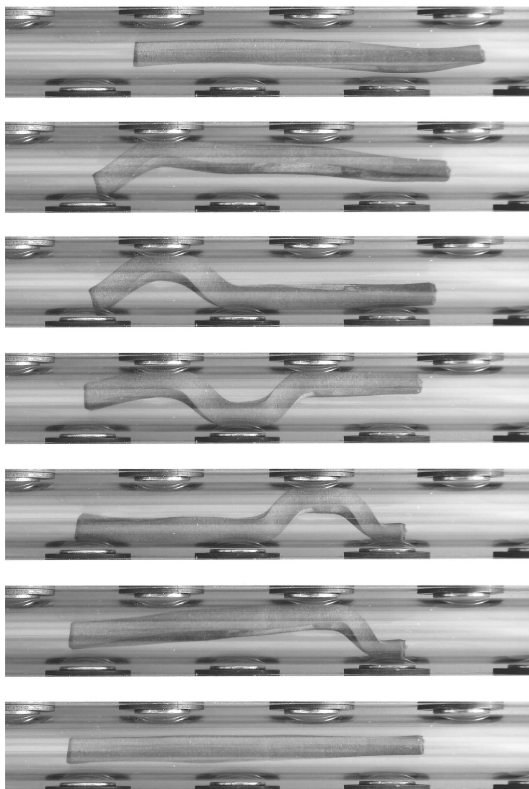
(d) Closeup of the slider.

Figure 7.4.: A passive ferrofluid based locomotion system (slider mass $m = 30$ g, number of bristles $n = 4$, inclination angle of bristles $\alpha = 45^\circ$, excitation time $T = 8$ s, electric current $I_{max} = \pm 2$ A, ferrofluid volume $V = 25$ cm³) [Zim08a].

7.3. Ferroelastomer Based Locomotion Systems

7.3.1. Worm-Like Locomotion Systems

Handling the process of ferroelastomer production with the necessary mechanical parameters (Young's modulus, tensile strength, shore hardness), the setup shown in figure 7.1 was directly used for experiments on a ferroelastomer worm [Zim07a].



(a) Motion of the ferroelastomer worm [Böh11].



(b) Setup: module with coil arrangement and tunnel in front, plus computer-aided control of voltage-driven power supply.

Figure 7.5.: Locomotion of the prototype of a ferroelastomer worm.

The uniaxial, bidirectional locomotion of the worm locomotion is realized in a glass pipe within a cascade of twelve electromagnets, figure 7.5(a). The maximum velocity of the worm is achieved by a switch-

7. Instead of a Summary

ing frequency of the coils of $f = 50 \text{ s}^{-1}$ is $v = 5.56 \text{ cm s}^{-1}$, figure 7.5(b).

Remark: During the investigations of technical non-pedal locomotion systems the paradigm of our research was the worm. Thus, our prototypes are called 'worms'. Indeed, the actual gait realized with the magneto-sensitive elastomer or the elastic capsule filled with ferrofluid is snake-like called *concertina motion*.

7.3.2. Vibration Driven Locomotion Systems

A new concept for locomotion of miniature robots is based on periodic electromagnetic actuation of magneto-sensitive elastomer bodies. The morphology of the robots relies on the dynamics of resonance. On the basis of forced oscillation of ferroelastomer elements, several prototypes are developed, [Böh11, Zim11]. The first two incorporate an inelastic polymeric frame with an integrated micro-coil and an attached magneto-sensitive elastomer body. The robots have no moving parts exposed to the environment. The motion of the robot I, see figure 7.6(a), is unidirectional, and the one of robot II, see figure 7.6(b), is bidirectional. The locomotion direction is frequency-controlled.

The other type of ferroelastomer robot, figure 7.7, consists of only one symmetric magneto-sensitive elastomer body with six embedded micro-coils. It is an example for a compliant planar locomotion system using the introduced actuating mechanism. The change of the equally excited micro-coils from 'A' and 'B' at the time $t = 2.1 \text{ s}$ to 'A' and 'C' causes the change of the locomotion direction. The maximum average speed of this system is $v = 5 \text{ mm s}^{-1}$ at the driving frequency $f = 20 \text{ Hz}$.

The working principle of all prototypes is discussed with the help of transient dynamic analyses and verified with experimental operation and measurement. By proper design, the mode of vibration can be varied in a wide range, depending on the driving frequency. The use of this effect allows the realization of micro-robots with simple designs and frequency controlled variable movement performance.

7.3. Ferroelastomer Based Locomotion Systems

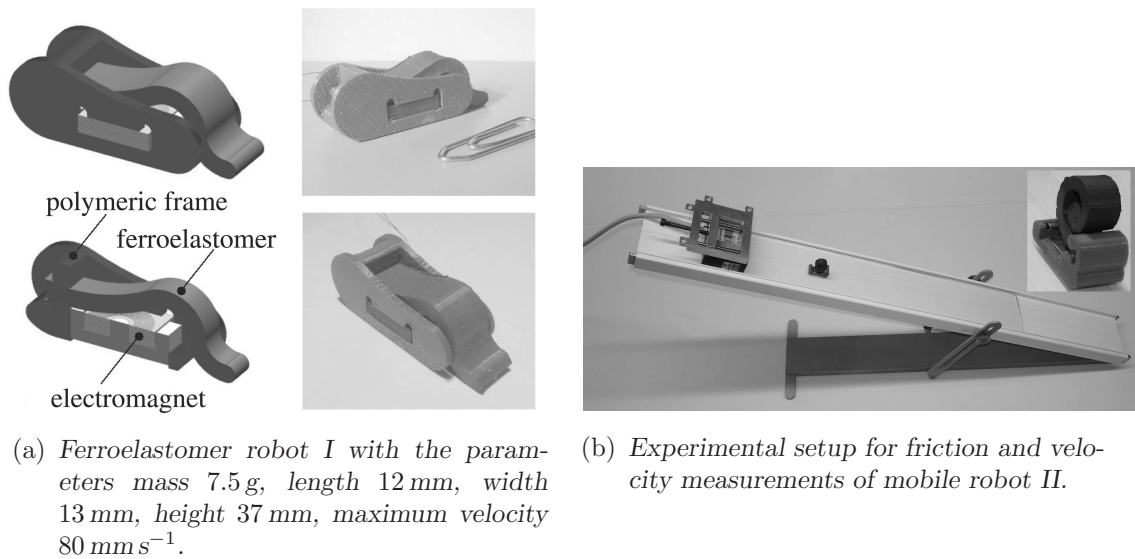


Figure 7.6.: Uniaxially moving robots made of ferroelastomer actuator and polymer frame.

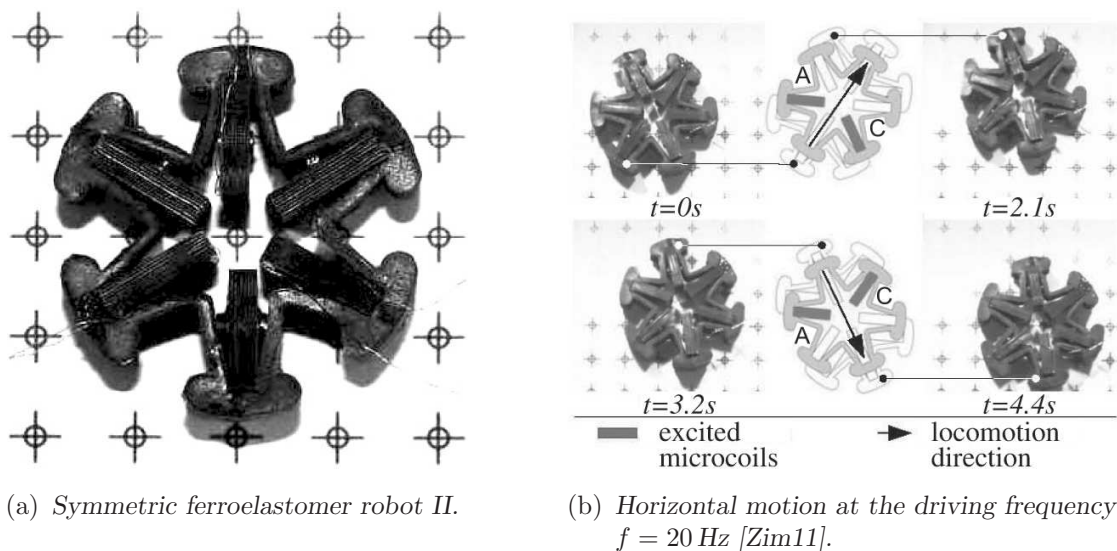


Figure 7.7.: Resonance driven robot moving in the horizontal plane consists solely of ferroelastomer.

7.4. Outlook

Within the frame of ferrofluid based locomotion systems (class-divided into direct and indirect forms), a variety of configurations and strategies are considered and investigated. The studies comprised theoretical analysis – e.g by analytical description, numerical FE simulation, which were closely accompanied by experimental analysis, often with prototypes. Thereby, we dealt not only with mechanic (dynamic and kinematic) subproblems, but the required knowledge about complex magnetic fields and the ways for suitable conditioning involved, of course, studying magnetic field matters and the control of electromagnets, too. The tasks of the experimental work included the creating of general concepts and special designs of setups, application of various measurement techniques and equipments as well as subsequent data processing. These analyses were accomplished in the main with MATLAB (The MathWorks, Inc.). Algorithms for video processing and edge detection came to work regular.

The study of ferrofluid based locomotion leads the author to some conclusions. Even if one accepts that ferrofluid driven locomotion systems are limited to centimeter scales, these special types of locomotion systems generally lack performance and usability. Currently (commercially) available ferrofluids generate an insufficient amount of serviceable force. Consequently, the power of passive locomotion systems is strongly limited. Additionally, the handling of those fluids is severely hindered due to the continuing problem of covering the ferrofluid durably with a flexible, but firm membrane to avoid staining of the contact area. Alternative development of ferroelastomer avoids the issue of wrapping up the material.

For the upcoming development, some prognoses can be formulated concerning ferrofluids, ferroelastomers and the related magnetic nanoparticles. **Ferrofluids** and their properties will be further developed. Properties will be more precisely tailored according to the application criteria. The success of ferrofluid application strongly depends on more powerful operating forces. Although, magnetic fluids are potentially suitable for locomotion purposes, it is questionable, whether

actual applications incorporating ferrofluid based locomotion will come in use in a medium-range perspective, due to the efficiency deficit. Even though future research may sufficiently solve the mentioned problems, one cannot expect ferrofluid properties changing significantly, because some desired alterations are rivaling each other. Most likely, the application of ferrofluid for locomotion systems will solve niche problems, where other solutions fail explicitly.

The thesis emphasized the problems of ferrofluid based locomotion in the macro scaled world. However, magnetic field controlled media celebrated first successful use in the micro- and nanoscaled sites. MNP application in nanotechnologies, especially in the medical engineering, is a cutting-edge resort with massive economic impact.

This did not happen by a lucky chance, but magnetic marking or manipulation works stably and independently from conventional chemical and biological processes. Most widely known in public are MNP applications in the medical technology. Specially conditioned MNP are used for studies on hyperthermia, magnetic particle imaging, bio-assets, magnetic drug targeting and magnetic separation. Similar procedures are used in other research areas, e.g. in the microfluidics. Despite the term 'smart materials', MNP are neither smart nor self-acting. These particles are conditioned for the individual application, and due to their given configuration (e.g. an electro-chemical surface characteristics) they can be applied for the intended biological or technical process. Future research has two tasks, perfection of the application technologies and of the precision of nanoparticle – cover molecule fit.

In recent years, the ferrofluid related research has been developed the new scope of magnetizable elastomers and gels. Especially in Germany, the trend is distinctive. The German Research Foundation (Deutsche Forschungsgemeinschaft) has established a new priority program. priority program (Schwerpunktprogramm) 1681 is named 'Field controlled particle matrix interaction: synthesis, multi-scale modelling and application of magnetic hybrid-materials', [Ode12]. It concerns compound materials with magnetizable particles embedded in a frame structure. Due to the resulting interaction, the properties of these **ferroelastomers** can be controlled by magnetic fields.

7. *Instead of a Summary*

As shown previously, ferroelastomers seem to be well suited for locomotion purposes. Mechanic compliance and magnetic excitation around the resonance result in locomotion due to asymmetric eigenmode motion (higher orders). But the potential of magneto-rheological elastomers is wider. By fixing the magnetic nanoparticles within a mechanic grid, in contrast to the ones in ferrofluids, the particles are not freely mobile. Thus, instead of superparamagnetism they possess a slight ferromagnetic behavior. Additionally, magnetizable elastic materials possess a magnetic field-sensitive YOUNG modulus. So, the actively controllable mechanical properties may yield to advanced vibration-driven locomotion systems with enhanced functionalities (e.g., systems with tunable natural frequencies), also including sensing capabilities. Novel methods for adaptive vibration reduction may be possible for vibration sensible systems.

Appendix

A. Magnetic Matters Influencing Surface Deformation and Subsequent Peristaltic Transport

A.1. Data Acquisition of the Magnetic Field by Measurement

Measuring parameter: Magnetic flux density $B(x, z)$ (see figure A.1)

- Horizontal and vertical component B_x, B_z

Measuring position

- Horizontal path along PM surface, path length $x = 56$ cm (in accordance with range of 56 (of 88) neighboring PMs)
- Vertical distance from PMs $z = 14$ mm (corresponding to distance: PM from unperturbed ferrofluid surface)

Derived magnetic field strength H (see figure A.2) in Oersted by

$$H[\text{Oe}] = B[\text{mT}] \times 10^{-3} \times 10^4 / (\mu_0 \mu_{r,a}) = B[\text{Gs}] / (\mu_0 \mu_{r,a})$$

taking into account the transition of Tesla to Gauss

$$1 \text{ T} = 10^4 \text{ Gs}$$

Absolute magnetic permeability $\mu_0 = 1$ (cgs),

Relative magnetic permeability of air $\mu_{r,a} = 1,000000032$ (cgs).

Offset value of magnetic field strength $H_{\text{const}} = 37.46$ Oe,

Amplitude of magnetic field strength (average) $\bar{A} = 7.84$ Oe.

Standard deviation of amplitude $S(A) = 1.25$ Oe.

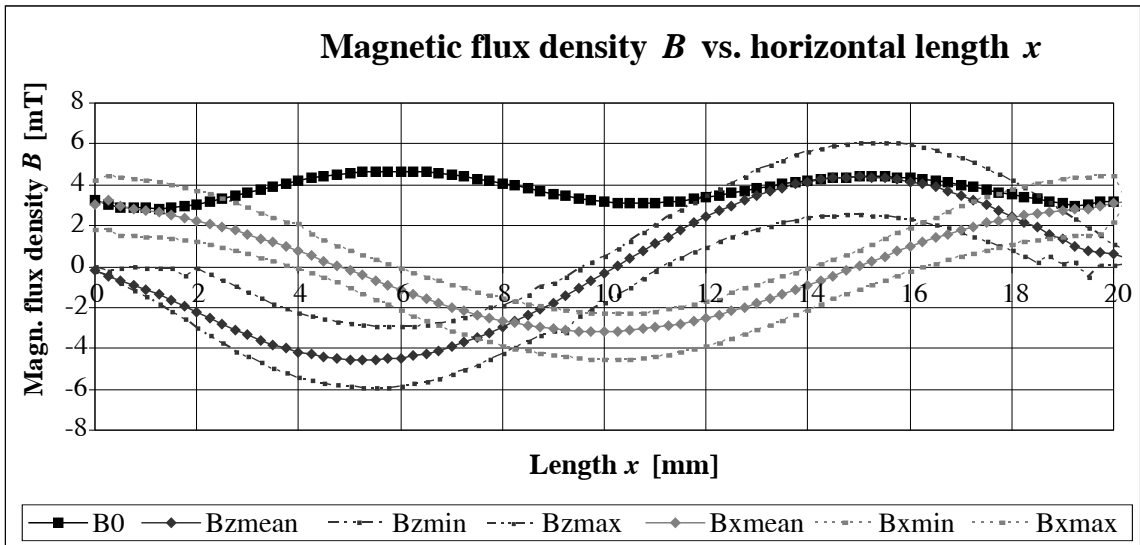


Figure A.1.: Measurement of magnetic flux density, horizontal component B_x [mT], vertical component B_z [mT], total quantity B_0 (average) derived by $\bar{B}_0[\text{mT}] = \sqrt{\bar{B}_x^2 + \bar{B}_z^2}$.

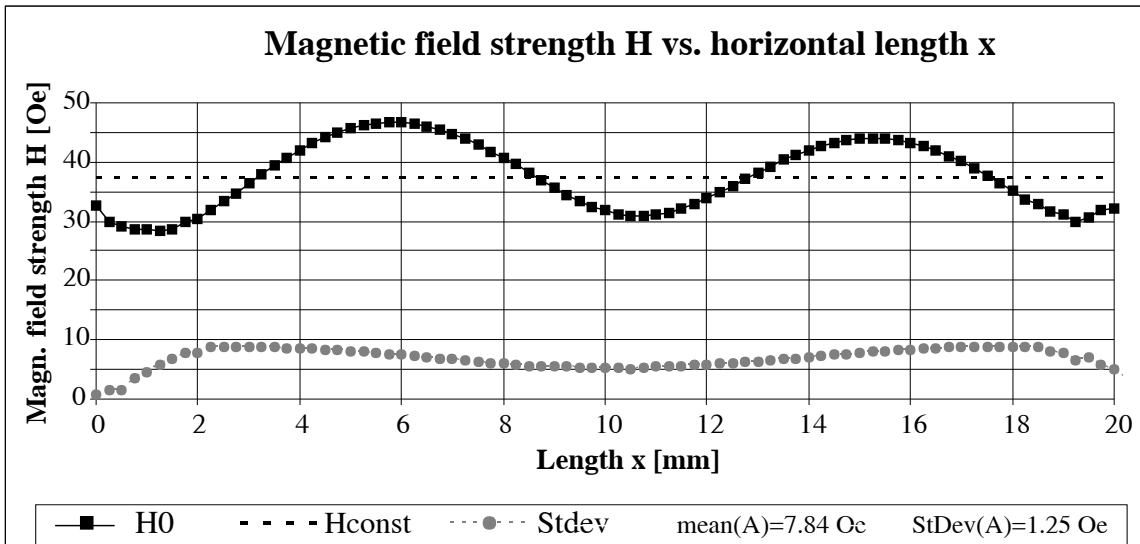


Figure A.2.: Magnetic field strength H .

A.2. Data Acquisition of the Magnetic Quantities of APG S12n by Measurement

Material properties of the ferrofluid APG S12n (Ferrotec, GmbH)
(Measurement and provision of data: D. Borin, TU Dresden.)

Derivation of the

- Magnetic susceptibility χ
- Magnetic permeability μ_r

in values of the Système international d'unités (SI) and the GAUSSIAN cgs-system:

Magnetic susceptibility χ of APG S12n:

$$\chi = dM/dH|_{H=0}$$

$$\chi^{(SI)} = \chi^{(cgs)} 4\pi$$

with

$$dM = 9427.07 \text{ A/m (SI) and}$$

$$dH = 6344.25 \text{ A/m (SI)}$$

$$\chi = 1.49 \text{ (SI)}$$

$$\chi = 0.118 \text{ (cgs)}$$

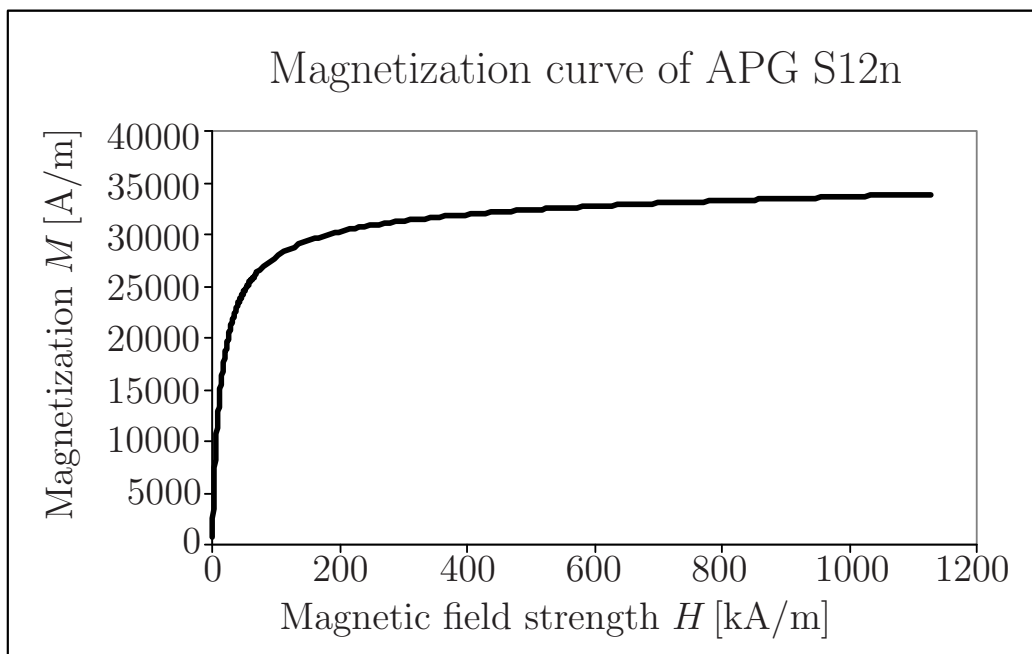
Relative magnetic permeability $\mu_{r,f}$ of APG S12n:

$$\mu_r = \chi + 1$$

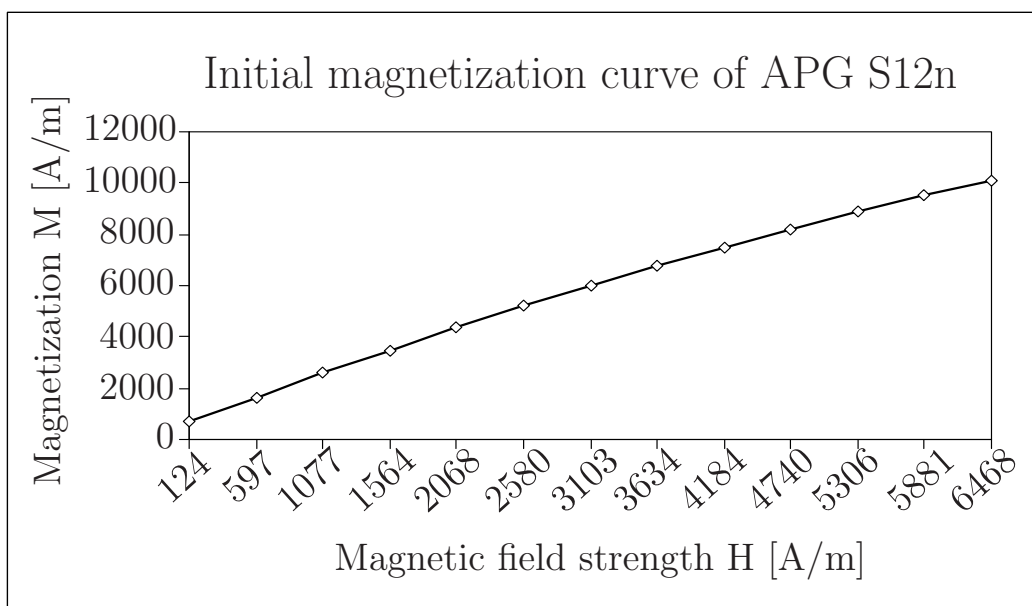
$$\mu_r^{(cgs)} = (\mu_r^{(SI)} - 1)/(4\pi) + 1$$

$$\mu_{r,f} = 2.49 \text{ (SI)}$$

$$\mu_{r,f} = 1.118 \text{ (cgs)}$$



(a) Full magnetization curve.



(b) Detail of M - H -curve.

Figure A.3.: (a) Measurement of the magnetization curve for susceptibility recovery, (b) approximated linear initial slope of $M = M(H)$ of APG S12n (Ferrotec, GmbH).

B. Additions to the Enhancement of Surface Deformation

Table B.1.: Phase transitions of the magnetic fluid contour behavior in the obliquely inclined successive and continuous field.

	Inclination angle of the magnetic field						
	$\alpha = 30^\circ$		$\alpha = 45^\circ$		$\alpha = 60^\circ$		
	Magnetic field strength H_∞ [10^3 A/m]						
	increase	increase	decrease	increase	decrease	increase	decrease
	-- ⁻	-- ⁻ /	/	-- ⁻ /	/	-- ⁻ /	/
i	6.30	6.30	7.08	9.40	7.90	7.90	3.47
ii	87.56	59.70	50.88	11.69			14.69
iii	103.48	71.64	55.486	46.27	35.82	59.57	32.64
.i			83.15	60.17		90.99	43.86
.ii			140.77			113.43	50.6
						122.4	55.08
						131.38	
iv	127.36	147.26	159.20	76.23	135.32	149.33	66.30

--⁻ Successive change of the magnetic field

/ Continuous change

Transitions and retransitions:

i One coherent to two separate volumes (core parts to both sides)

ii Appearance / disappearance of cavity in right portion

iii Two to three volumes (existence of separate center drop)

.i Leaps from bottom right to center drop

iv Three to two volumes (dissolution of right in center portion)

C. Velocity Distribution and Traveling Modes of the Channel Flow

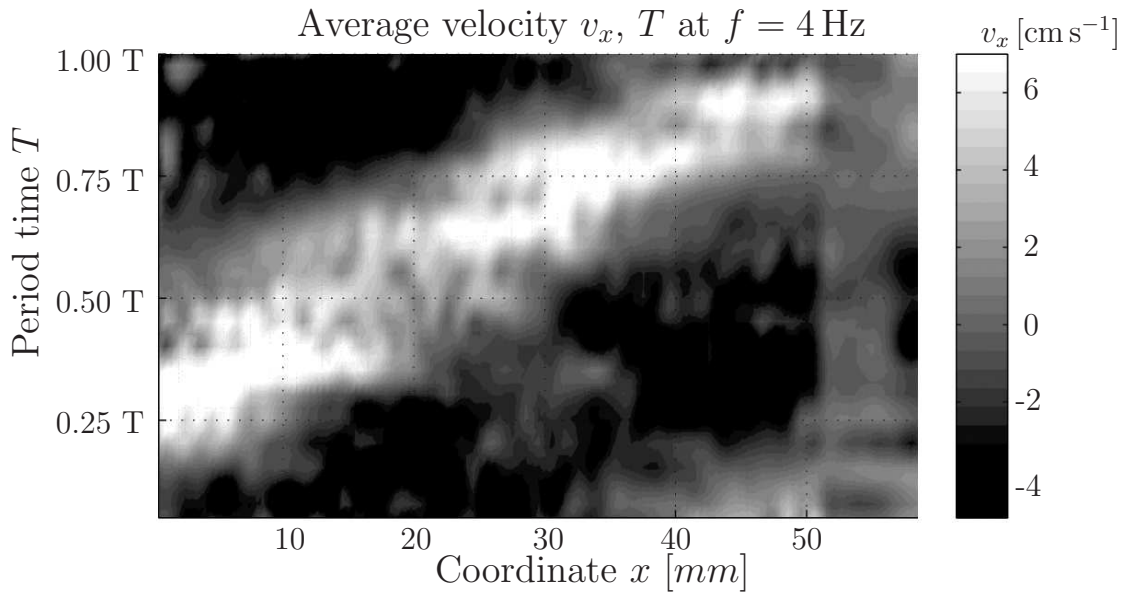


Figure C.4.: Average velocity* distribution at excitation period of $T = 0.25$ s ($f = 4$ Hz) along the channel length x ; * data include lateral velocity components (x -direction) and altitudinal averaging over upper half of fluid height.

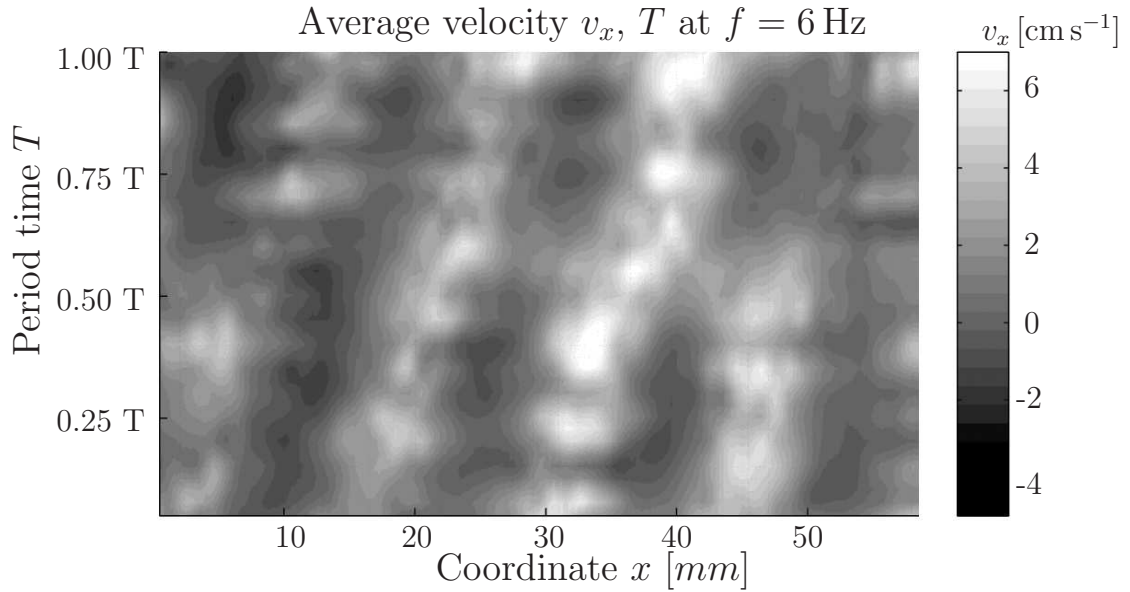


Figure C.5.: Average velocity* distribution at excitation period of $T = 0.167$ s ($f = 6$ Hz) along the channel length x ; * data include lateral velocity components (x -direction) and altitudinal averaging over upper half of fluid height.

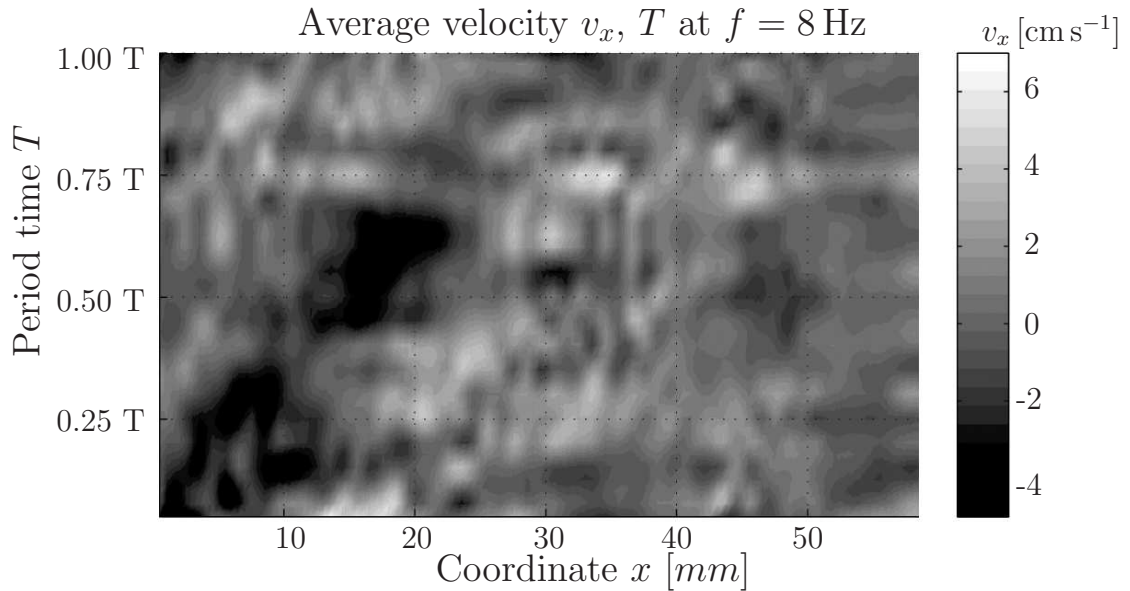


Figure C.6.: Average velocity* distribution at excitation period of $T = 0.125$ s ($f = 8$ Hz) along the channel length x ; * data include lateral velocity components (x -direction) and altitudinal averaging over upper half of fluid height.

Appendix

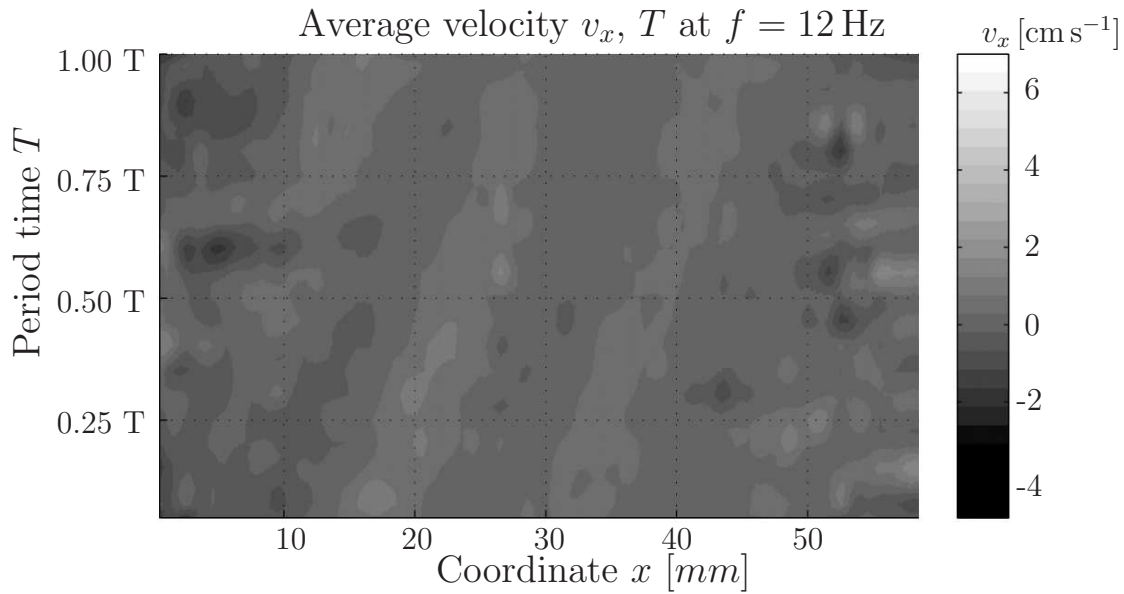


Figure C.7.: Average velocity* distribution at excitation period of $T = 0.083$ s ($f = 12$ Hz) along the channel length x ; * data include lateral velocity components (x -direction) and altitudinal averaging over upper half of fluid height.

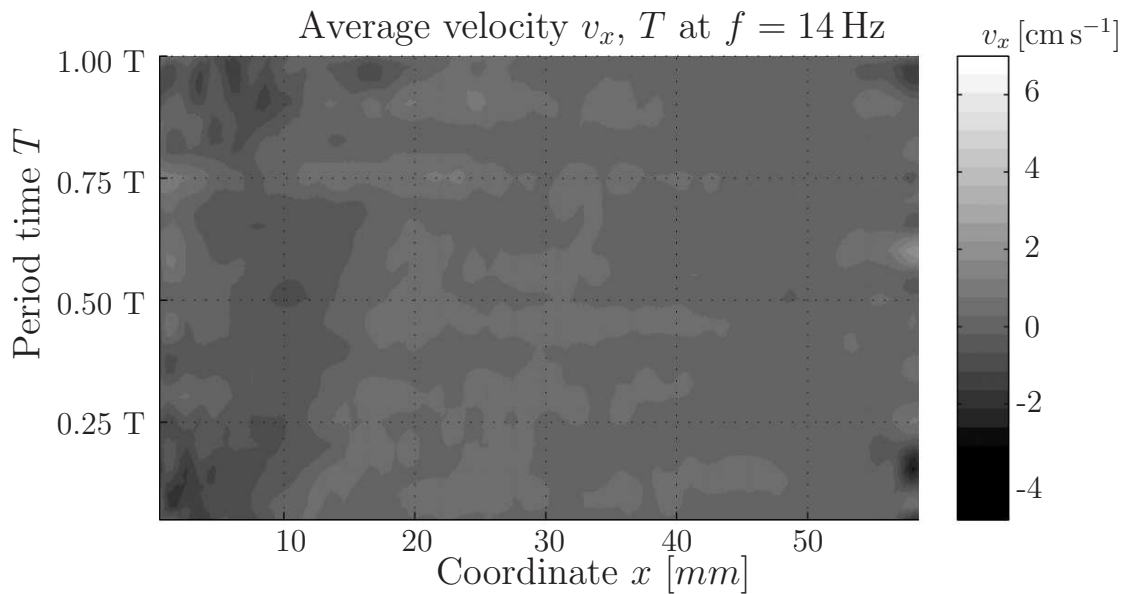


Figure C.8.: Average velocity* distribution at excitation period of $T = 0.071$ s ($f = 14$ Hz) along the channel length x ; * data include lateral velocity components (x -direction) and altitudinal averaging over upper half of fluid height.

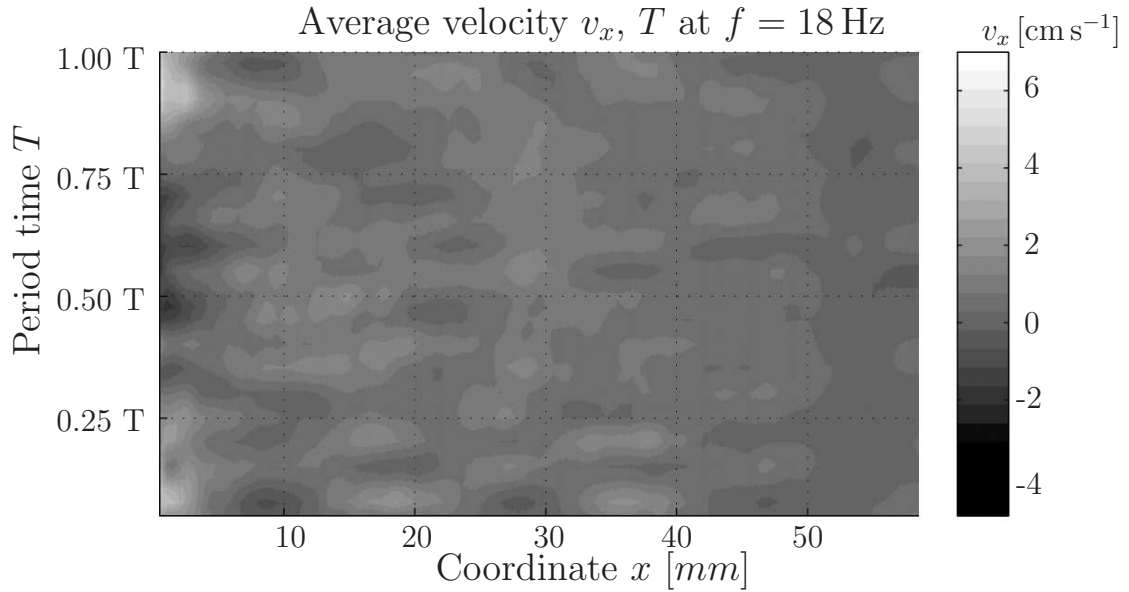


Figure C.9.: Average velocity* distribution at excitation period of $T = 0.055$ s ($f = 18$ Hz) along the channel length x ; * data include lateral velocity components (x -direction) and altitudinal averaging over upper half of fluid height.

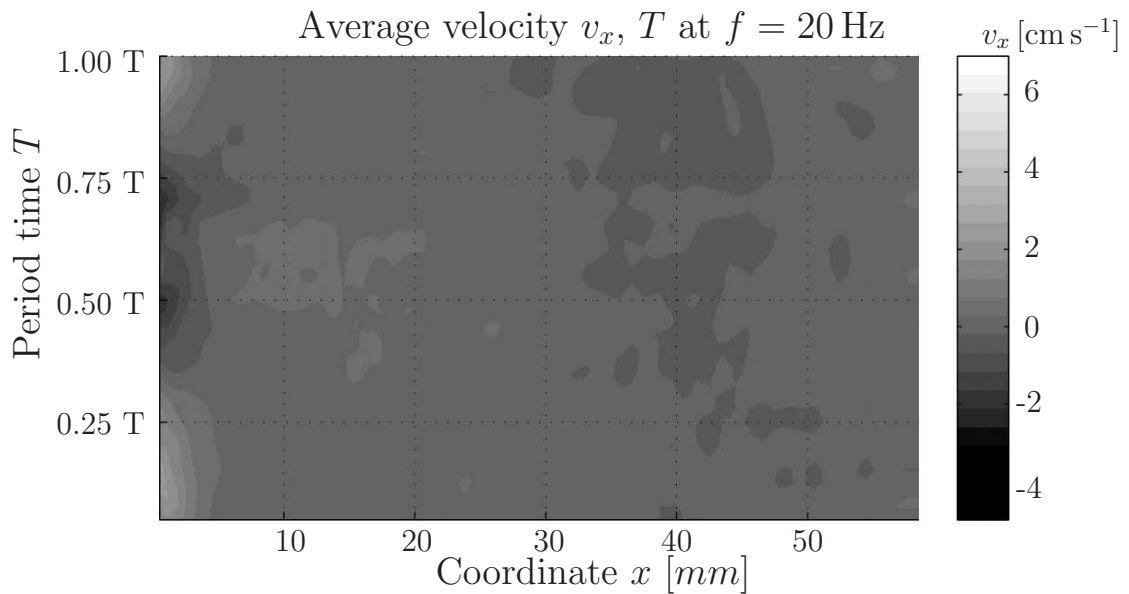


Figure C.10.: Average velocity* distribution at excitation period of $T = 0.05$ s ($f = 20$ Hz) along the channel length x ; * data include lateral velocity components (x -direction) and altitudinal averaging over upper half of fluid height.

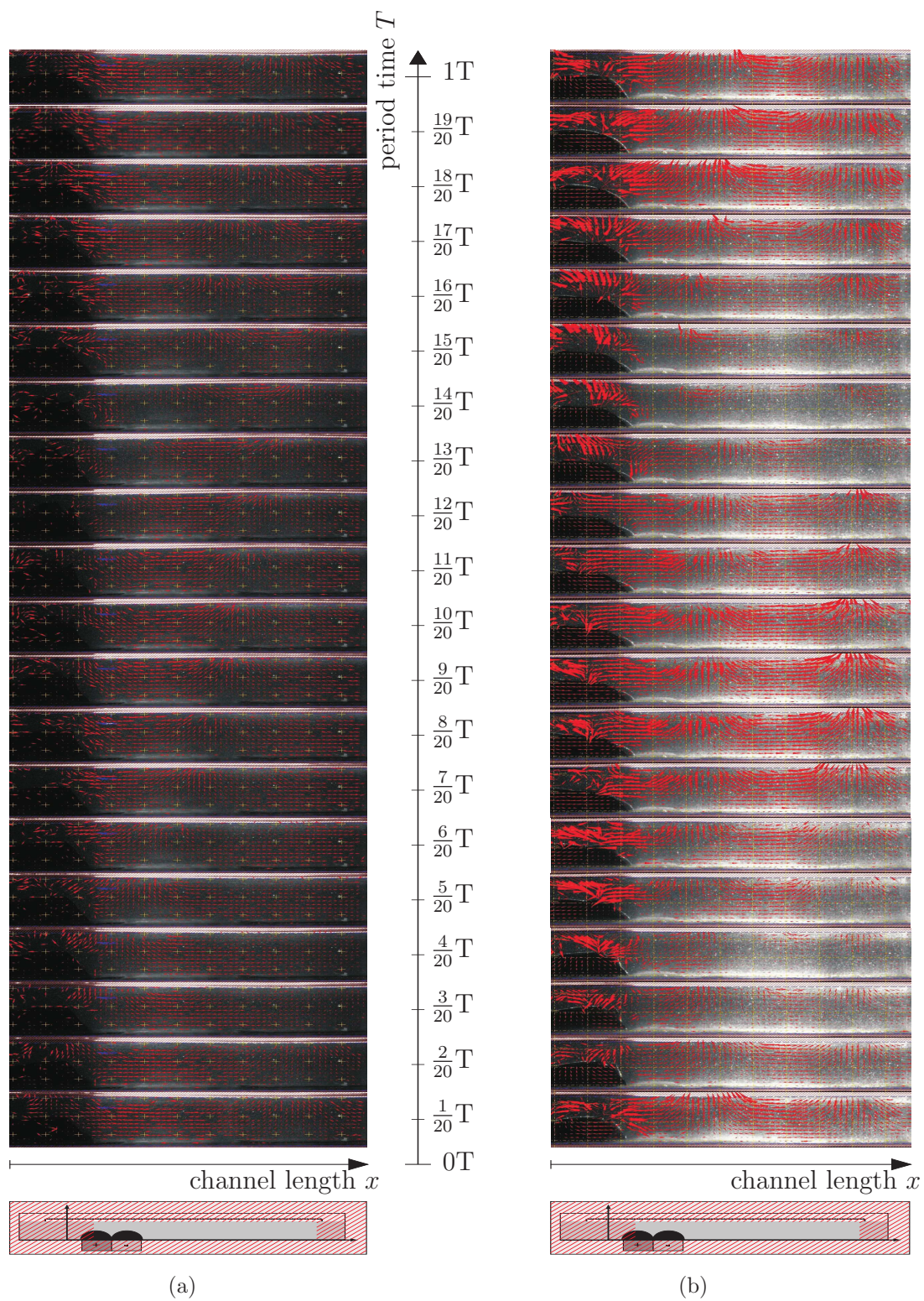


Figure C.11.: *Traveling flow modes at (a) 4 Hz, and (b) 6 Hz excitation frequency.*

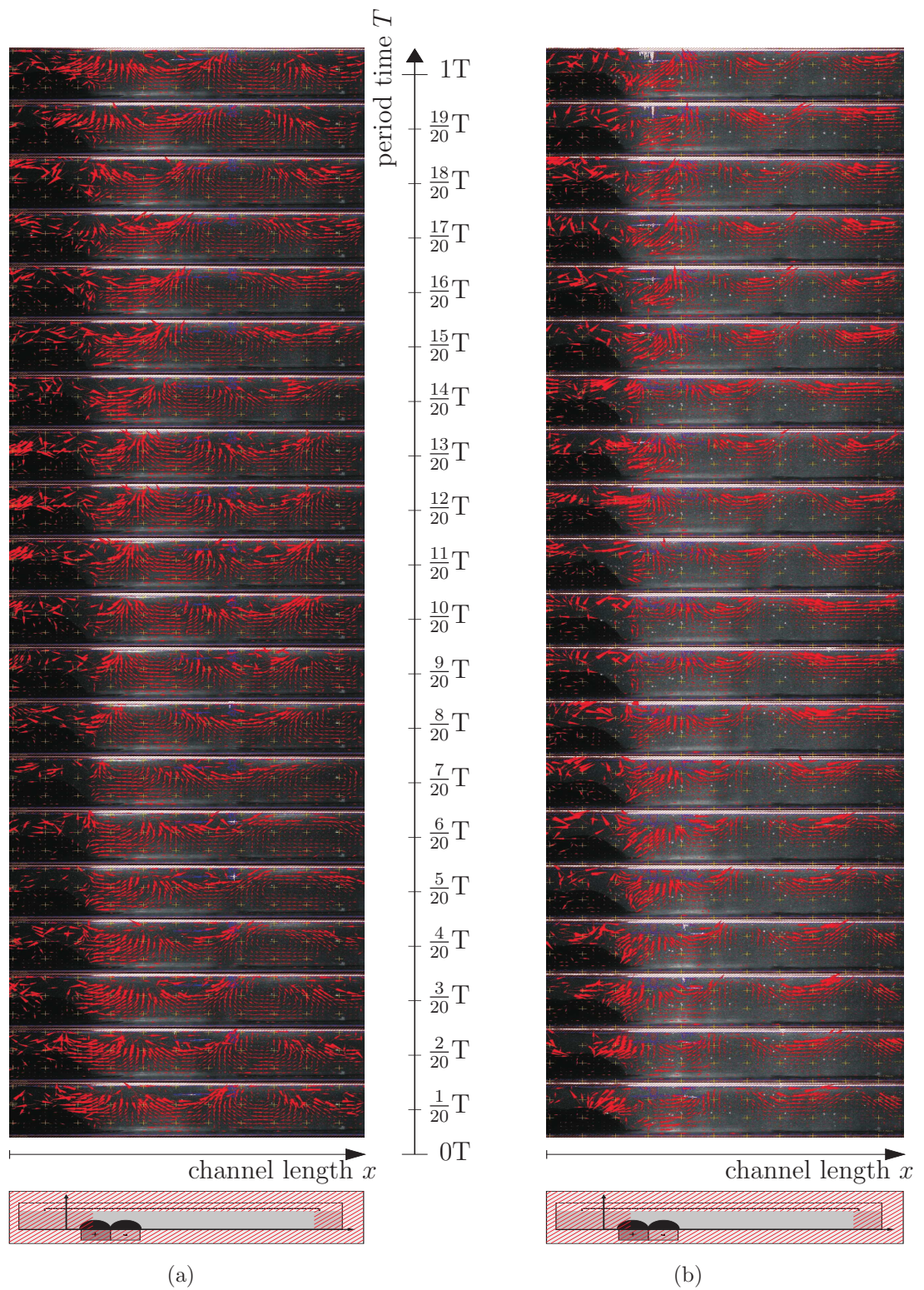


Figure C.12.: *Traveling flow modes at (a) 8 Hz, and (b) 10 Hz excitation frequency.*

Appendix



Figure C.13.: *Traveling flow modes at (a) 12 Hz, and (b) 14 Hz excitation frequency.*

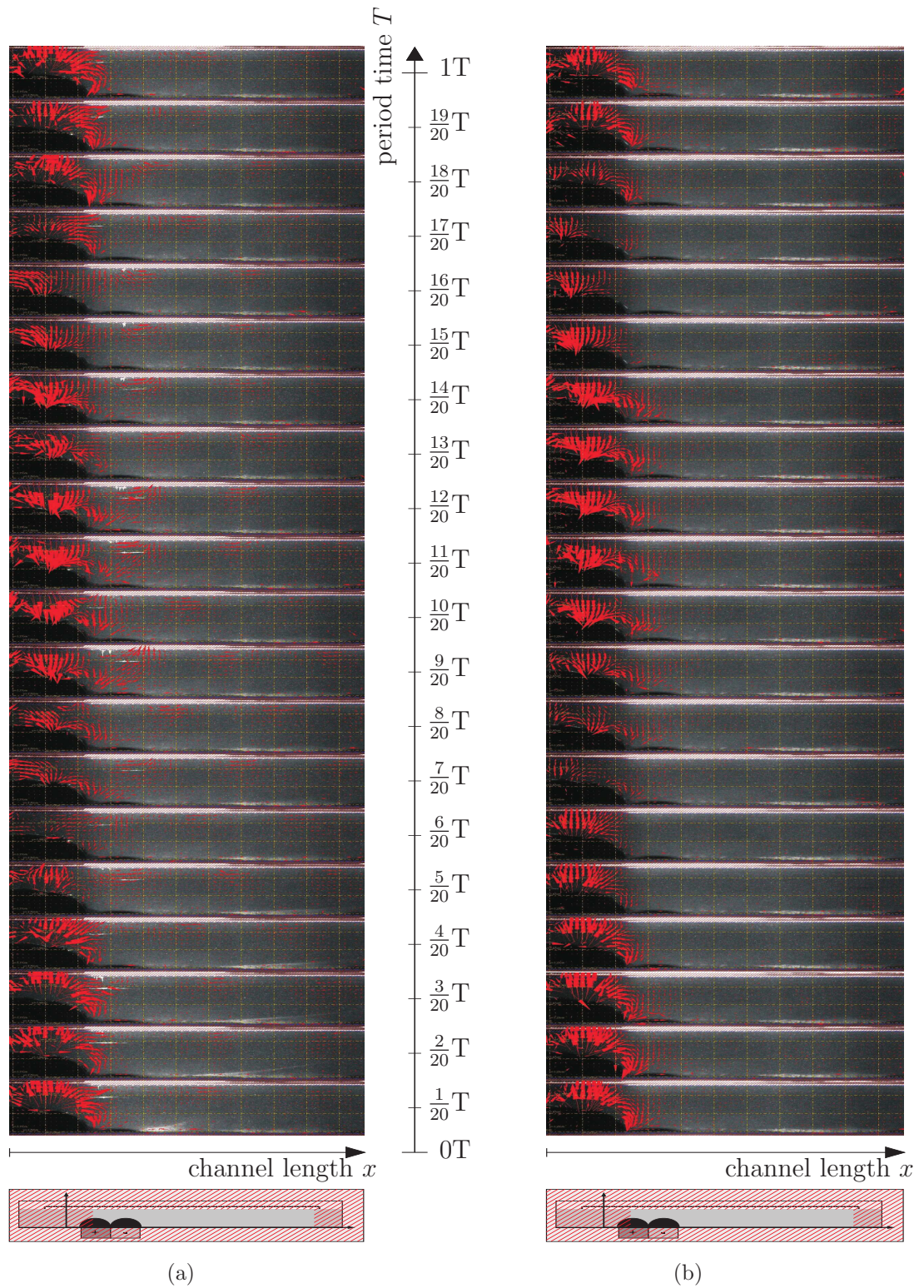


Figure C.14.: *Traveling flow modes at (a) 18 Hz, and (b) 20 Hz excitation frequency.*

List of Abbreviations

CCD	charge-coupled device
DFG	German Research Foundation (Deutsche Forschungsgemeinschaft)
EM	electromagnet
FE	finite element
FPGA	field-programmable gate array
MEMS	microelectromechanical systems
MNP	magnetic nanoparticles
MRF	magnetorheological fluid
PCB	printed circuit board
PIV	particle image velocimetry
PM	permanent magnet
PMMA	polymethylmethacrylat
PTFE	polytetrafluoroethylene
SSP	priority program (Schwerpunktprogramm)

Nomenclature

*	Asterisked quantity: dimensional
A	Magnetic field strength amplitude of field perturbation [1] [Oe] [A m ⁻¹]
$a_{3/4}$	Renamed Coefficient of the amplitude function η_{nm} [1] [cm ² s ⁻¹]
$a_{nm}^{(1-4)}$	Coefficient of amplitude function η_{nm} [1] [cm ² s ⁻¹]
B	Magnetic flux density [1] [Gs] [T]
B_n	Normal component of magnetic flux density [1] [Gs] [T]
b	Index, assigned to high permeable field concentrator
$b_{3/4}$	Renamed Coefficient of the amplitude function ξ_{nm} [1] [cm ² s ⁻¹]
$b_{nm}^{(1-4)}$	Coefficient of amplitude function ξ_{nm} [1] [cm ² s ⁻¹]
D	Determinant
D_i	Determinant of the subordinate coefficient matrix \mathbf{M}_i
d	Diameter [m]
$d\mathbf{l}$	Infinitesimal unit of length [m]
dt	Infinitesimal unit of time [1] [s]
dx	Infinitesimal unit of displacement [1] [cm] [m]
Eu	EULER number [1]
e_i	Common unit vector [1]
e_n	Unit vector in normal direction [1]
e_τ	Unit vector in tangential direction [1]

Appendix

\mathbf{e}_x	Unit vector in x -direction [1]
\mathbf{e}_z	Unit vector in z -direction [1]
F	Force [cm g s^{-2}] [N]
Fr	FROUDE number [1]
f	Frequency [Hz]
f	Index, assigned to magnetizable fluid
f_0	Force density [N m^3]
f_{FF}	Driving frequency of ferrofluid actuator [Hz]
f_{PIV}	Frequency of PIV measuring system [Hz]
g	Gravitational acceleration [cm s^{-2}] [m s^{-2}]
H	Magnetic field strength [1] [Oe] [A m^{-1}]
H_0	Constant part of magnetic field strength [1] [Oe] [A m^{-1}]
$h_{f1/f2/f3}$	Filling level of ferrofluid [mm] [m]
H_n	Normal component of magn. field strength [1] [Oe] [A m^{-1}]
H_τ	Tangential component of magn. field strength [1] [Oe] [A m^{-1}]
\mathbf{H}_∞	Magnetic field strength in proximity of field concentrator [A m^{-1}]
h	Contour function of free surface [1] [cm] [m]
h_0	Unperturbed fluid height [1] [cm] [m]
$h_{0,max}$	Fluid height causing maximum average flow rate \bar{Q} [cm] [m]
$h_{0,opt,max}$	Optimized fluid height for maximum av. flow rate [cm] [m]
h_1	Amplitude of surface perturbation of fluid [1] [cm] [m]
h_n	Term of contour function power series [1] [cm] [m]
h'_{x_i}	Deviation of $h(x_i)$ with regard to x_i [1]
\hat{h}	Measured amplitude of fluid surface deformation [cm] [m]

C. Additions to the Channel Flow

\tilde{h}	Amplitude of contour function [1] [cm] [m]
$\tilde{\tilde{h}}$	Amplitude of contour function [1] [cm] [m]
I	Electric current [A]
i	Counter index referring to spatial coordinate
j	Counter index referring to spatial coordinate
K	Substitution term
K_{0-2}	Substitution term
k	Wavenumber [1] [cm ⁻¹] [m ⁻¹]
k	BOLTZMANN constant [N m K ⁻¹]
k_{max}^*	Wavenumber causing maximum av. flow rate \bar{Q} [cm ⁻¹] [m ⁻¹]
$k_{opt,max}^*$	Optimized wavenumber for max. av. flow rate [cm ⁻¹] [m ⁻¹]
L	Length [m]
$L(\xi.)$	LANGEVIN function [1]
L_c	Length of edge of container [m]
\mathbf{M}	Coefficient matrix
M_b	Magnetization of magnetic field concentrator [A m ⁻¹]
\mathbf{M}_i	Subordinate coefficient matrix
M_{mf}	Saturation magnetization of fluid [A m ⁻¹]
$M^{(f)}$	Magnetization of fluid [A m ⁻¹]
m	Counter index of power series
m	Magnetic moment of ferrofluid particles [A m ²]
\mathbf{n}	Normal vector [1]
n	Concentration of ferrofluid particles [m ⁻³]
n	Counter (as symbol or index)

Appendix

n_j	Component of normal vector [1]
\mathcal{O}	LANDAU symbol
o	LANDAU symbol
$P(r, \phi, z)$	Point in space (cylindrical coordinates)
P_c	Characteristic pressure [$\text{cm}^{-1} \text{g s}^{-2}$] [N m^{-2}]
p	Index assigned to point of interest
p	Pressure function of magnetizable fluid [1] [$\text{cm}^{-1} \text{g s}^{-2}$] [N m^{-2}]
p_a	Atmospheric pressure [1] [$\text{cm}^{-1} \text{g s}^{-2}$] [N m^{-2}]
p_{mag}	Magnetic surface tension [1] [$\text{cm}^{-1} \text{g s}^{-2}$] [N m^{-2}]
p_n	Term of the pressure power series [1] [$\text{cm}^{-1} \text{g s}^{-2}$] [N m^{-2}]
p'_{x_i}	Deviation of $p(x_i)$ with regard to x_i [1] [$\text{cm}^{-2} \text{g s}^{-2}$] [N m^{-3}]
Q	Volume rate [1] [$\text{cm}^2 \text{s}^{-1}$] [$\text{m}^3 \text{s}^{-1}$]
\bar{Q}	Averaged volume rate [1] [$\text{cm}^2 \text{s}^{-1}$] [$\text{m}^3 \text{s}^{-1}$]
\bar{Q}_{max}^*	Maximum average flow rate [$\text{cm}^2 \text{s}^{-1}$]
$\bar{Q}_{opt,max}^*$	Optimized maximum average flow rate [$\text{cm}^2 \text{s}^{-1}$]
$q(t)$	Function of shape in dependency on time
R	Radius of contour curvature [1] [cm] [m]
R	Radius of the conductor loop [mm] [m]
R_c	Radius of magnetic field concentrator [m]
Re	REYNOLDS number [1]
R_{KR}	Radius of conductor loop [mm] [m]
\mathbf{r}	Position vector [m]
r	Index, radial direction
Sr	STROUHAL number [1]
s	Index, assigned to non-magnetic environment

C. Additions to the Channel Flow

\mathbf{s}	Tangential vector [1]
s_c	Length of magnetic field concentrator [m]
s_g	Width of ferrofluid filled gap [m]
T	Period time [s]
T	Temperature [K]
T_{1-6}	Substitution term
T_c	Characteristic period time [s]
T_f	General function of TAYLOR power series
T_{FF}	Period of ferrofluid actuator [s]
t	Time [1] [s]
t_0	Initial time [s]
U_c	Characteristic fluid velocity [cm s ⁻¹] [m s ⁻¹]
u	Component of fluid velocity in x -direction [1] [cm s ⁻¹] [m s ⁻¹]
V	Complete ferrofluid volume [1] [cm ³] [m ³]
$V_{f1/f2/f3}$	Filling volume of ferrofluid [cm ³] [m ³]
\mathbf{v}	Vector of velocity of magnetizable fluid [1] [cm s ⁻¹] [m s ⁻¹]
v_{av}	Average flow velocity [mm s ⁻¹] [m s ⁻¹]
v_{belt}	Translational velocity of the belt drive [1] [cm s ⁻¹] [m s ⁻¹]
We	WEBER number [1]
w	Component of fluid velocity in z -direction [1] [cm s ⁻¹] [m s ⁻¹]
w	Number of windings [1]
$X(t)$	Function of spatial position in dependency on time
$X(z)$	Function presenting squared ratio of function of perturbation amplitude vs. constant magnetic field [1]
x	Channel length [mm]

Appendix

x	Coordinate [1] [cm] [m]
$'x_i$	Index referring to partial derivation with regard to x_i
y	Coordinate [1] [m]
z	Coordinate [1] [cm] [m]
z_0	Vertical distance iron core to ferrofluid [mm] [m]
z_{KR}	Vertical distance conductor loop to ferrofluid [mm] [m]
α	Inclination angle [°]
β_r	Radial correction factor [1]
β_y	Vertical correction factor [1]
χ	Initial susceptibility [1]
Δ	LAPLACE operator [cm ⁻²] [m ⁻²]
∂	Operator for partial differentiation
δ	Summarizing parameter for gravitational load [1]
$\delta.$	Rate of magnetic field increase and decrease [A m ⁻¹ s ⁻¹]
ε	Squared ratio, perturbed : constant magn. field strength [1]
φ	Implicit function of the fluid surface [1] [cm] [m]
γ	Coefficient of surface tension [g s ⁻²] [N m ⁻¹]
η	Dynamic viscosity of magn. fluid [cm ⁻¹ g s ⁻¹] [kg m ⁻¹ s ⁻¹]
$\eta(z)$	Amplitude function of the stream function [1] [cm ² s ⁻¹]
$\eta_{mn}(z)$	Term of amplitude function power series [1] [cm ² s ⁻¹]
η'_{x_i}	Deviation of $\eta(x_i)$ with regard to x_i [1] [cm s ⁻¹] [m s ⁻¹]
\varkappa	Summarizing magnetic parameter [1] [V s A ⁻¹ m ⁻¹]
\varkappa_0	Summarizing magnetic parameter [1] [V s A ⁻¹ m ⁻¹]
Λ	Substitution term
λ	Wavelength of surface waves [1] [cm] [m]

C. Additions to the Channel Flow

λ_i	Eigenvalue
μ	(Summarized) magn. permeability [1] [$\text{V s A}^{-1} \text{m}^{-1}$]
μ_0	Absolute magn. permeability of ferrofluid [1] [$\text{V s A}^{-1} \text{m}^{-1}$]
μ_r	Relative magn. permeability of ferrofluid [1]
ν	Kinematic viscosity of magnetizable fluid [$\text{cm}^{-1} \text{g s}^{-1}$] [$\text{m}^2 \text{s}^{-1}$]
π	Mathematical constant [1]
θ_0	Contact angle between fluid and wall of container [$^\circ$]
θ_s	Contact angle between fluid and concentrator [$^\circ$]
ρ	Density of magnetizable fluid [1] [g cm^{-3}] [kg m^{-3}]
τ_{ij}	Component of viscous stress tensor [1] [$\text{cm}^{-1} \text{g s}^{-2}$] [N m^{-2}]
ω	Angular velocity [1] [s^{-1}]
ω_{max}^*	Angular frequency for maximum average flow rate \bar{Q} [s^{-1}]
$\omega_{opt,max}^*$	Optimized angular frequency for max. av. flow rate \bar{Q} [s^{-1}]
$\xi(z)$	Amplitude function of the the stream function [1] [$\text{cm}^2 \text{s}^{-1}$]
$\xi.$	LANGEVIN parameter [1]
ξ_{x_i}	Deviation of $\xi(x_i)$ with regard to x_i [1] [cm s^{-1}] [m s^{-1}]
$\xi_{mn}(z)$	Term of the amplitude function power series [1] [$\text{cm}^2 \text{s}^{-1}$]
Ψ	Stream function [1] [$\text{cm}^2 \text{s}^{-1}$] [$\text{m}^2 \text{s}^{-1}$]
Ψ_n	Term of stream function power series [1] [$\text{cm}^2 \text{s}^{-1}$] [$\text{m}^2 \text{s}^{-1}$]
Ψ'_{x_i}	Deviation of $\Psi(x_i)$ with regard to x_i [1] [$\text{cm}^2 \text{s}^{-1}$] [$\text{m}^2 \text{s}^{-1}$]
ζ	Argument of the periodic function [1]

Bibliography

- [AA11] ABD-ALLA, A. M.; YAHYA, G. A. and AL OSAIMI, H. S.: Peristaltic transport of micropolar fluid in a tubes under influence of rotation. *International Journal of Mechanical & Mechatronics Engineering* (2011), vol. 11(01):pp. 26–44
- [Aba06] ABAZA, Kh.: *Ein Beitrag zur Anwendung der Theorie undulatorischer Lokomotion auf mobile Roboter: Evaluierung theoretischer Ergebnisse an Prototypen*, Ph.D. thesis, Technische Universität Ilmenau (2006)
- [Afk08] AFKHAMI, S.; RENARDY, Y.; RENARDY, M.; RIFFLE, J. S. and ST PIERRE, T.: Field-induced motion of ferrofluid droplets through immiscible viscous media. *Journal of Fluid Mechanics* (2008), vol. 610:pp. 363–380
- [Amb92] AMBACHER, O.; ODENBACH, S. and STIERSTADT, K.: Rotational viscosity in ferrofluids. *Zeitschrift für Physik B Condensed Matter* (1992), vol. 86(1):pp. 29–32
- [And06] ANDÒ, B.; ASCIA, A.; BAGLIO, S. and PITRONE, N.: Development of novel ferrofluidic pumps, in: *Proceedings of the 28th IEEE EMBS Annual International Conference*, vol. 1, Engineering in Medicine and Biology Society, New York City, USA, pp. 2828–31
- [And07] ANDÒ, B.; ASCIA, A.; BAGLIO, S. and SAVALLI, N.: A Novel Ferrofluidic Inclinator. *IEEE Transactions on Instrumentation and Measurement* (2007), vol. 56(4):pp. 1114–1123
- [And09] ANDÒ, B.; ASCIA, A.; BAGLIO, S. and PITRONE, N.: Ferrofluidic Pumps: A Valuable Implementation Without Moving Parts. *IEEE Transactions on Instrumentation and Measurement* (2009), vol. 58(9):pp. 3232–3237
- [And10a] ANDÒ, B.; ASCIA, A. and BAGLIO, S.: A Ferrofluidic Inclinator in the Resonant Configuration. *IEEE Transactions*

Bibliography

- on Instrumentation and Measurement* (2010), vol. 59(3):pp. 558–564
- [And10b] ANDÒ, B.; ASCIA, A.; BAGLIO, S. and BENINATO, A.: A Ferrofluidic Inertial Sensor Exploiting the Rosensweig Effect. *IEEE Transactions on Instrumentation and Measurement* (2010), vol. 59(5):pp. 1471–1476
- [Bas73] BASHTOVOI, V. G. and BERKOVSKY, B. M.: The thermodynamics of ferromagnetic fluids. *Mag. Hidrodin.* (1973), (3):pp. 3–14, translated in *Magnetohydrodynamics*, vol. 9, no. 3, pp 291 – 300, Jul–Sep 1973
- [Bee08] BEETZ, A.; GOLLWITZER, C.; RICHTER, R. and REHBERG, I.: Response of a ferrofluid to traveling-stripe forcing. *J. Phys.: Condens. Matter* (2008), vol. 20, 204109
- [Ber73] BERKOVSKY, B. M. and ORLOV, L. P.: Investigation of free-surface forms in magnetic liquids’ analogue of pinch effect. *Mag. Hidrodin.* (1973), (4):pp. 38–44, translated in *Magnetohydrodynamics*, vol. 4, no. 9, pp 468 –473, Oct.-Dec. 1973
- [Ber93] BERKOVSKY, B. E.; MEDVEDEV, V. E. and KRAKOV, M. S.: *Magnetic Fluids Engineering Applications*, Oxford University Press (1993)
- [Ber02] BERTHIER, J. and RICOUL, F.: Numerical modeling of ferrofluid flow instabilities in a capillary tube at the vicinity of a magnet, in: *Technical Proceedings of the 2002 International Conference on Modeling and Simulation of Microsystems*, vol. 2, NanoTech, pp. 40–43, (2002)
- [BH05] BEREITER-HAHN, J.: Mechanics of crawling cells. *Medical Engineering & Physics* (2005), vol. 27(9):pp. 743–753
- [Böh08] BÖHM, V.; POPP, J.; ZIMMERMANN, K.; ZEIDIS, I. and GREISER, S.: Ferrofluid based 1D and 2D Locomotion Systems and their Control, in: *Benediktbeurer Ferrofluid-Rundgespräch*, pp. 37–38, (2008)
- [Böh11] BÖHM, V.; GÄRTNER, R.; NALETOVA, V. A.; POPP, J.; ZEIDIS, I. and ZIMMERMANN, K.: Ferrofluid and Ferroelastomer Based Locomotion Systems – Theory, Experiments and Pro-

- totypes, in: *Euromech Colloquium 526 'Patterns in Soft Magnetic Matter'*, pp. 14–15, (2011)
- [Boy64] BOYARSKY, S.: Surgical physiology of the renal pelvis and ureter. *Monographs in the surgical sciences* (1964), vol. 1:pp. 173–213
- [Bro99] BROWAEYS, J.; BACRI, J.-C.; FLAMENT, C.; NEVEU, S. and PERZYNSKI, R.: Surface waves in ferrofluids under vertical magnetic field. *The European Physical Journal B* (1999), vol. 9(2):pp. 335–341
- [Bur67] BURNS, J. C. and PARKES, T.: Peristaltic motion. *Journal of Fluid Mechanics* (1967), vol. 29:pp. 731–743
- [Ceb05] CEBERS, A.: Flexible Magnetic Swimmer. *Magnetohydrodynamics* (2005), vol. 41(1):pp. 63–72
- [Dob02] DOBROLYUBOV, A. I. and DOUCHYZ, G.: Peristaltic Transport as the Travelling Deformation Waves. *Journal of Theoretical Biology* (2002), vol. 219(1):pp. 55–61
- [Dor11] DORBOLO, S. and FALCON, E.: Wave turbulence on the surface of a ferrofluid in a horizontal magnetic field. *Phys. Rev. E* (2011), vol. 83(4):pp. 046303–8
- [euf11] EUFTEPAN: Slime mold (2011), URL <http://www.youtube.com/watch?v=GScyw3ammmk>, internet source august 2013, video
- [For76] FORTH, E. and SCHEWITZER, E.: Bionik, in: *Meyers Taschenlexikon*, VEB Bibliographisches Institut Leipzig, 1 edn. (1976)
- [Fra03] FRANKLIN, T.: *Ferrofluid Flow Phenomena*, Masterthesis, Massachusetts Institute of Technology (2003)
- [Fri10] FRIEDRICH, T.; REHBERG, I. and RICHTER, R.: Magnetic traveling-stripe forcing: Enhanced transport in the advent of the Rosensweig instability. *Phys. Rev. E* (2010), vol. 82(3), 036304
- [Gab50] GABRIELLI, G. and VON KARMAN, T.: What price speed – specific power required for propulsion of vehicles. *Mechanical Engineering, ASME* (1950), vol. 72(10):pp. 775–781

Bibliography

- [Gau05] GAUGER, E.: *Hydrodynamics of nanomachines in biology*, Ph.D. thesis, University of Konstanz (2005)
- [Gij04] GIJS, M. A. M.: Magnetic bead handling on-chip: new opportunities for analytical applications. *Microfluidics and Nanofluidics* (2004), vol. 1:pp. 22–40
- [Gog75] GOGOSOV, V. V.; VASIL’EVA, N. L.; TAKTAROV, N. G. and SHAPOSHNIKOVA, G. A.: Discontinuous Solutions to the Equations for a Polarizable and Magnetizable Multicomponent Multiphase Medium (1975)
- [Gon08] GONZÁLEZ GÓMEZ, J.: *Modular Robotics and Locomotion: Application to Limbless Robots*, Ph.D. thesis, Universidad Autónoma de Madrid (2008)
- [Gre06] GREISER, S.: Entwurf und Untersuchung eines Ferrofluid-Linearaktuators (2006), project thesis, Technische Universität Ilmenau
- [Gre07] GREISER, S.: 2D-Positionierung von Ferrofluiden in transparenten, unmischbaren Flüssigkeiten (2007), project thesis, Technische Universität Ilmenau
- [Gre08] GREISER, S.: Positionierung permeabler Stoffe im offenen Magnetkreis in Hinblick auf apedale Lokomotionssysteme (2008), diploma thesis, Technische Universität Ilmenau
- [Gre10a] GREISER, S.; BÖHM, V. and ZIMMERMANN, K.: Actuation of magnetic beads due to analogous position control by means of electromagnetic fields, in: WFB Wirtschaftsförderung Bremen (Editor) *Actuator 10 / International Conference on New Actuators*, pp. 685–688, (2010)
- [Gre10b] GREISER, S.; BÖHM, V. and ZIMMERMANN, K.: Position control of magnetic beads by means of electromagnetic fields with respect to apodal locomotion systems. *International Journal of Applied Electromagnetics and Mechanics* (2010), vol. 34:pp. 225–235
- [Har04] HARTSHORNE, H.: Ferrofluid-based microchip pump and valve. *Sensors and Actuators B: Chemical* (2004), vol. 99(2-3):pp. 592–600

- [Hat01] HATCH, A.; KAMHOLZ, A. E.; HOLMAN, G.; YAGER, P. and BOHRINGER, K. F.: A ferrofluidic magnetic micropump. *Journal of Microelectromechanical Systems* (2001), vol. 10(2):pp. 215–221
- [Hen07] HENNEBERG, R.: Untersuchung der Verformung von in einem flüssigen Trägermedium liegenden Ferrofluid-Tropfen im homogenen elektromagnetischen Feld und dessen Lageänderung infolge einer Feldverzerrung (2007), project thesis, Technische Universität Ilmenau
- [Hua02] HUANG, J.: *Modellierung, Simulation und Entwurf biomimetischer Roboter basierend auf apedaler undulatorischer Lokomotion*, Ph.D. thesis, Technische Universität Ilmenau (2002)
- [Kav11] KAVITHA, A.; HEMADRI REDDY, R.; SREENADH, S.; SARAVANA, R. and SRINIVAS, A. N. S.: Peristaltic flow of a micropolar fluid in a vertical channel with longwave length approximation. *Advances in Applied Science Research* (2011), vol. 2(1):pp. 269–279
- [Kii58] KIIL, F. M. D.: The function of the ureter and the renal pelvis. *American Journal of the Medical Sciences* (1958), vol. 235(5):p. 617
- [Kra05] KRAUSS, R.; REIMANN, B.; RICHTER, R.; REHBERG, I. and LIU, M.: Fluid pumped by magnetic stress. *Applied Physics Letters* (2005), vol. 86(2):p. 024102
- [Liu09] LIU, M. and STIERSTADT, K.: Colloidal Magnetic Fluids. *Lecture Notes in Physics* (2009), vol. 763:pp. 83–156
- [Lov05] LOVE, L. J.; JANSEN, J. F.; MCKNIGHT, T. E.; ROH, Y.; PHELPS, T. J.; YEARY, L. W. and CUNNINGHAM, G. T.: Ferrofluid Field Induced Flow for Microfluidic Applications. *IEEE/ASME Transactions on Mechatronics* (2005), vol. 10(1):pp. 68–76
- [Mal11] MALADEN, R. D.; DING, Y.; UMBANHOWAR, P. B.; KAMOR, A. and GOLDMAN, D. I.: Mechanical models of sandfish locomotion reveal principles of high performance subsurface sand-swimming. *Journal of the Royal Society Interface* (2011), vol. 8:pp. 1332–45

Bibliography

- [Mao05a] MAO, L. and KOSER, H.: Ferrohydrodynamic pumping in spatially traveling sinusoidally time-varying magnetic fields. *Journal of Magnetism and Magnetic Materials* (2005), vol. 289:pp. 199–202
- [Mao05b] MAO, L. and KOSER, H.: An Integrated, High Flow Rate MEMS Ferrofluid Pump, in: *Proceedings of the 9th International Conference on Miniaturized Systems for Chemistry and Life Sciences (μ TAS)*, (2005)
- [Mek05] MEKHEIMER, Kh. S.: Peristaltic Transport of a Newtonian Fluid Through a Uniform and Non-uniform Annulus. *The Arabian Journal for Science and Engineering* (2005), vol. 30(1):pp. 69–83
- [Mey99] MEYBERG, K. and VACHENAUER, P.: *Höhere Mathematik 1*, vol. 1, Springer-Verlag Berlin Heidelberg New York, 4 edn. (1999)
- [Mis03] MISHRA, M. and RAMACHANDRA RAO, A.: Peristaltic transport of a Newtonian fluid in an asymmetric channel. *Zeitschrift für Angewandte Mathematik und Physik (ZAMP)* (2003), vol. 54(3):pp. 532–550
- [Möh05] MÖHL, C.: Modellierung von Adhäsions- und Cytoskelett-Dynamik in Lamellipodien migratorischer Zellen (2005), master thesis, Rheinischen Friedrich-Wilhelms-Universität zu Bonn
- [Mor97] MORIDIS, G. J.; BORGH, S. E.; OLDENBURG, C. M. and BECKER, A.: Theoretical and Experimental Investigations of Ferrofluids for Guiding and Detecting Liquids in the Subsurface, Tech. Rep. March, Ernest Orlando Lawrence Berkeley National Laboratory (1997)
- [Moz09] MOZEIKA, A.; STELTZ, E. and JAEGER, H. M.: The first steps of a robot based on jamming skin enabled locomotion, in: *The 2009 IEEE/RSJ International Conference on Intelligent Robots and Systems*, pp. 408–409, (2009)
- [Nal76] NALETOVA, V. A. and SHAPOSHNIKOVA, G. A.: Disintegration of an arbitrary discontinuity in a perfectly conducting magnetizable incompressible medium. *Prikladnaia Matematika i Mekhanika* (1976), vol. 40:pp. 865–875, PMM - Journal

- of Applied Mathematics and Mechanics, vol. 40, no. 5, 1976, p. 816-826. Translation
- [Nal05] NALETOVA, V. A.: Lektii po Ferrohidrodinamike, Moskau Staatliche Universität M. V. Lomonosov, Fakultät für Mathematik und Mechanik, lecture script (2005)
- [Nal12] NALETOVA, V. A.; TURKOV, V. A.; PELEVINA, D. A.; ROZIN, V. A.; ZIMMERMANN, K.; POPP, J. and ZEIDIS, I.: Behavior of a free surface of a magnetic fluid containing a magnetizable cylinder. *Journal of Magnetism and Magnetic Materials* (2012), vol. 324:pp. 1253–1257
- [Neu64] NEURINGER, J. L. and ROSENSWEIG, R. E.: Ferrohydrodynamics. *Phys. Fluids* (1964), vol. 7:pp. 1927–1937
- [Ngu06] NGUYEN, N.-T.; NG, K. M. and HUANG, X.: Manipulation of ferrofluid droplets using planar coils. *Applied Physics Letters* (2006), vol. 89(5):p. 052509
- [od11] ONLINE DICTIONARY, IFToMM: locomotion (2011), URL http://www.iftomm.3me.tudelft.nl/2057_1031/frames.html, june 2011
- [Ode01] ODENBACH, S.: Ferrofluide - ihre Grundlagen und Anwendungen: Magnetische Flüssigkeiten kontrollieren. *Physik in unserer Zeit* (2001), vol. 32(3):pp. 122–127
- [Ode02a] ODENBACH, S. (Editor): *Ferrofluids - Magnetically controllable Fluids and their Applications*, Springer Lecture Notes in Physics 594, Berlin Heidelberg (2002)
- [Ode02b] ODENBACH, S.: *Magnetoviscous Effects in Ferrofluids*, Springer Lecture Notes in Physics, Springer Berlin (2002)
- [Ode09] ODENBACH, S. (Editor): *Colloidal Magnetic Fluids*, Springer, Lecture Notes in Physics 763, Berlin (2009)
- [Ode12] ODENBACH, S.: Feldgesteuerte Partikel-Matrix-Wechselwirkungen: Erzeugung, skalenübergreifende Modellierung und Anwendung magnetischer Hybridmaterialien, translation: field controlled particle matrix interaction: synthesis, multi-scale modelling and application of magnetic hybrid materials (2012), Announcement DFG priority program SPP 1681, Coordinator: S. Odenbach

Bibliography

- [Old00] OLDENBURG, C. M.; BORGLIN, S. E. and MORIDIS, G. J.: Numerical Simulation of Ferrofluid Flow for Subsurface Environmental Engineering Applications. *Transport in Porous Media* (2000), vol. 38(3):pp. 319–344
- [Ost95] OSTROWSKI, J.; BURDICK, J.; LEWIS, A. D. and MURRAY, R. M.: The mechanics of undulatory locomotion: the mixed kinematic and dynamic case, in: *Proceedings of 1995 IEEE International Conference on Robotics and Automation*, pp. 1945–1951
- [Ost98] OSTROWSKI, J. and BURDICK, J.: The Geometric Mechanics of Undulatory Robotic Locomotion. *The International Journal of Robotics Research* (1998), vol. 17(7):pp. 683–701
- [Pap65] PAPELL, S. S.: Low viscosity magnetic fluid obtained by the colloidal suspension of magnetic particles, Patent (1965), US 3 215 572 B1
- [Par00] PARK, G. S. and PARK, S. H.: New structure of the magnetic fluid linear pump. *Magnetics, IEEE Transactions on* (2000), vol. 36(5):pp. 3709–3711
- [Pop06] POPP, J.: Ferrofluide und Ferrogele - Neue Materialien in der Anwendung für Lokomotions- und Manipulationssysteme (2006), diploma thesis, Technische Universität Ilmenau
- [Pra09] PRASAD, K. M. and RADHAKRISHNAMACHARYA, G.: Effect of Peripheral Layer on Peristaltic Transport of a Micropolar Fluid. *Nonlinear Analysis: Modelling and Control* (2009), vol. 14(1):pp. 103–113
- [Ree87] REESE, G.: *Modelle peristaltischer Strömungen*, Ph.D. thesis, Universität Hannover, Fachbereich Physik (1987)
- [Ros85] ROSENSWEIG, R. E.: *Ferrohydrodynamics*, Cambridge University Press (1985)
- [Rub93] RUBI, J. M. and MIGUEL, M. C.: Transport phenomena in ferrofluids. *Physica A* (1993), vol. 194:pp. 209–217
- [Sch81] SCHATT, W.: *Einführung in die Werkstoffwissenschaft*, VEB Deutscher Verlag für Grundstoffindustrie Leipzig, 4. edn. (1981)

- [Sch05a] SCHERER, C. and FIGUEIREDO NETO, A. M.: Ferrofluids: properties and applications. *Brazilian Journal of Physics* (2005), vol. 35(3a):pp. 718–727
- [Sch05b] SCHNEIDER, F.; HOHLFELD, D.; VOGEL, W. and WALLRABE, U.: Evaluation von Ferrofluiden für hydraulische Aktoren, in: *Mikrosystemtechnik Kongress 2005*, VDE Verlag (Hrsg), pp. 831–834, (2005)
- [Sch06] SCHNEIDER, F.; HOHLFELD, D. and WALLRABE, U.: Miniaturized electromagnetic ferrofluid actuator, in: *ACTUATOR 2006, 10th International Conference on New Actuators*, pp. 289–292, (2006)
- [Sch09] SCHNACK, D. D.: *Lectures in Magnetohydrodynamics With an Appendix on Extended MHD*, The Lecture Notes in Physics, Springer, Berlin Heidelberg (2009)
- [Seo05] SEO, K. and PARK, G. S.: A Research on the Pumping Forces in the Magnetic Fluid Linear Pump. *IEEE Transactions on Magnetism* (2005), vol. 41(5):pp. 1580–1583
- [Spi06] SPIELMANN, C.: Entwicklung eines Sensors für einen ferrofluidischen Flächenaktor (2006), diploma thesis, Technische Universität Ilmenau
- [Ste08] STERR, V.; KRAUSS, R.; MOROZOV, K. I.; REHBERG, I.; ENGEL, A. and RICHTER, R.: Rolling ferrofluid drop on the surface of a liquid. *New Journal of Physics* (2008), vol. 10(6):p. 063029
- [Ste09] STERR, V.; MOROZOV, K. I. and ENGEL, A.: Ferrofluid drop rolling on the surface of a liquid. *Journal of Physics: Conference Series* (2009), vol. 149:p. 012112
- [Ste11] STEIGENBERGER, J.: Some theory towards a stringent definition of 'locomotion'. *Multibody System Dynamics* (2011), vol. 26:pp. 81–90
- [Ste12] STEIGENBERGER, J. and BEHN, C.: *Worm-Like Locomotion Systems – An intermediate theoretical Approach*, Oldenbourg, München (2012)
- [Tar69] TARAPOV, I. E.: Theory of magnetohydrodynamic lubrication. *Magnetohydrodynamics* (1969), vol. 5:pp. 104–108, en-

Bibliography

- glish translation: *Magneto hydrodynamics*, Vol. 5, No. 3, 65–69, 1969
- [Tar73] TARAPOV, I. E.: *Basic Problems in the Hydrodynamics of Magnetizable and Polarizable Media. Doctoral Dissertation [in Russian]*, Ph.D. thesis, Kharkov (1973)
- [Tar80] TARAPOV, I. E. and PATSEGON, N. P.: Nonlinear waves in conductive magnetizable fluid. *IEEE Transactions on Magnetics* (1980), vol. 16:pp. 309–316
- [Web02] WEBB, D. J.; PARSONS, T. J. and HORWITZ, A. F.: Adhesion assembly, disassembly and turnover in migrating cells – over and over and over again. *Nature cell biology* (2002), vol. 4(4):pp. E97–100
- [Wes85] WESER, T. and STIERSTADT, K.: Magnetoviscosity of Concentrated Ferrofluids. *Zeitschrift für Physik B Condensed Matter* (1985), vol. 59:pp. 257–260
- [Whi08] WHITE, M. F.: *Fluid Mechanics*, McCraw-Hill Companies, Inc., 6 edn. (2008)
- [Wit03] WITTE, H. and C., Schilling: Biologische Inspiration oligopodaler Laufmaschinen oder: Warum brauchen wir Biomechatroniker?, in: A. Wieser and W. Nachtigall (Editors) *BIONA-report 16. Technische Biologie und Bionik 6 – Mainz: Akad. der Wiss. und der Literatur*, vol. 16, Gesellschaft für Technische Biologie und Bionik (GTBB.) (2003), pp. 130–139
- [Wol90] WOLEDGE, R. C. and CURTIN, N. A.: The price of being a snake. *Nature* (1990), vol. 347:pp. 619–620
- [Yel05] YELLEN, B. B.; HOVORKA, O. and FRIEDMAN, G.: Arranging matter by magnetic nanoparticle assemblers. *Proceedings of the National Academy of Sciences of the United States of America* (2005), vol. 102(25)
- [Zah80] ZAHN, M. and SHENTON, K.: Magnetic fluids bibliography. *IEEE Transactions on Magnetics* (1980), vol. 16(2):pp. 387–415
- [Zai68] ZAITSEV, V. M. and SHLIOMIS, M. I.: The hydrodynamics of ferromagnetic fluids. *Zhurnal Prikladnoi Mekhaniki Tekhnicheskoi Fiziki* (1968), vol. 9(1):pp. 41–44, translated in **Journal**

- of Applied Mechanics and Technical Physics vol. 9, no. 1, pp 24–26, 1968
- [Zei00] ZEIDIS, I. and ZIMMERMANN, K.: Ein mathematisches Modell für die peristaltische Bewegung als Grundlage für das Design wurmartiger Mikroroboter, vol. 20 (2000), pp. 73–80
- [Zim04] ZIMMERMANN, K.; ZEIDIS, I.; NALETOVA, V. A. and TURKOV, V. A.: Waves on the surface of a magnetic fluid layer in a traveling magnetic field. *Journal of Magnetism and Magnetic Materials* (2004), vol. 268:pp. 227–231
- [Zim05] ZIMMERMANN, K.; ZEIDIS, I.; NALETOVA, V. A.; TURKOV, V. A. and BACHURIN, V. E.: Locomotion based on a two-layers flow of magnetizable nanosuspensions. *Journal of Magnetism and Magnetic Materials* (2005), vol. 290-291:pp. 808–810
- [Zim06a] ZIMMERMANN, K.; NALETOVA, V. A.; ZEIDIS, I.; BÖHM, V. and KOLEV, E.: Modelling of locomotion systems using deformable magnetizable media. *Journal of Physics: Condensed Matter* (2006), vol. 18(38):pp. 2973–2983
- [Zim06b] ZIMMERMANN, K.; ZEIDIS, I.; NALETOVA, V. A.; TURKOV, V. A.; BAYBURTSKIY, F. S.; LUKASHEVICH, M. V. and BÖHM, V.: Elastic Capsule Filled with Magnetic Fluid in an Alternative Magnetic Field, in: *EUROMECH Colloquium 470 Recent Development in Magnetic Fluid Research*, feb/mar, Technische Universität Dresden, pp. 41–42, (2006)
- [Zim07a] ZIMMERMANN, K.: Moving Like Worms : Without 'Legs'. *german research Magazine of the Deutsche Forschungsgemeinschaft* (2007), (3):pp. 24–26
- [Zim07b] ZIMMERMANN, K.; NALETOVA, V. A.; ZEIDIS, I.; TURKOV, V. A.; KOLEV, E.; LUKASHEVICH, M. V. and STEPANOV, G. V.: A deformable magnetizable worm in a magnetic field - A prototype of a mobile crawling robot. *Journal of Magnetism and Magnetic Materials* (2007), vol. 311(1):pp. 450–453
- [Zim07c] ZIMMERMANN, K.; ZEIDIS, I.; NALETOVA, V. A.; BÖHM, V. and POPP, J.: Locomotion Systems Basing upon Magnetisable, Highly Elastic Materials, in: *First Seminar on the Mechanics of Multifunctional Materials*, Bad Honnef, (2007)

Bibliography

- [Zim08a] ZIMMERMANN, K.; BÖHM, V.; POPP, J. and ZEIDIS, I.: A contribution about ferrofluid based apedal locomotion, in: *53. Internationales Wissenschaftliches Kolloquium*, Ilmenau, Germany, pp. 93–94, (2008)
- [Zim08b] ZIMMERMANN, K.; NALETOVA, V. A.; ZEIDIS, I.; TURKOV, V. A.; PELEVINA, D. A.; BÖHM, V. and POPP, J.: Surface of a magnetic fluid containing magnetizable bodies in an applied uniform magnetic field. *Magnetohydrodynamics. - Salaspils : Inst. of Physics, Univ. of Latvia* (2008), vol. 44(2):pp. 175–181
- [Zim09] ZIMMERMANN, K.; ZEIDIS, I.; BÖHM, V. and POPP, J.: A contribution about ferrofluid based flow manipulation and locomotion systems. *Journal of Physics: Conference Series* (2009), vol. 149:p. 012116
- [Zim10] ZIMMERMANN, K.; ZEIDIS, I.; BÖHM, V.; GREISER, S. and POPP, J.: Ferrofluid-based Flow Manipulation and Locomotion Systems. *Journal of Intelligent Material Systems and Structures* (2010), vol. 21:pp. 1559–1562
- [Zim11] ZIMMERMANN, K.; BÖHM, V. and ZEIDIS, I.: Vibration-driven mobile robots based on magneto-sensitive elastomers, in: *2011 IEEE/ASME International Conference on Advanced Intelligent Mechatronics (AIM2011)*, Budapest, Hungary, pp. 730–735, (2011)
- [Zr105] ZRÍNYI, M.; BARSÍ, L. and BÜKI, A.: Direct Observation of Discrete and Reversible Shape Transition in Magnetic Field Sensitive Polymer Gels (2005), URL <http://www.kfki.hu/about.cheminfo/hun/olvaso/zrinyi/polymgel.html>.

Acknowledgement

The research was financially supported by German Research Foundation (Deutsche Forschungsgemeinschaft) by the projects INK 22/C2, ZI 540/6-1, ZI 540/11-1 u.2, ZI 540/12-1 as well as by the graduation scholarship of the Free State of Thuringia.

Many people helped me in various ways to bring this thesis in the final state. I want to thank them all very dearly. Some have earned my special gratitude, because, without their help and encouragement, this thesis would not exist at all or not in this form.

Therefore, I thank K. Zimmermann for his mentorship, encourage and advise. With his quiet nature he managed to channel the appropriate energies of an unsettled spirit. It means a lot to me.

V. Böhm, always generous with his readiness to help – thank you, Valter, for so much.

I. Zeidis, who taught me and showed a great patience and ingenuity in doing so, thank you very much.

My colleagues and former colleagues of the Department of Technical Mechanics have deserved my special thank for various kinds of support, advise and fruitful discussions: F. Becker, C. Behn, B. Fiedler, E. Gerlach, I. Husung, T. Kästner, T. Kaufhold, H. Kirsten, E. Kolev, S. Stauche, J. Steigenberger, H.-P. Walkling and students, whose efforts I benefited from: R. Henneberg, S. Greiser, J. Molet Pérez, C. Spielmann.

I thank the colleagues of other departments, who provided me with measurement equipment, advise and more: O. Andrejew, L. Hartmann,

M. Hertl, C. Hecht, H. Hoppe, T. Linke, K.-P. Mangold, V. Minchenya, O. Radler, C. Resagk, C. Schilling, D. Voges, H. Witte.

I am very grateful to our partners from TU Dresden, the University of Bayreuth and from the M. V. Lomonosov Moscow State University in Russia, who have welcomed me always warmly and helped where they could: D. Borin, S. Odenbach and every other member of the team in Dresden, M. Krekhova, G. Lattermann, R. Richter from Bayreuth and S. Kalmykov, V. A. Naletova, D. Pelevina, V. A. Turkov, A. Vinogradova, T. Volkova from Moscow.

Thank you for the tedious work, like the drawings and the correction of the thesis: F. Heinz, C. Koch, J. Schieche.

Last but not least I thank my friends for good spirits, interesting views and holding up the moral, prominent among them: L., B. and S. Gossel, M. Müller, H.-C. Schwannecke, F. Schmidt, K. Wagner.

My family, my parents and sister, each of you brought me on my way and helped me to keep going on. Although not everyone of you came so far, although the troubled times are not finished: You are my family. I thank you.

Abstract

The presented thesis concerns the application of ferrofluids for biologically inspired, limbless and non-wheeling (nonpedal) locomotion systems. The theoretical and experimental treatment regards especially the technical implementation and the arising problems.

Chapter 1 gives a detailed introduction on the matters ferrofluids and locomotion. Among other issues, the attention is brought to practical aspects and the critical points are mentioned.

Chapter 2 presents the state of the art, which is divided into the publications of the Ilmenau research group and the author as well as the studies of others concerning ferrofluid based locomotion and closely related subjects. The core problem is pointed out: ferrofluids generate insufficient forces for locomotion purposes. The following motivation and the set tasks of this thesis take this issue into account.

Chapter 3 comprises a detailed analytic description of a peristaltic transport of a magnetic fluid, which is initially caused by an alternating magnetic field. The subsequent numerical calculation is based on realistic parameters obtained by the setup of an accompanying experiment. The numerical and experimental results are qualitatively compared and critically discussed.

The basic idea of chapter 4 is the increase of serviceable forces by enhancement of the surface deformation. The surface deformation of a magnetic fluid, which is amplified by the insertion of an iron cylinder within the magnetic field, is experimentally and theoretically analyzed. A discussion of the qualitative comparison is given.

Chapter 5 concerns an experiment, which avoids the persistent problem of covering the highly adhesive ferrofluid. Here, a ferrofluid actuator propels the channel flow of a secondary fluid. The functional parameters are obtained by measurement and discussed.

Chapter 6 focuses on the forces generated by ferrofluids. The first part regards the measurement of forces used in systems of an immobile ferrofluid volume assisting another object to perform locomotion (passive locomotion system). In the second part the forces are acquired by analytical and numerical calculations and by measurement. They are implemented in a close-loop-control system for positioning mobile ferrofluid portions (active locomotion system).

Chapter 7 summarizes the basic idea with regard to various projects. With the background of unfavorable properties of the ferrofluid it is questionable whether technical solutions of ferrofluid based locomotion systems will be widely used. The preview shows a promising development of ferroelastomers and -gels.

Kurzfassung

Basierend auf Bewegungsformen wie sie von biologischen Systemen bekannt sind, die mit Hilfe von (periodischer) Gestaltänderung Fortbewegung erzielen, und der kontrollierbaren Oberflächendeformation von Ferrofluiden, werden die Möglichkeiten Ferrofluide für Lokomotionszwecke zu nutzen untersucht. Dies wird belegt durch detaillierte Auseinandersetzung und Verweise auf entsprechende Literatur.

Großes Gewicht wird auf die technische Implementierung gesetzt und die daraus erwachsenden Problemfelder. Daher werden neben einem ausführlichen theoretischen Teil, in dem ein magnetfeldinduzierter peristaltischer Materialtransport einer magnetischen Flüssigkeit analytisch betrachtet wird, auch weitläufig praktisch-experimentelle Untersuchungen angestellt.

Wichtige Größen wie ferrofluiderzeugte Kräfte und Drücke werden messtechnisch für den Allgemeinfall ermittelt. Hierbei wird unterschieden zwischen Systemen, die mit lokal bewegten Ferrofluidportionen anderen Objekten zur Lokomotion verhelfen (passive Lokomotionssysteme) und Systemen, deren mobile Ferrofluidportionen selbst Position und Lage verändern (aktive Lokomotionssysteme). Anhand von Prototypen werden Prinzipien und Funktionsparameter gesondert analysiert und diskutiert. Diese speziellen Untersuchungen werden teilweise durch analytische und numerische Modelle gestützt.

Auf zwei Kernprobleme wird aufmerksam gemacht: Ferrofluide generieren geringe nutzbare Kräfte und aufgrund der starken Adhäsion ist eine schützende Einkapselung notwendig. Zwei Untersuchungen gehen hierauf ein. Mit der Idee, eine Steigerung der nutzbaren Kräfte hervorzurufen, wird die Verstärkung der Oberflächendeformation, die im Magnetfeld durch das Einführen hochpermeabler Körper hervorgerufen wird, analytisch und experimentell untersucht. Weiterhin wird ein Experiment vorgestellt, welches die Einkapselung des Ferrofluids umgeht. Hier ist ein Ferrofluidaktor eingebettet in einer Zweitflüssigkeit und treibt diese zur Kanalströmung an.

Mit Referenz auf die Grundidee ferrofluidbasierter Lokomotion werden die Teiluntersuchungen zusammengefasst. Vor dem Hintergrund, dass die nachteiligen Eigenschaften des Materials bislang nicht beherrscht werden, bleibt es abzuwarten inwiefern sich technische Lösungen ferrofluidbasierten Lokomotionssysteme verbreiten werden. Im Ausblick wird auf vielversprechende Entwicklungen magnetosensitiver Elastomere und Gele aufmerksam gemacht.